Coffin, M.F., Frey, F.A., Wallace, P.J., et al., 2000
Proceedings of the Ocean Drilling Program, Initial Reports Volume 183

7. Site 1139[1]

Shipboard Scientific Party[2]

BACKGROUND AND OBJECTIVES

Site 1139 lies on Skiff Bank (Leclaire Rise), a bathymetric and gravimetric high ~350 km west-southwest of the Kerguelen Archipelago (Fig. F1). Flanked to the south and west by Cretaceous oceanic crust of the Enderby Basin, Skiff Bank appears to be structurally related to and bathymetrically continuous with the northern Kerguelen Plateau (NKP) (Schlich et al., 1998). At least two major faults, however, offset interpreted igneous basement between Skiff Bank and the NKP massif (Coffin et al., 1986) containing the Kerguelen Archipelago. Skiff Bank has been proposed to be the current site of the Kerguelen hot spot (e.g., Duncan and Storey, 1992; Müller et al., 1993), but hundreds of meters of sediment cover in places argue against Skiff Bank originating entirely by Holocene volcanism (Figs. F2, F3). Both Skiff Bank and Elan Bank trend east–west (Fig. F1), approximately perpendicular to the trends of fracture zones in the Enderby Basin and, thus, parallel to the axis of breakup between Antarctica and India (Royer and Coffin, 1992). The free-air gravity signatures of the two features are also similar; pronounced negative anomalies flank their southern margins, but not their northern margins (Fig. F1). It is thus possible that Skiff and Elan (Site 1137) Banks originated via similar processes and are composed of basaltic and continental rocks. Many rock types, including both aphyric basalt and plutonic rocks (such as alkali granite), were recovered in a single dredge haul from Skiff Bank, quite close to Site 1139 (Figs. F1, F3). These plutonic rocks were interpreted as ice-rafted debris (Weis et al., 1998). Hence, the age and composition of Skiff Bank's igneous crust, and its relationship to the contiguous NKP are not established. Although the age of the NKP is commonly believed to be Cenozoic, having largely formed since ~40 Ma when the Southeast Indian Ridge separated Broken Ridge and the central Kerguelen Plateau (Royer and Coffin, 1992), submarine igneous basement of the NKP has never been

F1. Satellite-derived free-air gravity map of the Kerguelen Plateau, p. 62.

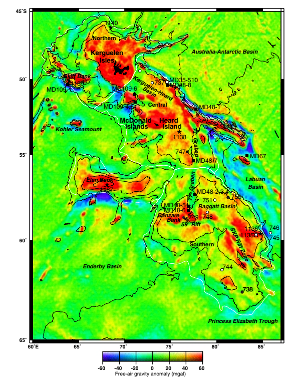

F2. Location of Site 1139 and site-survey data, p. 64.

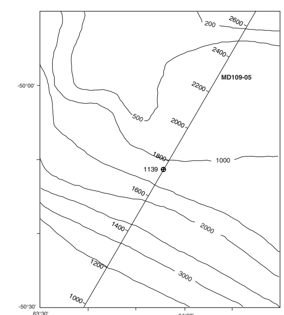

F3. *Marion Dufresne* MD109-05 multichannel seismic profile across Site 1139, p. 65.

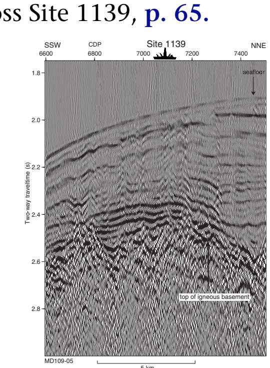

[1]Examples of how to reference the whole or part of this volume.
[2]Shipboard Scientific Party addresses.

Ms 183IR-107

drilled. We located Site 1139 on *Marion Dufresne* multichannel seismic (MCS) line MD109-05 (Fig. **F2**). Site 1139 lies at a depth of 1427 m on Skiff Bank's southwestern terrace, which lies >1000 m lower than the crest, located <50 km to the northeast. We chose this location primarily because of its thin sedimentary section (Fig. **F3**). The top of acoustic basement is flat lying, and overlying basement is a sediment sequence ~500 m thick. The fault scarp marking the boundary between Skiff Bank and the Enderby Basin lies ~20 km southwest of Site 1139, and it offsets basement by >2700 m.

Summary of Objectives

The main objectives at this site were to

1. Characterize the petrography and compositions of the lavas;
2. Determine the age of the lavas, testing the hypothesis that the uppermost igneous basement of Skiff Bank is ~40 Ma, the age of the oldest known igneous rock from the Kerguelen Archipelago (Giret and Lameyre, 1983; Giret and Beaux, 1984), or younger (e.g., Duncan and Storey, 1992; Müller et al., 1993);
3. Determine the physical characteristics of the lava flows;
4. Identify the environment of eruption (subaerial or submarine);
5. Obtain minimum estimates for the age of basement from overlying sediment;
6. Estimate the duration of possible subaerial and shallow marine environments from the sedimentary and igneous record;
7. Determine the facies of the seismic stratigraphic sequences;
8. Define the ages of seismic sequence boundaries; and
9. Determine the paleoceanographic history of this high-latitude site.

OPERATIONS

Site 1139

Favorable weather and wind direction resulted in good speed during the relatively short transit to Site 1139. The 910-km move was made in 51.8 hr at an average speed of 9.5 kt. We arrived on site midday on 15 January 1999. At 1023 hr on 15 January 1999, we deployed a beacon on the precise Global Positioning System coordinates for Site 1139.

Hole 1139A

We spudded Hole 1139A at 1525 hr on 15 January 1999. The seafloor depth adjusted to the rig floor was estimated at 1427.0 m below rig floor (mbrf), equivalent to 1415.3 m below sea level. The 3.5-kHz precision depth recorder had indicated an adjusted seafloor depth of 1431.4 mbrf.

Continuous wireline coring proceeded in foraminifer-bearing diatom ooze and nannofossil ooze through Core 183-1139-7R to a depth of 66.5 mbsf. No chert was encountered. Recovery for this interval averaged 52.0%, and the average rate of penetration (ROP) was 40.3 m/hr. The formation then graded into gray nannofossil clay to a depth of 104.7 mbsf. The average recovery in this interval was 39.1%, whereas the average ROP was 41.7 m/hr. Coring continued through gray nannofossil claystone (78.4% average recovery; 38.4 m/hr average ROP) and into packstone and grainstone with abundant shell fragments. The ROP through this unit was very fast (43.2 m/hr), and the average recovery dropped dramatically to 7.9%. Basement was encountered at ~460 mbsf. The uppermost basement unit consisted of cobbles of dense felsic volcanic rock, underlain by deposits of pumice breccia, welded tuff, and intensely altered felsic volcanic breccia. This unit drilled quite fast at 35.4 m/hr, but recovery remained very poor at 6.5%. From Cores 183-1139A-51R through 62R, more altered felsic volcanic and volcaniclastic rocks were recovered, coring at 12.4 m/hr with 20.7% average recovery. Basalt was reached at the base of Core 183-1139A-62R at ~595 mbsf. Recovery in the basalt improved remarkably to an average of 61.0%. The ROP average 4.0 m/hr but varied from a low of 3.0 m/hr to as much as 7.8 m/hr. Coring was terminated with the recovery of Core 183-1139A-73R from a depth of 694.2 mbsf. This was ~99 m into basalt, or ~204 m into volcanic and volcaniclastic rock, and exceeded the scientific depth objective for this site. A total of 356.63 m of core was recovered for an overall average of 51.4%. A summary of core numbers, depths, and recovery is given in Tables T1 and T2.

T1. Coring summary, p. 180.

T2. Expanded coring summary, p. 182.

During the coring operation, mud sweeps were pumped as needed. In basement, sweeps were pumped during every core. During the wiper trip made in preparation for wireline logging, the pipe was pulled to 525.0 mbsf using the top drive. Overpull was 20,000–40,000 lb, and torque ranged from 300 to 600. Circulation was not possible until that point. While running the pipe into the hole, the driller noted little trouble other than a slight hole drag of 20,000–30,000 lb until a hard bridge was identified ~8.0 m above the basalt contact at a depth of 587.0 mbsf. Drilling reaming from that point required 5 hr to reach a point 25 m above bottom, where progress slowed considerably. The hole was swept with sepiolite mud, and the bit was released. After displacing the hole with sepiolite mud, the end of the pipe was placed at a depth of 101.7 mbsf for logging.

The first wireline logging run included the natural gamma-ray tool (NGT), the dipole shear sonic imager (DSI), the dual induction-spherically focused resistivity tool (DITE-SFR), and the Lamont-Doherty Earth Observatory (LDEO) high temperature/acceleration/pressure tool (TAP). The loggers decided not to deploy a nuclear source because of questionable hole conditions, and the deteriorating weather would not allow use of the wireline heave compensator. This logging run reached a depth of 593.0 mbsf but could not pass below the basalt contact. Once logging was begun, this tool string failed and had to be recovered. After troubleshooting, the problem was determined to be the sonic tool. The DSI tool was replaced with the long spaced sonic (LSS) tool, and the tools were run in the hole for a second time. After once again reaching the basalt contact, the hole was logged from that point up.

The weather and sea state rapidly began to deteriorate as the logging tools reached the end of the drill pipe. At this point, logging was abandoned and all effort went into getting the drill string above the seafloor. By then the wind speed was consistently blowing ~45 kt with gusts over 50 kt, and the swells had grown to nearly 20 m. Once at the rig floor, the logging tools were quickly hung off, the logging electric line was pulled out of the way, and the circulating head was removed from the top of the drilling string. A total of five stands of drill pipe were pulled. With the pipe hung ~118 m above the seafloor, we began waiting on weather.

This weather was the worst we experienced during Leg 183. The force 10/11 storm resulted in a maximum average sustained wind from the west-southwest of 48 kt, gusting to >60 kt. The maximum average seas were 3–5 m, and the maximum average swell height was 7–10 m. Maximum pitch/roll was 9° and 6°, respectively. By 1300 hr on 21 January 1999, the sea state improved enough to safely allow resumption of the drill string trip. A total of 16 hr was spent waiting on weather.

While the drill string was being tripped, the positioning beacon was released and recovered. The end of the drill string reached the rig floor at 1625 hr. The ship was immediately secured for transit, and, at 1630 hr on 21 January 1999, we got under way for Site 1140.

LITHOSTRATIGRAPHY

Introduction

Site 1139 is located west of Kerguelen Island in 1415 m of water on Skiff Bank (Leclaire Rise) on the western flank of the Kerguelen Plateau. Hole 1139A was rotary cored continuously to a depth of 694.2 mbsf. Sediments were recovered from 0 to 461 mbsf. Extensively altered volcaniclastic rocks, basalts, and one minor sedimentary bed were recovered from the lower 233 m of the hole (Fig. F4). The sedimentary section above igneous basement consists of ~383 m of predominantly calcareous claystones and chalks with relatively thin intervals of calcareous ooze and calcareous chalk at the top and base, respectively. These sediments overlie a thin interval (<10 m) of sandy packstones and ~77 m of predominantly grainstones (Fig. F4; Table T3). The sedimentary section rests unconformably on igneous basement. We recognize five sedimentary lithologic units (Units I–V) in the upper part (0–461.7 mbsf) of Hole 1139A. The basement volcanic rocks are designated lithologic Unit VI and are subdivided into basement Units 1–19 (Fig. F4) (see **"Physical Volcanology,"** p. 13, **"Igneous Petrology,"** p. 36, and **"Alteration and Weathering,"** p. 42, for descriptions). Core recovery varied from good to poor throughout the sedimentary sections of Hole 1139A (Fig. F4).

F4. Composite stratigraphic section, p. 66.

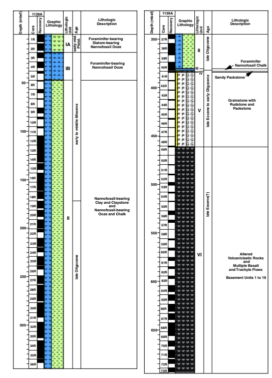

T3. Summary of lithologic and basement units, p. 189.

Unit I

Interval: 183-1139A-1R-1, 0 cm, to 5R-CC, 25 cm
Depth: 0 to 47.50 mbsf
Age: early Pleistocene to early Miocene

Unit I is calcareous ooze. In the top three cores, much of the sediment is highly disturbed or soupy from drilling; thus, we could not accurately determine the true thicknesses and stratigraphic positions of individual beds. We have divided Unit I into two subunits based on the abundance of diatoms (Fig. F4; Table T3). The lithology changes between Cores 183-1139A-2R and 3R, corresponding to a major hiatus (early Pleistocene to middle Miocene; see **"Biostratigraphy,"** p. 9).

Subunit IA (interval 183-1139A-1R-1, 0 cm, to 2R-CC, 19 cm; 0–19.00 mbsf) is predominantly tan to light gray foraminifer-bearing, diatom-bearing nannofossil ooze of middle to early Pleistocene age. X-ray diffraction (XRD) analysis shows calcite and amorphous silica. The carbonate content ranges from 64 to 75 wt% $CaCO_3$ (Table T4). In addition, thin intervals of deformed white foraminifer-bearing nannofossil ooze (intervals 183-1139A-1R-3, 48–95 cm; 2R-1, 28–53 cm; 2R-1,

T4. XRD results, carbonate contents, and total and organic carbon contents, p. 190.

98–136 cm; and 2R-2, 47–85 cm) are present within this unit, but we cannot determine if these intervals represent in situ mass-transport deposits (e.g., slump) or normal pelagic deposits disrupted by the drilling. Scattered basalt sand grains and rare small pebbles are disseminated throughout the subunit. We identified traces of pumice in smear slides. A major hiatus marks the base of Subunit IA.

Subunit IB (interval 183-1139A-3R-1, 0 cm, to 5R-CC, 25 cm; 19.00–47.50 mbsf) is predominantly foraminifer-bearing nannofossil ooze of middle to early Miocene age, which grades downward in color from white through very light gray and very pale brown to light greenish gray. Core 183-1139A-3R is composed of foraminifer-bearing, diatom-bearing nannofossil ooze. The carbonate content of the subunit ranges from 74 to 83 wt% $CaCO_3$ (Table **T4**), with a mean of 78 wt%. The organic carbon content in Sample 183-1139A-4R-1, 92 cm, is 0.3%. The XRD analyses show the presence of calcite, traces of alkali feldspar, and traces of opal-A in Core 183-1139A-3R (Table **T4**). Clay minerals are present in Core 183-1139A-5R, and sponge spicules are abundant. A few black pebbles of basalt and other volcanic material are present in Section 183-1139A-3R-1. Green mottles, most likely from traces of glauconite, are present around and within burrows scattered through Cores 183-1139A-4R and 5R. The basal contact of Subunit IB is gradational.

Unit II

Interval: 183-1139A-6R-1, 0 cm, to 40R-5, 92 cm
Depth: 47.50 to 380.72 mbsf
Age: late Oligocene to middle Miocene

Unit II comprises most of the sedimentary section at Site 1139 and is a thick (333 m) section of interbedded gray to greenish gray nannofossil-bearing clay and claystone and nannofossil-bearing ooze and chalk (Fig. **F4;** Table **T3**). The color ranges from dark greenish gray to greenish gray in the upper portion of the unit (47.5–170 mbsf, Cores 183-1139A-6R through 18R) and is primarily gray with several thin intervals of light gray in the lower portion (170–380.72 mbsf, Cores 183-1139A-18R through 40R). The sediments become progressively stiffer downhole and are sufficiently indurated by 100–110 mbsf (Cores 183-1139A-11R and 12R) to be classified as claystone and chalk. Most of the sediments of Unit II are extensively burrowed, including many good examples of *Zoophycos* and *Chondrites*.

The carbonate content of sediments in Unit II fluctuates widely and ranges from 7 to 72 wt% $CaCO_3$ (Table **T4**) with an average of 44 wt%. These fluctuations indicate that the sediments of Unit II are primarily nannofossil clay or claystone with interbeds of nannofossil ooze or chalk, nannofossil-bearing clay or claystone, and rare claystone (Table **T4**). Carbonate-rich intervals are found above Core 183-1139A-9R (<70 mbsf), between Cores 183-1139A-18R and 25R (160–230 mbsf), and below Core 183-1139A-36R (>340 mbsf). Much of the sediment in interval 183-1139A-8R-1, 0 cm, to 10R-CC, 19 cm (66.5–95.1 mbsf) is diatom-bearing, nannofossil-bearing clay and ooze. Near the base of the unit (interval 183-1139A-39R-1, 0 cm, to 40R-5, 92 cm), the sediment is foraminifer-bearing nannofossil claystone.

The XRD analyses (Table **T4**) show traces of sanidine throughout Unit II. Quartz is a rare trace component in Cores 183-1139A-13R, 14R, 16R, 28R, and 36R. Clay minerals, maghemite, pyrite, and glauconite are present in most cores. Clinoptilolite is present as a trace component below 250 mbsf. Organic-carbon contents vary from 0.03% to 0.36%, with an average of 0.17%.

Irregular green patches, mottles, and laminae, which we attribute to very fine glauconite, are common throughout many intervals of this unit. XRD analyses confirm the presence of glauconite throughout this unit (Table T4). This glauconite is found as discrete thin laminae (which both crosscut [Core 183-1139A-21R] and are cut by burrows), as diffuse laminae, as halos around burrows, concentrated within burrows, and as discrete dark blebs (possibly burrow cross sections). The laminae, which are generally 1 mm or less in thickness, commonly are in closely spaced groups. Each group is usually 3 to 10 cm thick, and groups of laminae are common (several to more than a dozen per core) in the lower portion of the unit (below 172 mbsf, Core 183-1139A-19R). The crosscutting relationships with burrows clearly indicate that the glauconite is an early diagenetic feature.

Chert is absent from the entire section except for a single nodule near the base of the unit (interval 183-1139A-40R-1, 26–27 cm). Tephra layers are very rare; however, an ash layer of medium thickness is in interval 183-1139A-38R-4, 62–88 cm. In addition, volcanic ash is locally concentrated in burrows and disseminated in thin, presumably bioturbated zones (intervals 183-1139A-11R-1, 107–120 cm; 18R-3, 9–10 cm; 33R-1, 107–115 cm; 38R-3, 0–19 cm, and 39R-2, 119–128 cm). Two minor faults with slickensides in the lower portion of the unit display steep to moderate dips. The slickensides attest to their origin by faulting, rather than drilling disturbance. The lower boundary of Unit II is fairly sharp, though obscured somewhat by burrowing, and color changes noticeably from gray to light brownish gray across the boundary (Fig. F5A).

F5. Examples of foraminifer nannofossil chalk in Unit III, p. 68.

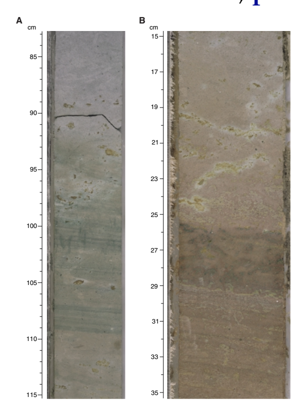

Unit III

Interval: 183-1139A-40R-5, 92 cm, to 40R-CC, 20 cm
Depth: 380.72 to 383.50 mbsf
Age: late Eocene to late Oligocene

Unit III is a thin interval of foraminifer nannofossil chalk (Fig. F4; Table T3), which is of strikingly different color than the overlying gray claystones and chalks of Unit II (Fig. F5). This chalk lightens in color from light brownish gray (10YR 6/2; Fig. F5A) in the top through reddish yellow (5YR 6/6; Fig. F5B, F5C) to pink (5YR 7/4) in the lower 20 cm. Groups of darker rusty brown laminae, which are <2 mm thick, are present in intervals 183-1139A-40R-6, 27–40 and 72–82 cm (Fig. F5C). The carbonate content is high throughout the unit and is 94% $CaCO_3$ near its base (Sample 183-1139A-40R-CC, 12 cm) (Table T4). The organic carbon content is 0.04%. The XRD analysis shows only calcite in Unit III.

The reddish colors of the sediment are not characteristic of deep-sea foraminifer nannofossil oozes and chalks and suggest that iron from the underlying sediments and/or basement rocks has been mobilized, transported upward into this unit, and precipitated during diagenesis. A major hiatus (~33–31 Ma) near or within interval 183-1139A-40R-6, 89–91 cm (see **"Biostratigraphy,"** p. 9) has no obvious lithologic expression.

Unit IV

Interval: 183-1139A-41R-1, 0 cm, to 41R-2, 40 cm

Depth: 383.50 to 384.87 mbsf
Age: Eocene or older

Unit IV consists of a thin interval of dusky red to greenish pink sandy packstone (Fig. F4; Table T4). Poorly sorted, subrounded to well-rounded sand-sized grains are predominantly composed of highly altered basaltic glass and volcanic rock fragments (Fig. F6). A thin section (Sample 183-1139A-41R-1, 40–43 cm) (Table T5) shows abundant microsparitic matrix (~30%–50%). Grains are predominantly volcanic lithic (~95%) and include a few vesicular grains. Altered basaltic glass is present and most of the volcanic material is highly altered. A single grain of silt-sized polycrystalline, slightly strained quartz with triple-junction crystal boundaries is present.

Bioclasts are rare (~5%). Benthic foraminifers and a few planktonic foraminifers document an open-marine depositional environment. Accessory bioclasts include echinoderms, ostracodes, and bivalve shell fragments. All bioclasts are strongly recrystallized. Cements are rare and mostly blocky and drusy calcite. Very thin fringes of fibrous calcite are rare. The cements are partially silicified.

F6. Sandy packstone of Unit IV, p. 70.

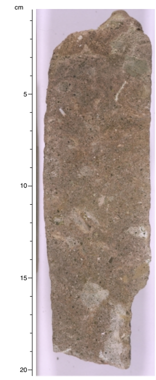

T5. Summary of thin sections, p. 191.

Unit V

Interval: 183-1139A-41R-2, 40 cm, to 49R-1, 110 cm
Depth: 384.87 to 461.70 mbsf
Age: Eocene or older

Unit V consists predominantly of grainstone with some thin interbeds of rudstone (e.g., interval 183-1139A-41R-2, 48 cm, to 42R-1, 9 cm) and packstone (e.g., interval 183-1139A-42R-1, 9–20 cm) (Figs. F4, F7; Table T3). These sediments are white to brownish gray in the upper part of the unit (Figs. F7A, F8) but are rusty yellowish brown in interval 183-1139A-46R-1, 0 cm, to 49R-1, 110 cm (Fig. F7B). White layers of subangular, coarse-grained bioclasts are interlaminated with brownish, siliciclastic, fine- to coarse-grained sands, which are well sorted, subrounded, and iron stained. Some layers (Cores 183-1139A-46R through 48R) include subangular to well-rounded siliciclastic granules and pebbles. Several intervals display well-developed cross-stratification with apparent dips up to 25° (Figs. F7C, F7D, F8A, F8B, F8C). A few burrows are present. The sorting and grain size indicate a high energy environment (e.g., a carbonate shoal).

F7. Examples of grainstones and packstones of Unit V, p. 71.

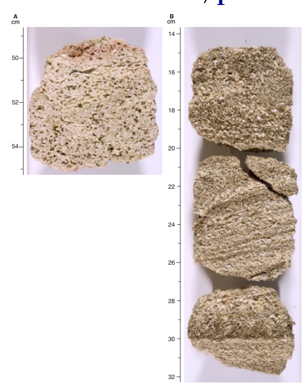

Two thin sections (Samples 183-1139A-41R-2, 50–54 cm, and 42R-1, 67–70 cm) (Table T5) confirm the very well-sorted nature of this coarse grainstone. In both thin sections, porosity is high (~20%–30%) and approximately half of the pores are filled with calcite cement. Bioclasts are highly fragmented and consist of shell fragments including serpulid worm tubes (50%), bryozoans (10%), echinoderms (<5%), and rare benthic foraminifers. Many shells are micritized. Although the size-sorting is entirely consistent with a high-energy environment, most of the bioclastic grains are angular. Mineral and rock grains make up only ~2% of the total volume. In interval 183-1139A-41R-2, 50–54 cm, they include volcanic fragments with phenocrysts of plagioclase and alkali feldspar. In interval 183-1139A-42R-1, 67–70 cm, the volcanic rock fragments have phenocrysts mainly composed of alkali feldspars.

F8. Examples of cross-stratified grainstones of Unit V, p. 73.

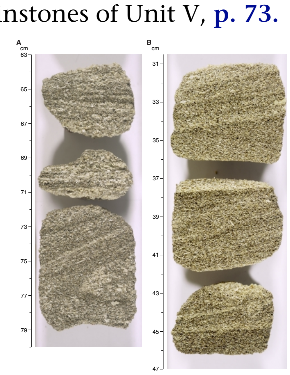

A thin section (Sample 183-1139A-41R-2, 50–54 cm) (Table T5) shows that irregular dog-tooth calcite cement fills some pores. Syntaxial rim cements on echinoderms and rare blocky calcite cement also are present. The syntaxial cements formed synchronously with the dog-tooth cements. In Sample 183-1139A-42R-1, 67–70 cm, echinoderm syntaxial rims are predominant. Other bioclasts show very thin fringes of dog-tooth cements.

Unit VI

Interval: 183-1139A-49R-1, 110 cm, to 73R-3, 148 cm
Depth: 461.70 to 694.20 mbsf
Age: Eocene or older

Lithologic Unit VI consists of highly altered volcaniclastic and felsic volcanic rocks, altered basalt flows, and minor sedimentary rock (Fig. **F4;** Table **T3**). Unit VI is subdivided into 19 basement units, which are described in the **"Physical Volcanology,"** p. 13, **"Igneous Petrology,"** p. 36, and **"Alteration and Weathering,"** p. 42. A 47-cm-thick bed of bioclast-bearing sandstone, which is very similar to the grainstones of Unit V, is present in the uppermost basement unit (Subunit 1B) (see **"Physical Volcanology,"** p. 13).

Discussion

Basaltic lava flows and overlying felsic volcanic rocks (Unit VI) were severely hydrothermally altered (see **"Alteration and Weathering,"** p. 42) before deposition of a marine sequence commenced in the Eocene. Well-rounded pebbles at the base of the marine sequence in the top of basement Subunit 1A (lithologic Unit VI) suggest beach deposition. Cross-stratified grainstones (Unit V) record a high-energy shallow marine (neritic) environment such as a carbonate shoal. The coarse grain sizes (granules and pebbles) in the terrigenous fraction suggest a nearshore setting. The siliciclastic component of the grainstones records erosion of the felsic volcanic rocks. The grainstone facies differs from Cretaceous neritic facies on the Kerguelen Plateau (Sites 747–750 and 1136–1138), which contain glauconite and micritic matrix and reflect a lower-energy environment than that of Site 1139. This ~80-m-thick grainstone deposit thus constitutes the first sequence of high-energy neritic carbonate facies recovered from the plateau.

With continued subsidence, grainstone deposition gave way to deposition of sandy packstone (Unit IV), which indicates a low-energy neritic environment. The presence of planktonic foraminifers indicates an open-marine setting. However, the predominance of sand-sized terrigenous material still indicates a position close to the shore. The strong recrystallization of the calcitic components of the packstone may be explained by meteoric diagenesis, in accordance with the presence of dog-tooth cements and echinoderm rim cements. Altered volcanic grains and abundant clay minerals suggest a weathered source terrane.

Chalk in Unit III indicates the onset of pelagic conditions in a bathyal environment during latest Eocene to early Oligocene time. From late Oligocene through middle Miocene time, the Site 1139 area received variable influxes of terrigenous (hemipelagic) clay from an adjacent volcanic landmass, and these formed the gray claystone and chalk of Unit II. These fluctuations may be related to sea-level changes, climatic fluctuations, or tectonic activity. Undiluted pelagic calcareous oozes (Subunit IB) were deposited from the later part of middle Miocene time until at least early Pleistocene time. The abundance of diatoms in

Subunit IA indicates that during the Pleistocene Site 1139 was subject to cold water masses south of the Polar Front.

BIOSTRATIGRAPHY

At Site 1139, a thin (19 m) Quaternary section of foraminifer/diatom-bearing nannofossil ooze (lithologic Subunit 1A) is underlain by a greatly expanded 364-m lower upper Miocene to mid-Oligocene calcareous pelagite with generally well-preserved siliceous and calcareous microfaunas and floras (lithologic Subunit IB to Unit III). There is no appreciable chert within this section, which was deposited well above the calcite compensation depth (present water depth = 1415.5 m).

Minimum sedimentation rates are ~18 m/m.y. in the Miocene and 29 m/m.y. in the Oligocene, or 23 m/m.y. for the entire Tertiary pelagic section (Fig. F9). We attribute the high sedimentation rates to high regional pelagic productivity, plus the influx of fine terrigenous clastics derived from the weathering of exposed portions of the volcanic edifice, Skiff Bank, on which the sediments were deposited (see "Lithostratigraphy," p. 4). The clastic input colored the normally white calcareous ooze and chalks gray to brownish gray. Only at the bottom of the section, where such input was minimal, are the sediments oxidized to a pinkish color.

F9. Age-depth plot, p. 75.

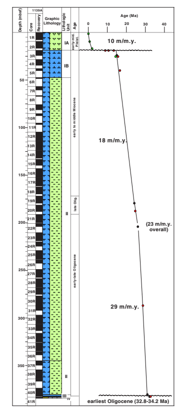

An unusual nannofossil *Braarudosphaera* bloom in the late Oligocene has been reported previously from the southern Kerguelen Plateau (Wei and Thierstein, 1991) and may correlate with other such occurrences of this age in the Atlantic and Indian Oceans. We date a foraminiferal nannofossil chalk at the base of the pelagic section (Section 183-1139-40R-6) as earliest Oligocene in age by nannofossils and foraminifers (within the interval 32.8 to 34.3 Ma; CP16a/b and basal AP13).

Calcareous Nannofossils and Diatoms

Calcareous nannofossils were generally well preserved and abundant in selected intervals only of the Quaternary of lithologic Subunit IA and are consistently abundant and generally well preserved in the Miocene–Pliocene nannofossil oozes of Subunit IB and Unit II. They were abundant and moderately well preserved in the lowermost Oligocene of Unit III, where some taxa show overgrowths.

Diatoms, observed only in smear slides, were abundant and pristine in the Quaternary section. In the middle Miocene at the top of lithologic Subunit IB (Sample 183-1139A-3R-CC), they are abundant and moderately well preserved. Diatoms were not studied systematically below that level, but useful occurrences were noted in some nannofossil smear slides.

Quaternary

A relatively pure nannofossil ooze in Sample 183-1139A-1R-1, 33 cm, consisted of common *Gephyrocapsa* sp. and *Coccolithus pelagicus,* but over 90% of the assemblage consisted of small 2- to 3-µm forms presumed to be *Emiliania huxleyi,* which indicates an age of about 84 ka for this sample. *C. pelagicus* was only present in the "few" to "common" categories in core-catcher Samples 183-1139A-1R-CC and 2R-CC. We dated these samples by using diatoms, which belonged to the *Actinocy-*

clus ingens Zone. In Sample 183-1139A-1R-CC, the nominate species abounds as does *Thalassiosira lentigenosa; T. elliptipora* are few.

Tertiary

Sample 183-1139A-3R-CC contains abundant *Cyclicargolithus abisectus, C. floridanus, Coccolithus miopelagicus, Helicosphaera granulosa,* common *Calcidiscus leptoporus/macintyrei,* and common *Discoaster variabilis,* which placed it in the combined CN5a/CN3 Zone (middle to latest early Miocene). Diatoms are abundant with common *A. ingens,* but no pennates were noted in the smear slide; this probably indicates that we can assign this sample to the early part of the middle Miocene (between ~15 and 16 Ma). This age date is consistent with the relatively large number of discoasters, which prefer warmer water conditions than prevailed at this site after that time.

Discoaster veriabilis is rare and cyclicargolithids are few in Sample 183-1139A-4R-CC, which is dominated by coccolithids and reticulofenestrids. These suggest cooler conditions than in the superjacent core. Climate-induced alternations are common in this part of the section but will not be described here in detail because of the wide spacing of the core-catcher samples.

Samples 183-1139A-5R-CC to 8R-CC are mid-early Miocene in age. Of these, Samples 183-1139A-5R-CC and 7R-CC contain few to common *Discoaster deflandrei*. Samples 183-1139A-9R-CC through 18R-CC lack *C. leptoporus/macintyrei,* and we assigned them to the lower Miocene Zones CN2–CN1 in a section greatly expanded by the influx of clays derived from volcanic parent materials (see **"Lithostratigraphy,"** p. 4). Among the diatoms, we noted *Raphidodiscus marylandicus* (early Miocene to earliest middle Miocene) in Sample 183-1139A-13R-CC, abundant *Atinopthycus undulatus* in Sample 183-1139A-15R-CC, and *Nitzschia maleinterpretaria* in 183-1139A-17R-CC.

The downhole last occurrence (LO) of *Reticulofenestra bisecta* in Sample 183-1139A-19-CC marks the nannofossil top of the Oligocene at these latitudes and also marks the top of the zone of that name. We also assigned the next two core-catcher samples to this zone, which is expanded here because of the input of fine clastics as described above. We noted *Helicosphaera euphrates* and *D. deflandrei* in Sample 183-1139A-20R-CC.

Samples 183-1139A-22R-CC to 40R-6, 22–24 cm, contain *Chiasmolithus altus* and *C. abisectus* in the absence of *Reticulofenestra umbilica;* we assigned the samples to the mid-Oligocene *C. altus* Zone. The LO of *Zygrhablithus bijugatus* occurs in Sample 183-1139A-2R-CC, which is near the top of the *C. altus* Zone. *Helicosphaera bramlettei* occurs sporadically in this part of the zone (Samples 183-1139A-26R-CC, 27R-CC, and 29R-CC), as do a small number of pontosphaerids (a few *Pontosphaera multipora* and *P.* sp. cf. *inconspicua* in Sample 183-1139A-26R-CC; a large, high-rimmed *Pontosphaera* sp. is found in Sample 183-1139A-30R-CC). *Discoaster deflandrei* is rare (Sample 183-1139A-30R-CC) as is *Coronocyclus* sp. (Sample 183-1139A-29R-CC).

An unusual occurrence is *Braarudosphaera bigelowii,* which is common as both whole and fragmented specimens in Sample 183-1139A-30R-CC. Wei and Thierstein (1991, table 3) recorded a similar occurrence of this normally neritic taxon in this part of the stratigraphic column in Hole 737B on the NKP. These occurrences might correspond to the rather widespread Oligocene *Braarudosphaera* blooms in the Atlantic (e.g., Parker et al. 1985) and Indian Ocean off northwest Australia (Siesser et al., 1992).

Diatoms are common in some intervals. We noted *Azpetia oligocenica* in Sample 183-1139A-32R-CC.

We noted a single reworked specimen of *Ismolithus recurvus* toward the bottom of the *C. altus* Zone in Sample 183-1139A-38R-CC. A few *Discoaster tanii* (five- and six-rayed) plus a flood of small reticulofenestrids are present in Sample 183-1139A-39R-CC, along with *Reticulofenestra daviesii,* which ranges higher in the zone. A few *D. deflandrei* and common *Helicosphaera perch-nielseniae* accompany *Sphenolithus moriformis* in Sample 183-1139A-40R-2, 25–27 cm, and small, delicate pontospherids that superficially resemble *Reticulofenestra oamaruensis* are found throughout much of this core; however, the overall assemblage is characteristic of the *C. altus* Zone. *Blackites spinosa* abounds in Sample 183-1139A-40R-5, 25–27 cm.

The color of the sediment changes in the lower part of Section 183-1139A-40R-5 downhole from a greenish to a reddish orange color, but the nannoflora do not change until an apparent disconformity is crossed between Samples 183-1139A-40R-6, 20–22 cm, and 40R-6, 89–91 cm, well within the oxidized sediments (see **"Lithostratigraphy,"** p. 4). The latter sample and Sample 183-1139A-40R-CC are characterized by abundant *Reticulofenestra hillae,* common to abundant *I. recurvus* along with few to common *Coccolithus formosus, D. deflandrei,* and *D. tanii,* abundant *Clausicoccus fenestratus, C. altus,* and *C. oamaruensis*. We observed no *C. abisectus, Discoaster saipanensis, R. oamaruensis,* or *Reticulofenestra reticulata.*

A broad age range for the assemblage described above is represented by the last occurrence of *C. formosus* (32.8 Ma) and the last occurrence of *R. reticulata* (35.4 Ma) or the first occurrence of *I. recurvus* (35.7–36.3 Ma at these latitudes according to Wei, 1992). This assumes that *D. saipanensis* and *R. oamaruensis* are not present here because of truncated upper ranges resulting from ecological restriction in these higher latitudes (e.g., Wei, 1992). Nevertheless, this age range spans the Eocene/Oligocene boundary. The high abundance of *Clausicoccus fenestratus,* however, suggests essentially an earliest Oligocene age (~CP16a/b) when compared with the Eocene/Oligocene sequence at Deep Sea Drilling Project Leg 71 Hole 511 on the Falkland Plateau and Ocean Drilling Program Leg 119 Hole 737B on the southern Kerguelen Plateau (Wise, 1983, table 1A; Wei and Thierstein, 1991, table 3, respectively). At these localities, *C. fenestratus* is quite rare or absent below the Eocene/Oligocene boundary.

Nevertheless, the co-occurrence of *Coccolithus formosus* and *Isthmolithus recurvus* below the disconformity and the co-occurrence of *C. abisectus* and *R. umbilica* above signals the absence of at least the *R. davesii* Zone and possibly more. The missing section would be equivalent to at least CP16c, CP17, and lower CP18.

Planktonic Foraminifers

We recovered relatively abundant and well-preserved assemblages of Quaternary (upper Pleistocene) and upper Neogene planktonic foraminifers from lithostratigraphic Subunits IA and IB. In contrast, middle Miocene to Oligocene assemblages in the nannofossil-bearing clays and claystones of Unit II contain sparse and only moderately well-preserved planktonic foraminifers. Preservation quality and abundance of microfossils increases dramatically in the reddish orange foraminifer nannofossil chalk of Unit III beneath the pelagic section. Individual foraminifers from this short interval exhibit pink iron oxide staining. Planktonic foraminifers are absent from the micritized grainstones and packstones of Unit V. These coarse and generally unconsolidated, shoaled-carbonate sediments contain abundant bryozoan fragments, rare mollusk-shell fragments, and occasional benthic foraminifers.

Quaternary

Planktonic foraminifer assemblages in Samples 183-1139-1R-CC and 2R-CC are dominated by *Neogloboquadrina pachyderma* and *Globigerina bulloides,* with less common *Globigerina falconensis, Turborotalia quinquelobula,* and *Globorotalia puncticulata*. This assemblage, typical of high-latitude Indian Ocean sites, is composed of long-ranging species (late Miocene to Holocene), which are of little biostratigraphic utility. Large, spherical radiolarians also abound in the Subunit IA diatom oozes.

Neogene

The cream-beige nannofossil ooze of Unit II exhibits the highest carbonate content for the entire sedimentary succession (see **"Organic and Inorganic Geochemistry,"** p. 54) but contains fewer planktonic foraminifers than the overlying diatom-ooze. Samples 183-1139-3R-CC and 4R-CC contain generally small but well-preserved *G. bulloides, Globigerina woodi, Globorotalia miozea, Globorotalia praescitula,* and *Globorotalia panda*. *Neogloboquadrina* spp. is absent, indicating that we can place these samples in the middle Miocene. The presence of *G. panda* is interesting. Berggren (1992) shows the range of this species on the central Kerguelen Plateau restricted to a short interval in the late middle Miocene. At lower latitudes, this species ranges into the lower middle Miocene (Kennett and Srinivasan, 1983). The more northerly position of this site (~ 49°S compared to ~56°S) and implied slightly warmer water conditions may allow a longer biostratigraphic range at Site 1139. Until additional samples are studied, we assign this assemblage to Zones NK4–NK5.

Abundance and preservation of microfossils is poor in the following 315 m of green-gray nannofossil clays and claystones (Unit II) because of dilution by abundant grain aggregates that did not break down during sample washing. Planktonic foraminifers are of limited biostratigraphic use in this section. Samples 183-1139-5R-CC to 39R-CC contain radiolarians and rare benthic and planktonic foraminifers, except for a few intervals where clay content decreases and microfossil abundance increases slightly. *Globorotalia zealandica, Paragloborotalia incognita, Catapsydrax unicavus, Globigerina brazieri, Globigerina praebulloides, Globigerina* spp. cf. *G. labiacrassata,* and *Tenuitella* spp. are sporadic in Samples 183-1139-5R-CC to 17R-CC, indicating an early to middle Miocene age.

Paleogene

After an interval of particularly poor preservation and low microfossil abundance in Cores 183-1139-18R to 29R, we recognize the upper Oligocene zonal marker *Globigerina euapertura* in Sample 183-1139-30R-CC. Also present in this sample are rare *C. unicavus, Globorotalia opima,* and *Globorotaloides* spp. *Chiloguembelina cubensis* appears to be absent, which suggests that we can place this sample in the AP16–AP15 zonal range.

The next sample with recognizable planktonic foraminifers is Sample 183-1139-32R-CC. Rare, but moderately well-preserved, specimens of *Tenuitella gemma, Tenuitella munda, Globrotalia opima,* and *Globorotaloides* spp. occur with *C. cubensis*. In the absence of the Zone AP13 marker *Subbotina angiporoides,* we assign this sample to mid-Oligocene Zone AP14. Despite low planktonic foraminifer abundance, we also assign Samples 183-1139-33R-CC and 34R-CC to Zone AP14 with reasonable confidence. The last five cores of Unit II, Cores 183-1139-35R to 39R, are essentially barren of planktonic foraminifers.

Unit III sediments were of dramatically different color and composition and yielded abundant and well-preserved planktonic foraminifers. Common *Subbotina angiporoides, Catapsydrax unicavus, C. cubensis, T. gemma,* and *Subbotina utilusindex* in Sample 183-1139-40R-CC, in the absence of *Globigerinatheka index,* indicate a latest Eocene to early Oligocene age (Zone AP13). We cannot delineate the Eocene/Oligocene boundary using planktonic foraminifers (denoted by the extinction of the Hantkeninidae at low to middle latitudes [Coccioni et al., 1988; Berggren et al., 1995]) because the important index species (*Hantkenina* spp. and *Cribrohantkenina* spp.) are not found at high latitudes. The core catcher of Core 183-1139-40R-CC is the last interval above igneous basement that contains datable microfossils. We estimate the maximum age of these to be 34.3–30.3 Ma.

PHYSICAL VOLCANOLOGY

The basement rocks of Site 1139 were divided into 19 pyroclastic and lava flow units (Table T6). However, because of significant alteration and faulting, many of the unit boundaries may not have primary volcanological significance. Even the identification of rock type has been difficult in several units. In the following, we describe the rocks in each unit and then, in the interpretive section that follows, we explain the rationale for our divisions. The distribution of volcaniclastic materials is summarized in Table T7.

T6. Basement unit contacts, p. 192.

T7. Summary of volcaniclastic components, p. 193.

Unit Descriptions

Lithologic Units

Units I–V: Fossiliferous Sediments (Interval 183-1139A-1R-1, 0 cm, to 49R-1, 109 cm)

Volcaniclastic materials in the sedimentary sequence at Site 1139 are present both as discrete tephra layers and disseminated in pelagic and hemipelagic sediments (Table T8). The foraminifer-bearing diatom-bearing nannofossil ooze in Subunit IA contains disseminated (<2%), sand-sized basaltic lithic fragments, rare small volcanic pebbles, and traces of very fine sand-sized pumice. In the foraminifer-bearing nannofossil ooze of Subunit IB, XRD analysis shows the presence of minor alkali feldspar (sanidine?) (Core 183-1139A-3R) (Table T4) (see **"Lithostratigraphy,"** p. 4), and a few small basalt pebbles are present in Section 183-1139A-3R-1. Volcanic components in core-catcher samples show that there was a concentration of basaltic glass in Cores 183-1139A-8R and 16 R (see Table T8); these may be primary, bioturbated glassy intervals.

T8. Distribution of volcanic components in Units I–V, p. 194.

Three tephra horizons (intervals 183-1139A-11R-1, 107–109 cm; 38R-3, 17–19 cm; 38R-4, 80–82 cm) (Table T9) were identified in nannofos-

T9. Identified pyroclastic ash-fall deposits, p. 195.

sil-bearing clay and claystone of Unit II. In the gray claystone and chalk of Unit II, concentrations of volcanic clays and lithic fragments may be associated with pulses of terrigenous (hemipelagic) clay-rich sediments from late Oligocene to middle Miocene time (see **"Lithostratigraphy,"** p. 4). Disseminated and bioturbated volcanic ash-rich domains were observed in intervals 183-1139A-18R-3, 9–10 cm, and 33R-1, 107–115 cm. Using XRD analysis, we identified alkali feldspar (sanidine?) and rare quartz distributed throughout this unit. Volcanic components were not apparent in the foraminifer nannofossil chalk (Unit III) but volcanic lithic fragments are abundant (make up ~95% of clasts) in the sandy packstone (Unit IV). Volcanic lithic and crystal (dominantly alkali feldspar) fragments make up <3% of the grainstone in Unit V.

Basement Units

Subunit 1A: Massive and Flow-Banded Felsic Volcanic Pebbles (Interval 183-1139A-49R-1, 109 cm, to 52R-1, 56 cm)

More than 30 subrounded (Fig. **F10A**), massive and flow-banded, pale orange to pale green rhyolitic lava cobbles and pebbles are present at the top of basement. All of the clasts have abraded outer surfaces consistent with reworking. There are a range of internal textures from massive or planar laminated to clasts with convoluted flow banding and a few breccia pebbles. However, planar flow-banded lava clasts are the most common with less and approximately equal amounts of convoluted flow-banded and massive cobbles (Fig. **F10B**). The average clast size is ~3 mm× 5 mm, and pebbles are elongate with a short axis to long axis ratio of ~70%. Most clasts have feldspar phenocrysts present, and, in the more massive cobbles, these phenocrysts are up to 2 mm in diameter. There are one or two dark gray to pink and white, altered (silicified), possibly mafic lithologies represented, but these form a minor component.

F10. Basement Subunit 1A, **p. 76.**

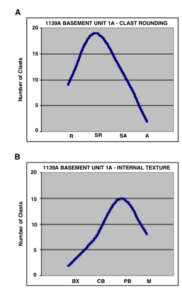

Subunit 1B: Bioclastic Sandstone (Interval 183-1139A-52R-1, 56 cm, to 52R-1, 103 cm)

This 47-cm-thick interval of bioclastic sandstone is very similar to the grainstone (Unit V) described in the lithologic section at Site 1139 (Figs. **F7, F8**). In thin section, there are <1% crystals, volcanic lithics, and glass shards in this interval (see **"Lithostratigraphy,"** p. 4).

F11. Close-up photograph of interval 183-1139A-52R-1, 117–130 cm, **p. 77.**

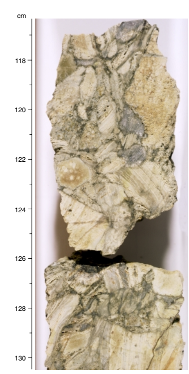

Subunit 1C: Pumice/Flow-Banded Felsic Breccia (Interval 183-1139A-52R-1, 103 cm, to 53R-1, 25 cm)

A 44-cm interval of altered, dominantly closed framework breccia, with white to pale green partially altered clasts, is best represented at the base of Section 183-1139A-52R-1 (Fig. **F11**). At the top of Section 183-1139A-53R-1, we find abraded rubble and a breccia cobble, a massive green flow-banded cobble, and a wholly silicified dark colored cobble that appear unrelated to the rest of Subunit 1C. The pumice/flow-banded felsic breccia has an average clast size of 1.0 cm × 1.7 cm and a maximum clast size of 2.5 cm × 5.0 cm. In thin section (interval 183-1139A-52R-1, 120–123 cm), the clasts are banded perlite. The spheroidal perlitic fractures reflect quenching and hydration of felsic glass and the alignment of perlite kernels suggests that these glassy clasts were originally flow banded (Fig. **F12**). Some clasts in the breccia resemble pumice, but pumice was not observed in thin section. The matrix contains coarse sand-sized fragments of similar composition to the clasts in a clay-sized matrix. The matrix is more indurated than the clasts.

F12. Photomicrograph showing banded perlite in breccia clasts and the tight contact between clasts, **p. 78.**

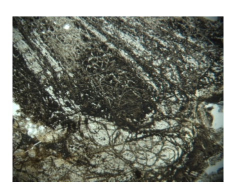

Subunit 1D: Altered Perlitic Felsic Glass (Interval 183-1139A-53R-1, 25 cm, to 54R1-1, 0 cm)

This interval is dominated by dark orange to red, altered, massive perlitic glass (Fig. **F13**) with <10% lithic clasts. The average lithic clast size is 1.3 cm × 2.0 cm and the maximum clast size is 2.5 cm × 3.5 cm. Spheroidal perlitic fracture sets, from 0.5 to 1.5 cm in diameter, are present in the glass and are best represented in interval 183-1139A-53R-1, 110–122 cm. In thin section (Sample 183-1139A-53R-1, 127–130 cm), excellent examples of perlitic fracture textures are preserved, including nested perlite kernels (Fig. **F14**) and evolution of longitudinal and secondary fractures. There are also flow textures in the glass and rotation of included clasts (Fig. **F15**). One fragment of phenocryst-rich banded perlite is incorporated in the thin section (Sample 183-1139A-56R-3, 93–97 cm) and is a flow-banded glass clast (Fig. **F16**).

A subhorizontal fracture set displaces the perlitic glass of interval 183-1139A-53R-2, 9–23 cm (Fig. **F17**). Near one large, relatively open fracture, there is more abundant clay-mineral formation around perlite kernels (Fig. **F17**). Toward the base of Subunit 1D, the disrupted perlitic glass is gradational into breccia with an indurated, massive, light-colored matrix. In the interval 183-1139A-53R-2, 38–127 cm, felsic breccia with variably altered clasts of perlitic glass and incorporated lithic fragments is the principal lithology (Fig. **F18**).

Subunit 1E: Sheared and Altered Volcaniclastic Sediment (Fault Zone; Interval 183-1139A-54R-1, 0 cm, to 55R-1, 0 cm)

Resinous to powdery, green and red (oxidized), clay-rich altered rock in interval 183-1139A-54R-1, 22–56 cm, has been intensely sheared. Below this (interval 183-1139A-54R-1, 56–108 cm) is a suite of variably sheared, dark and pale green, altered clastic rocks with subhorizontal fabric delineated by pale green wispy to angular granule-sized clasts. The preserved texture contains primary pyroclastic features, but alteration obscures the primary textures of the clasts (see **"Alteration and Weathering,"** p. 42). At the top of Section 183-1139A-54R-1 (interval 183-1139A-54R-1, 0–22 cm), there is an assortment of pebbles that appear similar to cobbles in Subunit 1A. These have probably fallen downhole during drilling. The uppermost piece (interval 183-1139A-54R-1, 0–10 cm) is a massive pale orange rhyolite. The second piece (interval 183-1139A-54R-1, 10–15 cm) is a massive bright orange pebble with incorporated lithic fragments and an abraded outer surface. In interval 183-1139A-54R-1, 15–22 cm, massive orange-brown rubble has little preserved internal texture. It is possible these pebbles are all derived from the same place as the collection of rounded cobbles observed in Subunit 1A.

Unit 2: Dark Red Welded Vesicular Rhyolite (Interval 183-1139A-55R-1, 0 cm, to 56R-1, 78 cm)

Unit 2 consists of dark red (oxidized) welded vesicular rhyolite with abundant (<20%), commonly broken, sanidine and minor quartz crystals (Sections 183-1139A-55R-1, 16–72 cm, and 56R-1, 11–78 cm). Flattening and agglutination textures are common (Fig. **F19**). Domains of flattened wispy clasts define a subhorizontal fabric in clasts with subparallel trains of void spaces (vesicles?) enhancing the texture. These rocks are very similar to the uppermost material in Unit 4. In thin section, the clear banded texture may reflect the flattening of clasts. No glass shards can be recognized; however, the sample is highly altered (Fig. **F20**). The lowermost part (interval 183-1139A-56R-1, 68–78 cm) is

F13. Close-up photograph of interval 183-1139A-53R-1, 110–121 cm, **p. 79.**

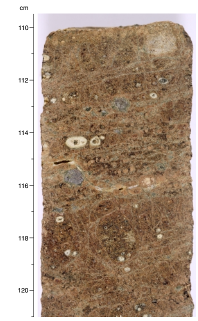

F14. Photomicrograph showing nested, spheroidal perlitic fractures in devitrified and altered felsic volcanic glass, **p. 80.**

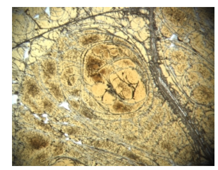

F15. Photomicrograph showing rotation of an enclosed clast within the glass **p. 81.**

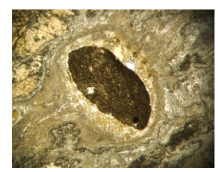

F16. Photomicrograph showing banded perlite, **p. 82.**

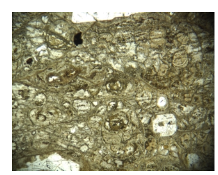

F17. Close-up photograph of interval 183-1139A-53R-2, 9–23 cm, **p. 83.**

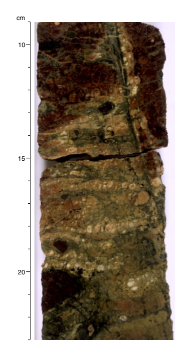

brecciated with matrix-supported clasts (0.2 cm × 0.3 cm) near the base; it has a more clastic texture than the overlying welded rhyolite and becomes green near the contact with Unit 3.

At the top of the Section 183-1139A-55R-1, there are two gray to pink and white rounded cobbles that look similar to those described as a wholly silicified (mafic?) lithology from Subunit 1A and one small altered white pebble of unknown origin. At the top of Section 183-1139A-56R-1, there are two small, green, silicified breccia pebbles with pale orange flow-banded clasts, which appear to be unrelated to the Unit 2 rocks. These rocks may have fallen downhole during drilling.

Unit 3: Altered Crystal Vitric Tuff-Breccia (Interval 183-1139A-56R-1, 78 cm, to 57R-1, 92 cm)

The contact between Unit 2 and Unit 3 (interval 183-1139A-56R-1, 78–80 cm) is sheared, and color changes from dark red to green across the contact. Although the crystal composition (sanidine and minor quartz) and abundance (<20%) remains similar across the contact, the internal texture of the rock changes significantly. The green crystal vitric tuff-breccia is highly altered to green clay, is largely unconsolidated, and has been disturbed by drilling at the top of Sections 183-1139A-56R-2 and 56R-3. The material can be crumbled and reduced to individual crystals and relict perlite kernels in a clay matrix. There are coherent domains in this interval that retain banded textures (e.g., intervals 183-1139A-56R-1, 126–133 cm; 56R-2, 50–56 cm; and 56R-3, 68–76 cm) (Fig. F21) and some subangular lithic pebbles (e.g., interval 183-1139A-56R-3, 117–119 cm). The lower part of Section 183-1139A-56R-3 (76–150 cm) is more consolidated, and a thin section from this part of the core (Sample 183-1139A-56R-3, 94–98 cm) shows ~15% sanidine and ~4% quartz suspended in relict perlitic glass (~40%) with clay minerals (~40%) in the interstices between perlite kernels (Fig. F22). At the base of Section 183-1139A-56R-3 (130–150 cm), there is a faint subhorizontal fabric within the tuff, which is not related to an enclosed clast.

In Section 183-1139A-57R-1, the green color continues through a finer grained domain (interval 183-1139A-57R-1, 8–45 cm), which has an oblique contact with the more crystal-rich tuff in Piece 2 and has a basal breccia in Piece 7. This finer grained material is massive and may be either a large clast or a finer grained interval lower in the stratigraphy of the tuff. Beneath this interval is a domain (interval 183-1139A-57R-1, 45–92 cm) of dark green material with up to granule-sized pale green clasts (pumice?) and a similar proportion of crystals (<20%) as the crystal-vitric tuff. In parts, this interval is red (oxidized), slightly brecciated, and has contacts with enclosed clasts (e.g., interval 183-1139A-57R-1, 84–92 cm). The contact with the underlying Unit 4 is defined by a strong color change from dark green to dark red.

Unit 4: Dark Red Welded Vesicular Rhyolite (Interval 183-1139A-57R-1, 92 cm, to 60R-2, 54 cm)

Unit 4 consists of dark red (oxidized) rock that is moderately vesicular, crystal rich, and massive. In these regards it is very similar in texture to Unit 2. In detail, the pieces show a variety of textures and two different styles of brecciation. Even relatively massive intervals contain clasts up to 10 cm long, with concentrations of elongated vesicles along the sutures (Fig. F23). Many of the vesicle-rich zones are subvertical. The rock contains ~5 vol% equant to elongate, very angular, 0.3- to 5-mm vesicles, though vesicularities as high as 15% are present locally. Only

F18. Close-up photograph of interval 183-1139A-53R-2, 51–60 cm, **p. 84.**

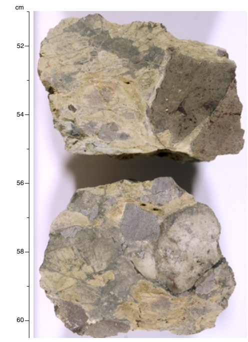

F19. Close-up photograph of interval 183-1139A-56R-1, 36–41 cm, **p. 85.**

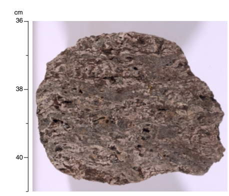

F20. Photomicrograph showing domains of flattened wispy clasts, **p. 86.**

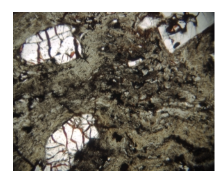

F21. Close-up photograph of interval 183-1139A-56R-3, 85–95 cm, **p. 87.**

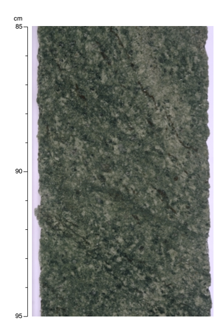

interval 183-1139A-60R-2, 60–127 cm, is massive with no evidence of brecciation. Phenocrysts are present and randomly oriented.

In the upper part of Unit 4, the breccia has 0.5- to 2-cm clasts with irregular shapes cemented to each other without filling voids and vesicles. Voids make up <50% of this type of breccia, giving it a highly vesicular to pumiceous appearance. A second breccia, with <1.5-cm angular fragments, commonly with jigsaw-fit textures, contains ~40% clay-rich matrix, makes up ~10% of Sections 183-1139A-57R-1, 57R-2, and 57R-3, and dominates Sections 183-1139A-59R-1, 60R-1, and 60R-2 (Fig. **F24**).

Unit 5 (Interval 183-1139A-61R-1, 0 cm, to 62R-1, 0 cm)

The 81 cm of rock recovered from Unit 5 consists of a highly fractured and brecciated moderately feldspar-phyric trachyte with pink, green, and white alteration (Fig. **F25**). The clasts and more coherent parts of the unit are massive and featureless, except for randomly oriented feldspar phenocrysts. Core 183-1139A-61R-1, 0–33 cm, consists of a breccia with >1-cm subangular, subequant clasts making up 50–60 vol%. Only 15–20 vol% of the breccia is <1 mm in size, mostly consisting of a reddish black (5R 2/2) clay. The clasts between 1 mm and 1 cm in size are mostly subrounded. The underlying rock appears to have been coherent with variable degrees of fracturing. The massive nature of the rock makes it difficult to assess the proportion of distinct clasts and the amount of clast rotation in the fractured zones. Many zones do not appear to be breccias related to the emplacement of the rocks of Unit 5; they have a cataclastic appearance. The bottom of the unit has a highly altered breccia with some matrix-supported textures.

Unit 6 (Interval 183-1139A-62R-1, 0 cm, to 64R-1, 0 cm)

The 6.72 m of aphyric trachybasalt recovered from Unit 6 consist of one core of highly altered and disturbed breccia and a second core of more coherent pieces. Core 183-1139A-62R consists of a very dark red to reddish black breccia with a clay-rich matrix (Fig. **F26**). The rock fragments within the clay matrix are angular, with fractures cutting through the smaller (more altered) clasts but generally circumventing the larger (~10 cm) less-altered clasts. The angular rock fragments and more coherent pieces of rock are from a volcanic breccia dominated by subangular-subrounded clasts of mafic lava. The lava has ~1–5 vol% vesicularity with 0.1- to 4-mm elongate, subrounded vesicles. Core 183-1139A-63R was also poorly recovered but the 5- to 30-cm-long pieces of core are mostly coherent lava petrographically similar to the clasts in Core 183-1139A-62R. However, the rocks in Core 183-1139A-63R are denser with ≤1 vol% vesicularity and a bimodal vesicle size distribution (<1-mm round and >1-cm elongated vesicles). Core 183-1139A-63R-2 also contains two 30-cm-long intervals of breccia with a clay-rich matrix. This breccia has a cataclastic morphology and the clay matrix contains abundant well-formed slickenslides.

Unit 7 (Interval 183-1139A-64R-1, 0 cm, to 64R-3, 0 cm)

The 2.72 m of aphyric basaltic trachyandesite recovered from Unit 7 consist of 1.88 m of coherent lava sandwiched between highly altered breccias. The top of Unit 7 (Core 183-1139A-64R-1, 0–46 cm) is a dusky red (5R 3/4) to reddish black (5R 2/2) breccia. The dominant clasts have horizontally elongated fluidal shapes with fine-grained margins along contacts with clasts of different lithologies. In some cases, the fluidal clasts envelop a medium-sand-sized, feldspar-rich sand. Vesicularity of

F22. Photomicrograph showing the internal texture of the crystal vitric tuff-breccia, **p. 88.**

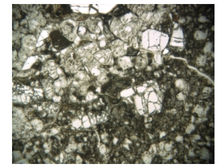

F23. Close-up photograph of interval 183-1139A-57R-2, 46–57 cm, **p. 89.**

F24. Close-up photograph of interval 183-1139A-60R-2, 54–61 cm, **p. 90.**

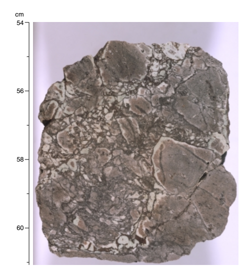

F25. Close-up photograph of interval 183-1139A-61R-1, 5–17 cm, **p. 91.**

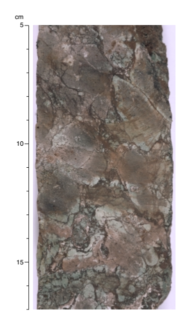

the clasts varies from 1 to 20 vol% with elongated to round, ≤1-mm vesicles. At Sample 183-1139A-64R-1 (Piece 9, 47 cm), there is an abrupt switch to a light gray coherent lava. Section 183-1139A-64R-1 (Pieces 9–12) contains 7% irregular <0.1- to 3-mm vesicles. Beneath these pieces to Section 183-1139A-64R-2, 80 cm, the lava generally has 3–5 vol% horizontally elongated ellipsoidal 2- to 5-mm-long vesicles. There are two exceptions. At interval 183-1139A-64R-1, 73–77 cm, a 1 cm × 3 cm rectangular vesicular domain is incorporated in the denser lava, and at interval 183-1139A-64R-1, 124–126 cm, a 1.5 cm × 2 cm megavesicle is found. Below Section 183-1139A-64R-2, 80 cm, the lava becomes much more vesicular with 15–20 vol% angular irregular 0.5-mm to 2-cm vesicles. Also, in the working half, at Section 183-1139A-64R-2 (Piece 4A, 93.5 cm) a 3 mm × 3 mm xenolith containing larger crystals is seen. The last coherent rock (interval 183-1139A-64R-2, 101–104 cm) has fewer and smaller vesicles. The remainder of Unit 7 is a sheared and altered breccia with pale red (5R 6/2) clasts in a light greenish gray (5GY 8/1) clay.

Unit 8 (Interval 183-1139A-64R-3, 0 cm, to 65R-1, 0 cm)

The 3.33 m of aphyric trachybasalt recovered from Unit 8 consists of a highly altered, sheared, and disturbed breccia overlying a more coherent lava. The breccia has black (N1) clasts with a pale blue (5B 6/2) clay matrix. Common slickenslides are found in the clay. The clasts up to 2 cm in size crumble in the hand, and original features are difficult to discern. The larger clasts have 5–7 vol% elongated round, <1-mm-diameter vesicles. The lava is less brecciated and altered (but still highly fractured) below Section 183-1139A-64R-3, 77 cm, except for interval 183-1139A-64R-4, 5–21 cm, with recovered pebble-sized loose pieces with >3-cm-diameter pancake-shaped vesicles. The lava from interval 183-1139A-64R-3, 77 cm, to 64R-3, 133 cm, has highly variable vesicularity with domains of uniform vesicularity defining horizontally elongated zones >5 cm long and 0.8–2 cm thick. The vesicular parts contain 20–50 vol% very irregular 0.5- to 15-mm vesicles, but the denser parts contain 1–2 vol% angular elongate <1- to 5-mm vesicles. The lava also contains large rounded "xenocrystic" feldspars (see **"Igneous Petrology,"** p. 36). From Section 183-1139A-64R-3, 133 cm, to the rubbly zone noted earlier (interval 183-1139A-64R-4, 5–21 cm), the lava is more uniform with ~3 vol% horizontally elongated generally 1- to 3-mm vesicles (Fig. **F27**). Vesicle size increases downward until the zone of low recovery. The first lava below this rubbly zone contains 2.5- to 5-cm horizontally elongated rounded vesicles. The remaining lava has 5%–15% inclined subrounded vesicles 0.5–15 mm in size with 3-cm vesicular clots. Vesicle size decreases and sphericity increases with depth. Vesicularity decreases to 2–5 vol% below Section 183-1139A-64R-4, 83 cm, with horizontally elongated ellipsoidal 0.5-to 20-mm vesicles. Inclined wispy mesostasis blebs also appear. Vesicularity increases at the base of the unit in Section 183-1139A-64R-5, from 3 vol% at 10–15 cm to 5 vol% at 21–29 cm, and reaching 7–10 vol% at 30–40 cm. Vesicle size also increases from 0.3–2 mm to 0.2–8 mm to 0.5–30 mm over this same interval. The last centimeter of Core 183-1139A-64R (and Unit 8) is altered to a dark gray.

Unit 9 (Interval 183-1139A-65R-1, 0 cm, to 65R-2, 46 cm)

The 1.61 m of aphyric trachybasalt recovered from Unit 9 is mostly coherent lava. The top 10 cm is a single piece of breccia with 1.5- to 4-cm rounded, folded clasts defined by vesicular domains. Vesicularity ranges from 5%–15% with irregular and elongate ellipsoidal vesicles

F26. Close-up photograph of interval 183-1139A-62R-3, 10–24 cm, **p. 92.**

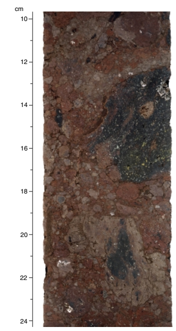

F27. Close-up photograph of interval 183-1139A-64R-4, 23–47 cm, **p. 93.**

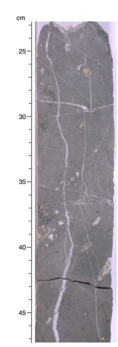

0.5–6 mm in size. The clasts have a uniform groundmass texture and are cemented to each other with no matrix. The underlying coherent lava exhibits a varied range of vesicularity and vesicle shapes (Fig. **F28**). The lowermost few centimeters of the coherent part of Unit 9 contain relatively few and small vesicles.

F28. Vesicularity, vesicle number density, and vesicle size as a function of depth in Unit 9, **p. 94.**

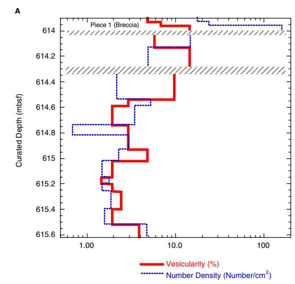

Unit 10 (Interval 183-1139A-65R-2, 46 cm, to 65R-4, 0 cm)

The 2.42 m of sparsely plagioclase-phyric trachybasalt recovered from Unit 10 is generally coherent, and the distribution of vesicles is plotted in Figure **F29.** The upper part of Unit 10 (Core 183-1139A-65R-2, 46–110 cm) consists of loose rounded pieces of altered lava. The uppermost pieces have fluidal shapes, 20% elongated to round vesicles (Fig. **F29**). Farther down, denser lava with ~3% coalesced round vesicles dominates. The black (N1) clasts are partially altered and are surrounded by greenish gray (5G 5/1) clays. The first piece of coherent lava is in Section 183-1139A-65R-2, 110 cm. The remainder of Section 183-1139A-65R-2 consists of irregular patchy 3- to 10-cm subcircular vesicular domains. Vesicularity varies from 5 to 30 vol% with smaller (0.1–0.3 mm vs. 0.5–4 mm) vesicles in the denser parts. Vesicle shapes are irregular and coalescing. Below these domains only loose pebble-sized rocks were recovered until Section 183-1139A-65R-3 (Piece 2), which contains a boundary between a vesicular lava with mesostasis blebs and a 5-cm-thick lower less-vesicular part that is darker. Below this dense zone, the lava becomes highly (≥20%) vesicular with irregular vesicles composed of coalescing round vesicles. This vesicular zone changes to less vesicular (≤1 vol%) lava over the interval 183-1139A-65R-3, 47–51 cm, (Fig. **F30**); this lava contains wispy mesostasis blebs in Core 183-1139A-65R-3, 82–85 cm. Vesicularity increases again at Section 183-1139A-65R-3, 90 cm, and subtle zonations in vesicularity zones become convoluted in interval 183-1139A-65R-3, 90–97 cm. A fine-grained zone surrounds a clast at 95–96 cm. A sharp subhorizontal, subplanar transition at interval 183-1139A-65R-3, 104–105 cm, contains lava with a high density of very small vesicles overlying lava with high vesicularity and larger vesicles (Fig. **F29**). A 0.5- to 1-cm vein follows this transition, obscuring the original millimeter-scale features. The vesicles in the underlying lava gradationally increase in size until reaching a sharp contact at Section 183-1139A-65R-3, 124 cm (Fig. **F31**). Below this contact the lava is nonvesicular until Sample 183-1139A-65R-3, 131.5–136 cm, where vesicularity increases and the vesicles show a strong fining downward sequence. At Core 183-1139A-65R-3, 136 cm, a 1-cm-thick subplanar dense zone with very small vesicles is present before vesicularity increases, then decreases again, reaching yet another subplanar dense zone with very small vesicles in Section 183-1139A-65R-3, 144 cm (Fig. **F32**). This lowermost zone partially envelops two 1- to 2-cm breccia clasts underneath it.

F29. Vesicularity, vesicle number density, and vesicle size as a function of depth in Unit 10, **p. 96.**

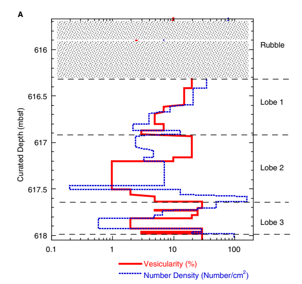

F30. Close-up photograph of interval 183-1139A-65R-3, 50–65 cm, **p. 98.**

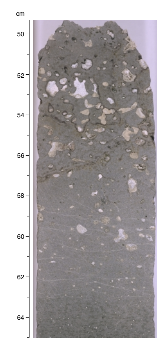

F31. Close-up photograph of interval 183-1139A-65R-3, 107–125 cm, **p. 99.**

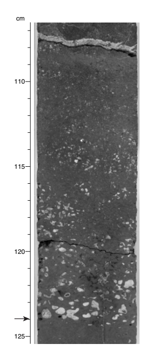

Unit 11 (interval 183-1139A-65R-4, 0 cm, to 66R-2, 0 cm)

The 3.26 m of aphyric trachybasalt recovered from Unit 11 consists of coherent lava sandwiched between two breccias. The uppermost part of Unit 11 (Section 183-1139A-65R-4) is poorly recovered and consists of loose pieces of breccia and a 10-cm piece of coherent lava. The breccia contains ~40% reddish black (5R 2/2) clasts in an ~60% dusky blue-green (5BG 3/2) clay matrix. The clasts contain 15%–20% irregular rounded vesicles and the coherent piece below contains ~3% angular vesicles. Section 183-1139A-65R-5 contains 135 cm of intact, well-preserved lava. The top of the lava has a breccia with 0.5- to 4-cm angular clasts containing 10% small irregular angular vesicles and a matrix of lava containing 15%–20% larger, extremely irregular and angular vesicles. The margins of the clasts are gradational and are marked by a zone of the matrix with decreased vesicularity (5–10 vol%). Mixing of denser and more vesicular lava continues through all of Section 183-1139A-65R-5 with dense (less vesicular) lava becoming more dominant at depth. The vesicular clast at Section 183-1139A-65R-5, 50 cm, is striking with a 2-cm vesicle or void attached to its upper surface (Fig. F33). The lava becomes more coherent in the upper part of Section 183-1139A-66R-1, with a gradual increase in vesicularity. Vesicular domains 1–1.5 cm in size reappear at interval 183-1139A-66R-1, 92–102 cm, immediately above the transition to a breccia with large (now carbonate- and zeolite-filled) voids. The breccia clasts have the classical jagged, gnarled, irregular shapes of aa clinker. The remainder of Unit 11 consists of loose altered rubble. Identifiable chunks within the rubble appear to be a breccia with similar vesicularity as the well-preserved aa clinker.

F32. Close-up photograph of interval 183-1139A-65R-3, 130–142 cm, p. 100.

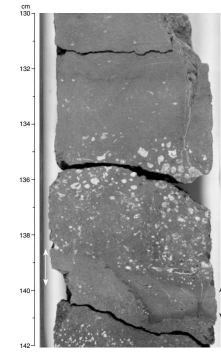

F33. Close-up photograph of interval 183-1139A-65R-5, 42–52 cm, p. 101.

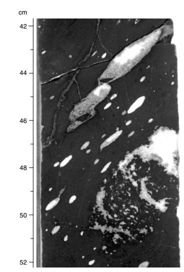

Unit 12 (Interval 183-1139A-66R-2, 0 cm, to 66R-4, 9 cm)

The 2.92 m of aphyric trachybasalt recovered from Unit 12 consists of an aphyric basalt with a heavily altered and brecciated top, massive interior, and a relatively well-preserved base. Only the top 50 cm of Unit 12 is a breccia, which exhibits a reddish black alteration and has a bluish gray clay matrix. The identifiable clasts have 25%–30% irregular but rounded vesicles 1–3 mm in size. These clasts are 0.5- to 1-cm angular fragments. The coherent lava underneath contains distinct clasts that are 1–3 cm in size and contain ~20% irregular and elongated vesicles 0.1–15 mm long. Within the coherent lava, more vesicular and denser parts alternate on a 10-cm scale. The lava becomes dense below Section 183-1139A-66R-2, 130 cm, with 3%–5% irregular elongated vesicles 0.3–10 mm in size. This massive lava also contains scattered megavesicles up to 6 cm in size and a highly vesicular zone in interval 183-1139A-66R-3, 24–34 cm. This interval contains 25%–30% highly irregular vesicles 0.1–6 mm in size. Near the base of Unit 12, vesicularity, fracturing, and alteration all increase. In interval 183-1139A-66R-3, 100–115 cm, vesicularity increases to 5%–7% and the subrounded vesicles are elongated horizontally. At the base of this vesicular zone, the groundmass becomes darker.

The most stunning feature in Unit 12 is a colorful package of sediments with contorted laminations (Fig. F34). The sediments include a layer of red clays, brown silty material, and green fine to very fine feldspar-rich sand. Beneath these sediments is a 15-cm-thick coherent lobe of lava with dark (chilled?) margins and 20%–25% large rounded vesicles that are elongated parallel to the margins of the lobe. Below this lobe, the lava consists of 1- to 5-cm fragments with dark (chilled?) margins. The margins themselves are fragmented and contain 3%–5% small round vesicles.

F34. Close-up photograph of interval 183-1139A-66R-5, 115–135 cm, p. 102.

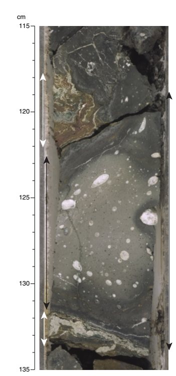

Unit 13 (Interval 183-1139A-66R-4, 9 cm, to 67R-1, 0 cm)

The 3.25 m of aphyric trachybasalt recovered from Unit 13 consists of a highly altered and disturbed brecciated top, a massive interior, and a poorly recovered fractured basal section. The breccia at the top of the unit extends through all of interval 183-1139A-66R-4 to 66R-5, 4 cm. The breccia consists of a mix of reddish black angular vesicular lava fragments with a matrix of bluish clays and white carbonates. The first moderately coherent lava is a 16-cm piece with vesicular margins where the vesicles are elongated parallel to the margins. This lava contains

5%–10% irregular angular vesicles 0.1–7 mm in size. Below this piece is another 10 cm of breccia with 2- to 5-cm equant rounded clasts. Very dark red (5R 2/6) 1- to 5-mm angular fragments surround these clasts. The clasts contain 3%–5%, generally <0.2-mm vesicles, and a few 2- to 8-mm irregular cavities. Below this breccia, the lava is coherent with the same characteristics as the 16-cm piece above. The vesicularity in the coherent lava varies on a 6- to 8-cm scale until Section 183-1139A-66R-5, 63 cm. In this variable upper part of the flow, vesicularity ranges from 3%–15% irregular rounded to subangular vesicles 0.1–10 mm in size. Below this, vesicularity and vesicle size continually and gradationally decrease, but vesicle shapes become more spherical. All of Section 183-1139A-66R-6 and the upper 16 cm of Section 183-1139A-66R-7 have 0.5%–1% vesicles and faint wispy mesostasis blebs. The lowermost 25 cm of Unit 13 is heavily fractured and is largely altered to a grayish red (5R 4/2) clay. The lava fragments contain 3%–7% irregular subhorizontally elongated vesicles 0.2–20 mm in size.

Unit 14 (Interval 183-1139A-67R-1, 0 cm, to 68R-1, 101 cm)

The 7.23 m of recovered rock from Unit 14 is basaltic trachyandesite with a complex, altered, and disturbed breccia overlying a more massive interior. From the top of Unit 14 until Section 183-1139A-67R-3, the breccia is highly altered and fractured and was recovered as rubble. The clasts are generally reddish black and the matrix includes a bluish clay. Intact clasts range from 3 to >15 cm in size and have preserved irregular fluidal shapes. Smaller clasts are not readily recognized amid the heavy alteration. The better preserved clasts have denser rims with smaller vesicles elongated parallel to the clast margins. Vesicularity in these clasts ranges from 7 to 20 vol%, from spherical to highly elongated and subrounded, and sizes from 0.1 to 5 mm. Clasts with irregular angular vesicles are notably absent. In Section 183-1139A-67R-1, 40 cm, an autolithic clast is present (Fig. F35), and, also in this section, clasts are commonly fused to each other without visible secondary cementation.

Below Section 183-1139A-67R-3, 70 cm, the volcanic breccia is no longer heavily fractured or altered and primary textures are more readily recognized. In this region, an entire continuum of fragment sizes is visible, ranging from fine sand to >6-cm cobbles. The larger clasts are generally equant and subangular to rounded but clasts <1 cm are sometimes angular (Fig. F36). In the upper part of the breccia, the clasts >1 cm in size make up 70–80 vol%, whereas sand-sized fragments make up 10–20 vol%. With depth, the alteration decreases, the fine-grained component becomes volumetrically more important, and coherence of the breccia increases. By interval 183-1139A-67R-4, 20–30 cm, clasts >1 cm in size make up only 10–20 vol%, and the fine-grained component has become a coherent lava. At this point the clast margins are also indistinct and are more defined as vesicular patches.

Interval 183-1139A-67R-4, 51–104 cm, has a different style of brecciation. The breccia consists of 0.5- to 15-mm very angular, subequant clasts of a single lithology. This region is heavily altered but contains 3%–5% irregular rounded vesicles 0.1–5 mm in size.

Below this breccia, the lava is massive with generally 0.1–0.5 vol% vesicularity. Inclined mesostasis blebs are common until Section 183-1139A-67R-5, at 50 cm. In the bottom 20 cm of the zone with mesostasis blebs, the blebs are associated with 0.1- to 0.5-mm irregular vesicles. Within the massive lava is a single 3-cm-diameter vesicular clot (inter-

F35. Close-up photograph of interval 183-1139A-67R-1, 35–47 cm, p. 103.

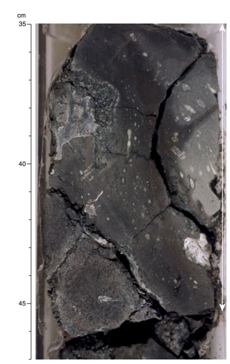

F36. Close-up photograph of interval 183-1139A-67R-3, 76–84 cm, p. 104.

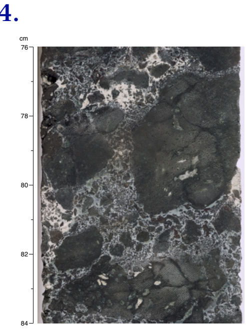

val 183-1139A-67R-5, 133–136 cm) with 5 vol% spherical 0.1- to 1-mm-diameter vesicles.

The lava becomes more vesicular near the base, starting in Section 183-1139A-67R-5, at 104 cm. Vesicularity increases as centimeter-scale indistinct vesicular pods. By interval 183-1139A-67R-5, 127–138 cm, the lava is dominated by the vesicular lava, and the dense lava makes up only 1–4 cm indistinct pods. The dense lava has identical character to the massive interior, whereas the vesicular lava has 7%–10% highly irregular vesicles 0.1–4 mm in size. Below this, the lava is highly fractured and altered. The lava appears to contain 0.5%–3% irregular angular vesicles 0.1–3 mm in size, and mesostasis blebs are common.

Unit 15 (Interval 183-1139A-68R-1, 101 cm, to 68R-4, 100 cm)

The recovered 4.16 m of Unit 15 is a sparsely plagioclase-phyric basaltic trachyandesite flow with a massive interior and a small basal vesicular zone. The top of Unit 15 is very highly altered, fractured, and disturbed, making it impossible to identify primary volcanic features. The degree of alteration and fracturing decreases with depth, and the first recognizable pieces of lava appear at Section 183-1139A-68R-2, 13 cm. This lava contains 5%–10% highly irregular, subrounded vesicles 0.1–15 mm in size. Within the fractured zone, there is no evidence for clast rotation, chill margins on clasts, or mixing of lava types. Over the interval 183-1139A-68R-2, 50–90 cm, the irregular vesicles become less common and a second population of more spherical vesicles appears. At the end of this interval, the lava contains only 1%–3% moderately spherical and highly rounded vesicles 2–4 mm in size. A high degree of fracturing hides most primary features in the lava below this level, but, in general, the lava becomes dense with a 0.5-m-long vesicular zone from Section 183-1139A-68R-3, 86 cm, to 68R-4, 16 cm. In the upper massive part, vesicularity appears to be <0.5 vol%, and a megavesicle and inclined mesostasis blebs are tentatively identified. The vesicular zone consistently contains 5–10 vol% vesicles, and vesicle sizes range from 0.1–25 mm. However, vesicle shape changes dramatically with depth. At the top, the vesicles are highly irregular and subangular. In the middle, the vesicles are rounded and elongated, in the vertical direction higher up and horizontally lower down. Toward the bottom of the vesicular zone, the vesicles are once again subangular and elongated in an inclined or subhorizontal direction. These vesicles are interleaved with, and grade into, faint wispy mesostasis blebs. The lower massive portion of the flow contains 0.5%–1% near spherical vesicles 0.5–1.5 mm in size.

The base of the flow grades into the basal vesicular zone. Vesicularity begins to increase in Section 183-1139A-68R-4, 77 cm, with the appearance of vesicular clots a few centimeters across. These become more dominant with depth so that in Section 183-1139A-68R-4, by 100 cm, the lava is entirely made up of coherent vesicular lava. In this basal vesicular zone, the “dense” lava actually contains 10%–15% small, extremely irregular and angular vesicles, whereas the vesicular clasts/lava contain 10% rounded vesicles, 1–6 mm in size.

Unit 16 (Interval 183-1139A-68R-4, 100 cm, to 68R-7, 38 cm)

The 2.85 m of recovered aphyric basaltic trachyandesite from Unit 16 contains a breccia overlying a massive interior. The upper part of the breccia (interval 183-1139A-68R-4, 100–145 cm) is too heavily altered, fractured, and disturbed to identify any features of the original lava. The lava is better preserved but brecciated down to near the base of Section 183-1139A-68R-5, 140 cm. This breccia shows a range of clast sizes with clasts >1 cm making up 30–40 vol%, clasts 1 cm–1 mm in size making up 40–50 vol%, and fines <1 mm making up 15–20 vol%. There is no visible size sorting in the well-preserved part of the breccia. The larger clasts are generally nearly equant and subangular. The <1-cm clasts are generally angular and can commonly be jigsaw fit to larger clasts with fine-grained alteration material filling the interstices. The clasts of lava exhibit a range of shapes with vesicularities ranging from <1% to 20%. In rare cases, the larger clasts have elongated vesicles parallel to the clast margins and more spherical vesicles in the center. The one clast that stands out extends across interval 183-1139A-68R-5, 100–116 cm, and consists of dense lava. The first coherent lava at the top of the massive interior of the flow has identical vesicularity. The top of the coherent lava also has contorted banding defined by stretched and contorted vesicles that are highlighted by alteration (Fig. F37). The massive lava that makes up the rest of Unit 16 has 5%–10% microscopic vesicles (<0.1 mm) and <1% macroscopic (0.5–3 mm) highly irregular vesicles. The lava is highly altered and fractured, but it appears that the lowermost 5 cm of Unit 16 is slightly more vesicular with 1%–2% irregular 0.1- to 0.5-mm vesicles.

Unit 17 (Interval 183-1139A-68R-7, 38 cm, to 70R-1, 0 cm)

The 5.01 m of sparsely plagioclase-phyric basaltic trachyandesite recovered from Unit 17 consist of a brecciated top over a massive interior. The breccia is highly altered but only moderately fractured and disturbed, allowing the identification of most features. However, the alteration gives a deceiving view of the clasts. The centers of the clasts are dark gray (N3) but have 1- to 2-cm-thick dark reddish gray (10R 3/1) rims the same color as the matrix (Fig. F38). Between 70% and 80% of the breccia is composed of clasts >1 cm in size, <1-mm fines make up ~5%. The larger clasts are subangular to subrounded, and vesicularity ranges from 3% to 25%. Vesicle size is almost exclusively <1 mm, but one clast has a 1-cm-long elongated vesicle. The high degree of alteration hides the internal features of the clasts.

In Section 183-1139A-68R-7, from 140 cm downward, the lava is generally coherent, massive, and aphyric. In fact, the lava is remarkable in its almost complete lack of features. The massive lava contains ≤0.1 vol% vesicles that are ≤0.5 mm in diameter. Some 2- to 3-cm irregular vesicular pods appear in interval 183-1139A-69R-1, 105–150 cm, and a few 3- to 5-cm irregular voids appear further down. There is no sign of increased vesicularity toward the base of the recovered rocks from Unit 17.

Unit 18 (Interval 183-1139A-70R-1, 0 cm, to 71R-4, 20 cm)

The 8.77 m of moderately feldspar phyric trachyandesite recovered from Unit 18 contains a brecciated top, a massive interior, and a brecciated basal section. Unit 18 is also highly altered in places, masking many primary features (see **"Alteration and Weathering,"** p. 42). Figure F39 plots vesicularity as a function of depth within Unit 18, but the identification of vesicles was commonly difficult because of the intense alteration. The breccia at the top is quite well preserved and contains many curious features (Fig. F40). The breccia generally has 60–70 vol% >1-cm clasts, and fines <1 mm make up ~10% of the breccia. However, the upper part has ~50% fine matrix and only 10% clasts >1 cm. This part of the breccia is matrix supported, and the clasts are rounded. Two other large, near-spherical clasts are present deeper in the breccia. These

F37. Close-up photograph of interval 183-1139A-68R-6, 6–20 cm, **p. 105.**

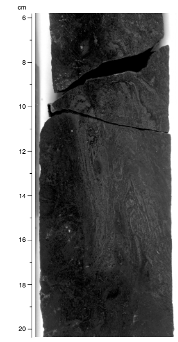

F38. Close-up photograph of interval 183-1139A-68R-7, 80–96 cm, **p. 106.**

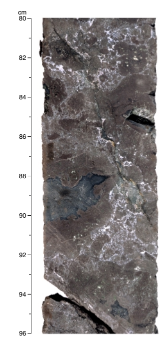

F39. Vesicularity, vesicle number density, and vesicle size as a function of depth in Unit 18, **p. 107.**

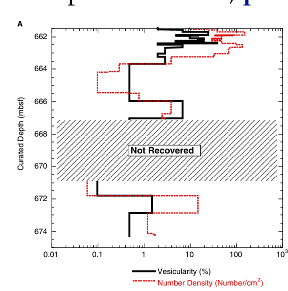

F40. Close-up photograph of interval 183-1139A-70R-1, 45–55 cm, **p. 109.**

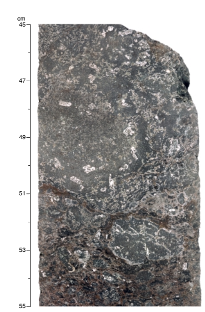

clasts have moderately vesicular margins. Inward of the vesicular margins is a sparsely vesicular concentric zone with large feldspar phenocrysts. The interiors of the clasts are again moderately vesicular. An interesting feature of the finer grained fraction of the breccia is the common presence of individual feldspar crystals in the matrix. The fractures within the clasts generally avoid the phenocrysts, and many small clasts are volumetrically dominated by a single phenocryst. Further into the breccia, alteration increases and the boundaries between clasts and matrix become indistinct in Section 183-1139A-70R-1, from 110 cm downward. There is no clear boundary between the brecciated and coherent lava. The massive interior generally has 1%–3% spherical vesicles 0.1–0.3 mm in diameter. Figure F39 shows the vesicular parts within the interior of the flow. Most of the visible color banding is caused by alteration.

The basal breccias of Unit 18 show distinctive features. In the lava, starting in Section 183-1139A-71R-3, at 47 cm, 1- to 2-cm rounded equant clasts appear. A 0.5- to 1-cm-thick zone of angular breccia with open void space is present in Section 183-1139A-71R-3, 58 cm (Fig. F41). Below this is a breccia containing dense lava with semicircular curved clasts and a matrix of red and very light green fine-grained material (Fig. F41). The lava below this breccia is made up of convoluted clasts with indistinct margins (Fig. F42). These clasts contain 0.5%–1% small spherical vesicles. Then, in interval 183-1139A-71R-3, 120–124 cm, another 0.5-cm-wide angular breccia zone with 1- to 4-mm fragments is present. Color banding is also prominent in several parts of this lower breccia. The very bottom of Unit 18 consists of a 15-cm-long lobate feature that has partially engulfed clasts of breccia underneath it. The feature contains 1–3 vol% rounded vesicles 0.1–1 mm in size. Elongated vesicles generally fan parallel to the margins of the lobate feature.

F41. Close-up photograph of interval 183-1139A-71R-3, 56–68 cm, p. 110.

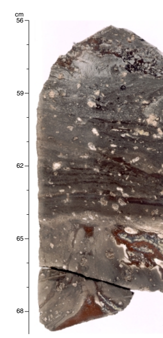

F42. Close-up photograph of interval 183-1139A-71R-3, 118–128 cm, p. 111.

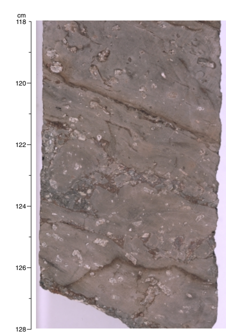

F43. Close-up photograph of interval 183-1139A-72R-1, 15–25 cm, p. 112.

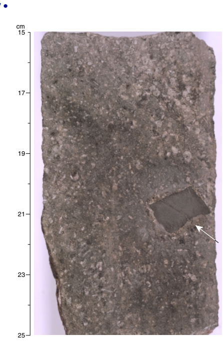

Unit 19 (Interval 183-1139A-71R-4, 20 cm, to 73R-3, 148 cm)

The 12.66 m of recovered moderately feldspar-phyric trachyte from Unit 19 is also highly altered with a breccia top over a more massive interior. The breccia on the top of Unit 19 shares many characteristics with the breccia at the top of Unit 18. Overall, clasts >1 cm make up 50–60 vol% of the breccia and <1-mm fines make up only 5%–10%. Clasts are rounded to subangular with no clear size sorting. Large clasts are distributed throughout most of the breccia but are not present at the base of the breccia. The uppermost clasts appear more rounded than those further inside the breccia. Lower in the breccia, the long axes of clasts are subhorizontal. In this same area, the edges of clasts become indistinct. Individual feldspar crystals are common in the fine-grained matrix.

The lava becomes coherent from interval 183-1139A-71R-5, 49–91 cm, downward. The interior of the flow is remarkably monotonous. Generally, cavities comprise ~1% of the interior, are 0.2–3 mm in diameter, have subangular shapes, and are filled with alteration minerals. Examination under the binocular microscope suggests that most, but not all, of these are altered phenocrysts. The only vesicle features we confidently identify are an irregular zone at interval 183-1139A-71R-6, 0–20 cm, and an inclined vesicle train in interval 183-1139A-72R-2, 31–70 cm. A 1.5 cm × 2 cm × >5 cm angular aphyric dark clast is present at interval 183-1139A-72R-1, 19–21 cm (Fig. F43). The last rocks recovered from Hole 1139A, in Section 183-1139A-73R-3 at 148 cm, were still in the massive interior of Unit 19.

Interpretation

Lithologic Units

Units I–V: Fossiliferous Sediments (Interval 183-1139A-1R-1, 0 cm, to 49R-1, 109 cm)

In the pelagic and hemipelagic sediments of Units I through III, the volcanic component is very dilute. It is either incorporated into the pelagic sediments as primary pyroclastic air fall, and subsequently redistributed, or as suspended material from influxes of hemipelagic clay-sized material into the deep marine basin. Three discrete tephras were sampled from Unit II (intervals 183-1139A-11R-1, 107–109 cm; 38R-3, 17–19 cm; and 38R-4, 80–82 cm) (Table T9) and are believed to be bioturbated primary pyroclastic fall deposits.

The proposed environment of deposition for the sandy packstone (Unit IV) is a low-energy neritic setting, near a weathered volcanic source area (see "Lithostratigraphy," p. 4). This explains why a significant component of the clastic component of this sediment is volcanic lithics and clay. The grainstone (Unit 5) may have formed in a high-energy shallow marine carbonate shoal where the reworked terrigenous component, although not transported far, was overwhelmed by the influx of particulate carbonate material. Although the proportion of volcanic components in this unit is not great, the grain size and abundance of lithic fragments and crystal implies the sediment was deposited near an eroding volcanic terrain.

Basement Units

Subunit 1A: Massive and Flow-Banded Felsic Volcanic Pebbles (Interval 183-1139A-49R-1, 109 cm, to 52R-1, 56 cm)

The pebbles and cobbles in Unit 1 are abraded and subrounded (Fig. F10A), and their surfaces are oxidized or weathered, implying that they are clasts and have been reworked, probably in a fluvial or littoral marine environment. Poor recovery in this interval (interval 183-1139A-49R-1, 109 cm, to 52R-1, 56 cm) does not allow us to attribute a thickness to a felsic lava, despite the recovery of several felsic lava clasts. Rounding and surficial weathering of the clasts provides evidence that the pebbles and cobbles form part of a pavement or conglomerate. Identification of this massive and flow-banded lava debris as beach pebbles and cobbles is consistent with the stratigraphic interpretation of the sedimentary sequence at Site 1139 (see "Lithostratigraphy," p. 4). These pebbles and cobbles may form part of a poorly consolidated conglomerate, from which the matrix has been lost during drilling. Several cobbles from this interval fell downhole during drilling and are present at the top of lower sections.

Subunit 1B: Bioclastic Sandstone (Interval 183-1139A-52R-1, 56–103 cm)

The bioclastic sandstone resembles the grainstone (Unit V) at the base of the sedimentary section and the environment of deposition is considered similar. Both units formed in a high-energy shallow marine environment (carbonate shoal?) where the reworked terrigenous component was overwhelmed by the influx of biogenic fragmental material. Although the proportion of crystals, glass, and volcanic lithic fragments is low, the presence of this volcaniclastic detritus indicates that the bioclastic sandstone was deposited near an eroding volcanic region.

Subunit 1C: Pumice/Flow-Banded Felsic Breccia (Interval 183-1139A-52R-1, 103 cm, to 53R-1, 25 cm)

Although little of this unit was recovered (47 cm), the largely clast-supported breccia has angular to subangular, pale green, altered, flow-banded felsic glassy clasts in a fine-grained matrix (Fig. F11). The matrix contains fine-grained glassy material that may have been derived from the grinding of clasts against each other. The clasts are not welded, indicating that they were not hot at the time of breccia formation. Many clasts are now banded perlites (Fig. F13), indicating the glassy nature of the clasts before devitrification. Some clasts appear pumiceous in core, but pumice was not observed in thin section. Banded perlite may impart a pseudopumiceous texture to the clasts. This breccia may either be the upper part of a autobreccia associated with a felsic lava flow, or a pyroclastic flow-top breccia.

Subunit 1D: Altered Perlitic Felsic Glass (Interval 183-1139A-53R-1, 25 cm, to 54R-1, 0 cm)

The exquisitely developed spheroidal perlitic fractures (Figs. F13, F14) in this interval indicate that this rock was dense glass before hydration and alteration. However, abundant lithic fragments in this interval are unusual for a lava flow, so we interpret this unit as the vitric core of a densely welded pyroclastic flow deposit (vitrophyre). The gradational transition from the glassy zone into a silicic breccia with lithic clasts at the base of the interval (Figs. F17, F18), and possibly also toward the top, is consistent with this interpretation. A welded pyroclastic flow is strong evidence for primary deposition in a subaerial environment.

Subunit 1E: Sheared and Altered Volcaniclastic Sediment (Fault Zone) (Interval 183-1139A-54R-1, 0 cm, to 55R-1, 0 cm)

In the lower part of this interval (interval 183-1139A-54R-1, 56–108 cm), some clastic textures are preserved in the highly altered rocks. Pale green, wispy pumice-like clasts are present in some places (interval 183-1139A-54R-1, 56–62 cm) and bedded angular granules in others (interval 183-1139A-54R-1, 67–79.5 cm). In the upper part of the sequence, the rock is intensely sheared to resinous and powdery, green, clay-rich materials. The sheared textures and intense alteration suggests that this is a fault zone (see **"Alteration and Weathering,"** p. 42).

Unit 2: Dark Red Welded Vesicular Rhyolite (Interval 183-1139A-55R-1, 0 cm, to 56R-1, 78 cm)

The drape, flattening, and welding textures of Unit 2 (Fig. F19) imply that it was formed by the agglutination of hot vesicular, glassy particles. The rocks have been identified as rhyolite on the basis of the sanidine (~10%) and quartz (~1%) phenocrysts. The welded rock is dark red (oxidized) and highly altered; glass shards are absent in thin section (Fig. F20). However, the rock has a flow-banded, draping, and flattening texture, with trains of small (<1 mm) irregular vesicles aligned subparallel to the flattening fabric. This material could have formed either as a primary spatter deposit or as a partially welded breccia associated with a hot pyroclastic flow deposit. We did not observe primary spatter fragments and bombs in this interval, suggesting that partial welding of a felsic pyroclastic flow is the more likely mechanism of formation. The dark red (oxidation) color of this interval may be a result of eruption and weathering in a subaerial environment.

Unit 2/Unit 3 Boundary (Section 183-1139A-56R-1, 78 cm)

The contact between the sanidine-phyric, partially welded breccia (Unit 2) and crystal vitric tuff-breccia (Unit 3) is defined by a color change from dark red to green. However, recovery of the contact is poor, so the nature of the transition between the two units is not clear.

Unit 3: Altered Crystal Vitric Tuff-Breccia (Interval 183-1139A-56R-1, 78 cm, to 57R-1, 92 cm)

The crystal vitric tuff-breccia is green, highly altered, and appears very different from the units that enclose it. However, the crystal content in Unit 3 (~15% sanidine and ~4% quartz) is similar to that in the dark red, vesicular, welded felsic rocks above (Unit 2) and below (Unit 4) (see **"Igneous Petrology,"** p. 36). The perlite identified in thin section is diagnostic of originally coherent felsic glass. The preservation of domains of more lithified material with diffuse banding (Fig. **F21**), and lithic fragments distributed throughout the section, suggests that this probably was not a lava. We infer that this is a pyroclastic flow deposit, but the felsic component has been altered, and the only preserved clasts are larger and indurated. This observation, together with ubiquitous spheroidally fractured (perlitic) glass (Fig. **F22**), implies that this unit was a densely welded glassy interval. This is supported by faint banding in more massive parts of the core (interval 183-1139A-56R-3, 130–150 cm) that are not associated with enclosed clasts. The unit was probably a welded zone in the core of a pyroclastic flow deposit.

Unit 3 looks different from the glassy perlite identified in Subunit 1D, largely because the former is much more intensely altered. However, at the upper contact between Units 2 and 3, where color changes (dark red to green), there is evidence of shearing, indicating faulting. Perhaps this contact was a fluid percolation pathway leading to alteration of the glassy material.

Unit 3/Unit 4 Boundary (Section 183-1139A-57R-1, 92 cm)

We define the contact between the crystal-vitric tuff breccia and alkali feldspar-bearing, partially welded breccia by a bold color change from green (Unit 3) to dark red (Unit 4). However, recovery over the contact is poor so the nature of the transition between the two units is not clear and may be gradational. We cannot determine if there was a break in time between their deposition.

Unit 4: Dark Red Welded Vesicular Rhyolite (Interval 183-1139A-57R-1, 92 cm, to 61R-1, 0 cm)

Poor recovery of Unit 4 and repeated brecciation make it a difficult section to interpret. However, the most common type of brecciation (Section 183-1139A-60R-1) with cataclastic textures could be a tectonic feature. The jigsaw fit across some of the clasts in this breccia suggests fragmentation in place with minimal transport. The other two well-cemented matrix-free breccias are likely to be welded. The uppermost breccia looks pumiceous and may be a slightly vesicle-poor pumice. Subvertically aligned elongated vesicles in the more massive rock may follow sutures where large (<10 cm), hot clasts were pressed together (Fig. **F23**). However, the lack of rheomorphic textures (e.g., laterally continuous flow banding) and the random orientation of feldspar phenocrysts argues against significant shear in the recovered parts of Unit 4. Both large (up to 10 cm) clasts and angular vesicles point to a very viscous lava, supporting the suggestion from the phenocryst assemblage that this is a felsic pyroclastic deposit.

Unit 4/Unit 5 Boundary (Section 183-1139A-60R-2, 54 cm)

The Unit 4 to Unit 5 boundary lies within a brecciated zone showing a change from a matrix-supported interval at the base of Unit 4 (Fig. F24) to a hydraulically fractured and altered breccia at the top of Unit 5 (Fig. F25). The precise contact is not clear.

Unit 5: Lava Flow(?)

The upper breccia in Unit 5 (Section 183-1139A-61R-1 [Pieces 1 and 2]) (Fig. F25) is, at least partly, brecciated as a result of crosscutting tectonic fracturing and veining during alteration. The random orientation of the large feldspar phenocrysts suggests that the recovered lavas were either disrupted and mixed by brecciation or were not subjected to high shear during crystallization. In thin section, the massive zone has a lava-like texture (see **"Igneous Petrology,"** p. 36) with microcrystallites in the mesostasis. The fractured zones within the massive part of the unit may be related to cataclasis and subsequent alteration (see **"Alteration and Weathering,"** p. 42). The recognition of a massive central zone with breccias above and below, and the thin section evidence that the massive interior have lava-like textures, supports the identification of this unit as a lava flow.

Unit 5/6 Boundary

The change from a feldspar-phyric trachyte to an aphyric trachybasalt is a clear boundary. However, no contact was recovered, making it impossible to interpret the relationship between the two units.

Unit 6: Lava Flow(s?), Type Unknown

The recovered rocks from Unit 6 (Fig. F26) indicate a lava with a dense interior and a more vesicular breccia top. However, it is not clear that the breccia on the top of Unit 6 is an autobreccia formed during emplacement; it could be an eroded and reworked vesicular flow top. The breccias within Unit 6 are probably tectonic in origin, but we cannot rule out the possibility that one or more are flow-top or basal breccias. If any are autobreccias, Unit 6 represents more than one package of lava.

Unit 6/Unit 7 Boundary

The morphology of the few well-preserved clasts within the breccia at the top of Unit 7 indicates that it formed during the emplacement of the flow. Thus, it must be part of a flow-top or basal breccia, indicating proximity to a flow boundary. However, the location of the unit boundary at the top of Core 183-1139A-64R is arbitrary. The actual contact is probably in the unrecovered portion of Core 183-1139A-63R, or somewhere within the heavily altered and fragmented rocks in Unit 6. Several points suggest that the breccia at the top of Unit 7 is actually a basal breccia to a flow that is mostly in Unit 6. Given the equivocal nature of the contact between Units 6 and 7, we do not attempt to interpret relationships between the two units.

Unit 7: Breccia-Topped Lava Flow

The fluidal shapes and the possible entrainment of sediments into some trachybasalt clasts argues for brecciation or disruption during emplacement. The fine-grained margins suggest chilling where the fluidal clasts were in contact with colder fragments of lava. The mixing with sediments and the horizontal (flattened) shapes of the fluidal clasts suggest a basal breccia. Alternatively, it could be a mix of spatter and lithics or even a lava-rich peperite. If these clasts are spatter, they have unusually low vesicularity. This might suggest an explosive interaction between somewhat degassed lava and near-surface water. The simplest interpretation is that this is a welded basal breccia. The shapes of the vesicles within the coherent part of Unit 7 indicates significant shear. We interpret the rectangular vesicular domain to be an entrained clast, suggesting entrainment of a disrupted upper crust. The small xenolith could be from the magma chamber or incorporated during flow, especially if the flow started as a mix of spatter and lithics. It is not clear if the breccia at the base of Unit 7 is related to emplacement or postemplacement processes. Given the equivocal nature of the breccia at the top of Unit 7 and the lack of information about its base, we cannot draw any definitive conclusions about the type of flow it contains.

Unit 7/Unit 8 Boundary

We placed the boundary between Units 7 and 8 at the point where the color of both the clasts and the matrix change distinctly within the highly fragmented breccia. It is not clear that this location represents any change in lava types, but it is a visually distinct boundary in the breccia that lies between two different flows.

Unit 8: Spatter-Topped(?) Lava Flow

The highly altered, fragmented, and disturbed breccia at the top of Unit 8 is difficult to interpret. The relatively low vesicularity of the identifiable clasts as compared to the top of the better recovered and preserved lava is particularly puzzling. We interpret the zone of variable vesicularity as a zone of welded clasts. The shapes, sizes, and high vesicularity of the clasts suggest primary spatter. Because the zone of variable vesicularity (i.e., welded clasts) grades into the coherent lava underneath, it is unlikely that this is a welded basal breccia of the overlying unit. The horizontally elongated, but well-rounded shapes of the vesicles in the coherent part of the lava suggest shear during crystallization of a relatively low viscosity lava. The increase in vesicle size with depth is consistent with increasing coalescence with time. We interpret the increased vesicularity toward the base of the unit to be the basal vesicular zone. The centimeter-thick zone that has altered to a dark gray may represent the basal chill.

Although the clasts in the upper part of Unit 8 may be spatter, proximity to the vent is not required. The welded spatter could easily have been transported tens of kilometers as a raft on an open lava channel. Also, the degree of coalescing implied by the very large vesicles and their sheared shapes suggest that the lava was transported before being frozen. It is not possible to confidently determine the lava flow type from these observations.

Unit 8/Unit 9 Boundary

The breccia at the top of Unit 9 indicates a boundary between two separate flows. The continuous groundmass size and the complete cementation of the clasts without any matrix suggests welding. Folded shapes suggest that the clasts were hot and plastic at the time of formation. The high density of very small vesicles at the base of breccia suggests a chill margin, perhaps indicating that it is more likely to be the base of Unit 8 rather than the top of Unit 9. However, given that only one isolated 10-cm piece of breccia was recovered, we cannot interpret relationships between Units 8 and 9 and the breccia unequivocally.

Unit 9 (Lava Flow, Type Unknown)

Interpreting the vesicle distribution within Unit 9 (Fig. **F28**) without recovery of a flow top or flow base is difficult. The relatively low vesicularity and subvertical elongation of the vesicles in the uppermost coherent lava is difficult to reconcile with a flow top; a significant amount of material may be missing from the top of the flow. The increased vesicularity and a switch to angular shapes would be easiest to explain as a zone of high shear, but this would have disrupted the crust above. An alternative is an entrained aa-like clast, but there is no evidence for clast boundaries, and this zone is much wider than typical entrained clasts. The zone of elongated but rounded vesicles below suggests a reduction in shear and a more fluid lava, but steeply inclined vesicle trains suggest significant nearby topography within the flow. The zone of increasing vesicle size with constant vesicularity (by volume) suggests increasing coalescence of vesicles.

Unit 9/Unit 10 Boundary

The top of Unit 10 is an altered and sheared breccia with some clasts similar to the lava in Unit 9. The contact between the lava flows of Units 9 and 10 could be anywhere within this breccia, and we cannot interpret the relationships between these flows.

Unit 10: Compound Pahoehoe and Unknown Lava Flows

The breccia at the top of Unit 10 is difficult to interpret. The fluidal shapes and higher vesicularity of some clasts could suggest spatter or a partially welded basal breccia, but given the degree of alteration, this material could have originally been a coherent flow. Within the better recovered lava, we interpret the zones with relatively low vesicularity, but high vesicle number density as altered, welded chill zones (Fig. **F29**). In general, the lobes separated by these chill zones have a vesicular upper crust, dense interior, and vesicular lower crust, as is typical of inflated pahoehoe flows. The boundaries between the upper vesicular crust and massive interior are unusually sharp for lobes this small. Smaller lobes tend to cool too quickly for the bubbles to segregate effectively from the stagnant interior of the flow. This suggests that either the lava was relatively fluid or that the lobe remained hot unusually long. This could be readily achieved if the flows were rapidly emplaced on top of each other, producing a single thick "cooling unit." The apparently welded contacts between the lobes support this idea. The somewhat circular vesicular patches in Section 183-1139A-65R-2 may be a stack of small pahoehoe lobes welded together, or they could be the transition from a brecciated flow top to coherent lava. This might suggest that the uppermost lobe was emplaced too rapidly to form a coherent pahoehoe crust. The zone of poor recovery at the top of Core 183-1139A-65R-3 could be the result of vesicle sizes approaching the size of the diameter of the core (Fig. **F29**). The clast near the base of the second lobe is probably a folded piece of the lower margin, possibly bent by local 5- to 10-cm-scale topography. This kind of folding again suggests relatively rapid emplacement of pahoehoe lava.

It is interesting that some features common in inflated pahoehoe flows are missing from Unit 10. In particular, there is no evidence for effective segregation of late stage liquids into vesicle cylinders and horizontal vesicle sheets. Instead, only wispy mesostasis blebs are present in the largest of these lobes. We speculate that these lobes did not have sufficient volume to segregate large bodies of late-stage volatile-rich melt.

Unit 10/Unit 11 Boundary

The base of Unit 10 is a clear boundary (Section 183-1139-65R-3, 146 cm) with a smooth pahoehoe surface partially engulfing breccia clasts. The breccia clasts are subrounded, suggesting sufficient time for secondary processes to smooth the clasts.

Unit 11: Aa Lava Flow

The breccia on the top of Unit 11 is too poorly recovered and too reworked/weathered/altered to identify the style of brecciation. However, the mixing of vesicular and denser lavas in the upper part of the coherent lava is diagnostic of entrainment of breccia clasts. This means that the breccia at the top of Unit 11 is an autobreccia and is not simply the breakdown product of a coherent lava. The morphology of clasts in the well-preserved basal breccia definitively identify Unit 11 as an aa flow. The vesicles in the upper part of the flow have the irregular, angular shapes typical of aa flows, but the interior includes more rounded vesicle shapes. This suggests that the interior of the flow was still somewhat fluid when the flow stopped. Wispy mesostasis blebs without larger segregation features are also consistent with most aa flows. The entrained clast with the large irregular vesicle at its top is very unusual (Fig. **F33**). We speculatively suggest that it may represent air or water (steam) incorporated into the lava when the clast was entrained into the flow. The vesicular domains in the lower part of the flow suggest that the basal breccia was also entrained into the interior of the flow.

Unit 11/Unit 12 Boundary (Section 183-1139A-66R-2, 0 cm)

Although a contact clearly exists between the massive interiors of Units 11 and 12, the basal breccia of Unit 11 and the flow top breccia on Unit 12 are too highly altered to accurately locate the boundary. The placement at a section break was convenient but arbitrary. Intense alteration precludes the determination of the precise contact between Units 11 and 12.

Unit 12: Transitional Lava Flow, Type Unknown

Unit 12 is a confusing lava that combines aspects of both aa and pahoehoe flows. The entrained clasts in the upper part of the coherent lava of Unit 12 require that the lava had a disrupted crust at the time of emplacement. The identifiable clasts in the breccia at the top of Unit 12 are angular but rather small to be true aa clasts. Also, the vesicles are not as angular as is typical in aa clinker. There is no straightforward explanation for the megavesicles and the zone of high vesicularity within the otherwise massive interior of the flow. Megavesicles imply coalescing of vesicles. How the vesicles were able to coalesce to form the megavesicles while coalescence was halted in the vesicular zone is unclear. The base of the flow poses additional puzzles. The dark groundmass is interpreted to be glassy margins that have altered to clay. These margins suggest a stack of 10- to 20-cm-thick pahoehoe lobes at the base of Unit 12. Relating these lobes to the brecciated flow top is difficult. Also, the contorted laminations in the sediments suggest that the lava plowed into the sediments and curled them over before baking them (Fig. **F34**). Retaining the original sedimentary laminations requires relatively gentle emplacement of the lava and suggests that the sediments were not very thick, probably <10 cm. Although the sediments may have been moist, the lack of disruption from steam generation implies minimal amounts of water or the emplacement may have been slow enough to gently boil off the water.

Unit 12/Unit 13 Boundary

There clearly is a contact between the massive interiors of Units 12 and 13. However, given the extensive alteration and disturbance of the breccia between the two massive parts, the exact location of the boundary is equivocal. In this case, we assigned the last somewhat recognizable pieces of lava to Unit 12 and placed everything else at the top of Unit 13. Although these rocks do not allow us to directly interpret relationships between Units 12 and 13, sediments in the lower part of Unit 12 imply a time break between the emplacement of these two flows.

Unit 13: Breccia-Topped Lava Flow

Unit 13 clearly had a brecciated flow top, but its features are not diagnostic of an aa flow. The first well-preserved piece of lava from Unit 13 has a vesicularity identical to the upper part of the coherent lava under the breccia, suggesting that an arm of the lava interior may have reached into the breccia. This arm contains more vesicles, especially larger ones, than dense arms intruding aa breccias commonly do. Clasts in the breccia now appear rounded, but the surrounding angular fragments suggest that this rounding likely results from in situ alteration rather than sedimentary reworking. The gradual decrease in vesicularity and vesicle size is consistent with a combination of larger vesicles rising and lithostatic pressure compressing the lower bubbles. The gradual increase in roundness of the vesicles with depth hints at a gradual stagnation of the flow. The basal section suggests shear, and a basal breccia could be expected below the base of Unit 13.

Unit 13/Unit 14 Boundary

A contact must exist between the massive interiors of Units 13 and 14. However, the exact location of the boundary is arbitrary, and, for convenience, we selected the top of Core 183-1139A-67R as the beginning of Unit 14. It is possible that some of the breccia at the top of Unit 14 is actually a basal breccia for Unit 13. Given the state of the recovered rocks, we did not interpret the relationship between Units 13 and 14.

Unit 14: Breccia-Topped Transitional Lava Flow

The relatively unaltered and undisturbed portion of the breccia in the upper part of Unit 14 is the first (partially) well-preserved flow-top breccia in Hole 1139A. However, we can also draw some important conclusions from the overlying altered part. First, an autolith is diagnostic of a breccia disrupted by melt during emplacement (Fig. **F35**). Second, the lack of angular vesicles (despite the wide range of observed vesicle morphologies) argues against a classic aa breccia. The elongated vesicles along the margins of the larger clasts are more typical of pahoehoe lobes or spatter. However, the moderate vesicularity and large size of the clasts argues against the clasts resulting from spatter.

The most striking feature of the well-preserved breccia is the gradational increase in the fine-grained matrix with depth and its gradual change to a coherent lava. Two explanations are (1) the lava contained a large amount of fines that became sintered into a coherent lava deep in the breccia or (2) the coherent lava disaggregated as it cooled higher in the breccia. The observations weakly favor the first possibility. Highly rounded equant shapes of the larger clasts suggest much mechanical abrasion that would produce many fines. Also, where we have observed disaggregating dense lava in Hole 1138A and Hawaii (L. Keszthelyi, unpubl. data), the transition occurs over a distance of a few centimeters, not the several tens of centimeters as observed here. In either case, the indistinct appearance of the clast margins deep in the breccia indicate gradual assimilation into the coherent lava.

The generally low vesicularity of the massive interior of Unit 14 suggests efficient degassing during emplacement of the flow. The lowermost interior with mesostasis blebs appears to record how the few small vesicles formed in the massive interior. These vesicles may have been escaping from the late-stage liquids represented by the mesostasis blebs. Their small size may have kept them from rising rapidly enough to escape through the disrupted upper crust before the flow stopped and solidified.

The basal part of Unit 14 records a process similar to that in the upper breccia. The gradual decrease in dense coherent lava and increase in the distinctness of the vesicular clasts with depth suggests that a basal breccia was being remelted and assimilated along the base of the flow interior. The lava in the highly fractured, altered, and disturbed breccia below this level is not clearly associated with Unit 14. In particular, the clasts with angular vesicles have no counterparts in the flow-top breccia. Also, mesostasis blebs are very rare in smaller lobes and are usually confined to the massive interiors of flows.

Unit 14/Unit 15 Boundary

For the reasons noted above, some of the breccia under the coherent part of Unit 14 may actually belong to Unit 15. Given the equivocal nature of this breccia, we make no attempt to interpret the relationship between Units 14 and 15.

Unit 15: Breccia-Topped(?) Lava Flow

The recovered rocks from Unit 15 show the features of the middle and lower parts of a lava flow. However, all we can infer about the flow top is that the basal brecciated zone assigned to Unit 14 implies a flow top breccia. The change from irregular to rounded vesicles at the top of the recognizable rocks in Unit 15 might be the transition from the upper coherent vesicular crust to the massive interior, suggesting that we have the entire interior of the flow. The vesicular zone within the massive interior exhibits features atypical of horizontal vesicular zones in inflated pahoehoe flows (see **"Physical Volcanology,"** p. 13, in the "Explanatory Notes" chapter). In particular, the changes in vesicle shapes but relatively constant vesicularity (in volume percent) and vesicle size are atypical. The gradation into mesostasis blebs at the base of the vesicular zone suggests that some of these vesicles may have formed during crystallization of the flow. The gradation from patchy vesicular zones to a coherent vesicular lava at the base of the flow suggests a welded basal breccia that has been disrupted by and incorporated into the floor interior.

Unit 15/Unit 16 Boundary

The nature of the base of Unit 15 suggests a basal breccia. However, for convenience we include all the breccia below the coherent part of Unit 15 in Unit 16. Thus, the location of the Unit 15/Unit 16 boundary probably does not reflect the contact between the two flows. However, no features in the breccia indicate exactly where the contact is. Given the nature of this boundary, it is clear that no significant weathering horizon or sedimentary interbed formed between the two flows. This suggests that the two units were emplaced closely in time.

Unit 16: Breccia-Topped Transitional Lava Flow

The better preserved parts of the breccia at the top of Unit 16 strongly indicate that it formed during emplacement of the flow. In particular, the unsorted mix of lithologies and angular to subangular shapes are not consistent with extensive reworking of the breccia. The clasts do not appear to include classic aa clinker but do include small partially fragmented pahoehoe lobes. The large dense clast (interval 183-1139A-68R-5, 100–116 cm) is likely to be an arm of the massive interior that has penetrated into the flow-top breccia. The banding in the arm is more reminiscent of felsic flow banding than that in basaltic flows. This suggests that the arm was more viscous than expected for basalt. The relatively poorly preserved massive interior appears similar to the interiors of other breccia-topped units though entrained clasts are notably absent. The slight increase in vesicularity at the base of the massive lava might be the start of a basal vesicular zone.

Unit 16/Unit 17 Boundary (Section 183-1139A-68R-7, 38 cm)

The contact between Units 16 and 17 is probably in the breccia, but its exact location is equivocal. We have chosen to place all the breccia at the top of Unit 17, even though some of this material may be a basal breccia for Unit 16. However, the breccia immediately below the coherent interior of Unit 16 is highly altered, and no contact between a flow-top and flow-base breccia can be discerned. Given the altered nature of the breccia, we cannot determine exact contact relationships between the two units.

Unit 17: Breccia-Topped(?) Lava Flow

The high degree of alteration of the breccia at the top of Unit 17 makes detailed interpretation difficult. In fact, there is no strong evidence that this breccia was formed during emplacement, but the clasts are generally similar to the autobreccias on the other flows. There is no apparent reason why the interior of Unit 17 is more massive and featureless than the interiors of the overlying units. The large irregular voids are as likely to have formed by alteration processes as during the original emplacement of the flow.

Unit 17/Unit 18 Boundary

The change from the sparsely plagioclase-phyric interior of Unit 17 to the moderately sanidine phyric top of Unit 18 is clear, but the contact was not recovered. The matrix supported conglomerate at the top of the Unit 18 breccia could be the result of reworking of a flow-top breccia. This tentatively suggests a significant time gap between the emplacement of Units 17 and 18.

Unit 18: Lava Flow(?)

The breccia on the top of Unit 18 is difficult to interpret. Although there is no definitive evidence that Unit 18 is a lava flow, the low vesicularity of the clasts in the breccia argues against a pyroclastic origin. Also, the largest clasts appear to be 10- to 20-cm-diameter lobes. Shear during flow through a lobe can mechanically push large phenocrysts to the lobe margin, possibly explaining the crystal-rich annuli. This suggests that the breccia top to Unit 18 might be similar to some of the transitional flows seen at earlier sites (see **"Physical Volcanology,"** p. 13, in the "Site 1137" chapter and **"Physical Volcanology,"** p. 22, in the "Site 1138" chapter). Brecciation has also apparently separated the large feldspar phenocrysts from the glassy matrix of some clasts. Resedimentation of the fines from breccias like those on top of Unit 18 could produce the feldspar-rich sands seen at various locations in Hole 1139A. The blurring of clast margins at the base of the breccia could be completely the result of alteration but also suggests some welding deep in the breccia.

The pattern of vesicularity in the interior of Unit 18 does not lend itself to a straightforward interpretation, especially because the identification of vesicles was commonly very difficult. However, the basal breccia shows a complex history and a wide range of rheologic behavior. The lobe at the base of Unit 18 suggests that the leading edge of this trachyte flow might not have been very different from a pahoehoe flow. The welded, contorted clasts above this lobe indicate that the lava that rode over the initial lobe was being disrupted. It also suggests that the breccia being shed from the front of this second wave was covered quickly enough for the clasts to be unable to freeze solid. The breccia with hemispherical clasts could be a trachytic version of slab pahoehoe top and would indicate that the lower ~1 m of Unit 18 is physically separate from the large overlying lobe. Finally, the narrow zones of angular breccia show evidence for shear (presumably continued flow of the lava) after the flow had cooled to the point where it could undergo brittle failure.

Unit 18/Unit 19 Boundary

The breccia at the top of Unit 19 has the same character as the breccia at the top of Unit 18, so we interpret it to be the flow top breccia for Unit 19. The increased rounding of the uppermost clasts again suggests of some significant time break between the emplacement of Units 18 and 19.

Unit 19: Lava Flow(?)

The interpretation of the breccia on Unit 19 poses similar problems as for Unit 18. However, in this case, lobe-like clasts are absent and the horizontal elongation of clasts suggest some flattening of the breccia. This makes it impossible to rule out a pyroclastic origin for this flow-top breccia. The massive, highly altered interior of the flow does not provide much to interpret. The curious lithic fragment (interval 183-1139A-72R-1, 19–21 cm) in the lava (Fig. **F43**) is very difficult to explain if it was not thrown onto the top of the flow by explosive activity and then entrained into the flow as it assimilated its brecciated crust. Xenoliths of such dense rock are expected to sink to the bottom of the flow rather than be suspended in the upper part of the interior of the flow.

Interpretation of Emplacement Conditions

Units 2, 3, and 4 might plausibly represent different welding zones within a single thick pyroclastic flow deposit. This interpretation is consistent with the similar phenocryst assemblage, abundance, and size in all three units (see **"Igneous Petrology,"** p. 36). In addition, Units 2 and 4 have very similar physical characteristics (see **"Physical Properties,"** p. 49, and **"Downhole Measurements,"** p. 56). The lower K_2O content of Unit 3 relative to Unit 4 is probably caused by differences in the type of alteration, as Unit 3 is pervasively altered to green clay, whereas Units 2 and 4 are red and oxidized and probably have been silicified (see **"Igneous Petrology,"** p. 36 and **"Alteration and Weathering,"** p. 42). Welded pyroclastic flow deposits only rarely form in submarine environments, and welding in such deposits is not sufficiently intense to form vitrophyre. Thus, the pyroclastic flow deposit in Units 2 through 4 was very likely emplaced subaerially. The oxidation of Units 2 and 4 further indicates weathering in a subaerial environment for a significant period of time following emplacement. However, given the poor recovery and intense alteration, we cannot reach definitive conclusions.

Given the highly altered and disturbed states of most contacts within the lava pile, it is difficult to make any confident generalizations about their style of emplacement and the environment they were emplaced into. However, there is no evidence for interaction with significant amounts of water. Also, the basaltic flows are probably <10-m-thick, making it unlikely that they traveled >100 km from their vents.

IGNEOUS PETROLOGY AND GEOCHEMISTRY

Lithology

We recognize 19 basement units at Site 1139 (Table T10; Fig. F44) recovered from a total thickness cored of 232.26 m. Unit 1 is composed of felsic volcanic and volcaniclastic rocks; Unit 2 is a vesicular, moderately sanidine-phyric rhyolite that may be a pyroclastic flow deposit; and Unit 3 is a highly altered crystal vitric tuff-breccia. Unit 4 is also a welded vesicular rhyolite that has many textural similarities to Unit 2. These units are described in detail in **"Physical Volcanology,"** p. 13.

Units 5–19 are lava flows that appear to have been erupted subaerially. Unit 5 is a ~10-m-thick moderately sanidine-phyric trachyte, with brecciated zones, which contains a small amount of phenocrystic clinopyroxene that is now completely altered. This unit has experienced high to very high degrees of alteration. Units 6–17 contain a sequence of aphyric to sparsely plagioclase-phyric flows ranging in composition from trachybasalt to trachyandesite. Many have brecciated and massive zones. The curated thicknesses of the units range from 1.8 to 19.3 m. We cannot interpret each unit as representing a separate eruption. Unit divisions were largely made on the basis of recognizing intraflow structures such as flow-top breccias and massive interiors (see **"Physical Volcanology,"** p. 13; Table T6). It should be noted that such recognition was made difficult by the intense alteration (see **"Alteration and Weathering,"** p. 42). For some brecciated zones, the basal breccia of the overlying flow could not be differentiated from the flow-top breccia of the underlying flow. In some cases, particularly in sections with poor recovery and/or significant faulting, breccias are not assignable to either the overlying or underlying massive lavas and may represent all that was recovered from additional flow units. The recovered units include aa-type (Unit 11) and compound-pahoehoe-type (Unit 10) flows; however, in most cases the morphologic type could not be determined from the rocks recovered (see **"Physical Volcanology,"** p. 13).

A serious difficulty in classifying and interpreting the core from Site 1139 is the strong fracturing or shattering of the core that obscures many original features of the rocks. Fracturing tends to be greatest in brecciated zones; slickensides in most of these zones document shearing. Generally, alteration is also highest in the breccias and many are completely altered (see **"Alteration and Weathering,"** p. 42). Massive interiors of the units are typically moderately to highly altered. The picture that emerges is of significant postemplacement fluid flow and faulting focused along flow boundaries.

T10. Petrographic summary of Site 1139 igneous units with mineralogies, **p. 196.**

F44. Interpretative summary diagram, **p. 113.**

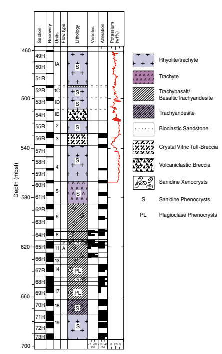

Unit 18 is a sanidine-phyric trachyandesite, and Unit 19 is a sanidine-phyric trachyte flow; both units have thin upper brecciated zones and comparatively thick, massive interiors. Unit 18 (12.9 m thick) is moderately sanidine-phyric and generally highly to completely altered, with a complex alteration history (see **"Alteration and Weathering,"** p. 42). A distinctive feature of this unit is its bleached appearance in the extensive alteration halos around veins. Unit 19 (≥19.8 m thick) is a moderately sanidine ± clinopyroxene-phyric trachyte. In contrast to Unit 18, alteration in Unit 19 is generally moderate. Parts of both Units 18 and 19 have variably colored alteration zones or bands; some of those in Unit 19 are particularly vivid.

Petrography

In this section, we describe the primary textures and mineralogy of igneous basement units. Units 1–5 and 18–19 belong to a felsic series, and Units 6–17 belong to a trachybasaltic series (Fig. **F44**) at Site 1139 (see **"Magmatic Characteristics,"** p. 40).

Unit 1 is composed of four variably altered and brecciated volcanic subunits and an interbed of bioclastic sandstone (Subunit 1B). We observe that the volcanic subunits are generally composed of felsic lavas and volcaniclastic rocks (Subunits 1A and 1C–1E). Flow banding is common in Subunits 1A and 1C, and highly vesicular material (pumice) is present in Subunit 1C. Quartz phenocrysts are present in the rhyolite of Subunit 1A, but quartz is only a minor groundmass phase in Subunits 1C–1E, where the major phenocryst phase is sanidine. Subunit 1C exhibits a striking perlitic texture (Fig. **F14**).

Units 2 and 4 are vesicular rhyolites that may represent parts of a welded pyroclastic flow. They are macroscopically similar and, although highly altered, the groundmass exhibits a flow texture (Fig. **F45A**). They contain relatively unaltered sanidine (8%–15%) and minor (1%) quartz phenocrysts (Fig. **F45B**). Unit 3 is a crystal vitric tuff-breccia consisting of a highly altered, glassy, perlitic groundmass that contains sanidine and quartz phenocrysts (Fig. **F46**). In addition, lithic clasts are present and occasionally the sanidines are brecciated or shattered.

Unit 5 is a trachyte containing phenocrysts of sanidine and completely altered mafic phenocrysts (probably clinopyroxene), which have been replaced by siderite (Figs. **F47**). The moderately to highly altered feldspathic groundmass exhibits a trachytic texture and contains minor quartz that is possibly of secondary origin.

Units 6–17 vary from trachybasalt to basaltic trachyandesite and are all moderately to highly altered. The top of Unit 7 is a generally clast-supported sediment, rich in sanidine crystals (Fig. **F48A**) and with very little matrix (now altered to opaque clay and hematite) (Fig. **F48B**). The sanidine crystals in this sediment and their absence as liquidus phases in the trachybasalt and basaltic trachyandesite lavas indicate derivation of the sediment from a separate, more evolved eruptive source.

Each mafic unit displays trachytic intergranular texture and is either aphyric or sparsely plagioclase-phyric (Figs. **F49, F50A**). The groundmass is composed of plagioclase (55% ± 10%), clinopyroxene (35% ± 10%), titanomagnetite (5% ± 3%), and mesostasis. Generally, the clinopyroxene and glass are moderately to completely altered, the plagioclase is moderately altered (to clay and replaced by carbonate), and the titanomagnetite is fresh to moderately altered (to maghemite and hematite) (Fig. **F51**). Fresh titanomagnetites exhibit rare maghemite exsolution. These lavas contain slightly more titanomagnetite, as much as

F45. Units 2 and 4 photomicrographs, **p. 114.**

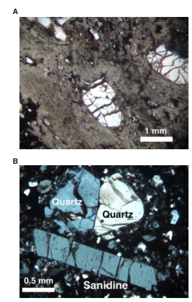

F46. Photomicrograph of sanidine phenocrysts in a perlitic glassy groundmass in Unit 3, **p. 115.**

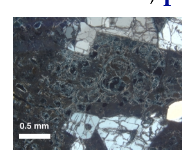

F47. Photomicrographs of sanidine and altered mafic phenotrysts, **p. 116.**

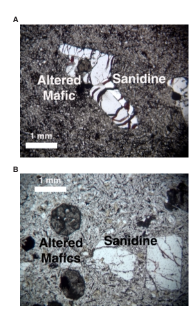

10 vol%, than lavas from other Leg 183 sites. A sulfide phase (pyrite? or pentlandite?) in Unit 17 may be primary because it is found as inclusions in unaltered primary minerals; the small size of this sulfide phase precludes positive identification.

Several petrographic features are significant. Firstly, every trachybasalt and basaltic trachyandesite contains large, euhedral sanidine crystals surrounded by a sieve-textured reaction rim (Fig. **F50A**). Rare examples have sieve-textured interiors. Some sanidine crystals exhibit highly resorbed outlines (Fig. **F50B**). In contrast, the presence of euhedral plagioclase microphenocrysts (i.e., Figs. **F49, F50A**) indicates that plagioclase is the probable liquidus phase. We conclude that the sanidine in these lavas is xenocrystic.

The second feature is the absence of albite twinning in many plagioclase phenocrysts. Only Carslbad twinning (Fig. **F52A**), which can cause plagioclase to be mistaken for alkali feldspar, is evident. It appears that strong compositional zoning in many of these laths (Fig. **F52B**) has inhibited the formation of albite twins, allowing only those of the Carlsbad variety to develop. Similar features were observed in some of the plagioclase glomerocrysts from other Leg 183 sites, especially at Site 1137, in basement Unit 10 (see **"Igneous Petrology and Geochemistry,"** p. 28, in the "Site 1137" chapter).

Many groundmass plagioclase laths also lack albite twinning and exhibit only Carlsbad twins, but unlike the plagioclase phenocrysts, no compositional zonation was observed. These groundmass feldspars exhibit undulatory extinction, and the Carlsbad twin plane is more diffuse than in the phenocrysts and in primary sanidines of the felsic rocks of Units 1–5 and 18–19 (Fig. **F53**). For example, in Figure **F52A** a groundmass feldspar exhibiting a "diffuse" Carlsbad twin (as well as undulatory extinction—see the inset box in Fig. **F52A**) is contrasted with that of the saniline phenocryst in this photomicrograph. We conclude that the groundmass plagioclase has been partially replaced by alkali-feldspar (plagioclase is still seen in the groundmass) and that the anomalous twinning and undulatory extinction result from this alteration. Similar features have been described elsewhere; for example, the altered basalts from the Ninetyeast Ridge (Frey et al., 1991). The replacement of plagioclase by potassic feldspar could indicate that the groundmass plagioclase was relatively Na-rich prior to alkali exchange with percolating K-rich fluids. Relatively sodic groundmass plagioclase is consistent with these lavas being more evolved than basalt.

The lowermost two units at Site 1139 (Units 18 and 19) are moderately sanidine ± clinopyroxene-phyric trachyandesite and trachyte, respectively. These units are completely altered, except for the top of Unit 18 and the bottom of Section 183-1139A-73R-3 in Unit 19, which are only moderately altered. In Unit 18, the sanidine phenocrysts are larger (≤8 mm) than in Unit 19 (≤3 mm) (compare Fig. **F54A** and **F54B**) Rare titanomagnetite phenocrysts, now altered to maghemite and hematite, are also present. Mafic phenocrysts are completely altered to clay and/or replaced by siderite (Fig. **F55;** see **"Alteration and Weathering,"** p. 42), as in Unit 5 (see Fig. **F47**). The sanidine phenocrysts and vesicles can be traced through zones of high (pink brown) to complete (white) alteration. In these areas of Unit 19, veins of carbonate and/or quartz pervade the rock, to the point of giving the rock a brecciated appearance (Fig. **F56**). Nevertheless, the groundmass in the completely altered areas preserves an original trachytic fabric (Fig. **F57**). In the least-altered samples, the groundmass is composed of alkali feldspar (perhaps formed by the secondary replacement of plagioclase), quartz

F48. Photomicrographs representing two different views of a sanidine-rich sandy layer, **p. 117.**

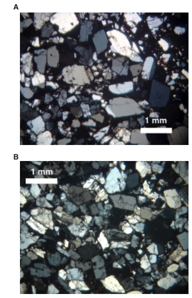

F49. Photomicrograph of a plagioclase microphenocryst, **p. 118.**

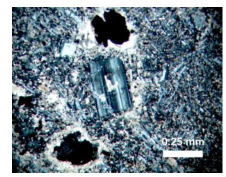

F50. Photomicrographs showing sanidine xenocrysts, **p. 119.**

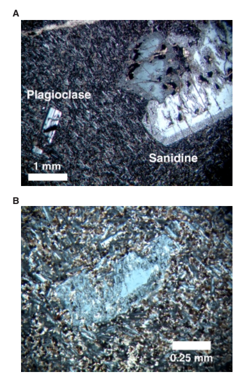

F51. Photomicrograph of a partially altered titanomagnetite, **p. 120.**

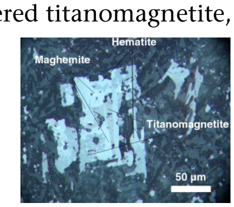

(perhaps primary although quartz-bearing veins are present), titanomagnetite (partially replaced by hematite), and a mesostasis composed of an intricate network of microcrystalline opaques set in a felsic glass (Fig. **F58**). All mafic minerals have been completely altered to clay or replaced by siderite and quartz. The microcrystalline clays suggest moderate alteration temperatures (see **"Alteration and Weathering,"** p. 42). At the base of the borehole, Unit 19 exhibits a recrystallized groundmass containing abundant small, oriented laths of feldspar poikilitically enclosed in larger grains of a second feldspar and quartz (Fig. **F59**).

Major and Trace Element Compositions

We report XRF data for 23 samples from Site 1139 (Table **T11**). Interpretation of these geochemical data is complicated by the moderate to high degree of alteration that has affected all Site 1139 basement samples. In the SiO_2 vs. total alkalis (Na_2O + K_2O) diagram (Fig. **F60**), the samples form an alkalic suite. Two samples (183-1139A-65R-3, 90–93 cm, Unit 10, and 66R7, 8–12 cm, Unit 13) that plot within the tephrite/basanite field are highly altered (>7% loss on ignition [LOI]) (Table **T11**) and probably have lost SiO_2 and/or gained alkalis during alteration (Fig. **F60A**). Yet, these samples are petrographically similar to the other trachybasalts. In the following discussion, these samples are grouped with the trachybasalts. The petrographically highly altered crystal-vitric tuff (Sample 183-1139A-56R-3, 92–95 cm, Unit 3) lies in the dacite field (Fig. **F60A**) but also has high LOI (~5.7%). The low-alkali, high-LOI, and high-MgO contents suggest that the tuff gained MgO during alteration, particularly since 4.2 wt% MgO is unusual in a rock with abundant quartz phenocrysts and high normative quartz (36.7%) (Table **T11**).

A change in the type of alteration is reflected in a downhole increase in CO_2 (Fig. **F61**). The CO_2 data, combined with identification of siderite in XRD analyses and petrographic observations of carbonate in the groundmass of many samples, suggest that fluxing of CO_2-rich fluids played an important part in the alteration process of Units 7–19 (see **"Alteration and Weathering,"** p. 42).

Six analyses of trachyandesite and trachyte from Units 18 and 19 demonstrate some of the characteristics of element mobility associated with alteration (e.g., in Fig. **F62,** the Unit 19 analyses are arranged in order of increasing alteration, as inferred from petrographic study and CO_2 and H_2O contents). There is a progressive decrease in SiO_2, Na_2O, and K_2O, and an increase in total Fe_2O_3* (* indicates the total iron as Fe_2O_3) and MgO, as the degree of alteration increases. In contrast, TiO_2 and Al_2O_3 have relatively constant concentrations and appear to be unaffected by the alteration. CaO and P_2O_5 have concentrations below detection limits in the two moderately altered samples and higher concentrations in the others. The alteration behavior of trace elements in Unit 19 is illustrated by Zr, Nb, Rb, and Ba. The first three show a decline with increasing alteration, whereas Ba varies more erratically. In contrast, the most altered sample from Unit 18 has a higher abundance of SiO_2, but a lower abundance of MgO, Al_2O_3, and Na_2O, and highly incompatible trace elements (Fig. **F60A;** Table **T11**). From these results it is clear that the chemical effects of alteration are complicated and that both the major and trace element data should be interpreted with caution.

F52. Photomicrographs depicting an apparent alkali feldspar phenocryst, **p. 122.**

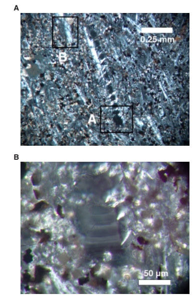

F53. Photomicrograph of a sanidine phenocryst, **p. 122.**

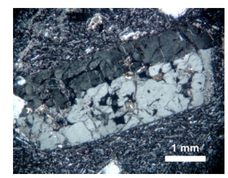

F54. Sanidine phenocrysts color close-ups, **p. 123.**

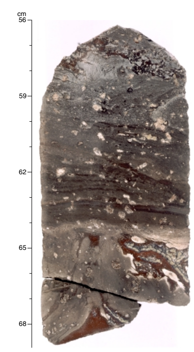

F55. Photomicrographs of altered mafic phenocrysts, **p. 125.**

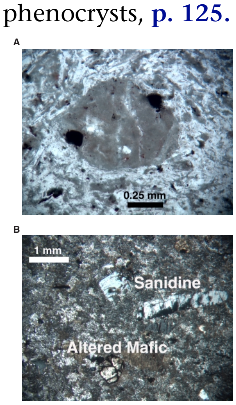

Magmatic Characteristics

Although the sequence has suffered relatively intense alteration, it is possible to extract some information about the magmatic characteristics of Site 1139 samples. The abundance of sanidine phenocrysts is consistent with the alkalic compositions of these rocks. When the petrographically more altered samples (Units 3, 10, 13, and 18) are excluded, compositions range from trachybasalt to rhyolite and plot entirely in the alkalic field (Fig. **F60A**). In general, these lavas are more alkalic than lavas from other Leg 183 sites (Fig. **F60B**). MgO and Ni contents are low (<4.3% and <13 ppm, respectively), and total alkalis are always >4.5% (Table **T11**). Concentrations of incompatible trace elements are also relatively high compared to the other Leg 183 sites (e.g., Zr contents are 292–420 ppm in the trachybasalts and basaltic trachyandesites) (Fig. **F63**).

Compositions change downhole from rhyolite and trachyte in Units 1–5, to trachybasalt (and one basaltic trachyandesite) in Units 6–13, to basaltic trachyandesite in Units 14–17, to trachyandesite in Unit 18 and trachyte in Unit 19 (Figs. **F60A, F64**). On the basis of TiO_2 and SiO_2 (Fig. **F64**), we separate the Site 1139 rocks into two groups that will be referred to subsequently, for convenience, as the mafic group (trachybasalts and basaltic trachyandesites) and the felsic group (trachyandesite, trachytes, and rhyolites). Although the Unit 3 crystal-vitric tuff has MgO and Al_2O_3 contents similar to those shown by Units 6–17, this may be a result of alteration, and we include this sample in the felsic group, especially since perlitic textures are identified in thin section.

In primitive mantle–normalized trace element diagrams (Fig. **F65**), samples from the mafic group have generally subparallel patterns that are surprisingly consistent considering the degree of alteration experienced by these units. In the felsic group, patterns are more variable as a result, at least in part, of the fractionation of feldspar and incompatible element-rich accessory phases (e.g., low Ba, Sr, and Ti relative to adjacent element concentrations). The crystal-vitric tuff sample (Unit 3) is again distinctive, having the lowest Zr and highest Nb compared to the other felsic units, but this may be a result of the high degree of alteration experienced by this sample.

Comparison with Other Kerguelen Plateau Sites

As noted above, volcanic rocks from Site 1139 are distinguished from all other samples drilled or dredged from the Kerguelen Plateau basement by their relatively evolved and alkalic character (Fig. **F60B**) and high concentrations of incompatible trace elements (Fig. **F63**). They more closely resemble the alkalic volcanic series from the Kerguelen Archipelago. The chemical trends shown by the Kerguelen Archipelago evolved suites have been interpreted to result from fractionation of feldspar, Fe-Ti oxides and accessory phases, such as apatite (Weis et al., 1993, 1998).

The mafic rocks from Site 1139 and the Kerguelen Archipelago generally overlap in K_2O, SiO_2, and Al_2O_3, but at a given MgO content, Site 1139 lavas trend to higher contents of TiO_2 (Fig. **F66**), Fe_2O_3* (not shown), and Y (Fig. **F67**) than their counterparts from the Kerguelen Archipelago. In the plots of SiO_2 and MgO vs. TiO_2 (Fig. **F66**), it is unclear whether these differences reflect real differences in magma compositions, caused perhaps by differences in crystallization histories, or result from alteration because we demonstrate that both silica and magne-

F56. Photomicrograph highlighting the extreme veining from Unit 19, **p. 126.**

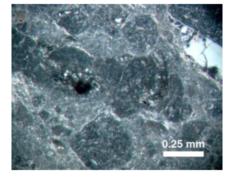

F57. Photomicrographs demonstrating the trachytic texture still evident from Unit 18, **p. 127.**

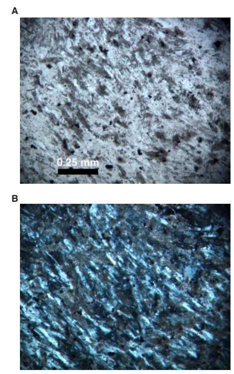

F58. Photomicrographs of the recrystallized mesostasis from Unit 18, **p. 128.**

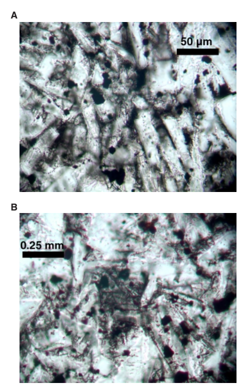

F59. Photomicrograph of the recrystallized groundmass from Unit 19, **p. 129.**

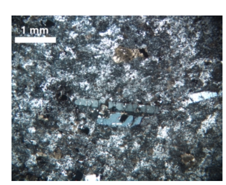

sium are affected by alteration. However, the high Y concentrations at Site 1139 likely indicate either a different parental magma composition or a different evolution trend than those for the Kerguelen Archipelago series. Primitive mantle–normalized trace element patterns of the mafic group (Fig. **F65A**) are strongly fractionated as indicated by Nb/Zr and Zr/Y ratios, but the Kerguelen Archipelago series extends to even higher ratios (Fig. **F67**). Even so, Nb/Zr ratios in the Site 1139 mafic group are significantly higher than those of other Kerguelen Plateau basement lavas. Therefore, there is no indication of the crustal component that was inferred in basalts from Sites 1137 and 738 on the basis of their low Nb/Zr ratios (Fig. **F63**).

The felsic group from Site 1139 (Units 1–5, 18, and 19) not only shows major element abundances offset from the Kerguelen Archipelago values, but also shows markedly different trends in TiO_2, Al_2O_3/TiO_2, and P_2O_5 vs. SiO_2 caused by the strong silica enrichment (Fig **F66**). The felsic rocks are strongly enriched in Nb, Zr, and Y, but show pronounced relative depletion of Ba, Sr, Ti, and P (Figs. **F65, F66B, F67**), which is the signature of felsic magmas that have evolved through the fractionation of feldspar, Fe oxides, and apatite (Weis et al., 1993). Because fractionation of these phases has also been invoked for the Kerguelen Archipelago series, the major element trends suggest that this fractionation continued to increase silica in the Site 1139 felsic magmas, whereas other elements had already been depleted by the removal of the fractionating phases (~0 wt% MgO, CaO, and P_2O_5) (Fig. **F65;** Table **T11**).

Summary

The Site 1139 basement sequence ranges from trachybasalt to trachyte and rhyolite and is the most alkalic and evolved suite of igneous rocks encountered during Leg 183. On the basis of macroscopic features, we conclude that this sequence erupted subaerially. In spite of the intense alteration that subsequently affected these rocks, petrographic and geochemical analyses reveal information regarding the igneous evolution of these lavas. The mafic lavas are generally aphyric and contain rare plagioclase phenocrysts and sanidine xenocrysts. The felsic lavas also contain sanidine phenocrysts, and the rhyolitic samples have quartz phenocrysts and microphenocrysts. The presence of the sanidine xenocrysts and disequilibrium textures within the mafic lavas and the occurrence of felsic lavas both above and below the mafic units suggest that magma mixing or wall-rock assimilation may have affected the trachybasalts and basaltic trachyandesites. However, geochemical evidence of magma mixing is not obvious from the current data set and will be the topic of further investigation.

Major and trace element data provide a compelling picture of feldspar, Fe-Ti oxide, and apatite fractionation in the petrogenesis of the Site 1139 lavas. In spite of the overprint of alteration, including evidence of silicification in Unit 18, the behavior of trace elements such as Ba, Sr, Zr, and Ti suggest that high degrees of fractionation are required to form the felsic lavas and volcaniclastic rocks. Shore-based isotopic data and mineral chemistry data will reveal whether the lavas were generated from similar parental melts or whether they originated from unrelated magmatic systems. We characterize postemplacement alteration as including both silica and rubidium loss and magnesium gain, in addition to mobilization of calcium, phosphorus, and highly incompati-

T11. XRF analyses of major and trace elements for Site 1139 igneous units, **p. 198.**

F60. Igneous and mafic rock compositions, **p. 130.**

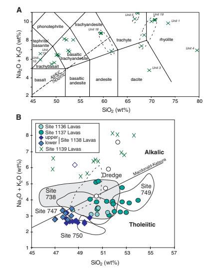

F61. Downhole variations in CO_2 and H_2O for Site 1139 igneous rock compositions, **p. 131.**

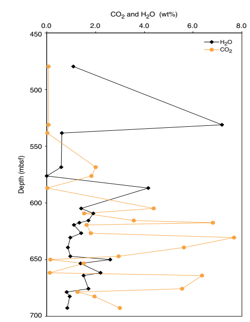

F62. Compositions of four samples from Unit 19 arranged in order of increasing alteration, **p. 132.**

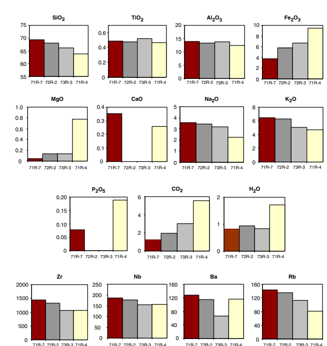

ble trace elements (Fig. **F62**). The fluids responsible for the alteration seem to have had varying amounts of H_2O and CO_2.

Site 1139 volcanic and volcaniclastic units cannot have evolved from tholeiitic melts that are the dominant lava type at other Kerguelen Plateau sites. Instead, the Site 1139 suite appears to have a magmatic history similar to the evolved lava suites exposed on the Kerguelen Archipelago, where the evolved lavas have been interpreted as products of feldspar, Fe-Ti oxide, and apatite fractionation from alkali basalt and basanite parental magmas. Primitive mantle–normalized ratios of Nb/Zr relative to Zr/Y provide, however, a preliminary indication that some aspects of the magmatic evolution of the Site 1139 sequence are different from the Kerguelen Archipelago series (Fig. **F67**). We expect that isotope analyses will further constrain similarities and differences between the formation of Site 1139 and Kerguelen Archipelago lavas.

ALTERATION AND WEATHERING

Nineteen basement units have been defined in Hole 1139A, including an upper succession of felsic volcanic and volcaniclastic rocks (Units 1–4) and a series of subaerial lava flows (trachybasalt to trachyte, Units 5–19), many with brecciated flow tops (see **"Igneous Petrology,"** p. 36, and **"Physical Volcanology,"** p. 13). Fluid/rock interaction has variably altered all basement units after emplacement, as indicated by secondary minerals that partly replace primary minerals, partly to completely replace mesostasis, and partly to completely fill veins, vesicles, and open spaces between clasts within breccias. We recorded the distribution of secondary minerals in the alteration and vein/structure logs (see the **"Supplementary Materials"** contents list) for Hole 1139A (Fig. **F68**). Shipboard time constraints precluded the detailed interpretation of structural data, but orientation measurements were made for the majority of features observed. In addition, we performed XRD analyses to identify secondary minerals (Table **T12**). These data show that rocks recovered from Hole 1139A display unique alteration patterns, relative to both the intensity of alteration and secondary mineralogy, when compared to other Leg 183 sites. In this section, we describe these unique alteration patterns and qualitatively estimate mass transfer of major elements associated with the most highly altered intervals.

Units 1–4

The upper part of the basement section in Hole 1139A (Units 1–4) comprises highly altered and variably oxidized felsic volcaniclastic rocks. Despite the high degree of alteration, primary igneous features such as flow banding and perlitic textures are still visible. Brecciated textures are extremely common and appear to have diverse origins that include primary volcanic processes, faulting, reworking, and secondary hydrothermal processes. Cataclastic fabrics are particularly common, and slickensides are a ubiquitous feature on broken clay-rich surfaces. In general, breccia clasts include pumice altered to light green clay and angular felsic and mafic rocks altered to brown or dark red clay in a matrix of variably oxidized green to brown clay. Other brecciated intervals have red-brown clasts with thin (<2 mm) rims altered to light green clay within a red, variably oxidized matrix (Fig. **F24**). Alkali feldspar phenocrysts are common in clasts and are particularly abundant within the welded rhyolite composing Unit 4; some phenocrysts are remarkably

F63. Mafic lava comparisons, **p. 133.**

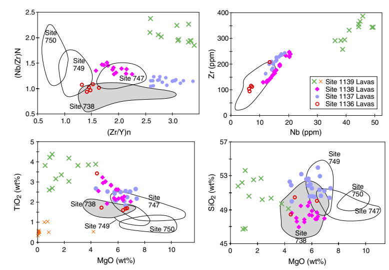

F64. Downhole variations in selected major and trace elements and loss on ignition, **p. 134.**

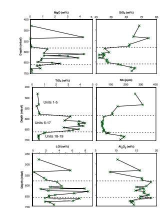

F65. Major element compositional variations for Site 1139 compared with Kerguelen Archipelago alkalic volcanic series, **p. 135.**

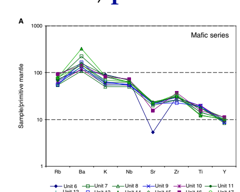

F66. Primitive mantle–normalized incompatible trace element patterns for Site 1139 igneous rocks, **p. 137.**

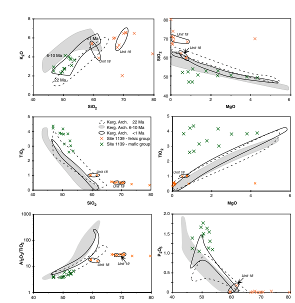

fresh or only slightly altered. In addition, patchy silicification of clasts and matrix is common in many brecciated intervals (e.g., interval 183-1139A-52R-1, 104–150 cm). We also observed a hydrothermal breccia within Unit 1D (Fig. F18), which is more highly silicified than other brecciated intervals. The matrix is composed of a distinct yellow clay, and the clasts are variably altered felsic and mafic volcanics. Veins and fractures are rare in Units 1–4, although subvertical fractures occur with light brown alteration halos. We also noted rare clay-filled veins that crosscut red alteration bands, suggesting that oxidation predates the veining event (e.g., interval 183-1139A-55R-1, 18–71 cm).

Units 5–19

The underlying trachybasalt through trachyte flows composing Units 5–19 (see "Igneous Petrology," p. 36) are heavily brecciated as a result of volcanic flow-top processes and faulting. Most flows have only thin massive interiors and bases. As in all other Leg 183 holes, the brecciated flow tops (Fig. F36) are much more highly altered compared to the less permeable and more massive flow interiors (Fig. F69). Slickensides are common on broken surfaces, and most clasts are angular. The proportion of matrix and clasts varies widely among different breccias, from ~20% to 80% clasts. Breccia clasts are variably oxidized and vary from black to brick red to pinkish gray; some intervals have clasts with light green rims (e.g., Sample 183-1139A-61R-1 [Pieces 1A–1C, 0–43 cm]), similar to those in Unit 4. In other cases, breccia clasts are completely altered to green clay, suggesting a locally progressive alteration to green clay following oxidation. The matrix of these flow-top breccias is variably oxidized and consists of small lithic clasts replaced by secondary minerals that also fill open spaces between clasts. Red-brown and light green saponite are common in the matrix (Table T12), although red-brown clay is more abundant, even in cases where breccia clasts have been altered to light green clay (e.g., Sample 183-1139A-61R-3 [Piece 1, 0–12 cm]). Calcite and siderite are common secondary minerals in the matrix of breccias, with some intervals composed of ~30% carbonate (e.g., Sample 183-1139A-66R-4 [Piece 1, 0–101 cm]). Amorphous silica and quartz are rarely present.

Units 5–17

The thin and more massive flow interiors of Units 5–17 are generally moderately altered. Color varies from gray to green to red, reflecting variable oxidation and different alteration processes in groundmass and phenocrysts. Dark green clays replace and accentuate the groundmass and mesostasis, whereas mafic and feldspar phenocrysts are variably altered to red-brown and green clay, respectively. Carbonate is absent from Unit 5 but is a common secondary mineral in the remainder of the basement of Hole 1139A. Rarely, these basement units have a pale gray hue, and the groundmass is bleached because of the replacement of primary igneous minerals by secondary calcite and siderite (e.g., Sample 183-1139A-64R-2 [Pieces 1–5, 0–143 cm]).

Vesicles generally compose <5% of Units 5–17, although in rare cases, vesicularity approaches 20%. Vesicles are completely filled with a secondary mineral assemblage that includes green clay, siderite, calcite, and, rarely, amorphous silica. Light brown siderite, white calcite, and, more rarely, green clay occur as alternating semicircular bands within

F67. Trace element compositional variations for Site 1139 compared with Kerguelen Archipelago alkalic volcanic series, p. 138.

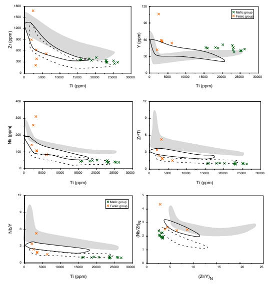

F68. Alteration and distribution of secondary minerals vs. depth, p. 139.

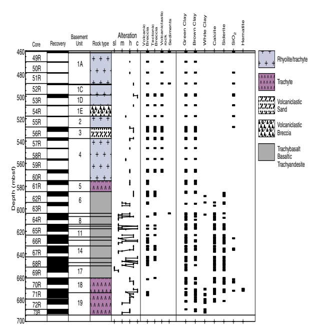

T12. Alteration minerals within basement units identified by X-ray diffraction, p. 201.

F69. Close-up photograph of Sample 183-1139A-64R-4 (Piece 3, 35–43 cm, dry surface), p. 140.

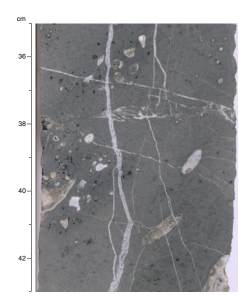

vesicles forming a colloform texture. Calcite typically fills the interior of these same vesicles (Fig. F69). Geopetal structures are rare.

Steeply to moderately dipping veins and fractures generally much less than 4 mm wide are common within Units 5–17. Calcite, siderite, and brown and green clay are the most abundant minerals filling veins or partially lining fractures. Green to red oxidation halos as much as 2 mm wide surround veins and fractures. We also observed multiple crosscutting, approximately orthogonal sets of calcite veins in some intervals that locally offset siderite-lined vesicles (Fig. F69). These relationships suggest early siderite formation followed by at least two calcite-forming events. The appearance of siderite as a secondary mineral cementing clasts within breccias and partly filling veins and vesicles is one characteristic that makes Hole 1139A unique when compared to other Leg 183 sites.

Units 18 and 19

Alteration increases abruptly within Units 18 and 19 and is characterized by two processes that have affected these lowermost flow units to different degrees: (1) oxidation characterized by red staining and (2) pervasive replacement of groundmass and phenocrysts by quartz and carbonate minerals, including siderite and calcite. Both types of alteration are most intense along veins, but many intervals appear to have been pervasively altered in the absence of permeability provided by fractures or vesicles. Based on visual core descriptions, rocks that have been only moderately changed are oxidized red gray and probably represent relatively unaltered trachytes in this part of the basement. In the most intensely altered intervals, the rocks are white with some pale pink patches and have a gritty or sandy texture. Our XRD and thin-section analyses of these intervals reveal that the groundmass and sanidine phenocrysts have been variably to completely altered to siderite and microcrystalline quartz with minor clay (Table T12). Based on our observations of crosscutting relationships, we believe that both styles of alteration have been superimposed on these lowermost basement units at different times. Similar processes probably affected Units 5–17 as well, although to a lesser extent.

The top of Unit 18 is a brecciated sanidine-phyric trachyandesite (Fig. F70). Breccia clasts have diffuse margins and are variably flattened with possible welded textures (see **"Physical Volcanology,"** p. 13). The color is generally red brown to gray brown, suggesting variable degrees of oxidation and differing amounts of siderite. These relatively fresh rocks gradually become more silicified and more oxidized with depth, as indicated by a change in color to very light gray and the appearance of local 2-mm streaks of brick red (hematite?) alteration (e.g., Sample 183-1139A-70R-2 [Pieces 1A–1D, 30–68 cm]). The intensity of alteration increases abruptly in Section 183-1139A-70R-2 at 68 cm with the first appearance of pale green to white trachyandesite that has been replaced by quartz and siderite (Fig. F71). Sanidine phenocrysts are variably replaced by these same phases, and some fresh phenocrysts are present, even in the most altered rocks. In general, the most intense alteration (white to pale pink) is present as 1- to 2-cm halos around veins partly filled with quartz, siderite, and calcite. We observed this style of alteration to the bottom of Section 183-1139A-70R-4. Within this depth range, completely altered white to light pink trachyandesite is moderately vesicular with siderite- and quartz-filling vesicles (Fig. F72). Also, brick red oxidation halos 1–2 mm wide appear along veins that crosscut

F70. Close-up photograph of Sample 183-1139A-70R-1 (Piece 3, 45–55 cm), **p. 141.**

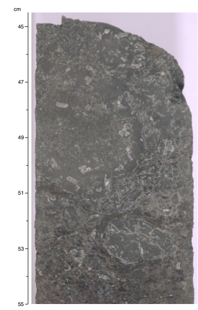

F71. Close-up photograph of Sample 183-1139A-70R-2 (Piece 1, 122–135 cm), **p. 142.**

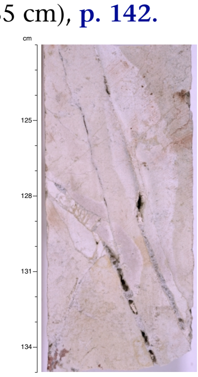

F72. Close-up photograph of Sample 183-1139A-70R-4 (Piece 4, 56–66 cm), **p. 143.**

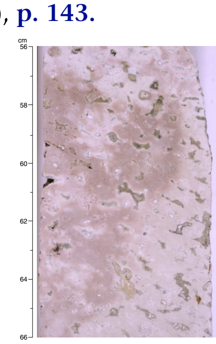

the intense white to pale green alteration zones and small patches of relatively fresh red-gray trachyandesite (Fig. F73). These relationships suggest a relatively intense oxidation event after the alteration that replaced the trachyandesite with quartz and siderite.

The remainder of Unit 18 (Sections 183-1139A-70R-5 through 71R-4) exhibits complex paragenetic relationships among different alteration and oxidation events of varying intensity. In general, the most intense white to pale green to pale pink alteration facies composes <10% of the rock over this interval and is completely absent in some sections. Very light gray to yellow-gray variably altered (silicified?) trachyandesite is more abundant within this part of Unit 18 (as much as 30%) and locally replaces the relatively fresh and moderately oxidized red-gray trachyandesite. We interpret these alteration zones to represent somewhat less intense examples of the white to pale green to pale pink horizons in the upper part of Unit 18, although this requires confirmation with more extensive chemical analyses of the bulk rock. Typically, these very light gray to yellow-gray zones are crosscut by prominent red alteration halos around veins filled with hematite, quartz, siderite, and calcite (Figs. F74, F75). Irregular cavities filled with these same secondary minerals also are present (Fig. F76). Intense oxidation accentuates primary igneous textures, particularly the mesostasis. We also noted narrow white to pale pink alteration halos around veins filled with quartz, siderite, and calcite (Fig. F77). These veins crosscut and locally offset dark red oxidation bands and light gray silicified(?) trachyandesite, consistent with an oxidation event before replacement of wall rock with quartz and siderite. Thus, our observations are consistent with a complex alteration history characterized by multiple oxidation events occurring both before and after multiple silicification(?) or silica-mobilization events and replacement of the trachyandesite by quartz and siderite.

The upper part of Unit 19 (Sections 183-1139A-71R-4 [Piece 1B, 19 cm] through 71R-6, Piece 1D) is highly brecciated and variable in color, reflecting differing degrees of oxidation of both matrix and clasts. The brecciated intervals are uniformly clast dominated with clasts representing 75%–90% of the rock. Clasts and matrix are very light greenish gray near the top of the unit (Fig. F78) and gradually become more oxidized with depth. Within some intervals (e.g., interval 183-1139A-71R-5, 0–45 cm), clasts are red with light green rims, similar to the alteration patterns we observed in basement units at much shallower depths in Hole 1139A (e.g., Unit 5). At deeper intervals, color changes gradually with clasts becoming very pale brown (Fig. F79) and finally very pale green to light red (Fig. F80) within a red oxidized matrix. Thin-section and XRD analyses of these different breccias reveal no significant change in secondary mineralogy despite the color variations. Quartz is a common phase replacing groundmass in clasts and partly replacing sanidine phenocrysts. Relatively small amounts of clay (illite) were also identified in thin section and by XRD (Table T12). It is noteworthy that XRD analyses of the breccia clasts did not reveal any significant carbonate minerals; however, moderate amounts of carbonate-replacing groundmass and phenocrysts could be identified in thin section. This may be a result of sampling heterogeneous breccias that have been less pervasively altered to carbonate minerals. Thus, carbonates may be less abundant in some parts of Unit 19. Silicification (or silica mobilization), however, is just as pervasive as that observed in the completely altered white to pale pink alteration zones in Unit 18.

F73. Close-up photograph of Sample 183-1139A-70R-4 (Piece 5A, 94–104 cm), p. 144.

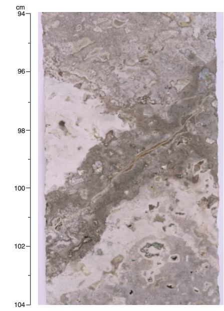

F74. Close-up photograph of Sample 183-1139A-71R-1 (Piece 2, 27–42 cm), p. 145.

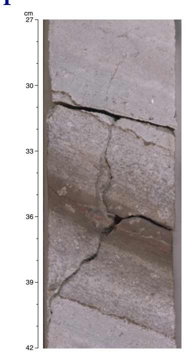

F75. Close-up photograph of Sample 183-1139A-71R-1 (Piece 2, 44–64 cm), p. 146.

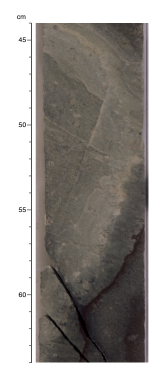

F76. Close-up photograph of Sample 183-1139A-71R-3 (Piece 2A, 62–67 cm), p. 147.

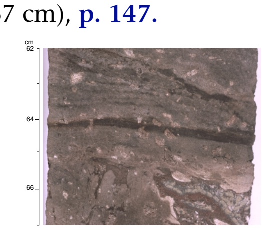

Unit 19 is more massive from Section 183-1139A-71R-7 to the bottom of the hole in Section 183-1139A-73R-3. The color of the flow varies from red brown to gray, with gray intervals representing some of the freshest rocks encountered in Hole 1139A (e.g., interval 1139A-72R-2, 0–85 cm). Sanidine phenocrysts are variably altered and rarely replaced by calcite. Minor carbonate is also found in glassy vesicular areas, and the groundmass is locally mottled and possibly silicified. Otherwise, vesicles are absent. Variable oxidation of the trachyte gives the rock a red-banded appearance (Fig. **F81**), and both the mesostasis and mafic phenocrysts with acicular textures are locally oxidized. Veins and fractures are numerous in Unit 19, are generally <2 mm wide, and are filled with brown clays, calcite, white clay(?), and rare siderite. White alteration halos, as wide as 10 mm, are common around veins filled with brown clay and calcite. We also observed numerous slickensides on fractured surfaces lined with clay.

Downhole variations in CO_2 and H_2O concentrations of basement units (see **"Organic and Inorganic Geochemistry,"** p. 54, and **"Igneous Petrology,"** p. 36) indicate that alteration in the bottom part of the basement in Hole 1139A is not associated with extensive hydration of volcanic protoliths but is instead characterized by carbonate metasomatism. Indeed, thin-section and XRD analyses do not reveal any abundant hydrous secondary phases, but siderite is ubiquitous. Thus, alteration was likely produced by the interaction of relatively siliceous volcanic rocks with hydrothermal solutions that have unusual compositions compared to those normally associated with alteration of typical oceanic crust. Moreover, it is not clear whether alteration occurred in submarine or subaerial environments.

We have compared the chemical compositions of the most highly altered "bleached" rocks in Units 18 and 19 with the least-altered compositions to qualitatively determine the extent of mass transfer during alteration (Fig. **F82**). For this analysis, we used the chemical compositions of highly altered rock close to relatively fresh rock (based on visual examination of the core) with similar TiO_2 concentrations. Titanium is assumed to be immobile during alteration, and rock pairs with similar TiO_2 concentrations should have had similar compositions before alteration. The results demonstrate that alteration is accompanied by the removal of alkali and alkaline earth elements and aluminum, presumably related to replacement of glass, groundmass, and sanidine phenocrysts by secondary minerals. Surprisingly, there is no net gain in silica. In fact, silica may have decreased slightly during alteration of Unit 19, despite clearly visible quartz partly replacing groundmass and sanidine phenocrysts in thin section. This suggests that silica may simply be remobilized from relatively siliceous protoliths during alteration. Water exhibits a net loss from Unit 18 during alteration but a prominent net gain in the bleached horizon from Unit 19. This is consistent with the presence of illite or possibly some other clay minerals in Unit 19, as determined from thin-section and XRD analyses (Table **T12**). In contrast, CO_2 shows large net mass gains in the bleached horizons from both Units 18 and 19. Total iron appears to have been added to the rock during alteration of Unit 19, whereas the bleached horizon in Unit 18 shows no significant increase when compared to the protolith composition. Manganese shows the opposite behavior, with a net gain in Unit 18 and no change in Unit 19. Although iron-rich solutions were likely involved, iron may be locally transferred from silicate minerals into siderite during interaction with carbonate-rich solutions.

F77. Close-up photograph of Sample 183-1139A-71R-2 (Piece 1, 48–60 cm), **p. 148.**

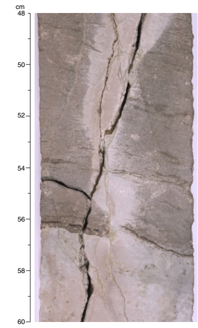

F78. Close-up photograph of Sample 183-1139A-71R-4 (Piece 1, 105–120 cm), **p. 149.**

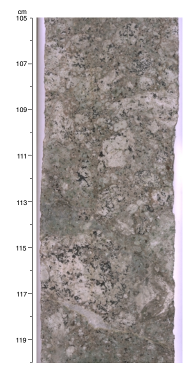

F79. Close-up photograph of Sample 183-1139A-71R-5 (Piece 1, 40–55 cm), **p. 150.**

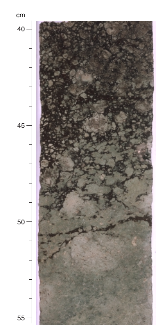

Clearly, a more quantitative analysis of this type requires trace element and isotope data to better constrain protolith composition, the temperature of alteration, and the provenance of hydrothermal fluids. This will be the subject of postcruise research.

PALEOMAGNETISM

We measured the natural remanent magnetization (NRM) of most archive halves from Hole 1139A with the pass-through cryogenic magnetometer using measurement intervals of 5 and 2.5 cm for sediment and basement rocks, respectively. Subsequently, sediment and basement core sections were demagnetized with peak alternating fields (AF) of 20 and 50 mT, respectively. Discrete sediment samples were stepwise AF demagnetized up to 30 mT. Some archive sections with high recovery and complete basement pieces were stepwise AF demagnetized up to 60 mT. Discrete basement samples were stepwise thermally demagnetized at temperatures of up to 620°C. We determined the anisotropy of magnetic susceptibility (AMS) of discrete samples of five basement units to obtain information about the magnetic fabric.

We obtained stable and reliable paleomagnetic directions from the sediments of Hole 1139A. Correlation of polarity reversals with biostratigraphic data suggests that the reversed and normal chrons are early Miocene to early Oligocene in age. We compared magnetic properties with lithologic and basement units. The trachybasalt-trachyandesite lava flows have stronger NRM intensities than the trachyte and rhyolite units. From the stable high-temperature component of the basement magnetization, we obtained reliable paleomagnetic directions and a reversed polarity. We found a difference of ~4° between the mean inclination of the basement units (64°) and the present inclination (–68°) of Site 1139, assuming a geocentric dipole field.

Sediments

We measured the remanent magnetization of all archive halves from Hole 1139A except for highly disturbed sections. One archive section for each core was demagnetized stepwise up to 30 mT. We took one or two discrete samples per section, and 11 samples were stepwise AF demagnetized up to 30 mT to confirm the reliability of the whole-core measurements. We obtained reliable results in undisturbed cores and correlated normal and reversed segments with biostratigraphic zones (see **"Biostratigraphy,"** p. 9). The sediments of Hole 1139A generally have a stable magnetization, which was obtained after AF demagnetization at 10 mT. Most discrete samples have a high median destructive field (MDF), and the remanent direction is stable in demagnetization steps between 10 and 30 mT (Fig. **F83**). We, therefore, used the remanent magnetization after AF demagnetization at 20 mT to correlate the paleomagnetic record with geomagnetic chrons. Furthermore, we used the data selection criteria as described in **"Paleomagnetism,"** p. 27, in the "Explanatory Notes" chapter for magnetostratigraphic studies of Hole 1139A (Fig. **F84**). The selection criteria were that (1) the intensity of remanent magnetization after AF demagnetization at 20 mT was >2 × 10^{-4} A/m, (2) the inclination was >±30°, (3) at least two consecutive values (which corresponds to a 10-cm length of split core) had the same polarity, and (4) there was no significant core disturbance. Characteristic inclinations from discrete samples generally agree well with selected

F80. Close-up photograph of Sample 183-1139A-71R-6 (Piece 1, 45–55 cm), **p. 151.**

F81. Close-up photograph of Sample 183-1139A-73R-2 (Piece 12, 112–134 cm), **p. 152.**

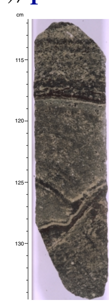

F82. Net mass gain or loss of rock components from the most highly altered intervals, **p. 153.**

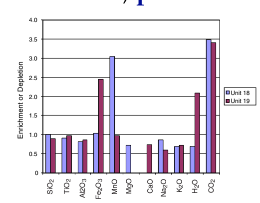

F83. AF demagnetization of a discrete sediment sample, **p. 154.**

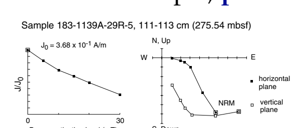

F84. Inclination, intensity, and susceptibility of sediments, **p. 155.**

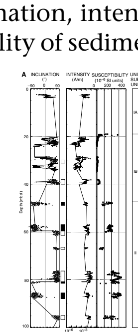

inclinations from whole-core measurements (Fig. **F84**). A reliable polarity sequence with high recovery and stable remanent magnetization was recorded in lithologic Unit II (see **"Lithostratigraphy,"** p. 4).

Correlation of biostratigraphic data and polarity reversals (Fig. **F84**) suggests that the reversed and normal chrons between 77 and 382 mbsf are early Miocene to early Oligocene in age (see **"Biostratigraphy,"** p. 9). In the uppermost 70 m, no continuous paleomagnetic record could be provided because of the low recovery and high drilling disturbance. We propose the following correlations with paleontological data from the core catcher of each core (see **"Biostratigraphy,"** p. 9). We correlate the normal and reversed segments between 77 and 180 mbsf with early Miocene Chrons C5Dr to C6Cn, based on the assignment of Sections 183-1139A-9R-CC through 18R-CC to nannofossil Zone CN2–CN1 (see **"Biostratigraphy,"** p. 9). The underlying normal and reversed segments between 182 and 200 mbsf correspond to the latest Oligocene chrons between C6Cr and C7n (Sections 183-1139A-19R-CC through 21R-CC; nannofossil Zone *R. bisecta*). We correlate the sequences between 200 and 363 mbsf with late Oligocene Chrons C7 to C12n (Sections 183-1139A-22R-CC through 39R-CC; nannofossil Zone *C. altus*). Section 183-1139A-40R-CC lies within nannofossil Zones *Blackites spinosus* to *R. oamaruensis,* suggesting that the normal and reversed polarities at ~380 mbsf correlate with early Oligocene Chrons C12n and C12r or with C12n/C12r and C13n/C13r.

We obtained a reliable paleomagnetic record from most sediments of Hole 1139A. The sediments have strong NRM intensities (average = 1.07 × 10^{-1} A/m) and high susceptibilities (average = 3.03 × 10^{-4} SI units; whole-core multisensor track (MST) measurements, see **"Physical Properties,"** p. 49). Lithologic Unit II (clay, claystones, ooze and chalk, see **"Lithostratigraphy,"** p. 4) has the strongest average intensity and the highest average susceptibility among the sediments (Fig. **F85**). The strong intensity and high susceptibility are probably caused by terrigenous materials. Lithologic Unit I (foraminifer-bearing, nannofossil-bearing, diatom-bearing ooze, see **"Lithostratigraphy,"** p. 4) has weaker intensities and lower susceptibilities than the other units; however, the NRM intensity (average = 5.14 × 10^{-3} A/m) is strong enough to measure the remanent magnetization with the shipboard magnetometer. The drilling disturbance of lithologic Unit I resulted in unreliable paleomagnetic data.

F85. Average intensity and susceptibility of all units, **p. 159.**

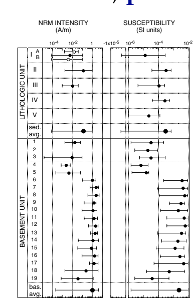

Basement Rocks

We determined the magnetic properties of each basement unit (see **"Igneous Petrology,"** p. 36, and **"Physical Volcanology,"** p. 13) and the variation of magnetic properties within each unit (Fig. **F86**). Three independent types of susceptibility measurements, MST, AMST, and discrete samples, generally show consistent results. We observed no significant differences in the average susceptibility and NRM intensity within or between the trachybasalt-trachyandesite lava flows (basement Units 6 through 17) (Figs. **F85, F86**). Average NRM intensities range from 2.4 (Unit 8) to 0.72 (Unit 15) A/m. Average susceptibilities range from 5.9 × 10^{-3} (basement Unit 12) to 1.3 × 10^{-3} SI units (basement Unit 15). Trachyte and rhyolite lava (basement Units 4, 5, 18, and 19; see **"Igneous Petrology,"** p. 36, and **"Physical Volcanology,"** p. 13) have lower average NRM intensities and susceptibilities than the trachybasalt-basaltic trachyandesite units (Figs. **F85, F86**). Volcaniclastic rocks (basement Units 1, 2, and 3; see **"Physical Volcanology,"** p. 13) also have lower NRM intensities and susceptibilities. We observed significantly higher

F86. Inclination, intensity, and susceptibility of basement rocks, **p. 160.**

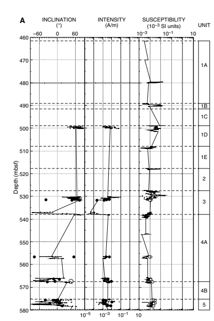

susceptibilities and stronger NRM intensities in the uppermost 2 m than in the lower part of Unit 18 (Fig. F86).

From 30 basalt samples of basement Units 7, 8, 9, 11, and 17, we measured magnetic susceptibility in 15 different directions to determine the AMS and magnetic fabric. The degree of anisotropy (ratio between maximum and minimum axes) ranged from 1.036 (Unit 9) to 1.062 (Unit 17). In Units 8, 9, and 17, we found both positive and negative shape parameters; hence, no shape predominates and no grouping of any (maximum and/or minimum) axes was observed. In Units 7 and 11, we obtained positive shape parameters, which correspond to oblate shapes (Fig. F87), and observed a grouping of the minimum axes along the horizontal plane.

F87. Directional anisotropy data from Unit 7, p. 162.

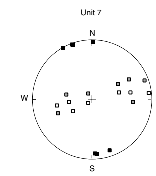

Six discrete samples from basement Units 4, 7, 8, 10, 11, and 18 were stepwise thermally demagnetized up to 620°C. We measured susceptibility of the samples after each heating step to detect changes of their magnetic minerals. Stepwise AF demagnetization up to 60 mT was applied to the archive half of Section 183-1139A-69R-2 from Unit 17. We chose a rock piece (interval 183-1139A-69R-2 [Piece 5, 44–109.5 cm]) that is longer than the effective sensitivity of the pass-through magnetometer (~15 cm) and analyzed its behavior during demagnetization at 72.5 cm in the section (Fig. F88). The magnetization has a MDF of 10 mT and a single-component magnetization, as shown by the straight lines in the orthogonal vector projection.

F88. AF demagnetization of a basement archive half, p. 163.

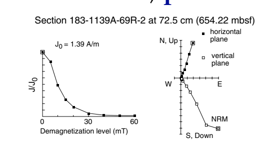

We found two-component directions during the stepwise thermal demagnetization of Sample 183-1139A-64R-2, 41–43 cm, from Unit 7 (Fig. F89A). The low-temperature component is scattered, and the high-temperature component has a stable direction toward the origin. Sample 183-1139A-65R-3, 22–24 cm, from Unit 10 shows only small scattering in both high- and low-temperature component directions (Fig. F89B). The thermal demagnetization of Sample 183-1139A-71R-3, 98–100 cm, from Unit 18 produced only a high-temperature single component (Fig. F89C). The high-temperature phase probably corresponds to magnetite or titanium-poor titanomagnetite, and the low-temperature phase to (titano) maghemite.

F89. Thermal demagnetization of discrete basement samples, p. 164.

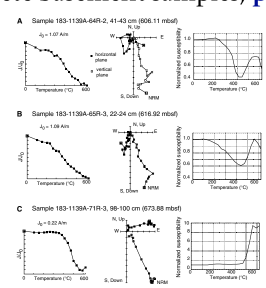

From the high-temperature component, we calculated the characteristic inclinations of the discrete samples using component analysis (Table T13). Inclinations are positive, indicating a reversed polarity, and range from 44° to 80°. The variation in inclinations among samples is probably caused by geomagnetic secular variation and/or limited precision in determining the primary direction. We calculated a mean inclination of 64° with a large error of >10°. The calculated present inclination of –68° for Site 1139, assuming a geocentric dipole field, differs by 4° and is, thus, within the error.

T13. Characteristic inclinations and NRM intensities of discrete basalt samples, p. 202.

PHYSICAL PROPERTIES

Introduction

Physical properties measurements of whole-core sections from Hole 1139A using the MST included magnetic susceptibility, gamma-ray attenuation porosity evaluator (GRAPE) bulk density, and natural gamma radiation (NGR) measurements. We determined compressional wave velocities (V_p) from the split cores in transverse x directions for soft sediments in liners and for hard-rock pieces without the liner. Measurements in the longitudinal (z) and transverse (x and y) directions on cut samples of consolidated sediment and hard rock allowed us to investigate velocity anisotropy. We estimated the magnitude of velocity anisotropy by dividing differences between the maximum and minimum velocities (among the three mutually perpendicular directions, x, y, and z) by the mean velocity of the sample. Index properties determinations included bulk density, water content, porosity, and grain density. We calculated index properties from wet and dry sample weights and dry volumes. We also determined thermal conductivity for sediment and basalt.

Index Properties

We determined index properties by using gravimetric methods on discrete samples (Table T14). Downhole trends in index properties show several changes and offsets in slope (Figs. F90, F91), generally corresponding to changes in lithology.

T14. Index properties data, p. 203.

In Subunit IB (19.0–47.5 mbsf), bulk densities vary from 1.5 to 1.7 g/cm³, grain densities range between 2.6 and 2.7 g/cm³, and porosity changes from 60% at the top to 70% at the bottom. This increase in porosity is consistent with an increase in carbonate content and may be related to better sorting of sediments downhole. Lower porosity values at the top of the interval may also result from the hiatus separating Subunits IA and IB. Sediments in this interval consist of middle Miocene foraminifer-bearing nannofossil ooze, and carbonate content of sediments in Unit I vary from 64 wt% $CaCO_3$ at ~5 mbsf to 83 wt% at ~30 mbsf (see "Lithostratigraphy," p. 4).

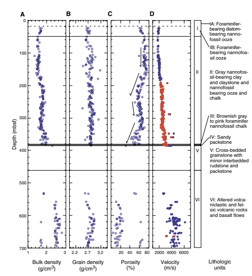

F90. Downhole physical properties and compressional wave velocities, p. 165.

Between ~58 and ~153 mbsf in Unit II, bulk densities change little, averaging 1.5 g/cm³. Porosity also remains constant at 70% (Fig. F90C). Grain densities, however, exhibit large scatter in this interval, with values between 1.8 and 3.1 g/cm³. The lithology in this interval changes from foraminifer-bearing nannofossil ooze at the top of the sequence to clay and claystone at the bottom, with a corresponding decrease in carbonate content (from ~60 to ~30 wt% $CaCO_3$) and higher magnetic susceptibility (Fig. F92B; Table T4). The increasing downward proportion of clay may explain the near uniform porosity.

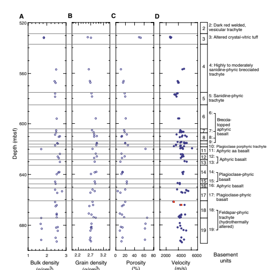

F91. Downhole physical properties profiles of basement Units 2–19, p. 166.

From ~159 to ~242 mbsf in Unit II, bulk density increases slightly, from 1.4 to 1.8 g/cm³. Grain density ranges from 2.6 to 3.0 g/cm³ and averages 2.8 g/cm³. Porosity decreases significantly from 74% to 54% (Fig. F90C). Sediments in this depth interval are mainly calcareous claystone and nannofossil-bearing ooze and chalk. Accordingly, carbonate content increases from ~30 to >60 wt% $CaCO_3$.

Between ~250 and ~330 mbsf in Unit II, bulk and grain densities as well as porosity remain relatively constant, ranging from 1.5 to 1.9 g/cm³, 2.5 to 3.1 g/cm³, and 49% to 70%, respectively. The lithology is dominantly claystone in this interval, and the carbonate content is low, averaging 30 wt% $CaCO_3$. As in the uppermost part of Unit I, the higher clay content in this depth interval may account for the preservation of porosity. Magnetic susceptibility also has higher values in this interval (Fig. F92B).

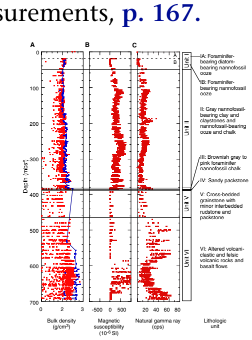

F92. Downhole profiles of MST measurements along with discrete measurements, p. 167.

Between ~333 and ~381 mbsf, still within Unit II, some index properties change significantly. Bulk density gradually increases from ~1.6 to ~2.1 g/cm³, grain density is fairly constant, and porosity gradually decreases from ~66% to ~42% downhole through this interval. Carbonate content increases sharply from ~40 to >90 wt% $CaCO_3$ (see "Litho-

stratigraphy," p. 4). The sediments in this interval are mainly calcareous clay and nannofossil-bearing ooze and chalk.

We only have three data points between ~381.4 and 384.4 mbsf, which spans Units III and IV. Bulk density averages 2.0 g/cm^3, grain density maintains a nearly constant value of 2.8 g/cm^3, and porosity is ~49% (Unit III) and ~31% (Unit IV). Sediments recovered from this interval are thin layers of brown and red foraminifer nannofossil chalk and sandy packstone. A hiatus (~31–33 Ma) is also present within this zone (see **"Biostratigraphy,"** p. 9).

Index properties were not determined in Unit V and basement Units 1 and 2. Within basement (below 530 mbsf), all index properties change sharply. In basement Unit 3, which is crystal vitric tuff (see **"Physical Volcanology,"** p. 13), bulk density is <2.0 g/cm^3, and porosity is questionably high (~50%; see Fig. **F91C**). Throughout basement Units 4 and 5 (~531–585 mbsf), bulk densities increase to ~2.4 g/cm^3. Grain densities gradually increase from 2.6 to 2.7 g/cm^3, and porosities vary from 10% to 19%. Lithologies in this interval include oxidized hydrothermally altered trachyte (see **"Physical Volcanology,"** p. 13).

In the remaining basement Units 6 through 18 (~605 to ~674 mbsf), bulk densities vary widely with a mean of 2.4 g/cm^3, grain density approaches a mean of 2.8 g/cm^3 and decreases slightly in the deeper rocks, and porosity varies widely from 65% to 3% (Fig. **F91**). The dominant lithologies are feldspar-phyric basalts with brecciated flow tops and increased vesicularity toward the margins of the flows. Carbonate veins pervade this zone (see **"Alteration and Weathering,"** p. 42). In basement Unit 19, grain density averages ~2.7 g/cm^3 and is fairly constant. The major minerals are quartz, sanidine, and siderite (see **"Alteration and Weathering,"** p. 42). Several samples from the basement Unit 19 exhibited abnormal porosity values >60%, which cannot be explained by a combination of swelling and dehydrating clays alone.

MST Measurements

GRAPE Density

Bulk density was measured by the GRAPE every 4 cm on whole sections of cores recovered from Hole 1139A. GRAPE data offer the potential for direct correlation with downhole bulk density of discrete samples and can be compared with logging data (Fig. **F92A**). In Units I through IV (from ~19 to ~385 mbsf), the maximum values of GRAPE densities correspond well with wet bulk densities determined from discrete samples and fluctuates similar to shallow resistivity values from the logging data (Fig. **F92A**) (see **"Downhole Measurements,"** p. 56, and **"Seismic Stratigraphy,"** p. 54).

Below ~380 mbsf, bulk densities are much more scattered than in overlying sediments. As previously noted, the larger scatter in the GRAPE bulk density data for the deeper units results from empty space between pieces of core and the core's fractured nature, whereas the generally lower maximum GRAPE values are caused by the smaller diameters of the cores.

Natural Gamma Radiation

We measured NGR every 12 cm on unsplit sections of cores from Site 1139. Gamma-ray values are fairly constant in Unit I (<10 counts per second [cps]) (Fig. **F92**). NGR count increases distinctly at a depth of

~50 mbsf, corresponding to the boundary between Units I and II. Within Unit II, we observe three positive peaks of >15 cps at depth ranges centered around ~100, ~190, and ~250 mbsf (Fig. **F92**). These intervals correspond to the darker gray nannofossil-bearing clay (Core 183-1139A-12R), the nannofossil-bearing claystone (Core 183-1139A-20R), and the dark gray claystone (Core 183-1139A-27R), respectively. NGR values reached a peak value of >20 cps at a depth of ~381 mbsf, corresponding to the brown and red foraminifer nannofossil chalk and sandy packstone in Unit III and IV. In Unit V, NGR values are similar to those of Unit II. In Unit VI, values increase downhole, approaching ~60 cps near a depth of 500 mbsf. Between ~518 and ~604 mbsf, in the basement Units 1 to 5, the NGR count fluctuates with a maximum peak near ~538 mbsf, corresponding to the clay-rich coarse green sands from basement Unit 3 (see **"Igneous Petrology,"** p. 36). In this interval, NGR values decrease from ~570 to ~600 mbsf, probably reflecting the highly fractured and altered trachyte. Between ~605 and ~694 mbsf, within basement Units 6–17, gamma-ray values increase fairly rapidly downhole, and drop again in basements Units 18 and 19, consisting of sanidine-phyric trachyte (see **"Igneous Petrology,"** p. 36). The downhole spectral gamma-ray logging data (see **"Downhole Measurements,"** p. 56; Fig. **F98**) reveal fluctuations very similar to those of downhole NGR profile, corroborating the shipboard measurements.

Magnetic Susceptibility

We determined magnetic susceptibility on all cores from Site 1139 (Fig. **F92B**). The results are discussed in **"Paleomagnetism,"** p. 47.

Compressional Wave Velocity

At Site 1139, we determined compressional wave velocity from both split-core sections and discrete samples measurements (Figs. **F90D, F91D**). The compressional wave velocity data for Subunit IB and the upper sequence of Unit II, which consist of foraminifer-bearing diatom and nannofossil ooze, show very little scatter, with a mean value of 1822 m/s (Table **T15;** Fig. **F90**). Compressional wave velocity in the lower part of Unit II increase linearly with depth, from 1785 to 4331 m/s. These changes correspond to a decrease in porosity from 75% to 42%, as mentioned above. Four outliers of data points (occurring at 191.61, 287.78, 346.87, and 360.01 mbsf, respectively) display much higher velocity values compared to coeval data at the same depth (Fig. **F90D;** Table **T15**). We do not have an explanation for the data point at a depth of 191.61 mbsf, but core photos and the corresponding visual core descriptions reveal that the other three intervals correspond to dark banded layers of volcanic material. In particular, an almost pure basaltic ash layer in Section 183-1139A-38R-4 near ~360 mbsf suggests that such layers account for the observed high velocity values, as opposed to experimental errors.

T15. V_p in discrete samples, **p. 206**.

The compressional wave velocities for sedimentary Units III and IV increase downhole, with an average value of 3616 m/s. Velocities correlate with changes in lithology, from nannofossil-bearing claystone at the bottom of Unit II to the brownish to pink foraminifer nannofossil chalk in Unit III to sandy packstone in Unit V.

No samples were available for velocity determinations in the uppermost two basement Units. Velocities in basement Unit 3, a crystal-vitric tuff has low velocities, with values between 2590 and 2792 m/s (Fig. **F91**).

Basement Units 4 and 5 are sanidine-phyric trachytes, their velocities decrease from 4770 m/s in the upper part to 3322 m/s in the lower part. Velocities in the bottom of basement Units 6 to 17 typically range from 3500 to 4600 m/s, with few values >5000 m/s. The trachyandesite and trachyte of the lowermost basement Units 18 and 19 have velocities similar to those of the overlying basalts. However, basement Unit 18 appears to show a trend of decreasing velocity (Fig. **F91D**), corresponding to the inverse trend in both grain densities and porosity (Fig. **F91B, F91C**). In the upper half of basement Unit 19, velocities increase from ~4000 to >5000 m/s, whereas grain densities are uniform, suggesting a constant mineralogical composition for the rocks. Discrete velocity determinations generally show higher values than the values obtained from downhole logging (Fig. **F98**). This is expected at the top of the hole as a result of enlargement caused by the drilling procedure and wiper trip. Below ~575 mbsf, the hole was not logged, but in the basement units above this depth the data somewhat agree (see **"Downhole Measurements,"** p. 56).

Velocity anisotropy in sedimentary Units I through III is negligible, typically <4%. Two samples from Unit IV, however, exhibit velocity anisotropy as high as 16% (Table **T15**).

Thermal Conductivity

We determined thermal conductivities for soft sediment cores and basement rocks, although we could not determine thermal conductivity in cores recovered in the lower part of Unit II and/or in Units III to V (Fig. **F93;** Table **T16**). Thermal conductivity values for sediments from Units I and II are commonly between 0.8 and 1.1 W/(m·K), with a mean value of 0.9 W/(m·K), and show little scatter. For the basement units, thermal conductivity values vary widely, from a low value of 0.7 W/(m·K) to a value as high as 3.7 W/(m·K) (Table **T16**). We obtained the lowest value (0.7 W/[m·K]) from a highly fractured basalt piece (within Unit 14) in interval 183-1139A-67R-5, 45–55 cm (638.65 mbsf), and the highest value (3.7 W/[m·K]) was in a plagioclase-phyric trachyte in basement Unit 4 in interval 183-1139A-60R-2, 14–26 cm (567.34 mbsf).

Although data are scattered, thermal conductivity values in the basement units appear to have a C-shaped trend, from a relative high value of 1.8 W/(m·K) at a depth of 556.7 mbsf to a low value 0.7 W/(m·K) at ~639 mbsf, followed by an average high value of 2.2 W/(m·K) at ~690 mbsf (Fig. **F93**). The trend seems to follow the same trend as the natural gamma-ray profile (Fig. **F92**). Despite the highly variable values, the mean value of thermal conductivity in the basement Units is 1.7 W/(m·K), similar to values in basement rocks at other Leg 183 sites.

Concluding Discussion

Trends in index properties and MST measurements, coupled with changes in compressional wave velocity and thermal conductivity, compare well with the lithologic units and logging data for Hole 1139A. The overall downhole trends in index properties and changes in velocity gradients define several intervals with distinct physical properties. Variations in the physical properties of the sediments and rocks recovered at Site 1139 are the combined result of changes in lithology, depth of burial, diagenesis, and/or alteration.

F93. Downhole profile of whole-core measurements of thermal conductivity on whole-core soft sediments and on split-core pieces of hard rocks, **p. 168.**

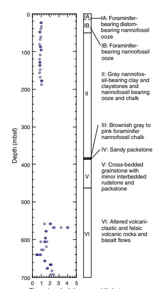

T16. Thermal conductivity values, **p. 210.**

ORGANIC AND INORGANIC GEOCHEMISTRY

We measured concentrations of carbonate in sediments from Hole 1139A on ~1 sample per core (Table T17). In addition, we analyzed 14 of the sediment samples for organic carbon, total nitrogen, sulfur, and hydrogen. The results of the analyses are discussed in "Lithostratigraphy," p. 4.

T17. Carbon, nitrogen, sulfur, and hydrogen analyses of sediments, p. 211.

For volcanic and volcaniclastic rocks that were analyzed by XRF, we measured total carbon, total nitrogen, sulfur, and hydrogen using the NCS analyzer (Table T18). These data are useful for assessing the degree of alteration in the basalts (e.g., total carbon and hydrogen can be converted to CO_2 and H_2O, respectively, and compared with LOI values). Further discussion of these data can be found in "Igneous Petrology," p. 36, and "Alteration and Weathering," p. 42.

T18. Carbon, nitrogen, sulfur, and hydrogen analyses of volcanic and volcaniclastic rocks, p. 212.

SEISMIC STRATIGRAPHY

Data

We used densities and compressional wave velocities combined from index properties, MST measurements, and a velocity log (Fig. F94) to synthesize seismograms at Site 1139. A detailed comparison of velocities from samples and logs is given in "Downhole Measurements," p. 54, in the "Site 1137" chapter. Based on the coherence analysis carried out for the velocity data from Site 1137 (Fig. F98), we filtered the sample velocities from Site 1139 using a filter of 5 m length. The data were resampled simultaneously every 2 m, and data gaps >5 m were linearly interpolated. More closely spaced sampling results in the inclusion of noise in the filtered profiles. We used a robust-mode filter (i.e., a maximum likelihood probability estimator) that calculated the mode within the given data window. In addition, the median of the filtered data set was computed during filtering, and outliers, whose values exceed 2.5 times the L1 scale, were replaced with the median, as described in "Downhole Measurements," p. 54, in the "Site 1137" chapter.

F94. Comparison of densities determined from core samples and GRAPE and V_p from downhole logs and core samples, p. 169.

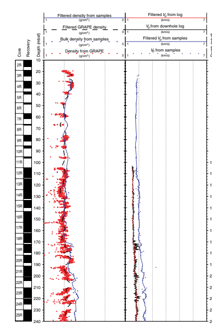

Downhole velocity logs are extremely noisy at this site because of bad weather conditions during logging. Further, velocities from discrete samples and downhole logs are offset for the entire length of the log, with the latter displaying velocities substantially lower than those from discrete samples, on average by >0.5 km/s (see "Physical Properties," p. 49). The origin of this offset is unknown. Within basement, below 460 mbsf, it is difficult to determine whether the two data sets are offset, as only a few sample measurements are available (Fig. F94A). No sample velocity data exist between 385 and 530 mbsf. Therefore, we include basement log velocities from 490 to 575 mbsf in a composite velocity profile used for synthesizing seismograms (Fig. F95A). In this depth interval, the smoothed velocity and density profiles correlate, with both showing substantial variations between 530 and 575 mbsf (Fig. F94C). The uppermost of the composite velocity log is based on sample velocities, except for depths from 490 to 570 mbsf, where the offset between log and sample velocities appears to be small, based on samples from 550 and 575 mbsf.

F95. Composite of core recovery, depth, curated stratigraphy, age, lithology, density and velocity, p. 172.

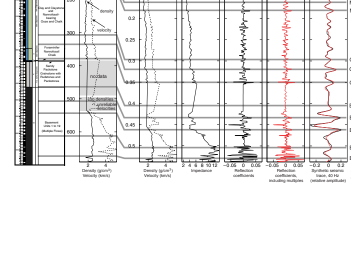

Nevertheless, artifacts likely exist where we have sparse data. The negative slope that results from linearly interpolating through the velocity data gap from 385 to 490 mbsf (i.e., between a sample velocity at 385 mbsf and a log velocity at 490 mbsf) results in an apparent velocity inversion (Fig. F95A). This inversion is most likely an artifact, as velocities from the downhole log are apparently lower than formation velocities. We make no attempt to correct the velocities. The shift may or may not be constant with depth, but given scant sample velocity information at depths between 380 and 580 mbsf, the exact nature of the shift remains unknown. Therefore, we use the logged basement velocities, as their relative variation include some information useful for computing impedance contrasts. Sample velocity data within basement exhibit three velocity inversions at 630–645, 655–660, and 665–670 mbsf (Fig. F94C), all of which result in reflections that tie to the MCS data (Figs. F95, F96).

GRAPE and discrete sample densities agree fairly well at depths above ~170 mbsf. At greater depths, all GRAPE density determinations are lower than those from discrete samples. No densities are available between 380 and 530 mbsf. Also, we have no downhole density log for this site because of bad weather conditions. We smoothed and resampled sample densities similarly to the velocities (see discussion above).

Synthetic Seismogram

We synthesized seismograms for Site 1139 (see "Seismic Stratigraphy," p. 52, in the "Site 1137" chapter). We resampled both densities and velocities every 0.5 ms as a function of two-way traveltime (TWT) (Fig. F95B), and we created profiles for impedance, reflection coefficients, and a seismic trace (Fig. F95C, F95D, F95E, F95F, respectively). The seismic trace is based on convolution with a Ricker wavelet with a peak frequency of 40 Hz. Reflection coefficients with and without multiples and transmission losses do not show distinct differences at this site, and those differences that exist should not be overinterpreted given the variable sampling rate with depth and poor quality of some data.

Seismic Stratigraphy

Despite variable data quality (Fig. F96B), we can link most major MCS reflections with the lithostratigraphy. The lower to middle Miocene section includes three reflections labeled M1–M3, mainly because of density contrasts within Unit II at ~65, 170, and 170 m. The reflections at 65 and 170 mbsf correlate with increases in $CaCO_3$ content (see "Lithostratigraphy," p. 4).

Three reflections in the mid-Oligocene section (labeled O1–O3 at 375, 340, 305 mbsf, respectively) are caused by both density and velocity contrasts. All reflections correlate with increases in $CaCO_3$ content (see "Lithostratigraphy," p. 4). The increase in $CaCO_3$ content related to reflection O1 marks the transition of nannofossil chalk in Unit II to a sandy packstone in Unit III.

Density and velocity data are not available from Unit III downward through Units IV and V into the underlying basement. However, the synthetic seismogram shows five prominent reflections (B1–B5) within basement (Fig. F95F). The position of the uppermost of these reflections, B5, marks the transition from a data gap to that part of the basement section where data are available. Therefore, its stratigraphic position is not meaningful. However, the upper inflection point of B5 roughly corresponds to the top of felsic basement at 460 mbsf (Fig. F95F). The four remaining basement reflections are at depths of ~615–

F96. Seismic reflection data and a synthetic seismic trace, p. 174.

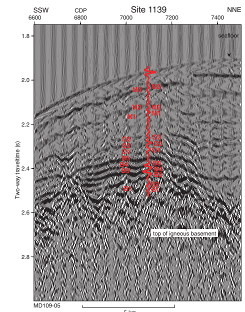

620 mbsf (B1), ~605–610 mbsf (B2), ~535–540 mbsf (B3), and ~500–505 mbsf (B4). B4 is associated with a velocity inversion of unknown cause as a result of a lack of core recovery within Subunit 1D, B3 is caused by a velocity inversion resulting from a low-velocity volcaniclastic sand (Unit 3) between trachyte units (see **"Physical Volcanology,"** p. 13), and B2 and B1 are associated with velocity and density contrasts within basalt flows (Units 6–17).

All reflections within basement and those identified by synthetic seismograms are deeper than those on the MCS data because the velocities and densities of the packstone overlying basement are not constrained. In particular, we believe that velocities have been underestimated, resulting in overestimated two-way traveltimes for all reflections underlying the data gap (i.e., all reflections within basement). However, the relative two-way traveltimes of reflections B1–B5 are roughly correct and correlate well with five reflections in the MCS data (Fig. **F96**).

The observed match between the reflections from synthetic seismogram and those on the MCS data allows us to re-evaluate the cause for the shift between velocities from downhole logs and discrete samples from 100 to 390 mbsf (Fig. **F94**). If we would use log velocities for synthetic seismogram construction for this depth interval, instead of sample velocities, then the synthetic seismic trace would be more than 100 ms longer compared to the traces shown on Figure **F95F** (see Fig. **F95** for comparison of TWT-depth relationships of Sites 1139 and 1140). The resulting match of synthetic basement reflections with observed reflections in the MCS data would be extremely poor. Based on this observation, we argue that it is likely that the shift between log and sample velocities is caused by incorrect log velocities, possibly a result of an extremely large hole diameter. As no caliper log is available because of the bad weather conditions, the hole size remains unknown. The above conclusion is corroborated by a qualitative evaluation of extremely low log velocities of 1.55–1.6 km/s obtained at depths between 110 and 150 mbsf, where clays and relatively consolidated claystones were recovered (see **"Lithostratigraphy,"** p. 4). These lithologies are more consistent with velocities around 2 km/s, as determined by velocity measurements on discrete samples (Fig. **F94**).

DOWNHOLE MEASUREMENTS

Logging Operations

After finishing the wiper trip and releasing the bit, the wireline tools were rigged and deployed (Table **T19**) (see **"Operations,"** p. 2). Because of rough seas, we decided not to use the triple combo to avoid damaging its calipers or losing the radioactive source. Instead, we used the DITE-DSI-NGT (resistivity, velocity, and natural gamma ray) combination which does not include a caliper. When we started pulling the tools up the hole, we lost communications with the tools. The DSI had malfunctioned, rendering the entire tool string inoperative. After replacing the DSI with the LSS, we re-entered Hole 1139A. However, we could not pass a bridge at 593 mbsf, which marks the transition to the basaltic lava flows. Thus, we started to log from 593 mbsf to the end of pipe at 101.7 mbsf. The seas were too heavy to run the wireline heave compensator, but the data were corrected by using acceleration measurements from LDEO-TAP.

T19. Summary of logging operations, **p. 213.**

Log Quality

Logging data from Site 1139 are generally of good quality (Fig. F97), although the lack of borehole diameter measurements compromises downhole measurement accuracy. However, good correlation between MST and downhole natural gamma-ray data suggest that our data are accurate (Fig. F98). We can clearly see the tephra layer between 190 and 200 mbsf (see "Lithostratigraphy," p. 4), indicated by high natural gamma radiation data. Resistivity data resemble the MST density data in quality. For example, changes in density at 188, 295, and 336 mbsf are also evident in downhole resistivity measurements and are related to lithologic changes.

The velocity data are of low quality in the basement section (Fig. F98). While logging, the bowsprings, used for centralizing the tool, produced noise that disturbed the velocity measurements. Shore-based processing enhanced the data quality and eliminated effects caused by cycle skipping. Although the data are noisy, the average values are reliable, and general trends correlate with those in resistivity data. We cannot yet explain the general offset between core velocity and log data in the sediments. In the basement section, the log data are only slightly lower than the core measurements (see "Seismic Stratigraphy," p. 54).

Results

The logging data delineate lithologic Units II to VI (Figs. F97, F98). As expected, pelagic sediments of Unit II show the lowest natural gamma ray (SGR) (<50 gAPI). At the base of Unit II, SGR values increase and, in Units III and IV, vary at a high frequency (Fig. F99). Volcanic lithics found in Unit IV (see "Lithostratigraphy," p. 4) are characterized by slightly increased resistivities. In Unit V, SGR values continue to increase (>70 gAPI), primarily because of K and Th. Core recovery is low in this unit, and natural gamma-ray data from the MST are comparably low (Fig. F97). This suggests that sediment enriched in clays or volcanic material was not recovered.

The transition to basement is marked by a thin layer of high K content (458–460 mbsf) (Fig. F99). This layer probably overlies igneous basement. The top of the igneous basement (Unit 1A) (461.7–489.7 mbsf) consists of rounded rhyolite cobbles that are interpreted as a weathered pavement or conglomerate (see "Physical Volcanology," p. 13).

The upper part of the basement is composed of felsic volcanics (see "Igneous Petrology," p. 36) enriched in Th and K. We distinguish basement Units 1–4 by differing Th, U, and K contents. Because of poor recovery of basement units, core-log integration is difficult. The radioactive nuclides highlight general chemical differences among igneous rocks, but they are also affected by alteration. Aside from geochemistry, alteration also affects resistivities and velocities, particularly where alteration accompanies changes in structure (e.g., grain-size differences and faulting).

Figure F99 illustrates our attempt to relate the logging data to the different basement units. Subunit 1A can be subdivided into two intervals (460–479 and 479–490 mbsf). At 479 mbsf, the values of total gamma ray, resistivities, and velocity increase, indicating a lithologic change. Subunit 1B, a bioclastic sandstone, was probably completely recovered. The logs suggest a thin bed at 489.5–490 mbsf, where low natural gamma-ray values (~60 gAPI) indicate low K, Th, and U content, as ex-

F97. Overview of the logging data, p. 175.

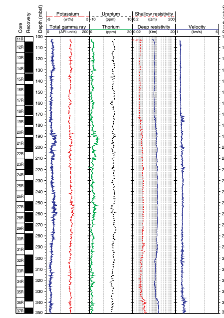

F98. Comparison of core and log measurements to assess log quality, p. 177.

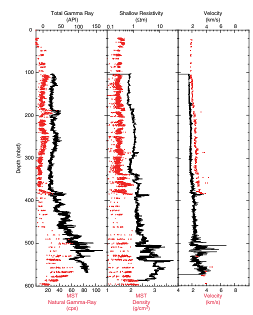

F99. Correlation of core lithology and logging results, p. 178.

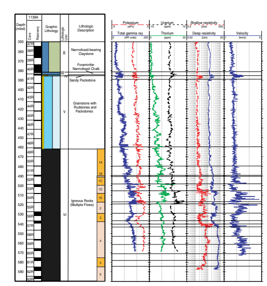

pected for bioclastic sandstone. The region from which Subunit 1C was recovered shows fairly constant resistivity data. However, K increases slightly toward the base (from 2 to 3.2 wt%). At the base of this interval are the highest K and Th (~20 ppm) values. It is not clear whether this layer belongs to Subunit 1C or is a separate unrecovered lithology. Subunit 1D, which is a perlitic felsic glass, is characterized by low resistivity data (~2 Ωm), which might result from rock alteration and structure. Subunit 1E is composed of altered and sheared volcaniclastics and may correspond to a zone of U enrichment (5–10 ppm) seen in the logs. This enrichment might be related to fluid flow and the incorporation of U into secondary phases. Basement Unit 2 is a dark red welded rhyolite that shows relatively constant and high SGR (~100 gAPI), Th (~9 ppm), U (~1.5 ppm), K (~3.5 wt%), and resistivity (~4.5 Ωm) data. In the altered crystal vitric tuff in basement Unit 3, the K content decreases downhole to 1 wt% in the lower third of the layer, and then starts to increase again. Resistivity and velocity are low overall. Basement Unit 4 is similar to basement Unit 2; basement Unit 4 shows comparable K and slightly higher Th and U values. We cannot identify the boundaries of basement Unit 5 on the basis of the resistivity data alone.

Temperature data from the TAP tool clearly show the sediment/basement boundary (Fig. **F100**). Generally, measurements taken uphole are slightly higher than those taken downhole; the variations in tool speed account for the difference. Also, when attempting to pass the ledge, we disturbed the hole's temperature regime. While logging upward, temperatures are lower at the bottom and higher above 540 mbsf than data from the downgoing measurements. At ~380 mbsf, the temperature starts to increase downhole from 5.2° to ~8°C. This corresponds to the sediment–basement transition. The maximum detected temperature in the hole is 11.2°C at 595 mbsf.

F100. Temperatures measured by the LDEO TAP tool show a different temperature gradient in the basement than in the overlying sediments, **p. 179.**

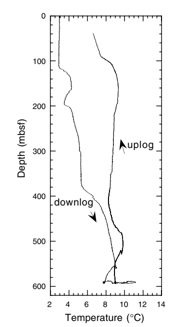

REFERENCES

Alibert, C., 1991. Mineralogy and geochemistry of a basalt from Site 738: implications for the tectonic history of the southernmost part of the Kerguelen Plateau. *In* Barron, J., Larsen, B., et al., *Proc. ODP, Sci. Results,* 119: College Station, TX (Ocean Drilling Program), 293–298.

Berggren, W.A., 1992. Neogene planktonic foraminifer magnetobiostratigraphy of the southern Kerguelen Plateau (Sites 747, 748, and 751). *In* Wise, S.W., Jr., Schlich, R., et al., *Proc. ODP, Sci. Results,* 120 (Pt. 2): College Station, TX (Ocean Drilling Program), 631–647.

Berggren, W.A., Kent, D.V., Swisher, C.C., III, and Aubry, M.-P., 1995. A revised Cenozoic geochronology and chronostratigraphy. *In* Berggren, W.A., Kent, D.V., Aubry, M.-P., and Hardenbol, J. (Eds.), *Geochronology, Time Scales and Global Stratigraphic Correlation*. Spec. Publ.—Soc. Econ. Paleontol. Mineral. (Soc. Sediment. Geol.), 54:129–212.

Coccioni, R., Monaco, P., Monechi, S., Nocchi, M., and Parisi, G., 1988. Biostratigraphy of the Eocene-Oligocene boundary at Massignano (Ancona, Italy). *In* Premoli Silva, I., Coccioni, R., and Montanari, A. (Eds.), *The Eocene-Oligocene Boundary in the Marche-Umbria Basin (Italy)*. Int. Subcomm. Paleogr. Strat., Eocene/Oligocene Meeting, Spec. Publ., II, 1:59–80.

Coffin, M.F., Davies, H.L., and Haxby, W.F., 1986. Structure of the Kerguelen Plateau province from SEASAT altimetry and seismic reflection data. *Nature,* 324:134–136.

Davies, H.L., Sun, S.-S., Frey, F.A., Gautier, I., McCulloch, M.T., Price, R.C., Bassias, Y., Klootwijk, C.T., and Leclaire, L., 1989. Basalt basement from the Kerguelen Plateau and the trail of the DUPAL plume. *Contrib. Mineral. Petrol.,* 103:457–469.

Duncan, R.A., and Storey, M., 1992. The life cycle of Indian Ocean hotspots. *In* Duncan, R.A., Rea, D.K., Kidd, R.B., von Rad, U., and Weissel, J.K. (Eds.), *Synthesis of Results from Scientific Drilling in the Indian Ocean*. Geophys. Monogr., Am. Geophys. Union, 70:91–103.

Fisher, R.L., 1997. Bathymetry of the Southern Indian Ocean. *General Bathymetric Chart of the Oceans*. GEBCO, Sheet 97.1.

Frey, F.A., Jones, W.B., Davies, H., and Weis, D., 1991. Geochemical and petrologic data for basalts from Sites 756, 757, and 758: implications for the origin and evolution of the Ninetyeast Ridge. *In* Weissel, J., Peirce, J., Taylor, E., Alt, J., et al., *Proc. ODP, Sci. Results,* 121: College Station, TX (Ocean Drilling Program), 611–659.

Giret, A., and Beaux, J.-F., 1984. The plutonic massif of Val Gabbro (Kerguelen Islands), a tholeiitic complex related to the activity of the East-Indian paleo-ridge. *C. R. Acad. Sci. Ser. 2,* 299:965–970.

Giret, A., and Lameyre, J., 1983. A study of Kerguelen plutonism: petrology, geochronology and geological implications. *In* Oliver, R.L., James, P.R., and Jago, J.B. (Eds.), *Antarctic Earth Science:* Cambridge (Cambridge Univ. Press), 646–651.

Kennett, J.P., and Srinivasan, M.S., 1983. *Neogene Planktonic Foraminifera: A Phylogenetic Atlas:* Stroudsburg, PA (Hutchinson Ross).

Le Bas, M.J., Le Maitre, R.W., Streckeisen, A., and Zanettin, B., 1986. A chemical classification of volcanic rocks based on the total alkali-silica diagram. *J. Petrol.,* 27:745–750.

Macdonald, G.A., and Katsura, T., 1964. Chemical composition of Hawaiian lavas. *J. Petrol.,* 5:82–133.

Mahoney, J.J., Jones, W.B., Frey, F.A., Salters, V.J.M., Pyle, D.G., and Davies, H.L., 1995. Geochemical characteristics of lavas from Broken Ridge, the Naturaliste Plateau and southernmost Kerguelen Plateau: Cretaceous plateau volcanism in the Southeast Indian Ocean. *Chem. Geol.,* 120:315–345.

Mehl, K.W., Bitschene, P. R., Schminke, H.-U., and Hertogen, J., 1991. Composition, alteration, and origin of the basement lavas and volcaniclastic rocks at Site 738, southern Kerguelen Plateau. *In* Barron, J., Larsen, B., et al., *Proc. ODP, Sci. Results,* 119: College Station, TX (Ocean Drilling Program), 299–322.

Müller R.D., Royer J.Y., and Lawver L.A., 1993. Revised plate motions relative to the hotspots from combined Atlantic and Indian-Ocean hotspot tracks. *Geology,* 21:275–278.

Parker, M.E., Clark, M., and Wise, S.W., Jr., 1985. Calcareous nannofossils of Deep Sea Drilling Project Sites 558 and 563, North Atlantic Ocean: biostratigraphy and the distribution of Oligocene braarudosphaerids. *In* Bougault, H., Cande, S.C., et al., *Init. Repts. DSDP,* 82: Washington (U.S. Govt. Printing Office), 559–589.

Pringle, M.S., Storey, M., and Wijbrans, J., 1994. ^{40}Ar/^{39}Ar geochronology of mid-Cretaceous Indian ocean basalts: constraints on the origin of large flood basalt. *Eos,* 75:728.

Royer, J.-Y., and Coffin, M.F., 1992. Jurassic to Eocene plate tectonic reconstructions in the Kerguelen Plateau region. *In* Wise, S.W., Jr., Schlich, R., et al., *Proc. ODP, Sci. Results,* 120: College Station, TX (Ocean Drilling Program), 917–928.

Salters, V.J.M., Storey, M., Sevigny, J.H., and Whitechurch, H., 1992. Trace element and isotopic characteristics of Kerguelen-Heard Plateau basalts. *In* Wise, S.W., Jr., Schlich, R., et al., *Proc. ODP, Sci. Results,* 120: College Station, TX (Ocean Drilling Program), 55–62.

Sandwell, D.T., and Smith, W.H.F., 1997. Marine gravity anomaly from Geosat and ERS-1 satellite altimetry. *J. Geophys. Res.,* 102:10039–10054.

Schlich, R., Schaming, M., Weis, D., Montigny, R., and Damasceno, D., 1998. New structural and tectonic data in the northern Kerguelen Plateau. *Eos,* 79:F871.

Shipboard Scientific Party, 1989. Site 737. *In* Barron, J., Larsen, B., et al., *Proc. ODP, Init. Repts.,* 119: College Station, TX (Ocean Drilling Program), 159–227.

Siesser, W.G., Bralower, T.J., and De Carlo, E.H., 1992. Mid-Tertiary *Braarudosphaera*-rich sediments on the Exmouth Plateau. *In* von Rad, U., Haq, B.U., et al., *Proc. ODP, Sci. Results,* 122: College Station, TX (Ocean Drilling Program), 653–663.

Storey, M., Kent, R.W., Saunders, A.D., Salters, V.J., Hergt, J., Whitechurch, H., Sevigny, J.H., Thirlwall, M.F., Leat, P., Ghose, N.C., and Gifford, M., 1992. Lower Cretaceous volcanic rocks on continental margins and their relationship to the Kerguelen Plateau. *In* Wise, S.W., Jr., Schlich, R., et al., *Proc. ODP, Sci. Results,* 120: College Station, TX (Ocean Drilling Program), 33–53.

Storey, M., Pringle, M.S., Coffin, M.F., and Wijbrans, J., 1996. Geochemistry and geochronology of Kerguelen Plateau basalts: results from ODP Legs 119 and 120. *Eos,* 76:123.

Sun, S.-S., and McDonough, W.F., 1989. Chemical and isotopic systematics of oceanic basalts: implications for mantle composition and processes. *In* Saunders, A.D., and Norry, M.J. (Eds.), *Magmatism in the Ocean Basins.* Geol. Soc. Spec. Publ. London, 42:313–345.

Wei, W., 1992. Paleogene chronology of Southern Ocean drill holes: an update. *In* Kennett, J.P., and Warnke, D.A. (Eds.), *The Antarctic Paleoenvironment: a Perspective on Global Change.* Antarct. Res. Ser., 56:75–96.

Wei, W., and Thierstein, H.R., 1991. Upper Cretaceous and Cenozoic calcareous nannofossils of the Kerguelen Plateau (southern Indian Ocean) and Prydz Bay (East Antarctica). *In* Barron, J., Larsen, B., et al., *Proc. ODP, Sci. Results,* 119: College Station, TX (Ocean Drilling Program), 467–494.

Weis, D., Bassias, Y., Gautier, I., and Mennessier, J.-P., 1989. DUPAL anomaly in existence 115 Ma ago: evidence from isotopic study of the Kerguelen Plateau (South Indian Ocean). *Geochim. Cosmochim. Acta,* 53:2125–2131.

Weis, D., Damasceno, D., Scoates, J.S., Schlich, R., Schaming, M., Montigny, R., and Frey, F.A., 1998. Submarine alkali lavas (14–19 Ma) erupted between Heard Island and the Kerguelen Archipelago, Indian Ocean. *Eos,* 79:944.

Weis, D., Frey, F.A., Giret, A., and Cantagrel, J.M., 1998. Geochemical characteristics of the youngest volcano (Mount Ross) in the Kerguelen Archipelago: inferences for magma flux and composition of the Kerguelen plume. *J. Petrol.,* 39:973–994.

Weis, D., Frey, F.A., Leyrit, H., and Gautier, I., 1993. Kerguelen Archipelago revisited: geochemical and isotopic study of the Southeast Province lavas. *Earth Planet. Sci. Lett.,* 118:101–119.

Wise, S.W., Jr., 1983. Mesozoic and Cenozoic calcareous nannofossils recovered by Deep Sea Drilling Project Leg 71 in the Falkland Plateau region, Southwest Atlantic Ocean. *In* Ludwig, W.J., Krasheninnikov, V.A., et al., *Init. Repts. DSDP,* 71 (Pt. 2): Washington (U.S. Govt. Printing Office), 481–550.

Figure F1. Satellite-derived free-air gravity map of the Kerguelen Plateau (after Sandwell and Smith, 1997). The five plateau province sectors are northern, central, southern, Elan Bank, and Labuan Basin (outlined in white). Leg 183 and previous (Legs 119 and 120) sites are indicated by stars and circles, respectively (black = basement sites; white = sediment sites). Squares indicate dredge and piston core sites where igneous rock (black) and sediment (white) were recovered. **(Figure shown on next page.)**

Figure F1. (Caption on previous page.)

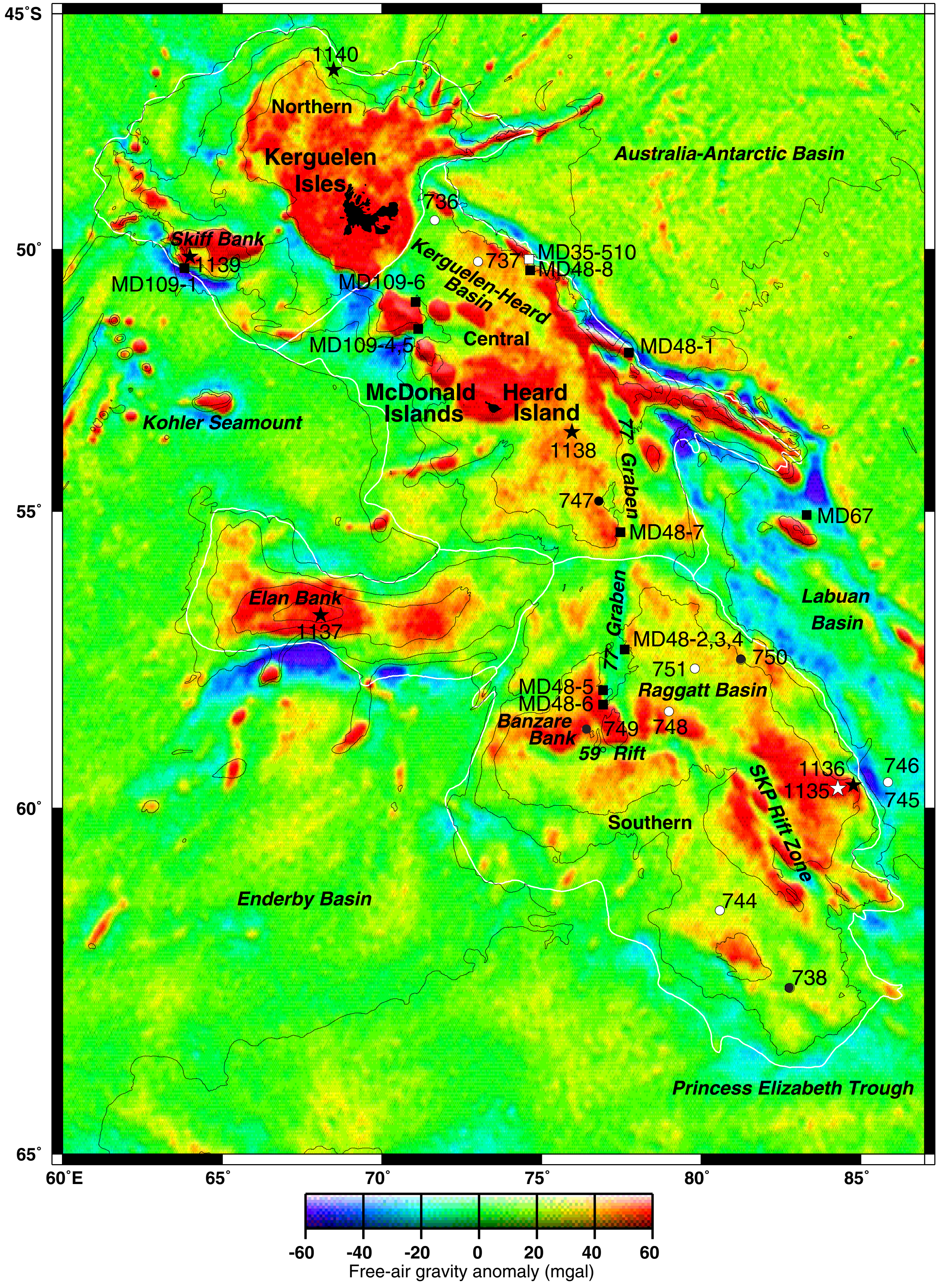

Figure F2. Location of Site 1139 and site-survey data. Navigation for *Marion Dufresne* survey 109, line 05 (MD109-05) data is shown in shotpoints. Bathymetric contour interval = 500 m (Fisher, 1997).

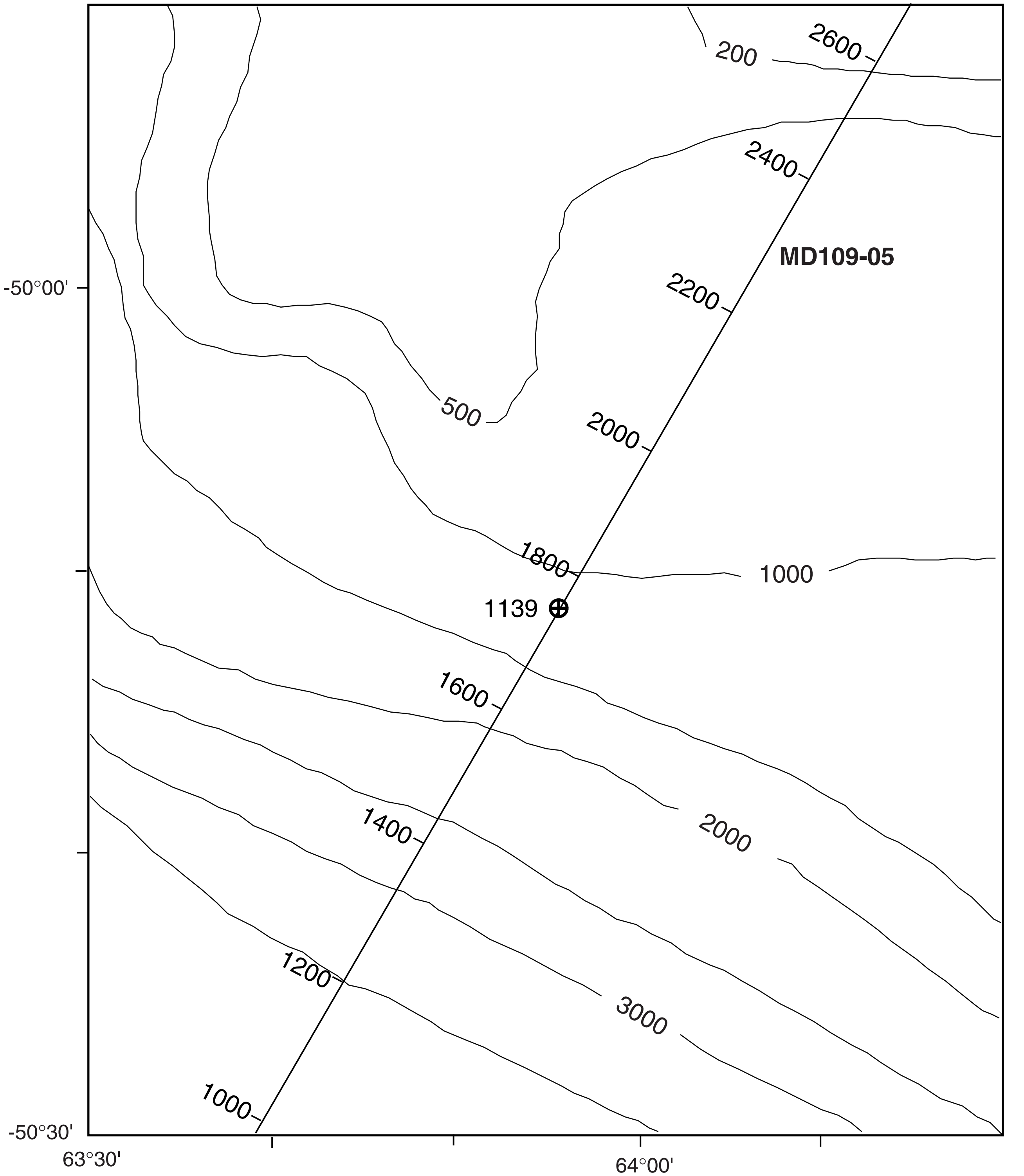

Figure F3. *Marion Dufresne* MD109-05 multichannel seismic profile across Site 1139. Vertical exaggeration = ~16 at seafloor.

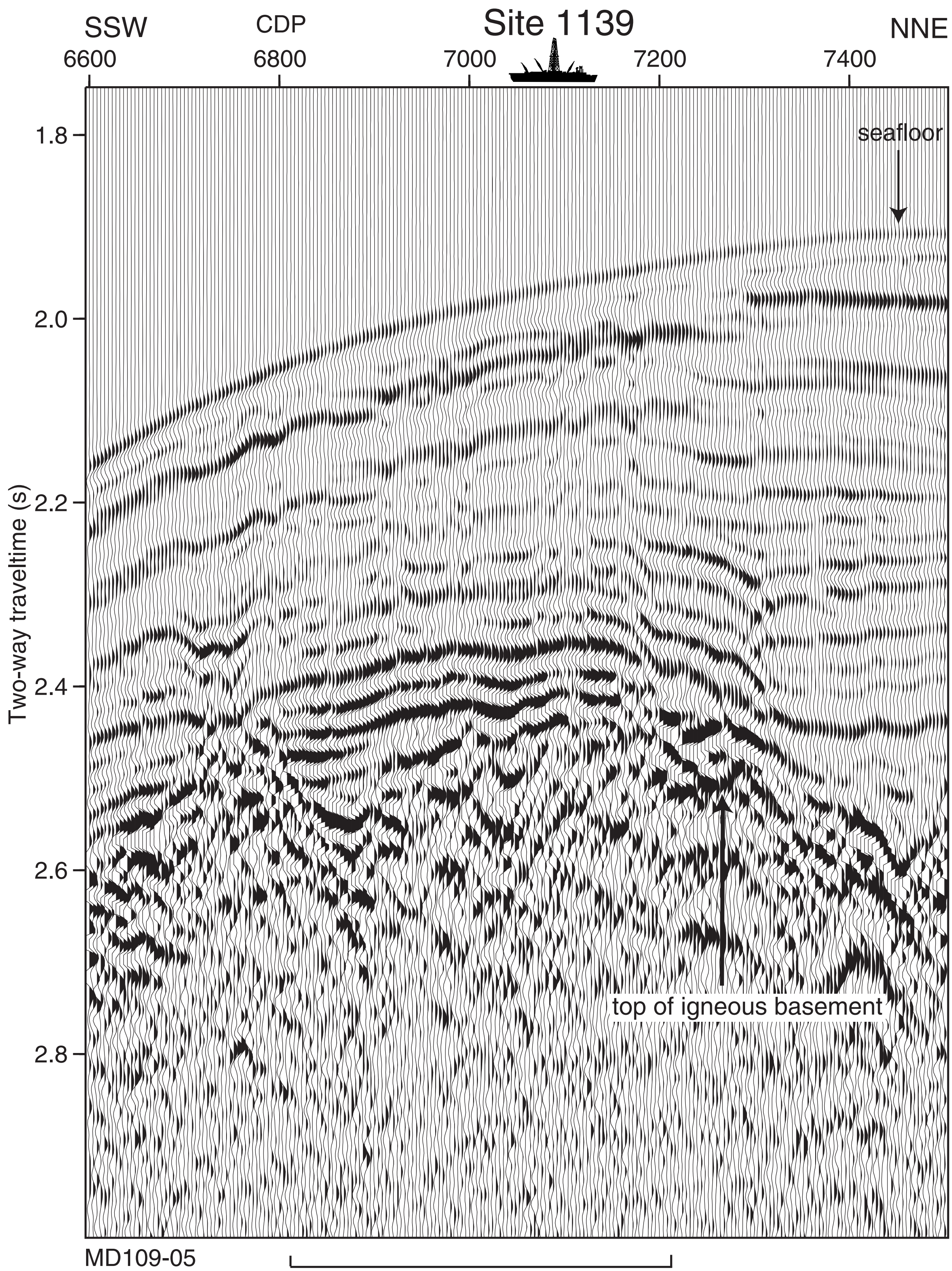

Figure F4. Composite stratigraphic section for Site 1139 showing core recovery, a simplified summary of lithology, lithologic unit boundaries, ages of units, and names of lithologies. The lithologic symbols are explained in Figure F3, p. 57, of the "Explanatory Notes" chapter. **(Figure shown on next page.)**

Figure F4. (Caption on previous page.)

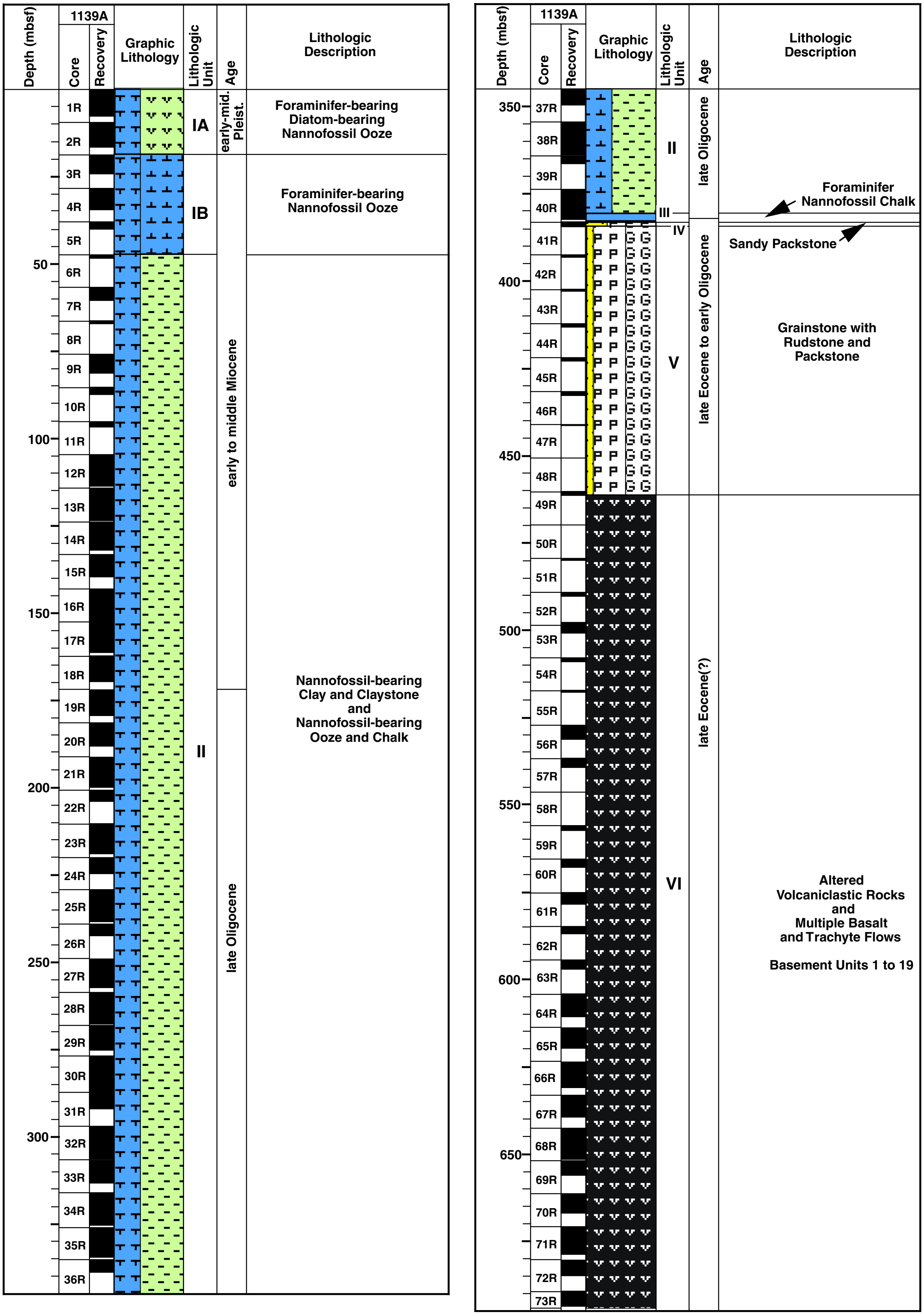

Figure F5. Examples of foraminifer nannofossil chalk in Unit III. **A.** Contact between gray nannofossil chalk of Unit II and brownish foraminifer nannofossil chalk of unit III; contact is at 92 cm. The green laminae at 99–102 and 107–109 cm are diagenetic glauconite (interval 183-1139A-40R-5, 83–115 cm). **B.** Lower portion of Unit III (interval 183-1139A-40R-6, 15–35 cm). (Continued on next page.)

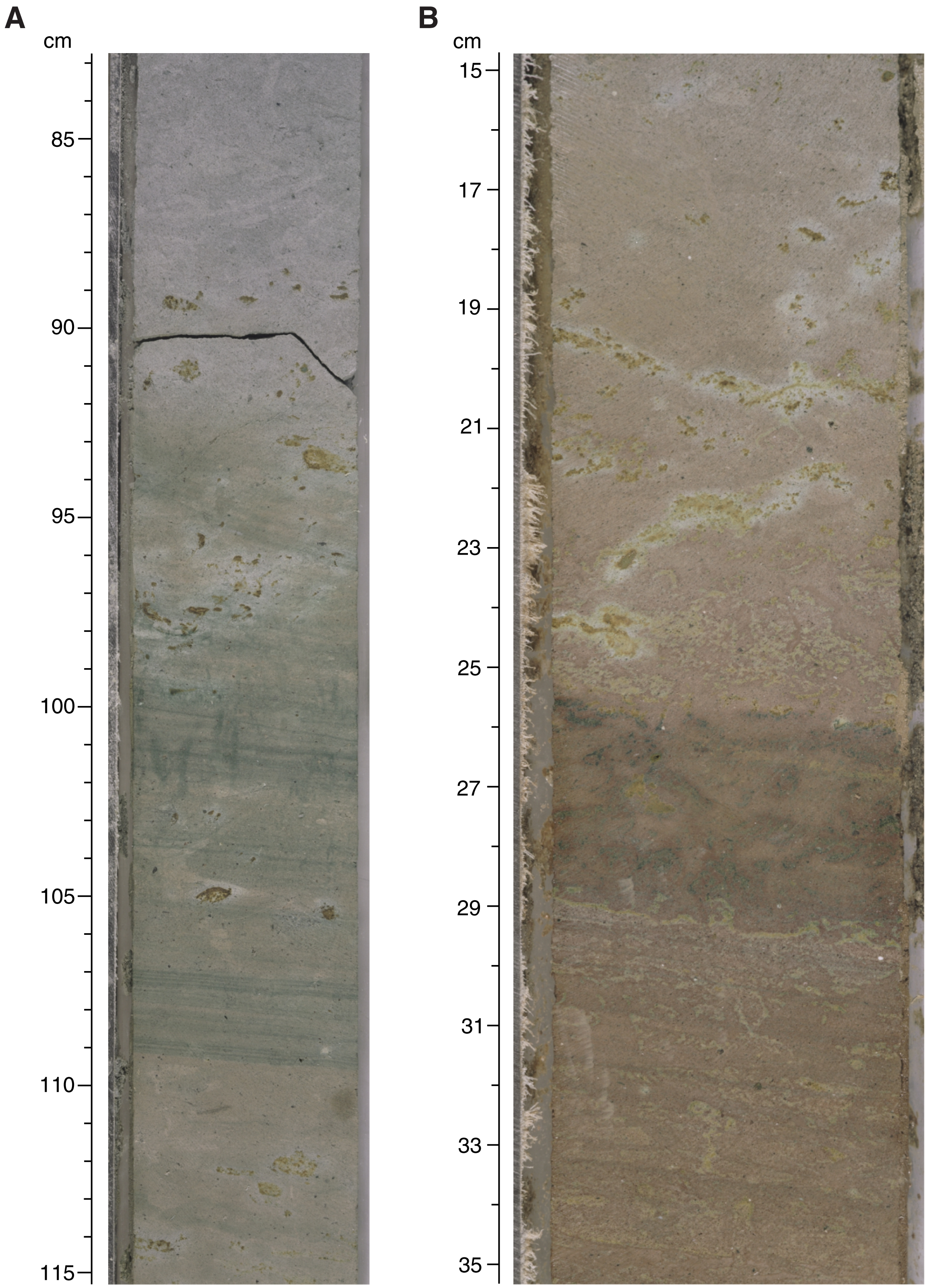

Figure F5 (continued). C. Lower portion of Unit III (interval 183-1139A-40R-6, 73–94 cm).

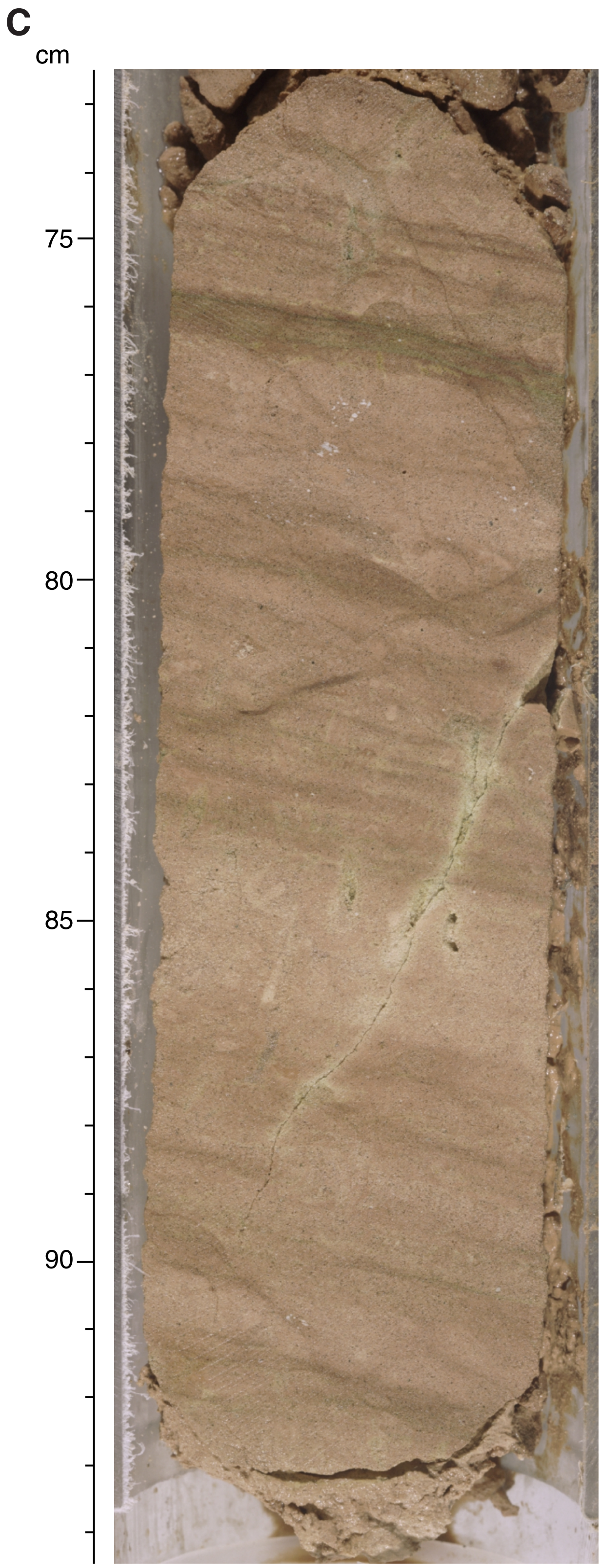

Figure F6. Sandy packstone of Unit IV (interval 183-1139A-41R-1, 0.5–20 cm).

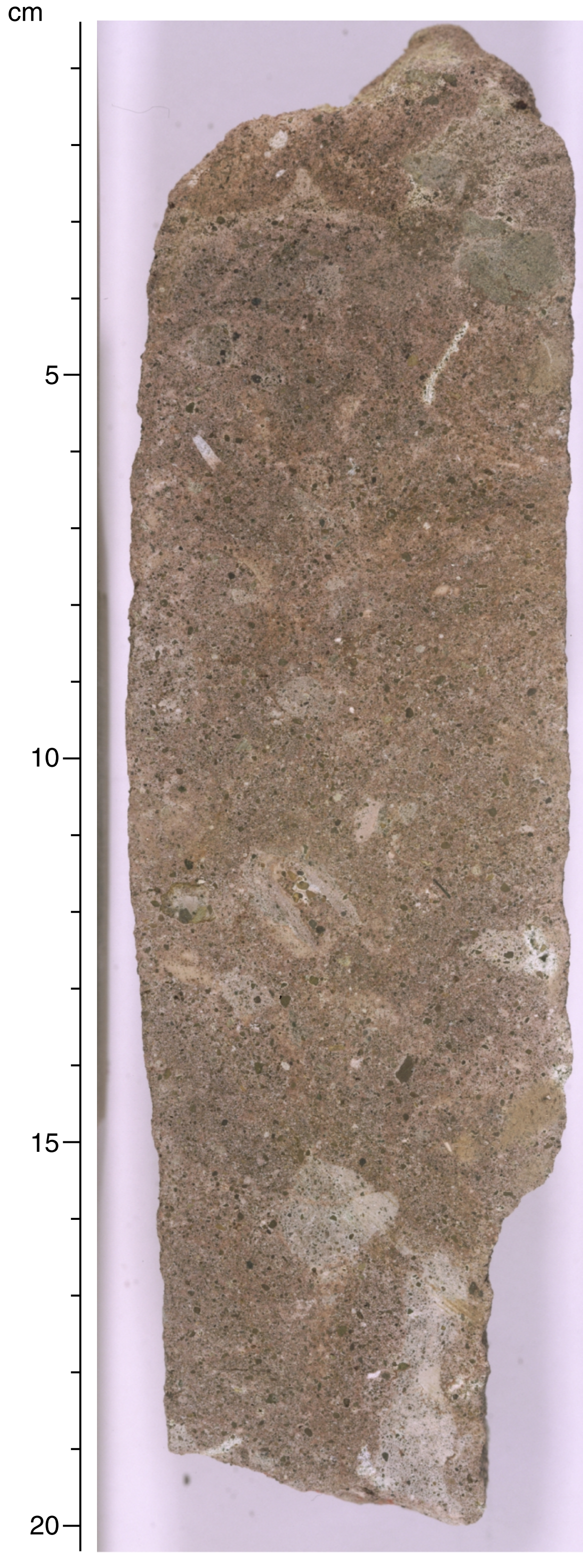

Figure F7. Examples of grainstones and packstones of Unit V. **A.** Packstone (interval 183-1139A-41R-2, 49–55 cm). **B.** Light-colored grainstones with cross-stratification (intervals 183-1139A-44R-1, 14–32 cm). (Continued on next page.)

Figure F7 (continued). **C.** Light-colored grainstones with cross-stratification (intervals 183-1139A-44R-1, 44R-1, 40–54 cm). **D.** Rusty yellowish brown colored grainstone from lower part of the unit (interval 183-1139A-49R-1, 27–33 cm).

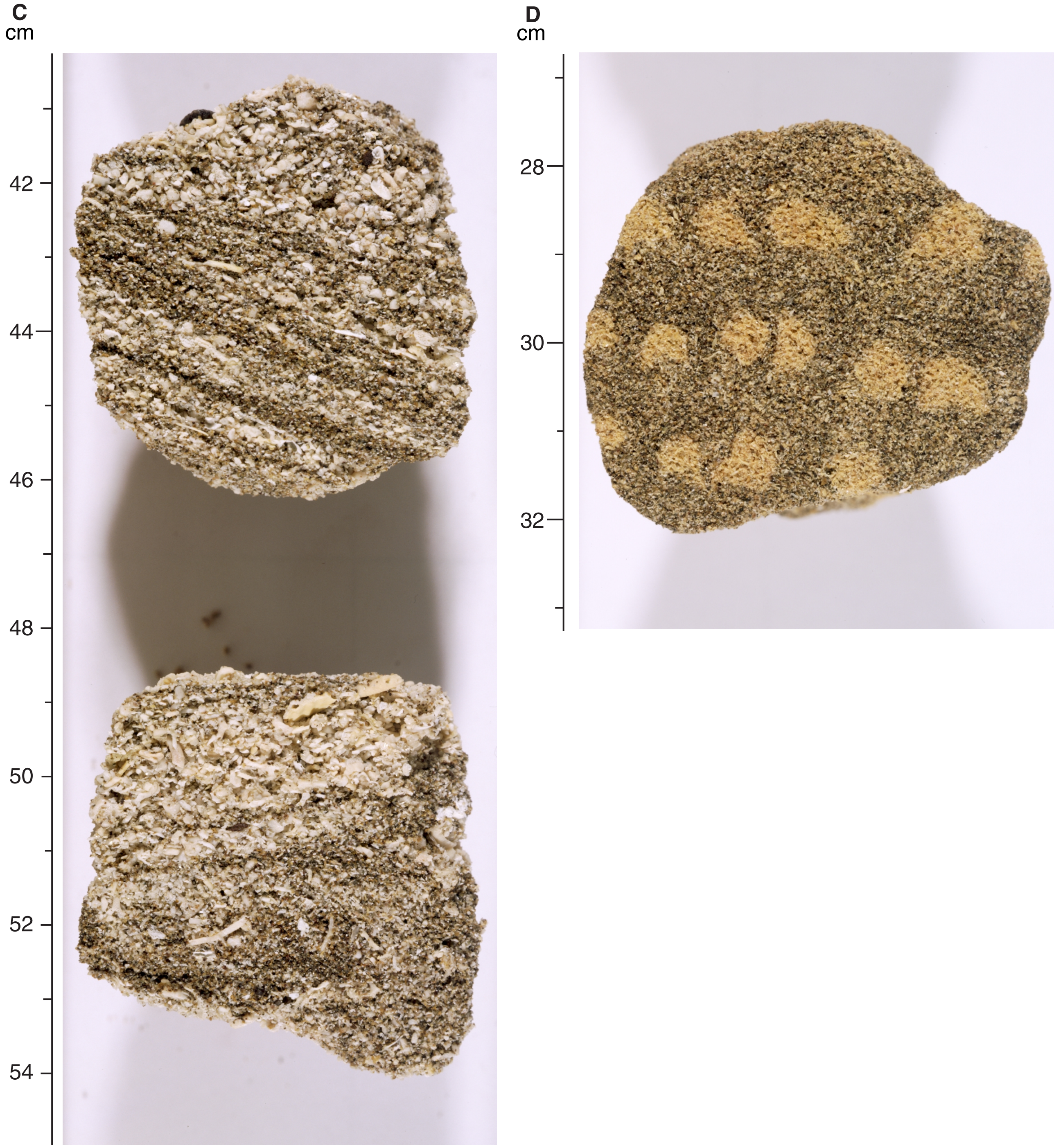

Figure F8. Examples of cross-stratified grainstones of Unit V. **A.** Interval 183-1139A-44R-1, 63–80 cm. **B.** Interval 183-1139A-45R-1, 30–47 cm. (Continued on next page.)

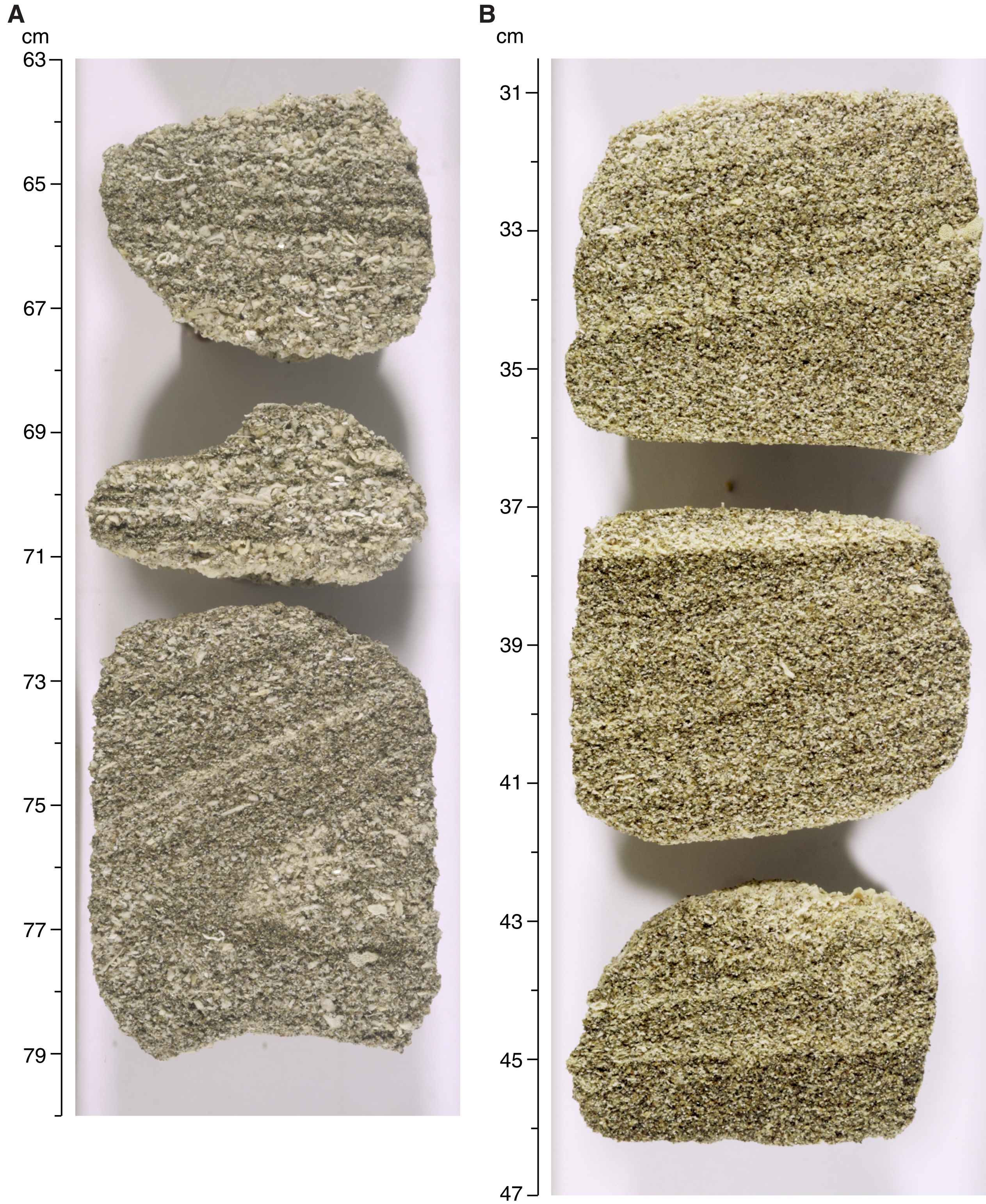

Figure F8 (continued). C. Interval 183-1139A-45R-1, 89–106 cm.

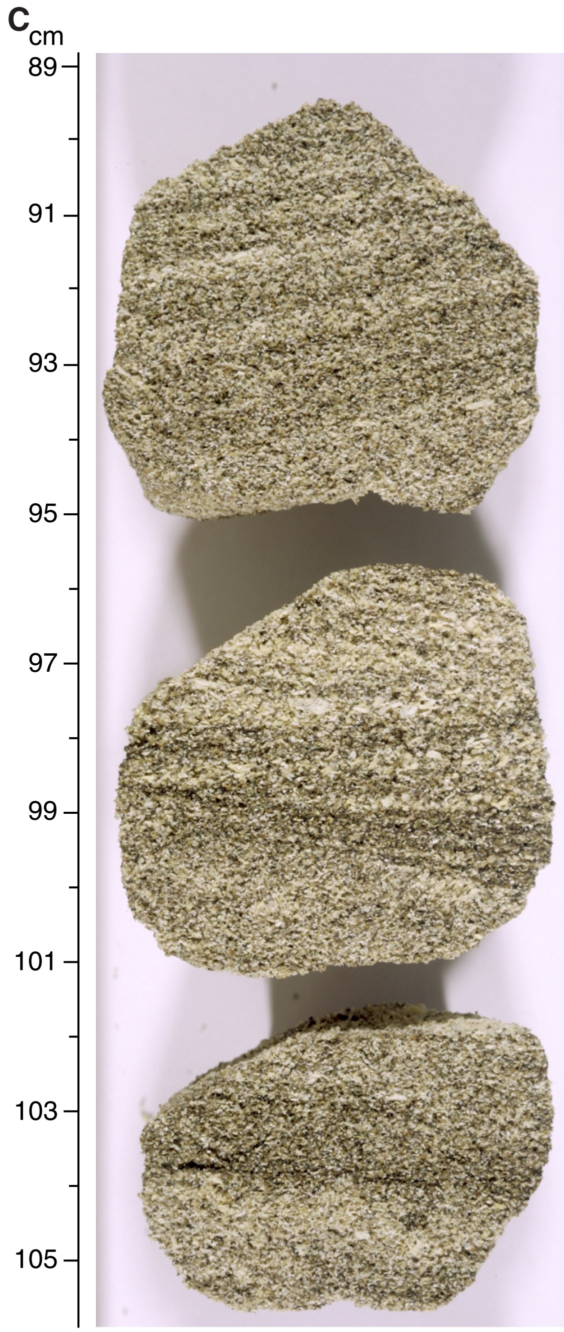

Figure F9. Site 1139 age-depth plot.

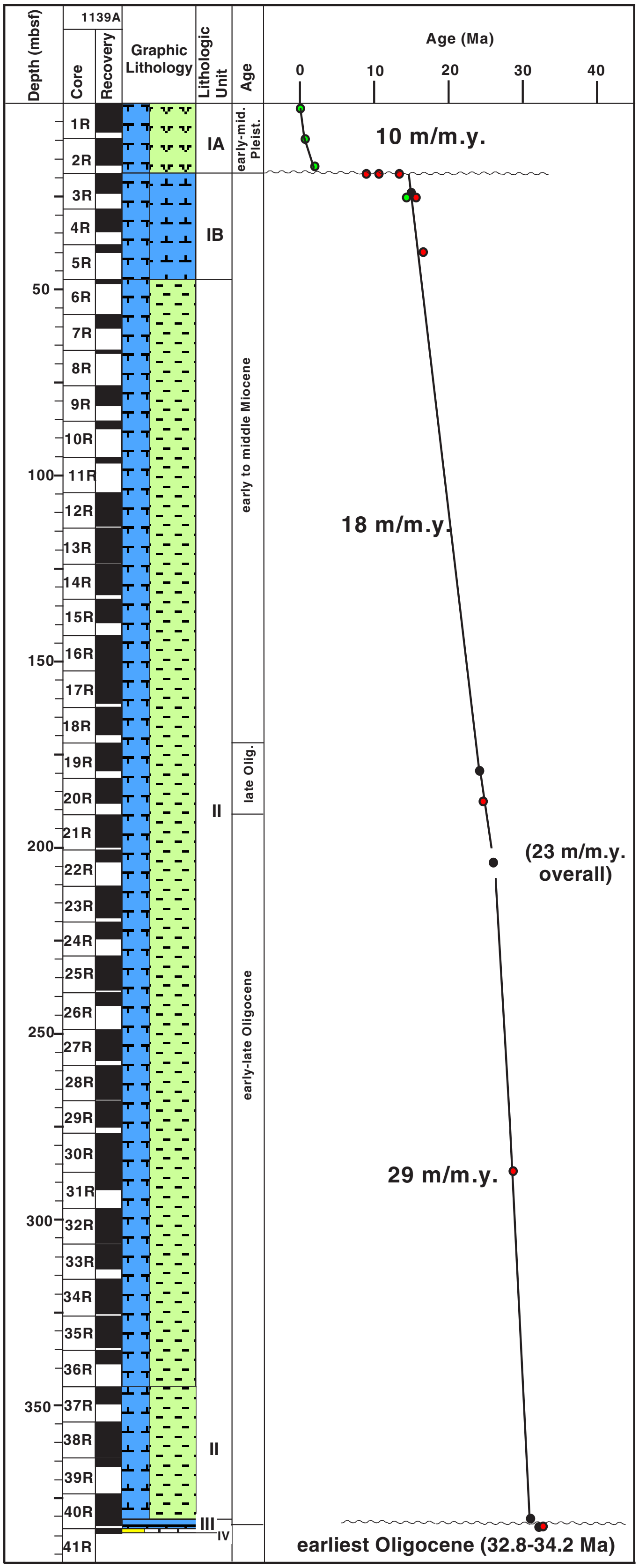

Figure F10. Basement Subunit 1A. **A.** Clast rounding vs. number of clasts (R = rounded, SR = subrounded, SA = subangular, A = angular). Clasts are dominated by subrounded shapes. **B.** Internal texture vs. number of clasts (BX = breccia, CB = contorted flow banding, PB = planar flow-banding, M = massive). Clasts are dominated by planar flow-banded internal textures with lesser and approximately equal numbers of massive clasts and clasts with contorted flow banding.

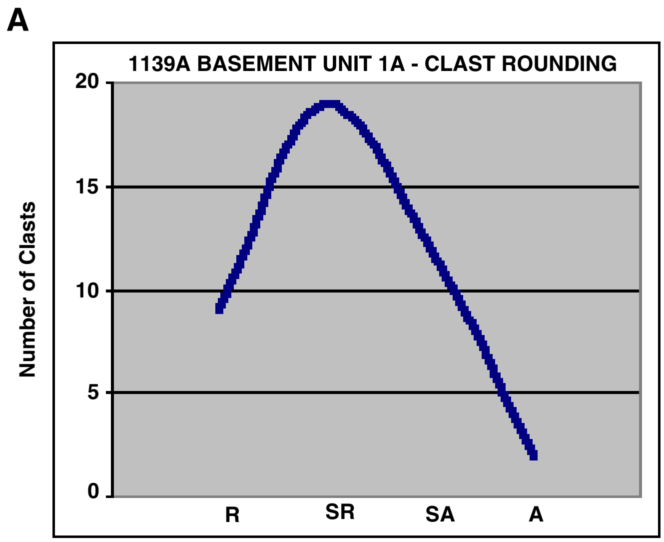

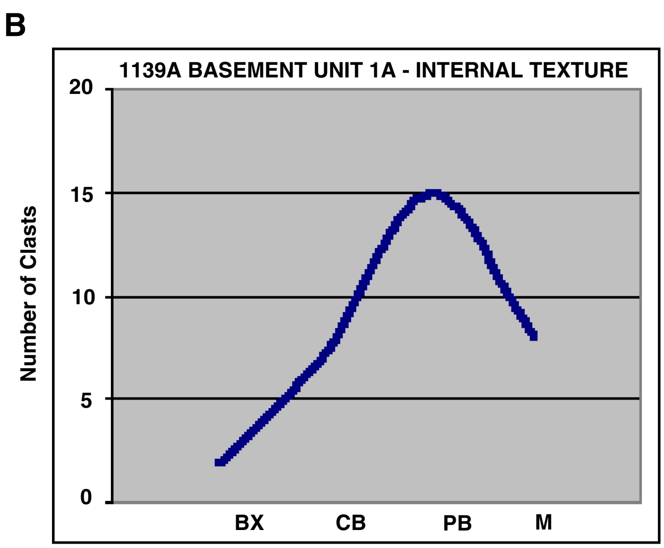

Figure F11. Close-up photograph of interval 183-1139A-52R-1, 117–130 cm, showing internal texture in the pumice/flow-banded rhyolite breccia (basement Subunit 1C). Note flow banding in clasts and small round perlitic fracture texture along bands.

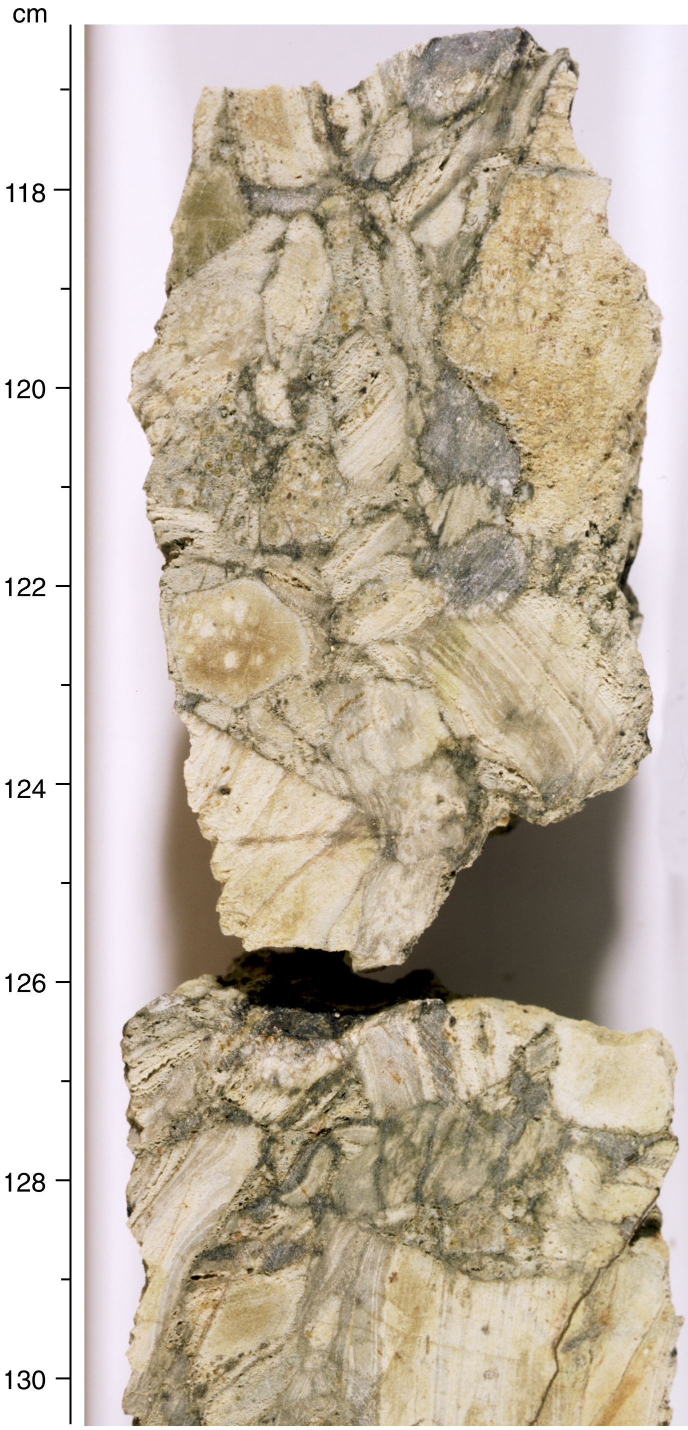

Figure F12. Photomicrograph (Sample 183-1139A-52R-1, 120–123 cm) showing banded perlite in breccia clasts and the tight contact between clasts. Field of view = 5.5 mm (in plane-polarized light).

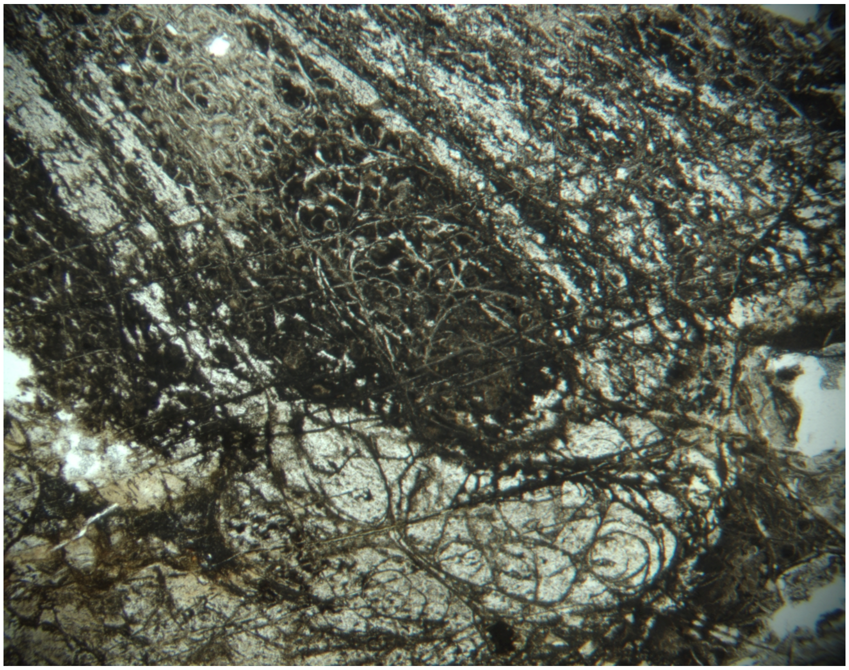

Figure F13. Close-up photograph of interval 183-1139A-53R-1, 110–121 cm, showing the perlitic fracturing in altered felsic volcanic glass (basement Subunit 1D). Notice alteration around some spheroidal perlite kernels. Some perlite kernels have been plucked out.

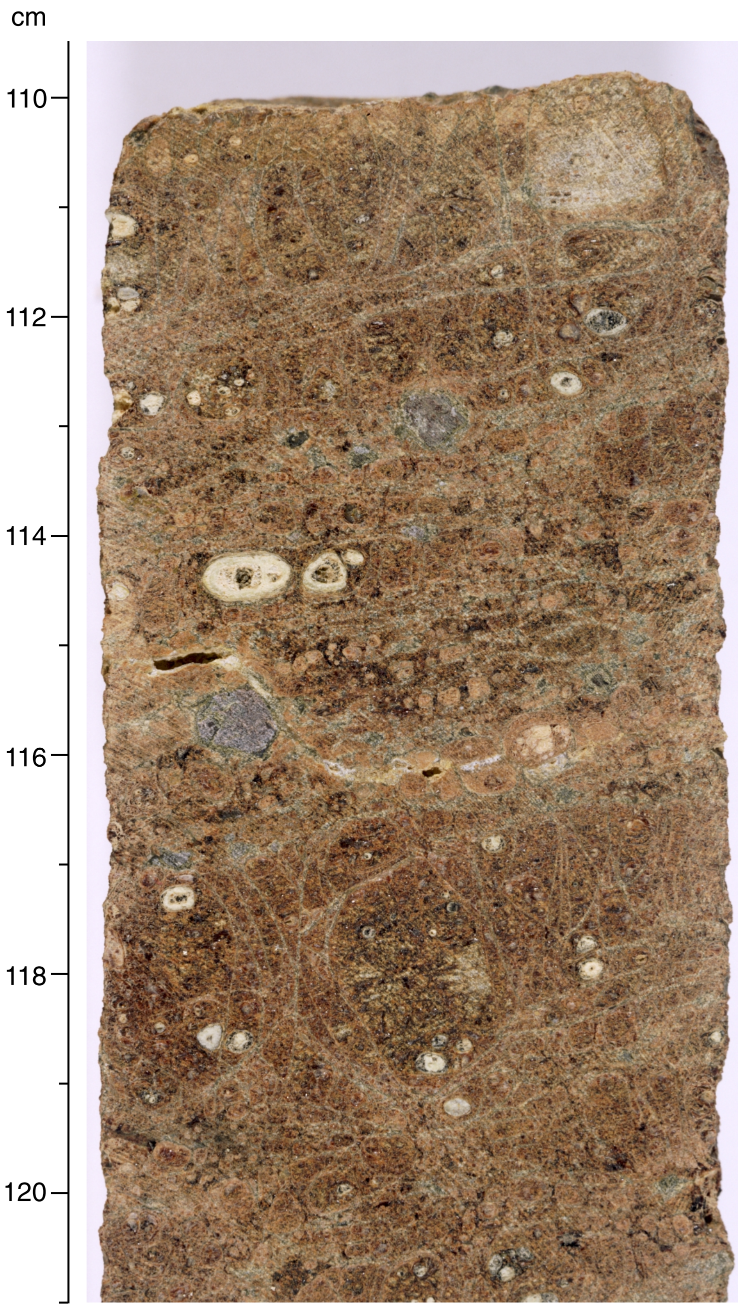

Figure F14. Photomicrograph of Sample 183-1139A-53R-1, 127–130 cm, showing nested, spheroidal perlitic fractures in devitrified and altered felsic volcanic glass. These fractures are subordinate to penetrative longitudinal fractures. Field of view = 5.5 mm (in plane-polarized light).

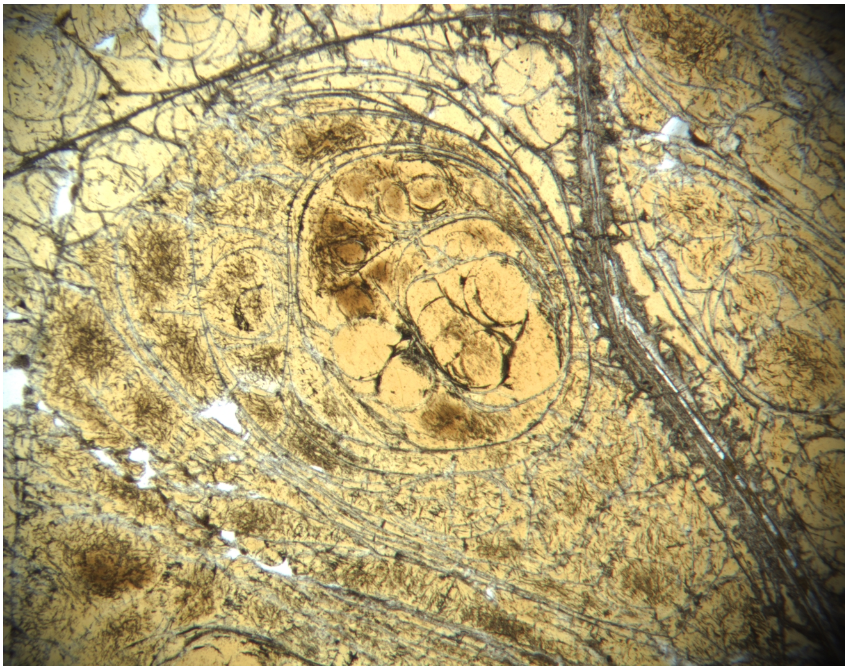

Figure F15. Photomicrograph of Sample 183-1139A-53R-1, 127–130 cm, showing rotation of an enclosed clast within the glass, and the flowage of glassy material around the clast as indicated by the patterns in the flow banding. Field of view = 5.5 mm (in plane-polarized light).

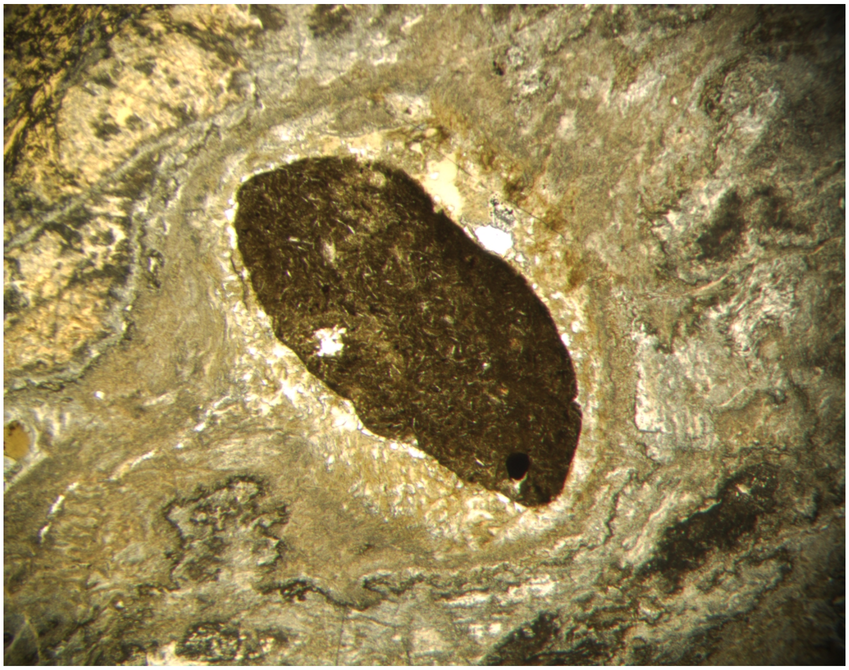

Figure F16. Photomicrograph of Sample 183-1139A-53R-1, 127–130 cm, showing banded perlite within a flow-banded, glassy clast in the perlitic glass. This clast has a higher crystal content than the enclosing glass. Field of view = 5.5 mm (in plane-polarized light).

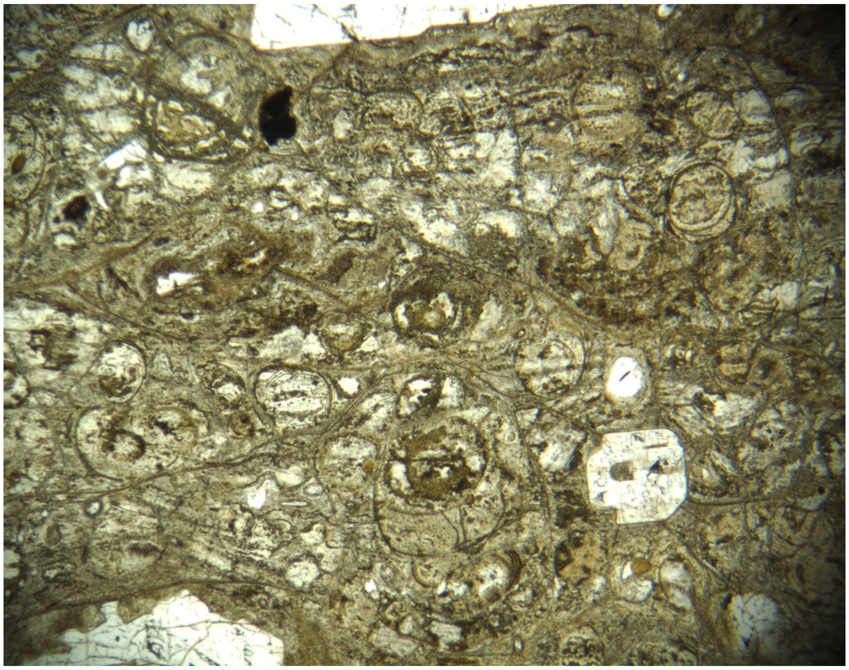

Figure F17. Close-up photograph of interval 183-1139A-53R-2, 9–23 cm, showing subhorizontal fracturing and silicification (green) of the reddish orange, perlitic volcanic glass. One large open fracture has also caused enhanced alteration through this interval. Note the preferential alteration along spheroidal perlitic fractures.

Figure F18. Close-up photograph of interval 183-1139A-53R-2, 51–60 cm, showing the mixed nature of clasts in the silicified basal breccia of basement Subunit 1D. Incorporation of lithic fragments in this interval suggests that the glassy material is not a lava. Minor flow banding is visible in some relatively fresh clasts. The breccia matrix consists of yellow-green to dark green clay.

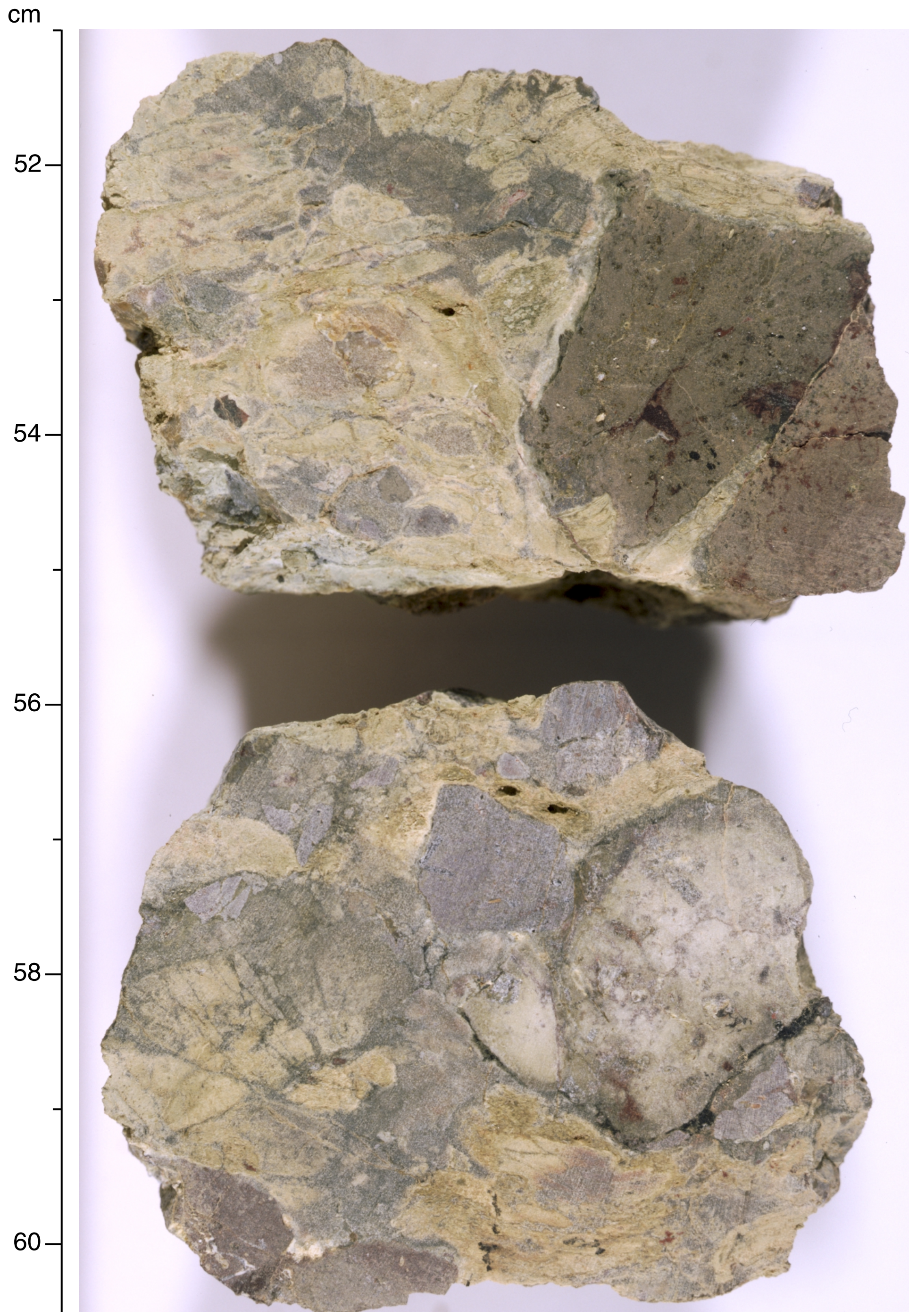

Figure F19. Close-up photograph of interval 183-1139A-56R-1, 36–41 cm, showing the subparallel draping and welding fabric in the dark red, vesicular, rhyolite agglutinate (basement Unit 2). Alkali feldspar (sanidine?) crystal content is ~15%.

Figure F20. Photomicrograph of Sample 183-1139A-56R-1, 37–40 cm, showing domains of flattened wispy clasts, defining a layered and banded texture. No glass shards are preserved, and the glassy material is highly altered. Field of view =5.5 mm (in plane-polarized light).

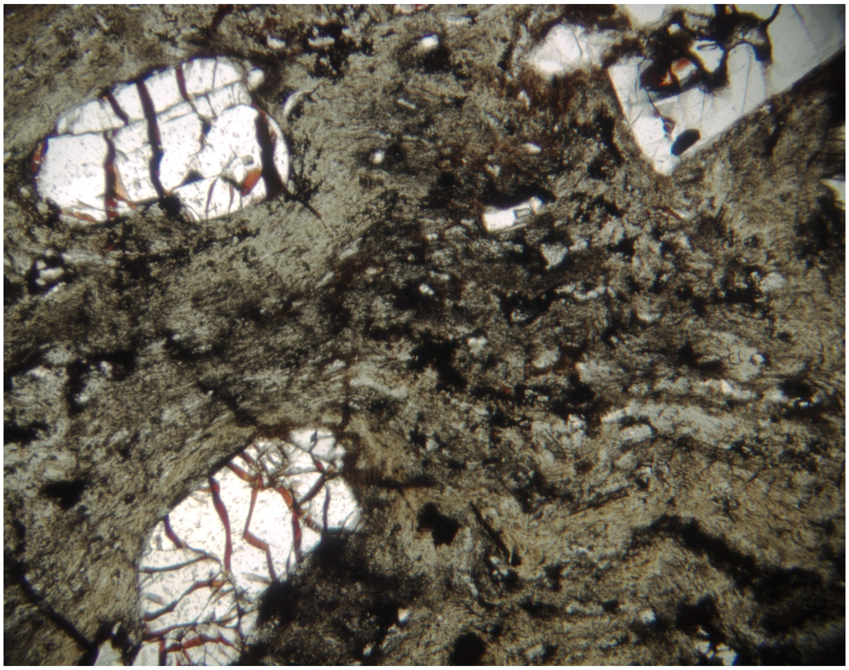

Figure F21. Close-up photograph of interval 183-1139A-56R-3, 85–95 cm, showing the internal texture in the green, altered, crystal vitric tuff-breccia (basement Unit 3). Note faint banding in this interval. Alkali feldspar (sanidine?) crystal content is ~15%.

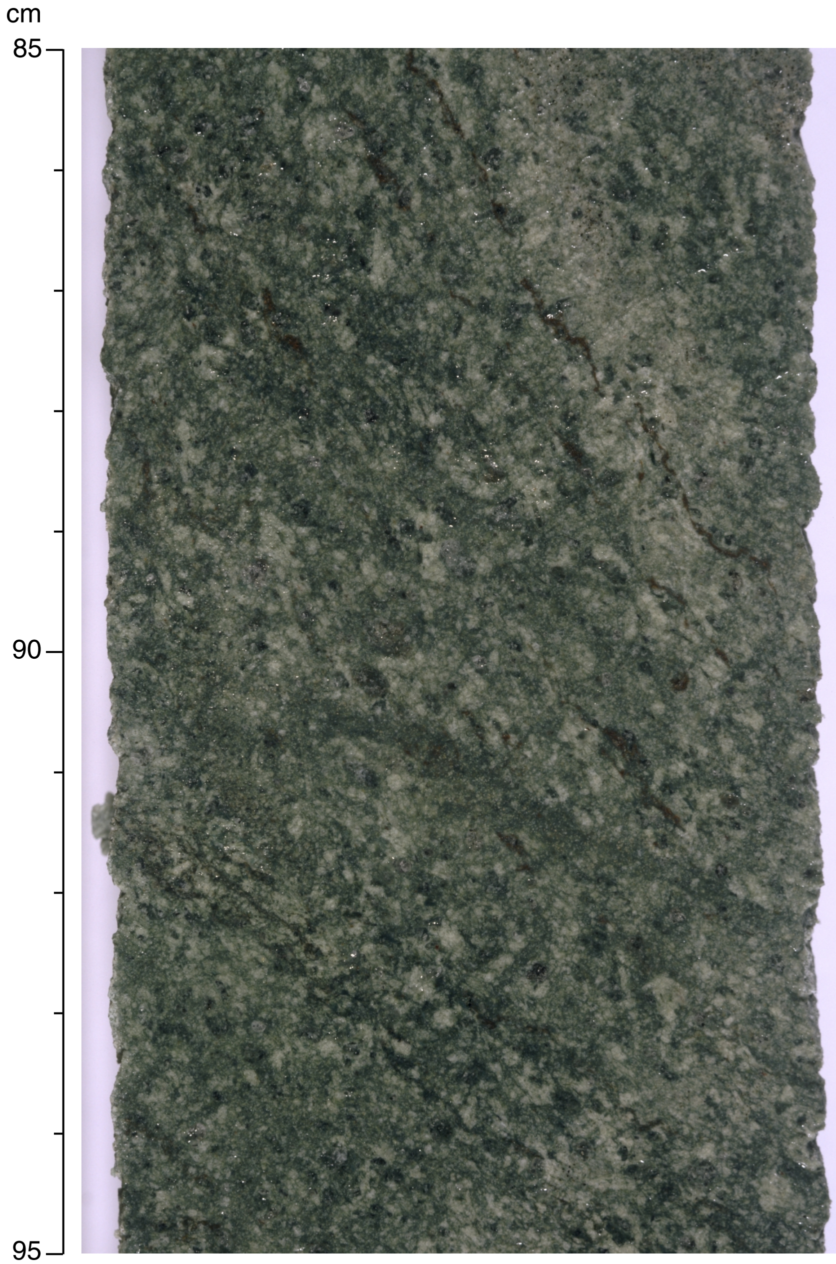

Figure F22. Photomicrograph of Sample 183-1139A-56R-3, 93–97 cm, showing the internal texture of the crystal vitric tuff-breccia. Note the ubiquitous spheroidal perlitic fractures with clay-rich material in the interstices. Field of view = 5.5 mm (in plane-polarized light).

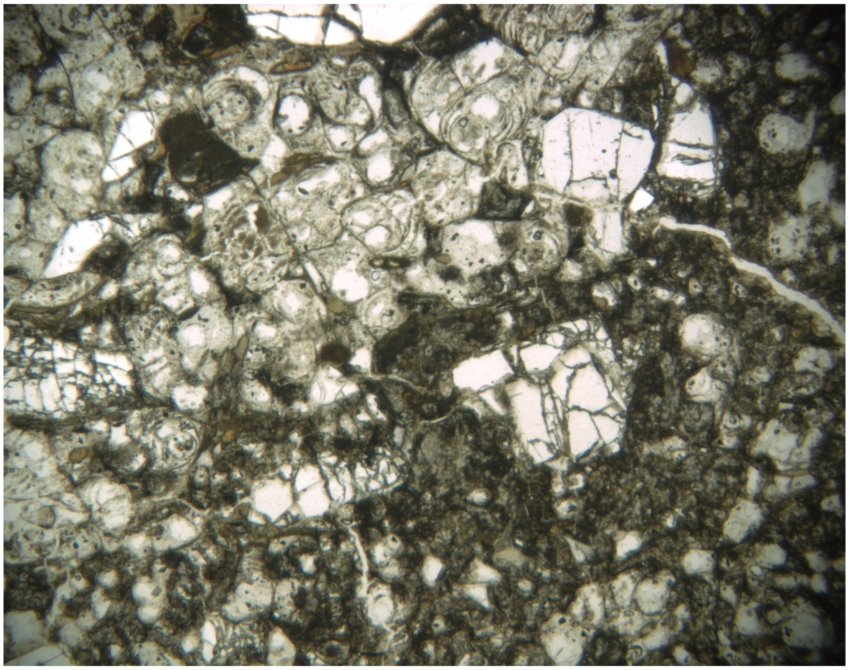

Figure F23. Close-up photograph of interval 183-1139A-57R-2, 46–57 cm, showing possible welding along a suture between two dark red, vesicular rhyolite clasts in basement Unit 4. Textures in this interval are similar to those observed in basement Unit 2. Alteration is enhanced along zones adjacent to the suture, perhaps because of a permeability contrast.

Figure F24. Close-up photograph of interval 183-1139A-60R-2, 54–61 cm, showing the dark red highly altered, rhyolite breccia at the base of basement Unit 4. The breccia has an open framework texture and is not welded. This differs from the welded material observed at the top of basement Unit 4. Red clasts have thin (<2 mm), light green alteration rims and are set in a red clay-rich matrix. Some fresh phenocrysts are present.

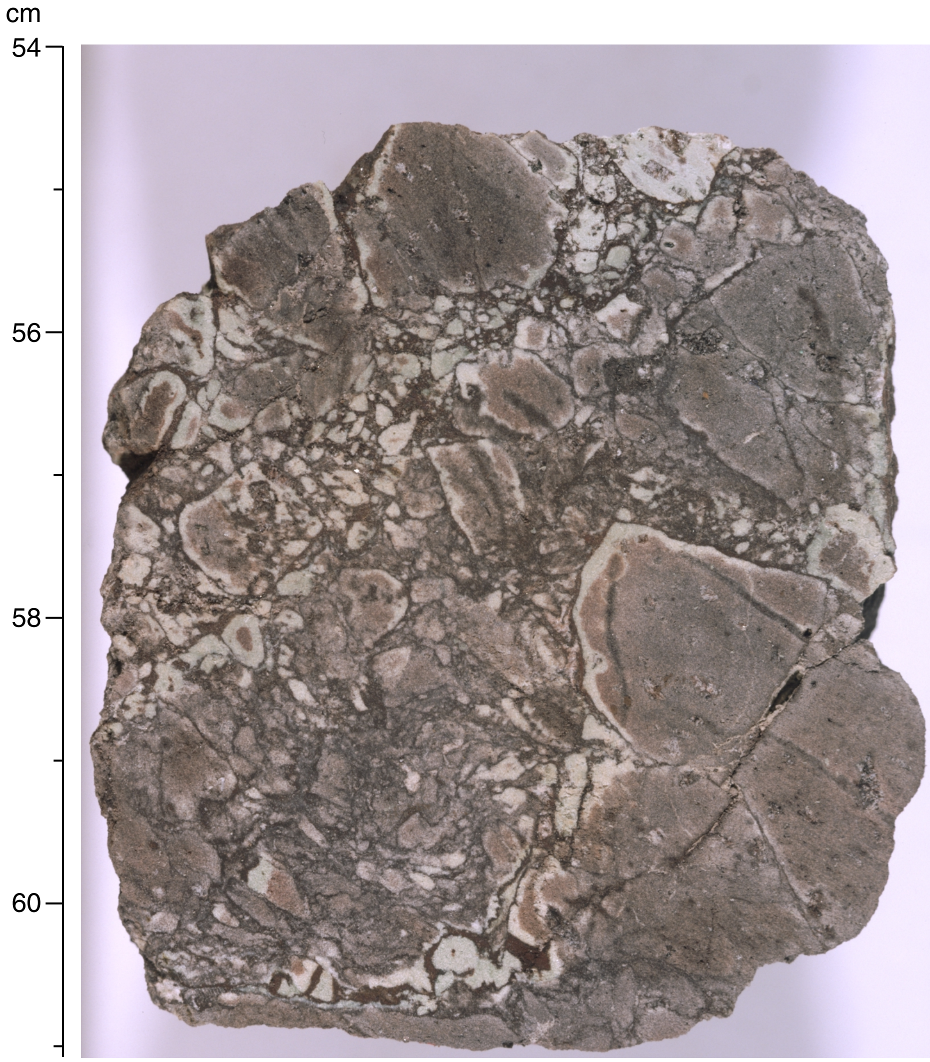

Figure F25. Close-up photograph of interval 183-1139A-61R-1, 5–17 cm, showing the breccia that overlies the massive central part of Unit 5. This breccia is highly altered and some penetrative fractures appear to be related to alteration. It might be a flow-top breccia that has been subsequently modified by alteration.

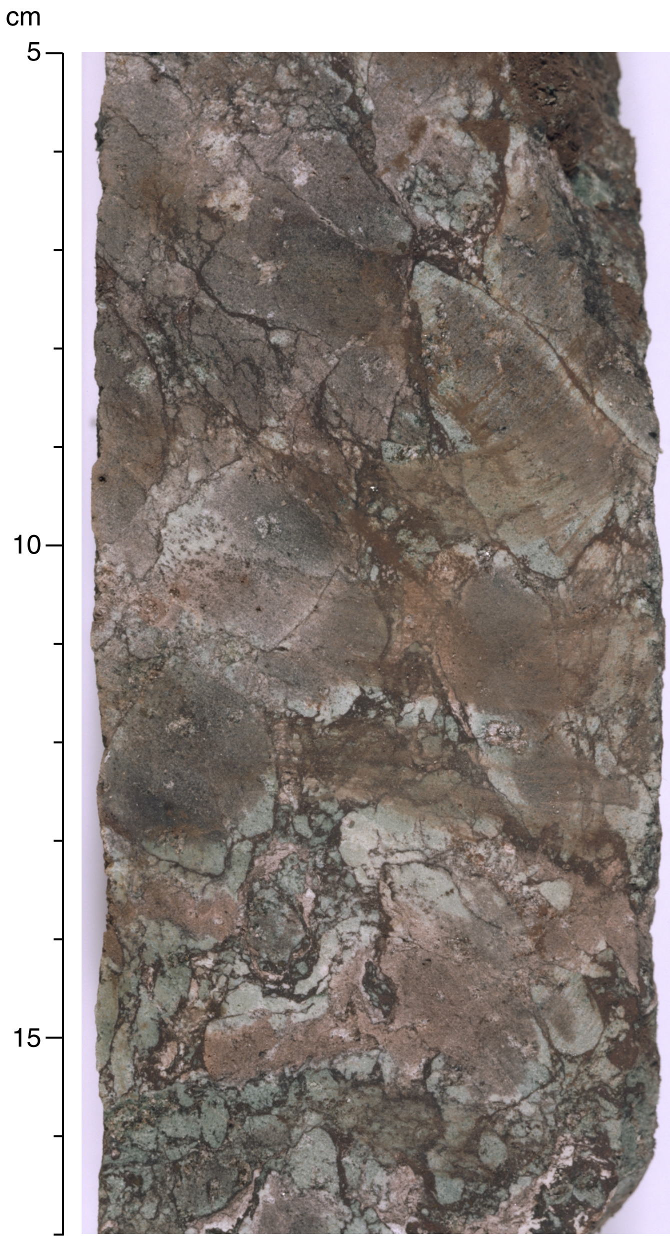

Figure F26. Close-up photograph of interval 183-1139A-62R-3, 10–24 cm, showing the altered breccia texture at the top of basement Unit 6.

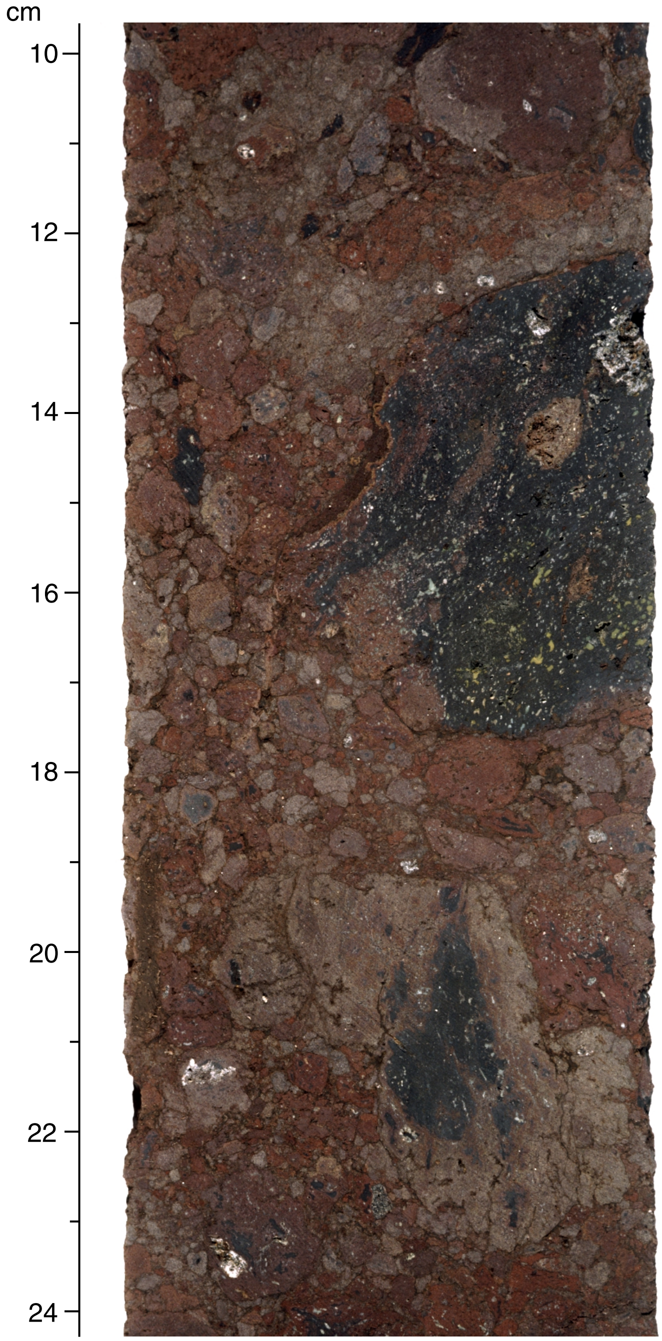

Figure F27. Close-up photograph of interval 183-1139A-64R-4, 23–47 cm, showing elongated vesicles in the upper part of the interior of basement Unit 8.

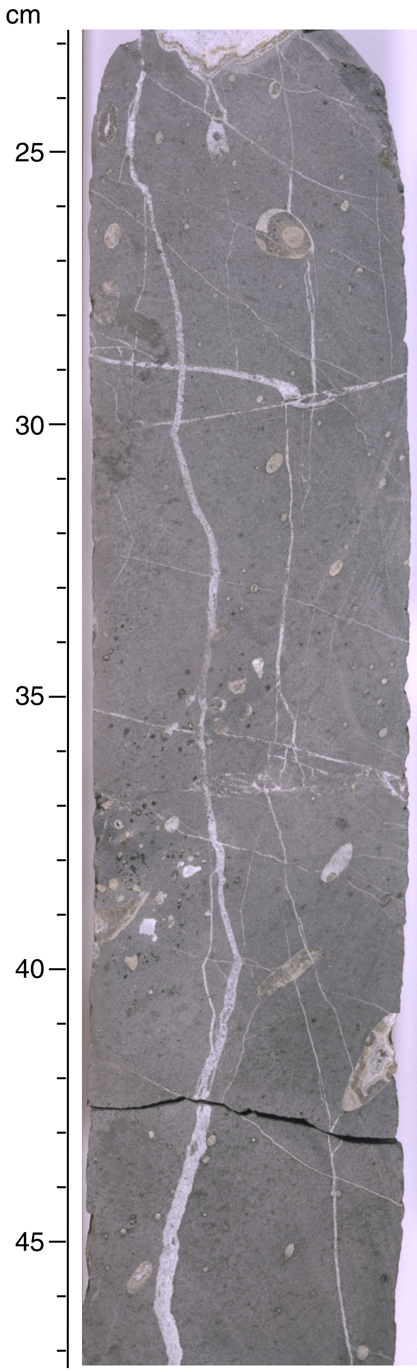

Figure F28. A. Vesicularity and vesicle number density as a function of depth within basement Unit 9. Hatched intervals = zones of no recovery. (Continued on next page.)

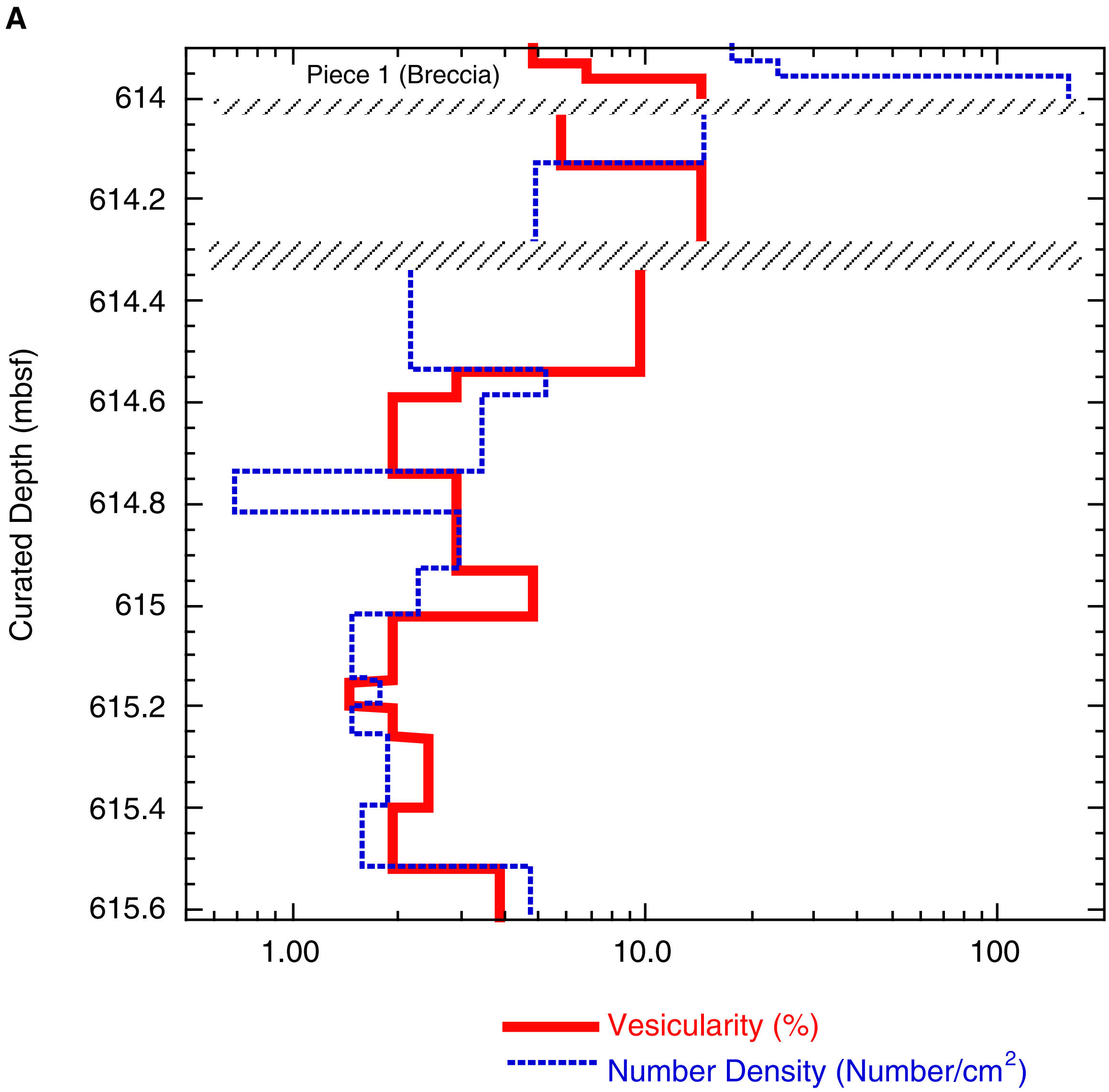

Figure F28 (continued). B. Vesicle size as a function of depth within basement Unit 9. Hatch intervals = zones of no recovery.

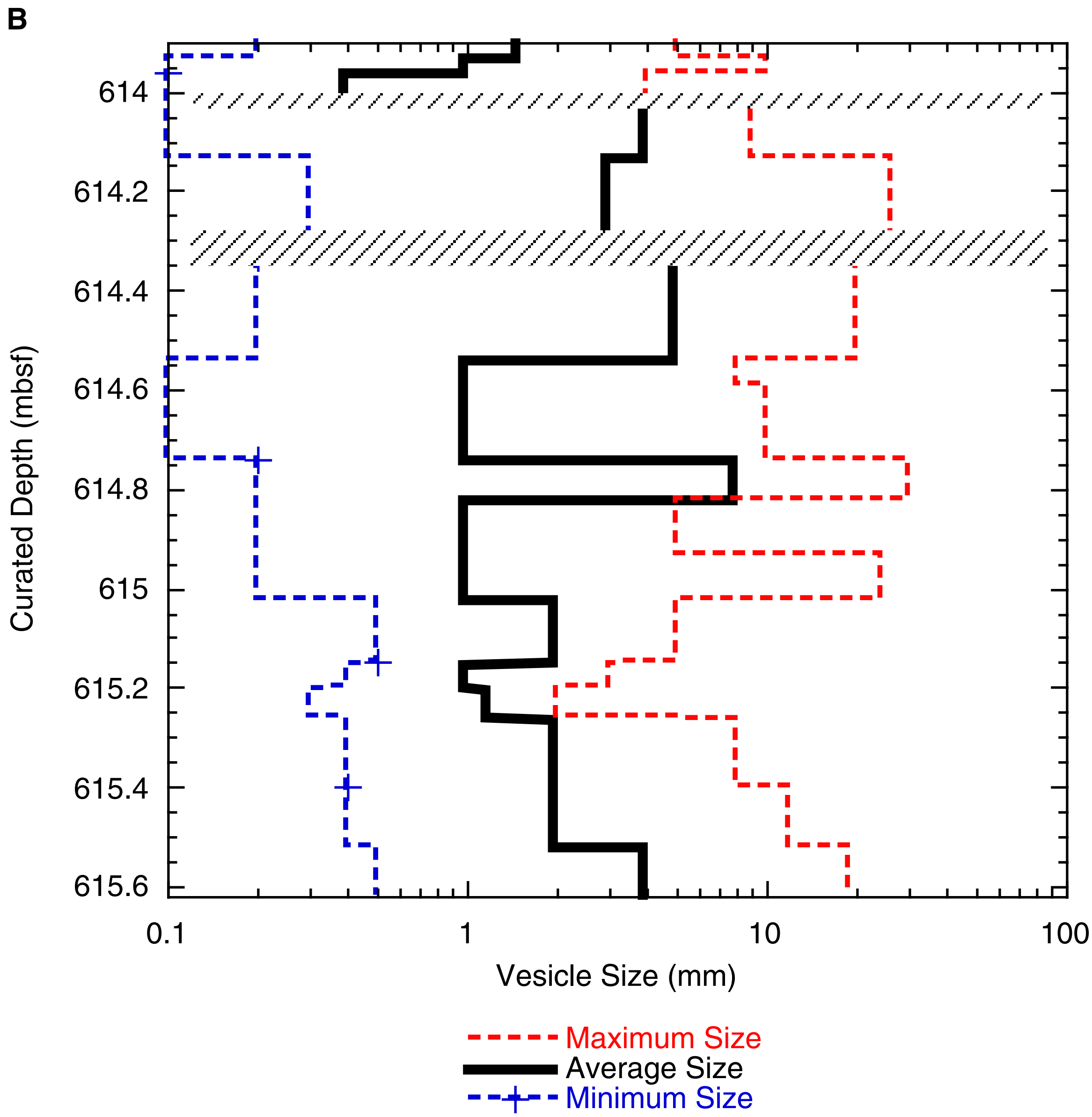

Figure F29. A. Vesicularity and vesicle number density as a function of depth within basement Unit 10. Stippled area = rubble. (Continued on next page.)

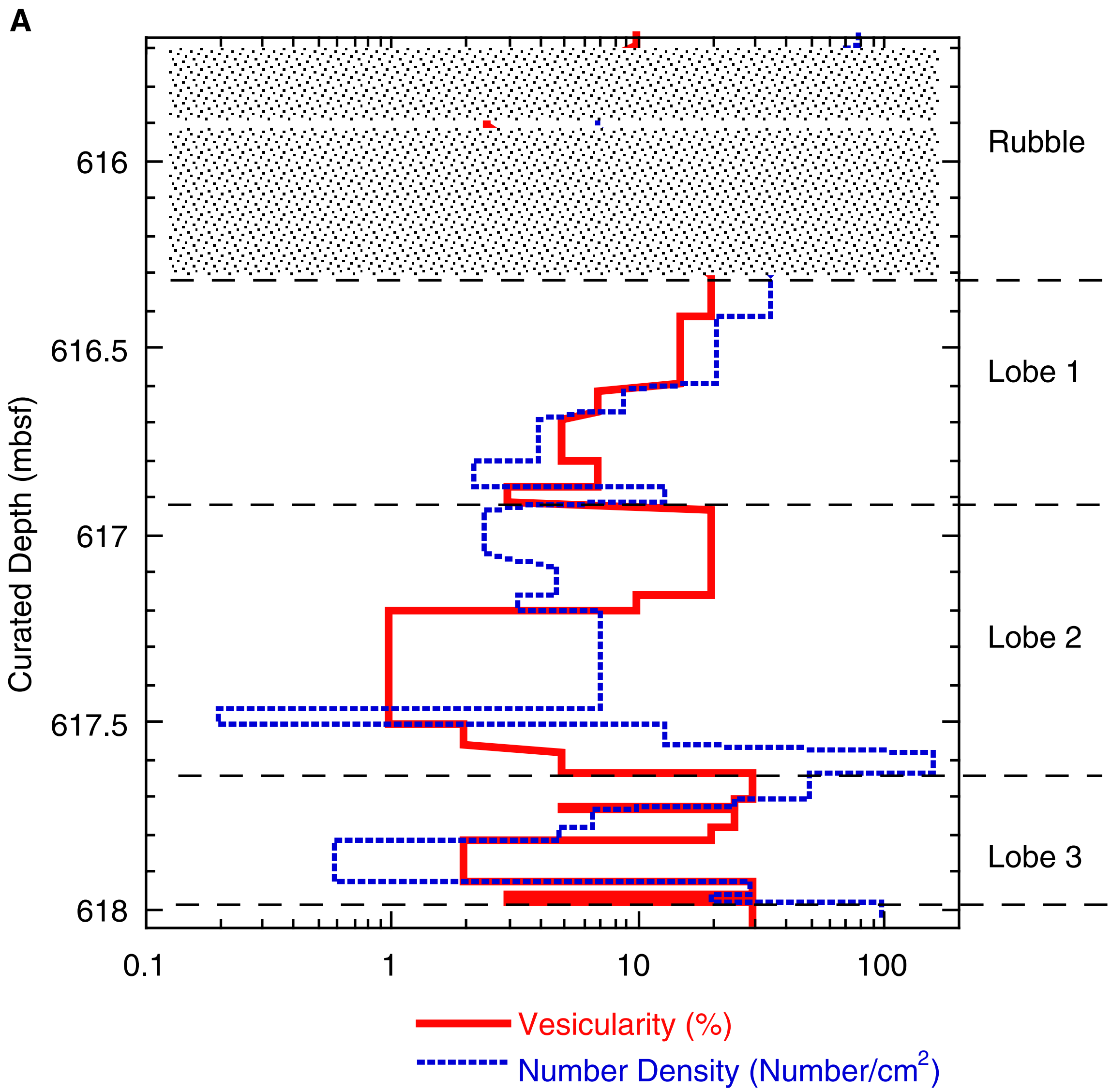

Figure F29 (continued). B. Vesicle size as a function of depth within basement Unit 10. Stippled area = rubble.

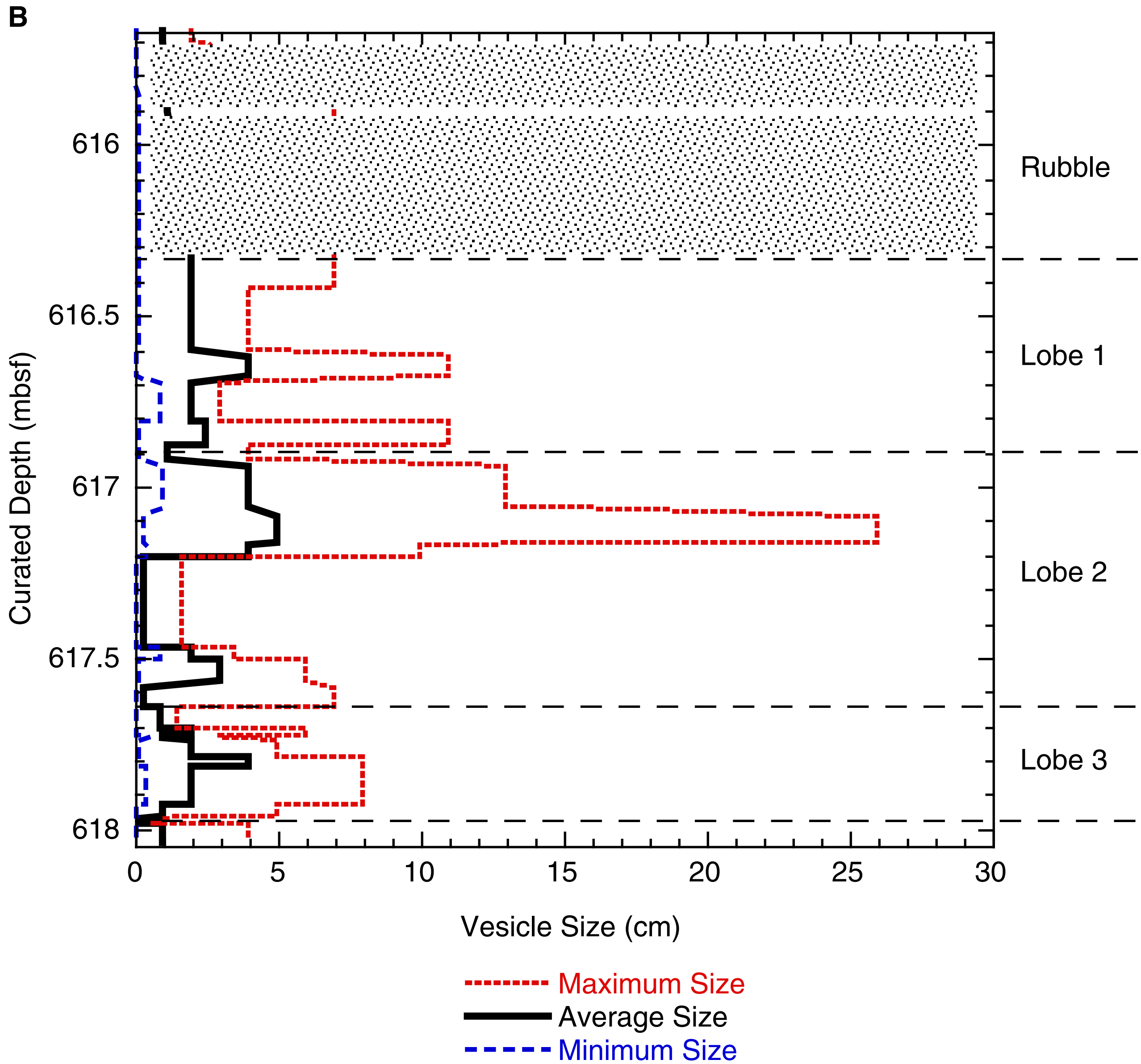

Figure F30. Close-up photograph of interval 183-1139A-65R-3, 50–65 cm, showing the vesicular top and dense (less vesicular) interior of second lobe in basement Unit 10.

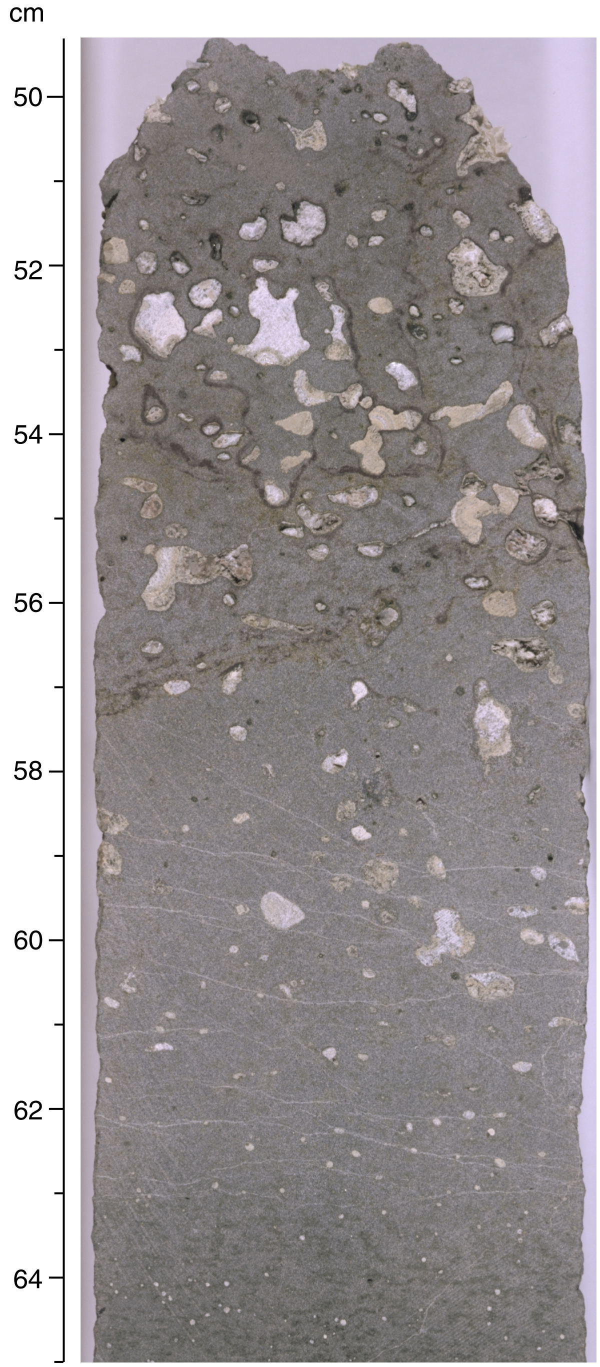

Figure F31. Close-up photograph of interval 183-1139A-65R-3, 107–125 cm, showing a sharp transition at 124 cm from the vesicular top to the dense interior of the third lobe in basement Unit 10.

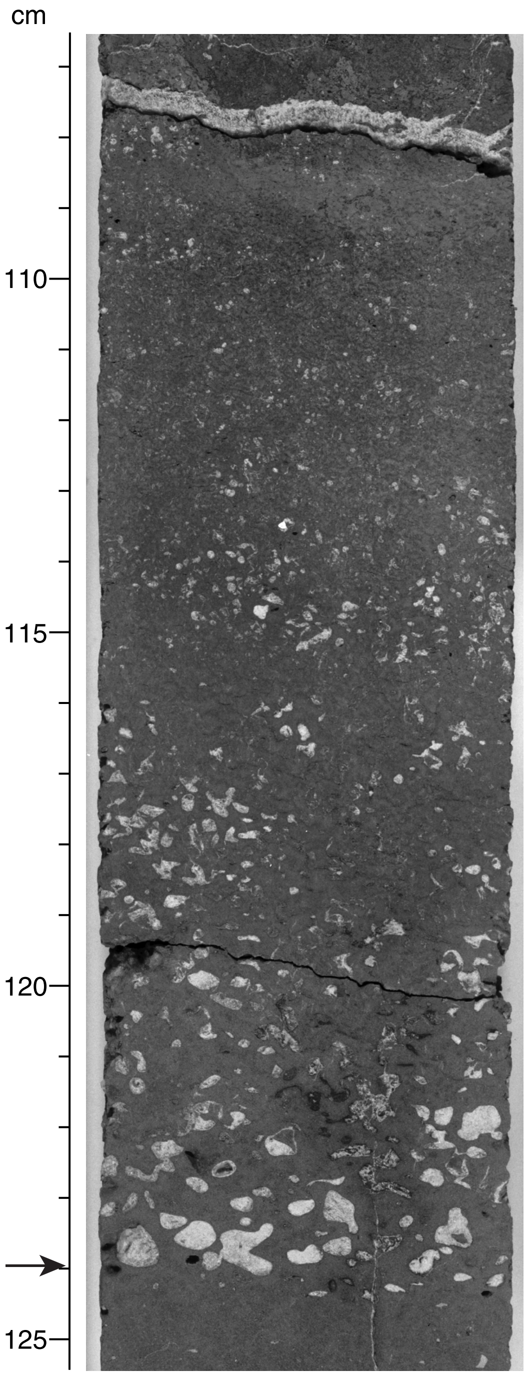

Figure F32. Close-up photograph of interval 183-1139A-65R-3, 130–142 cm, showing welded lobe margins at the base of basement Unit 10.

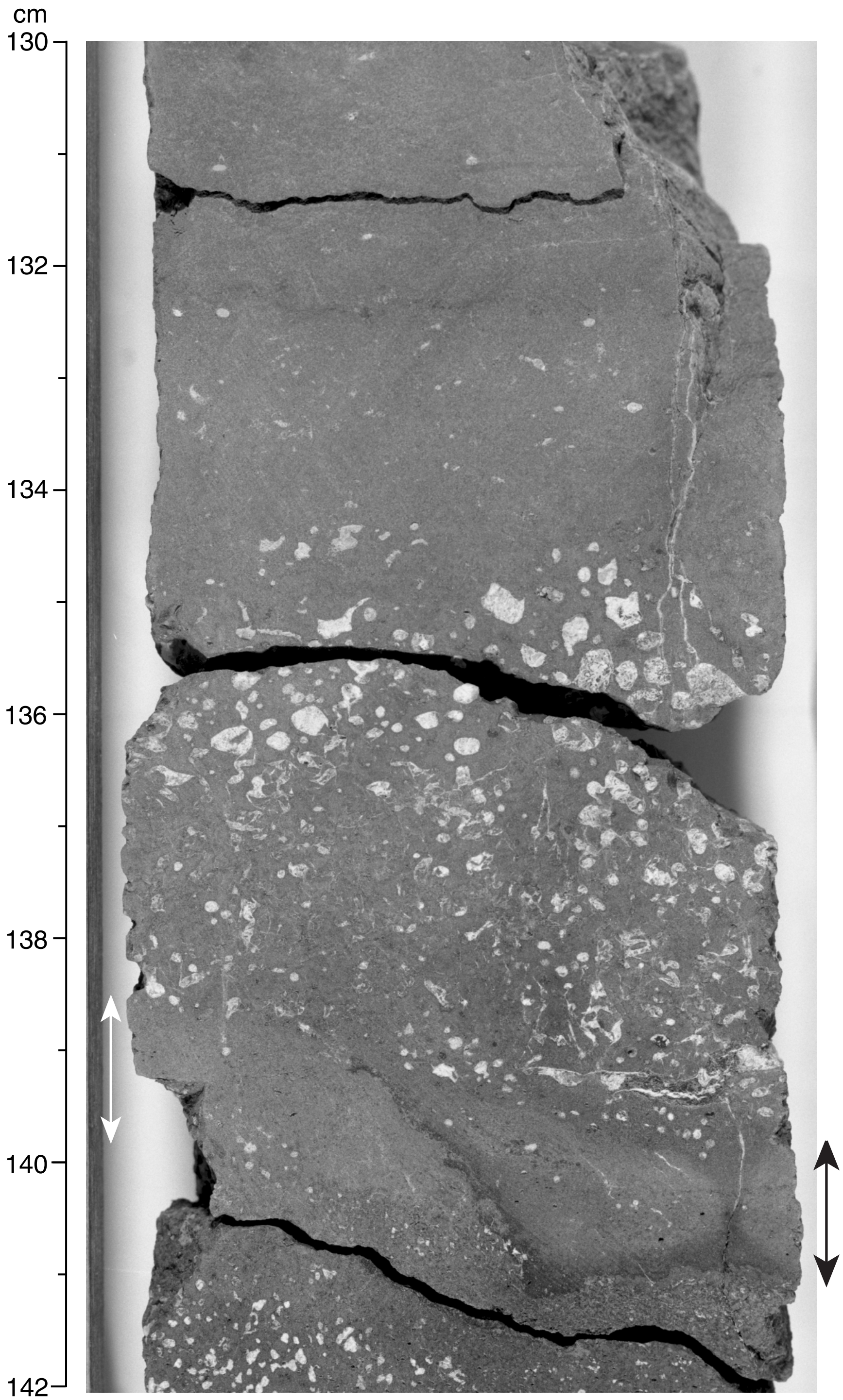

Figure F33. Close-up photograph of interval 183-1139A-65R-5, 42–52 cm, showing a large entrained clast and inclined elongate vesicles in the interior of basement Unit 11.

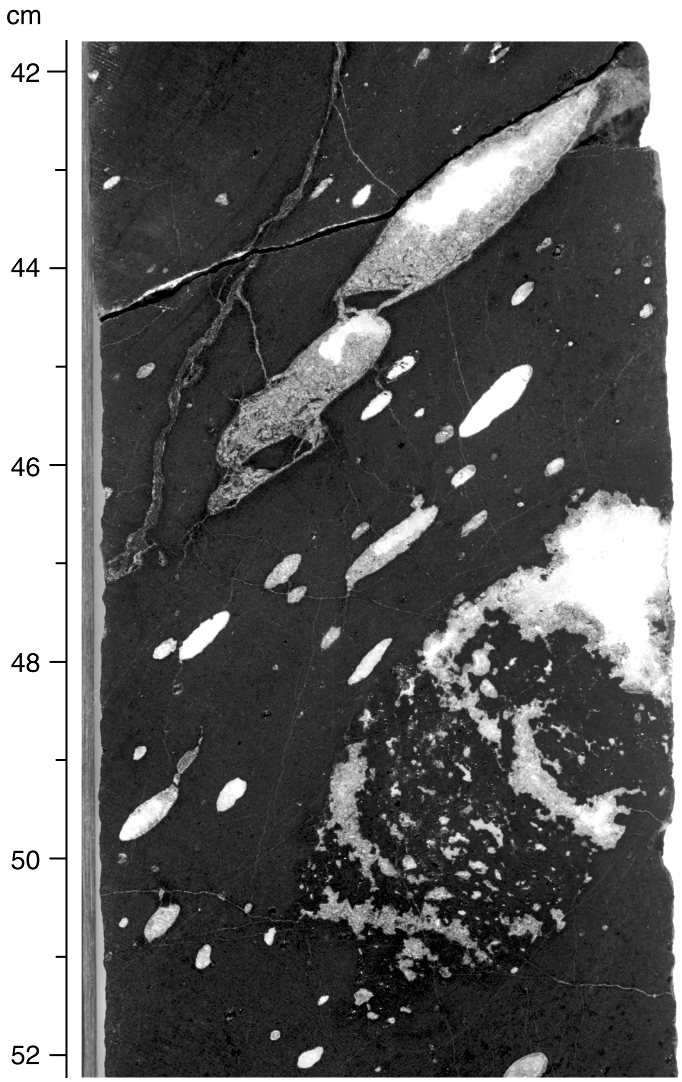

Figure F34. Close-up photograph of interval 183-1139A-66R-5, 115–135 cm, showing a pahoehoe lobe at the base of basement Unit 12 pushing into sediments.

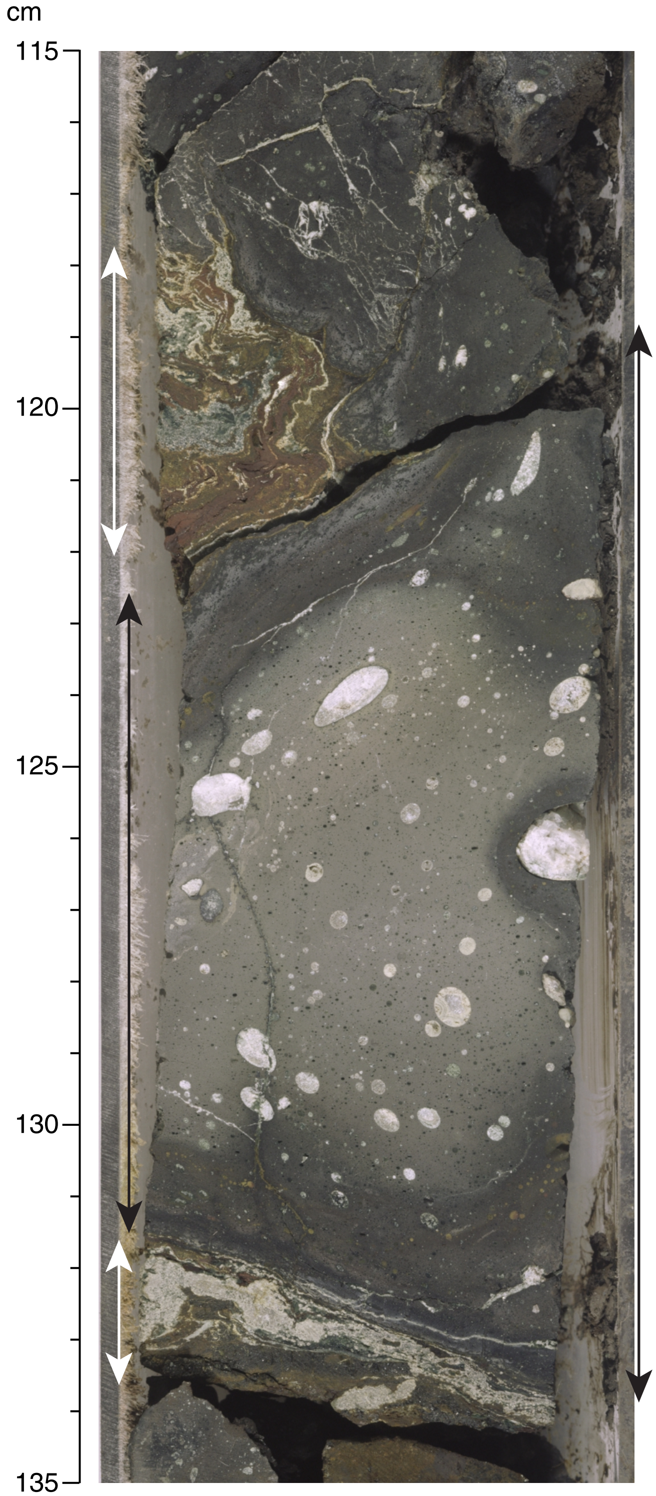

Figure F35. Close-up photograph of interval 183-1139A-67R-1, 35–47 cm, showing an autolithic breccia clast in the top of basement Unit 14.

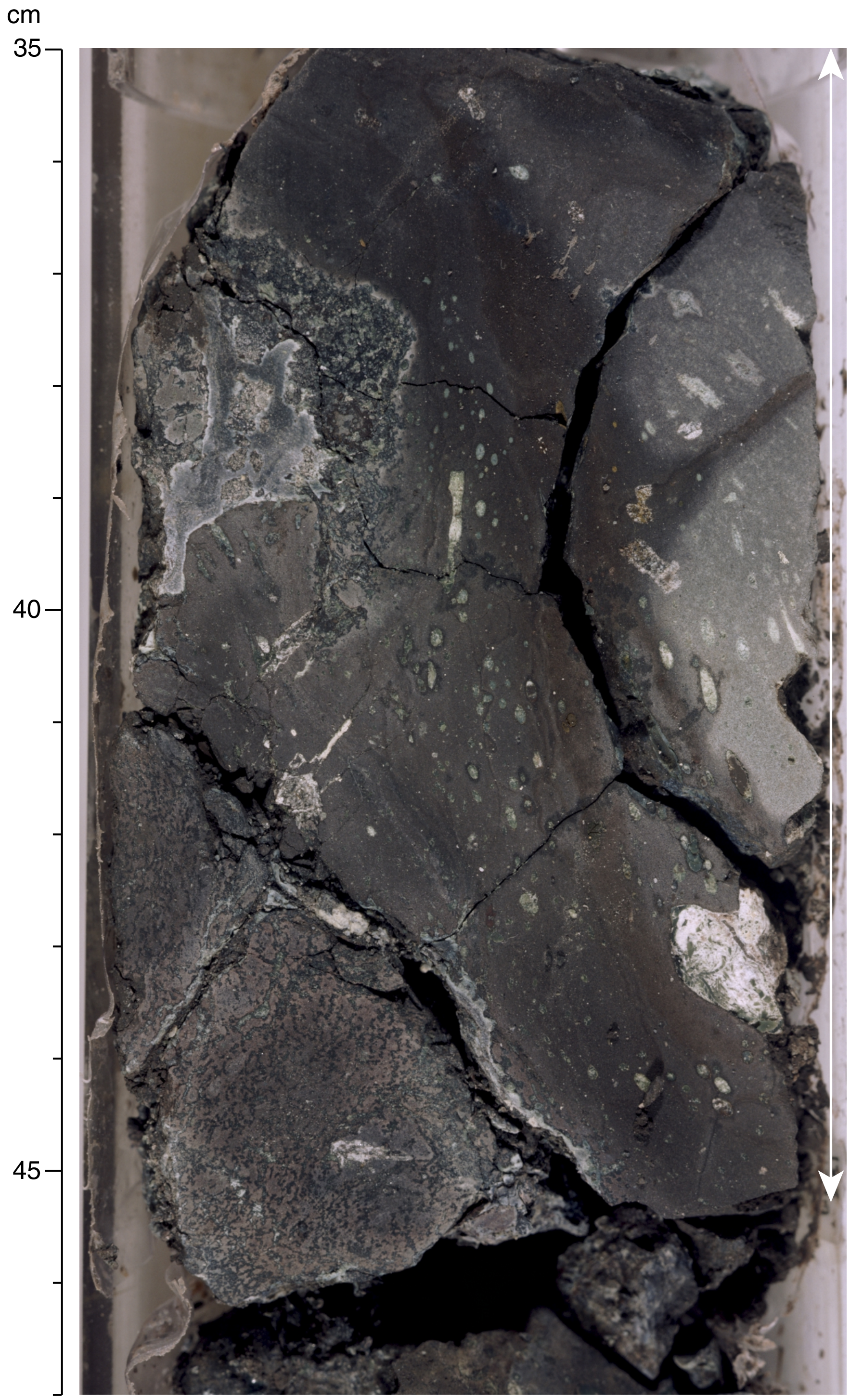

Figure F36. Close-up photograph of interval 183-1139A-67R-3, 76–84 cm, showing morphology of basement Unit 14 flow-top breccia. Breccia clasts and matrix are highly altered to saponite, and the matrix also contains small amounts of quartz and carbonate.

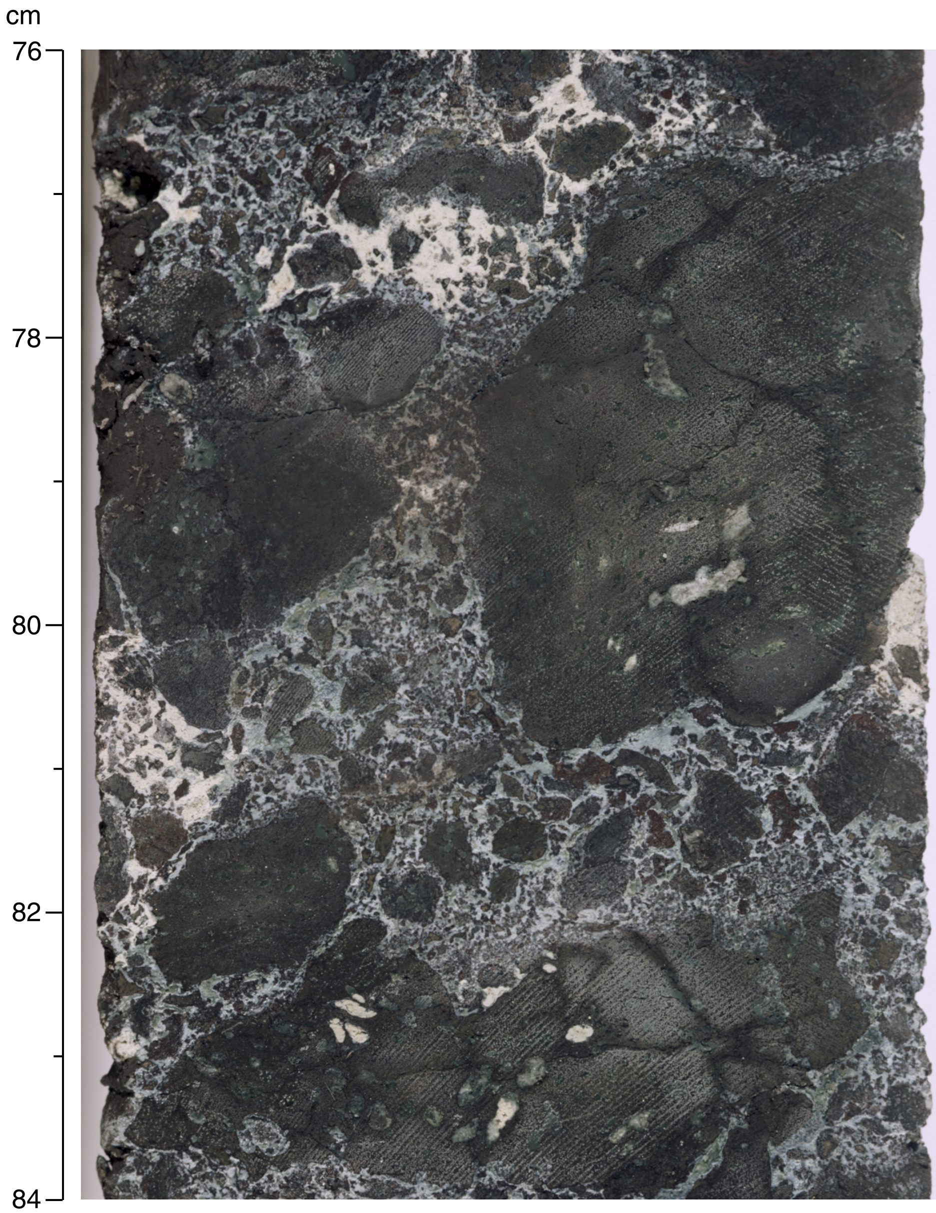

Figure F37. Close-up photograph of interval 183-1139A-68R-6, 6–20 cm, showing stretched vesicles producing a "flow banding" in a dense arm of the interior of basement Unit 16 intruding its flow-top breccia.

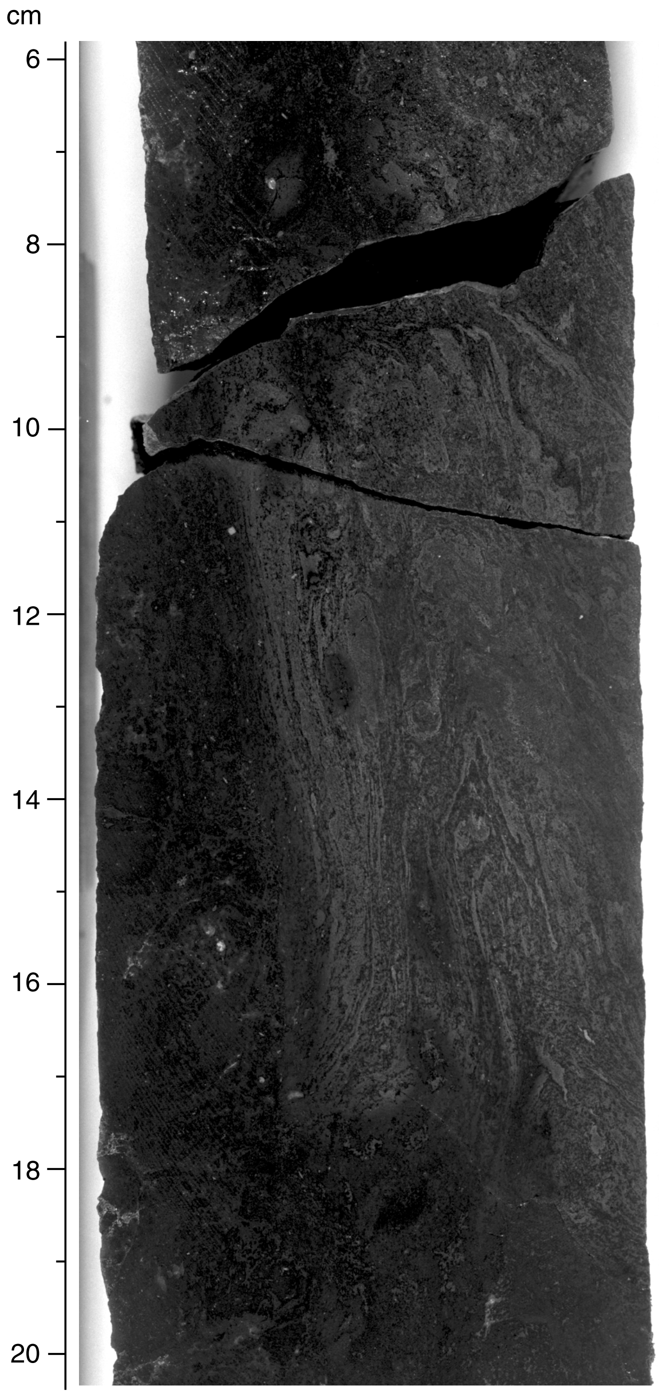

Figure F38. Close-up photograph of interval 183-1139A-68R-7, 80–96 cm, showing altered clasts in the top of basement Unit 17 with black cores and red rims.

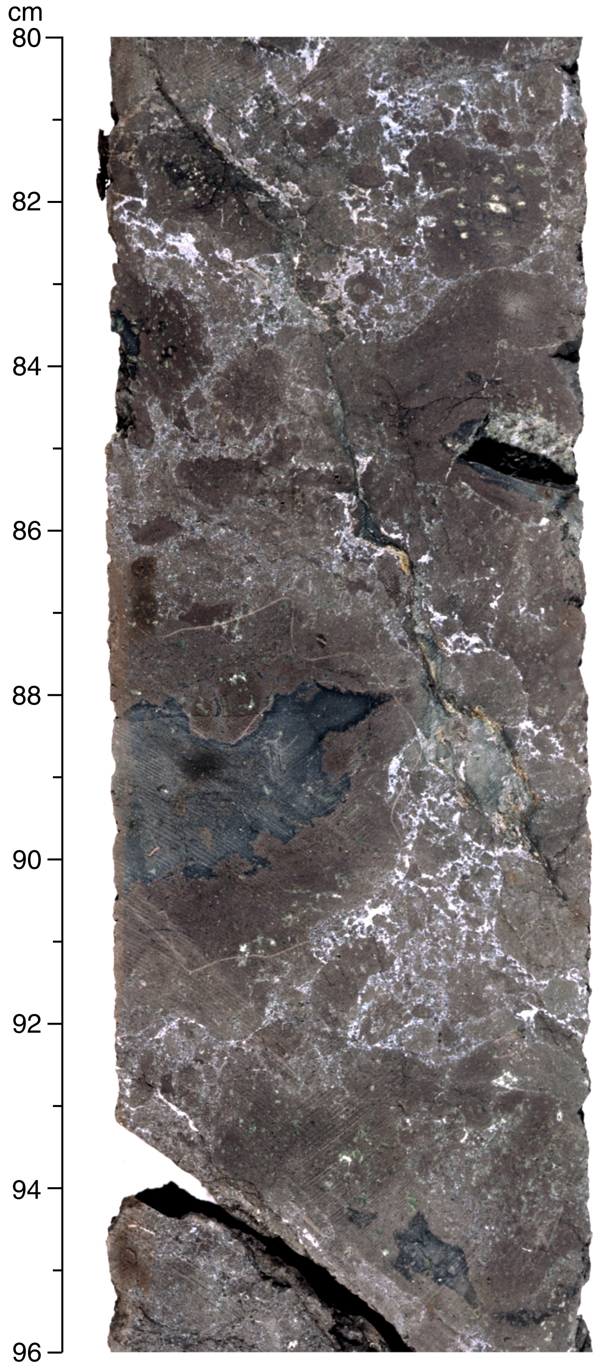

Figure F39. A. Vesicularity and vesicle density as a function of depth within basement Unit 18. (Continued on next page.)

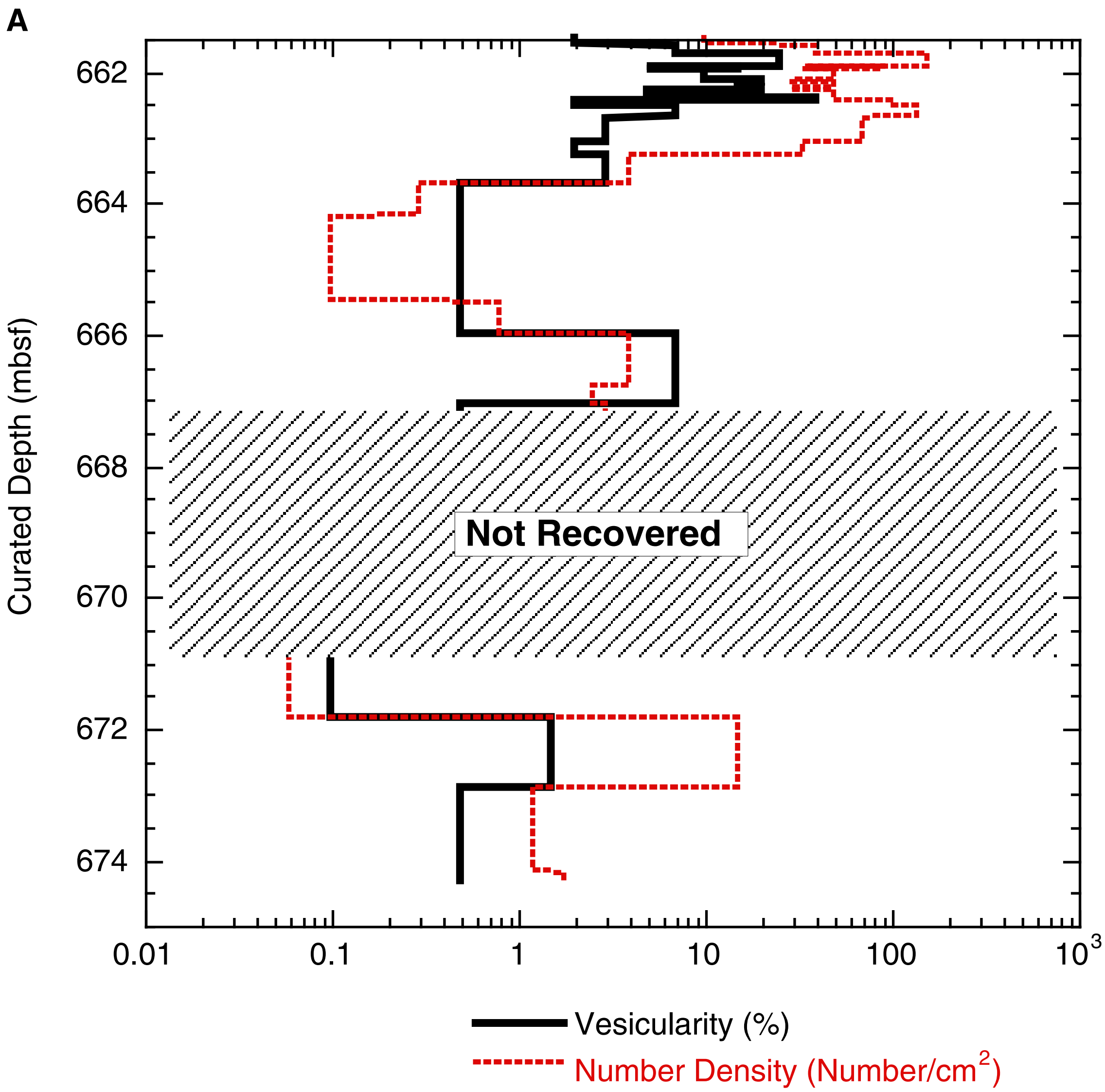

Figure F39 (continued). B. Vesicle size as a function of depth within basement Unit 18.

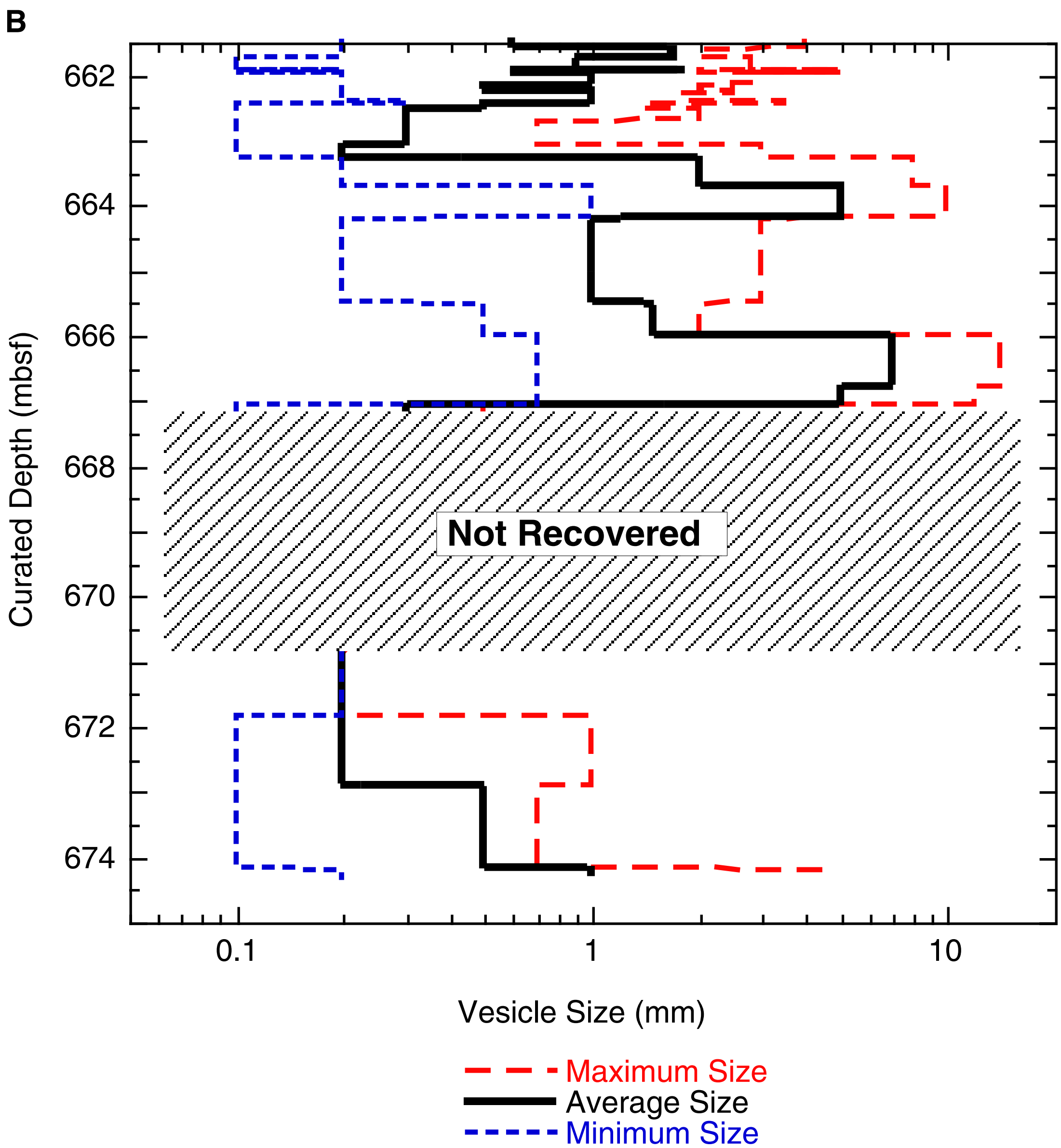

Figure F40. Close-up photograph of interval 183-1139A-70R-1, 45–55 cm, showing morphology of breccia at the top of basement Unit 18.

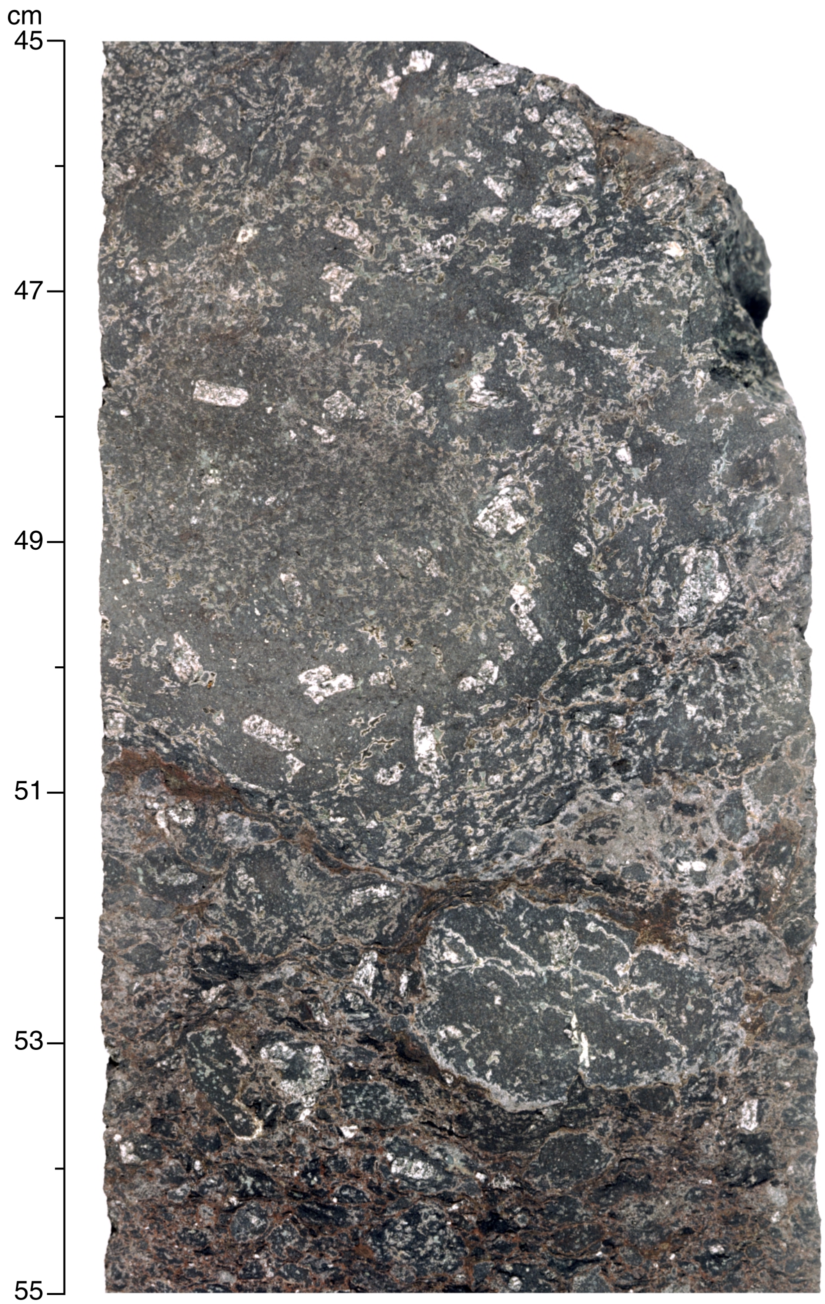

Figure F41. Close-up photograph of interval 183-1139A-71R-3, 56–68 cm, showing a brecciated shear zone in the lower part of basement Unit 18.

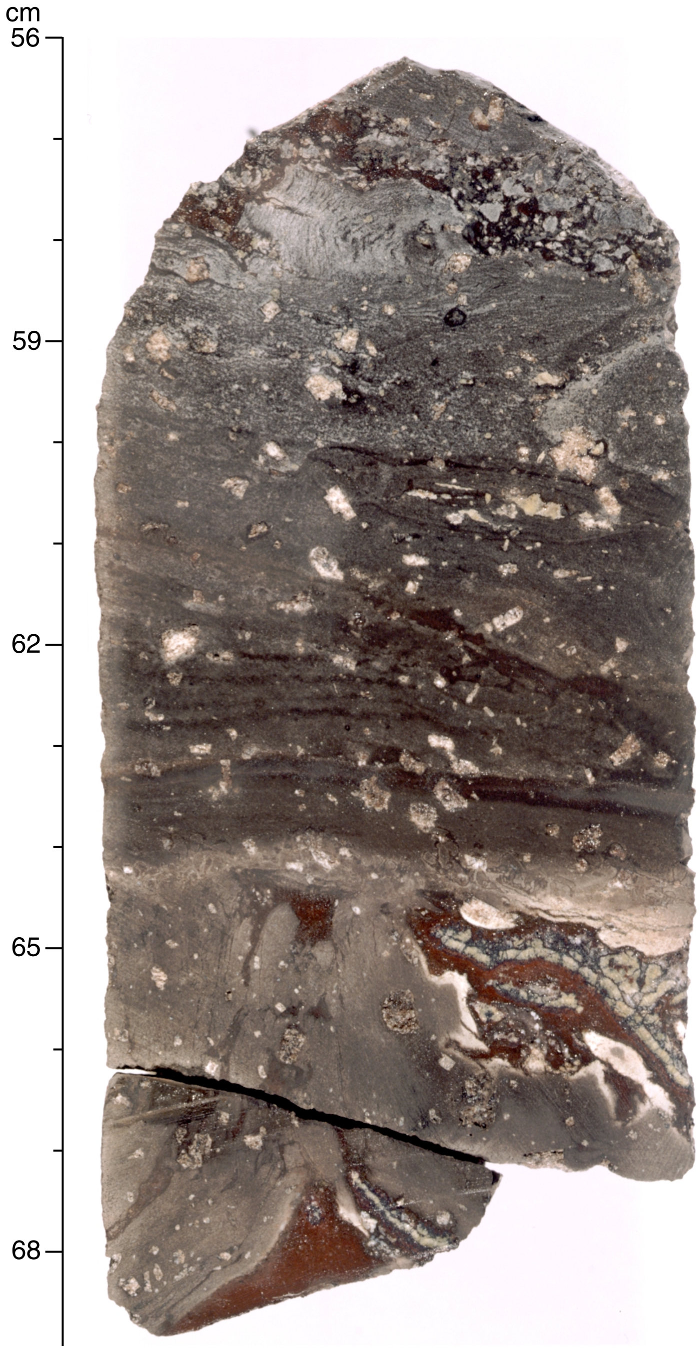

Figure F42. Close-up photograph of interval 183-1139A-71R-3, 118–128 cm, showing a breccia at the base of basement Unit 18, interpreted to be a welded and sheared basal breccia for this flow.

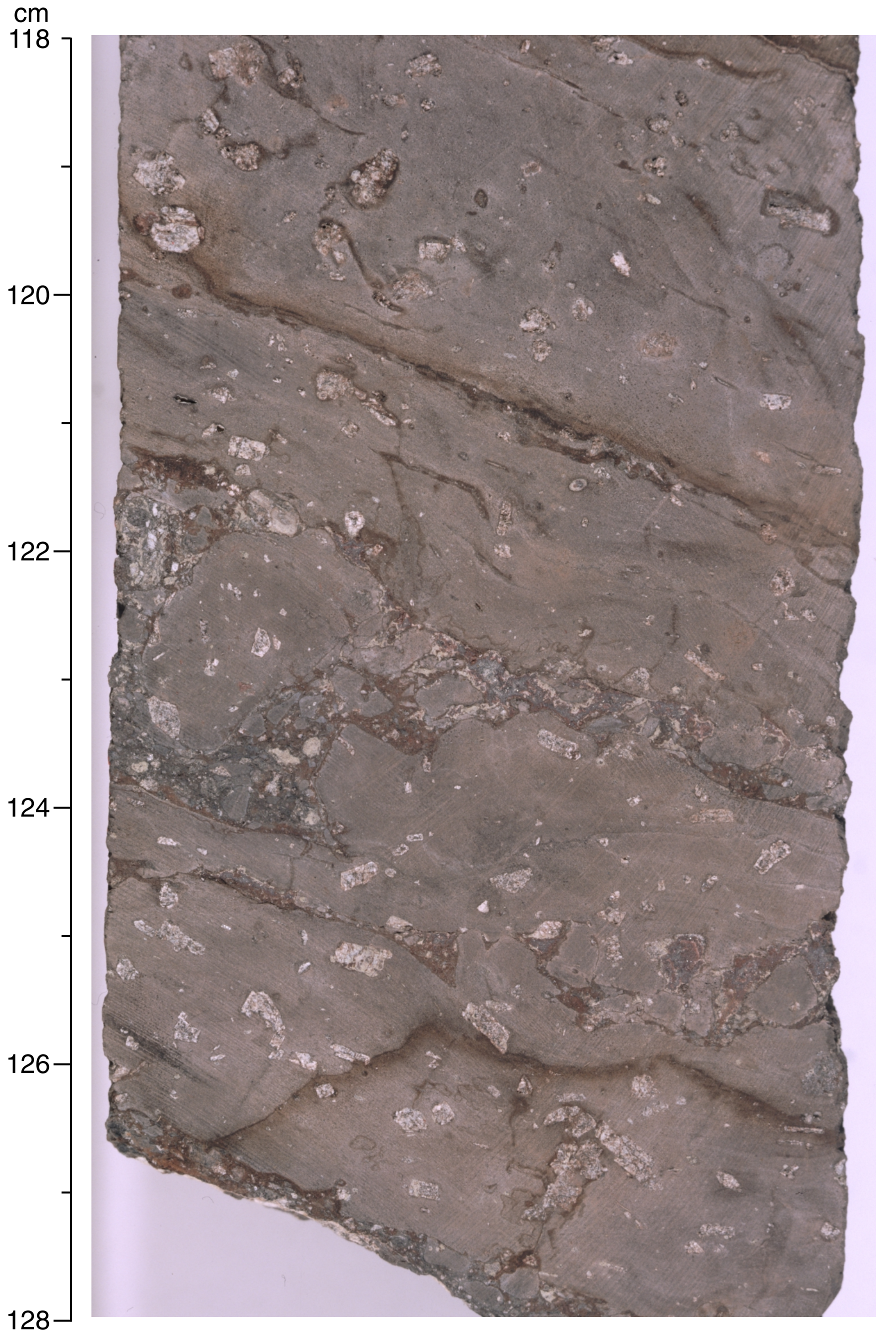

Figure F43. Close-up photograph of interval 183-1139A-72R-1, 15–25 cm, showing a lithic clast within the coherent interior of basement Unit 19.

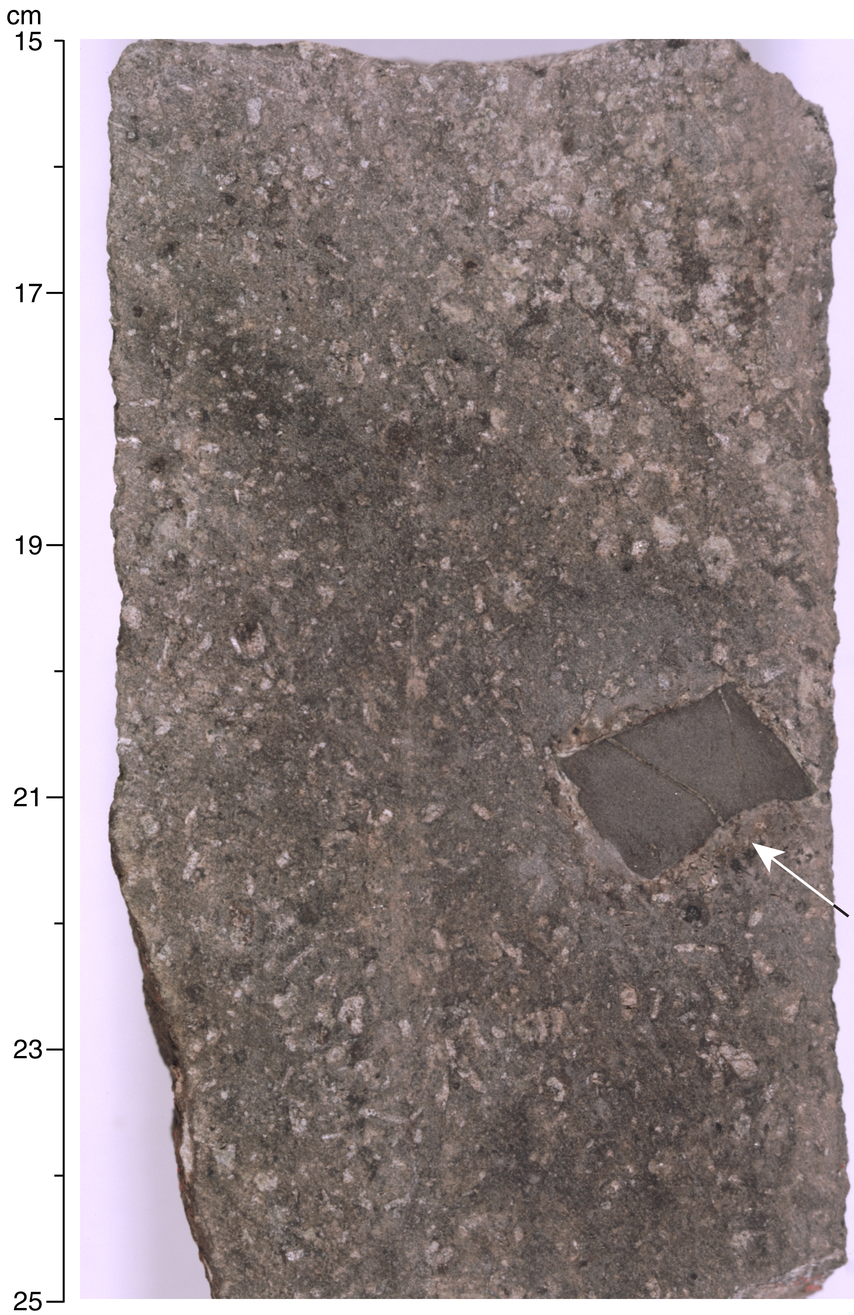

Figure F44. The interpretative summary diagram for Site 1139 shows the 19 igneous units that range from basalt to rhyolite and from bioclastic sandstone to volcaniclastic breccia. In general, the primary vesicularity of the lava flows and marginal breccias is obscured by the effects of alteration. Sanidine xenocrysts are distributed throughout the more mafic flows. Although changes in K concentration from downhole natural-gamma measurements correlate generally with the defined igneous units, the logging data show more complexity indicating unrecovered changes in lithology.

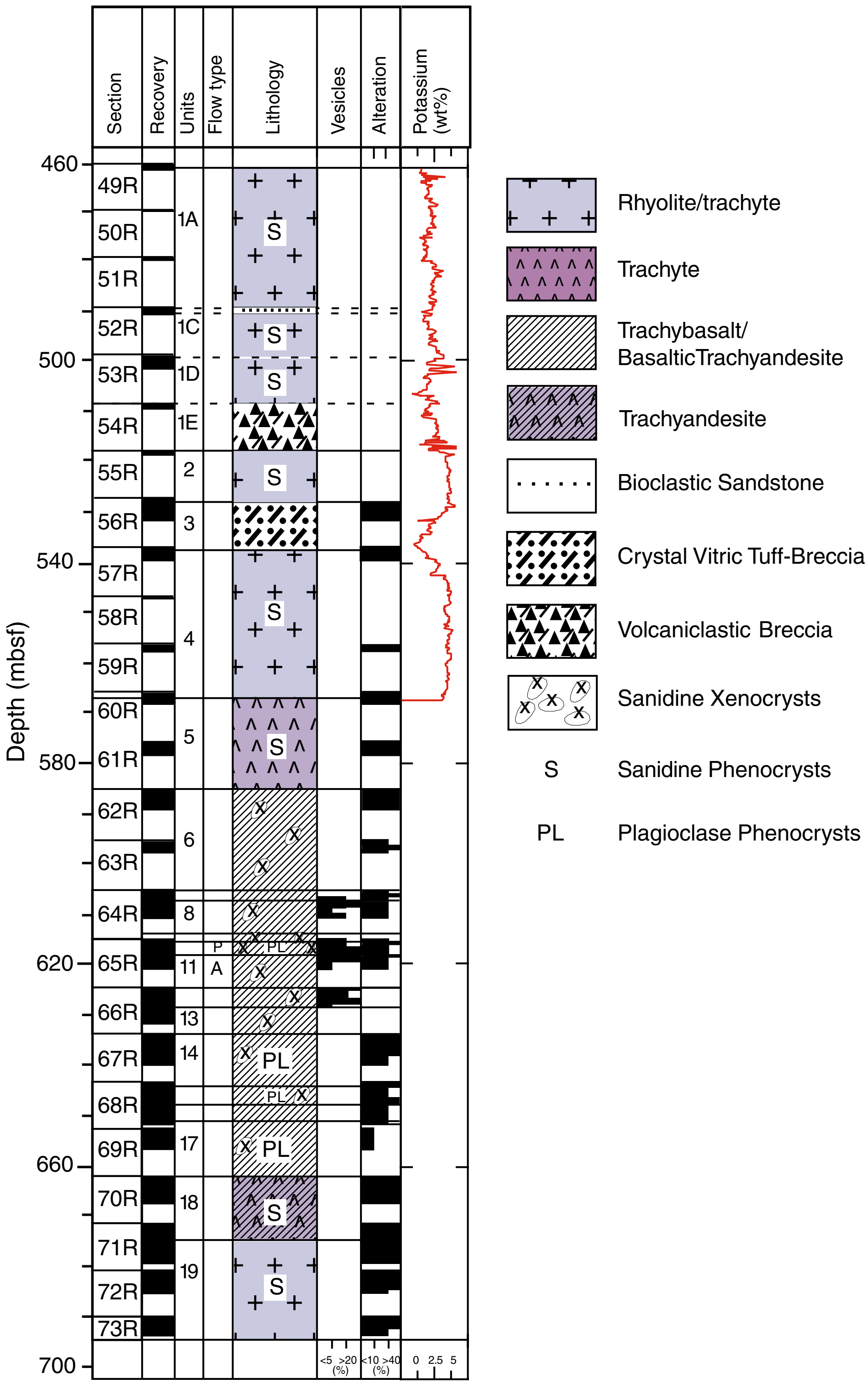

Figure F45. A. Photomicrograph from Unit 2 in Sample 183-1139A-56R-1, 37–40 cm (in plane-polarized light), showing sanidine phenocrysts in an altered feldspathic, trachytic groundmass. **B.** Photomicrograph of sanidine and quartz phenocrysts at the top of Unit 4 from Sample 183-1139A-57R-1, 120–123 cm (in cross-polarized light).

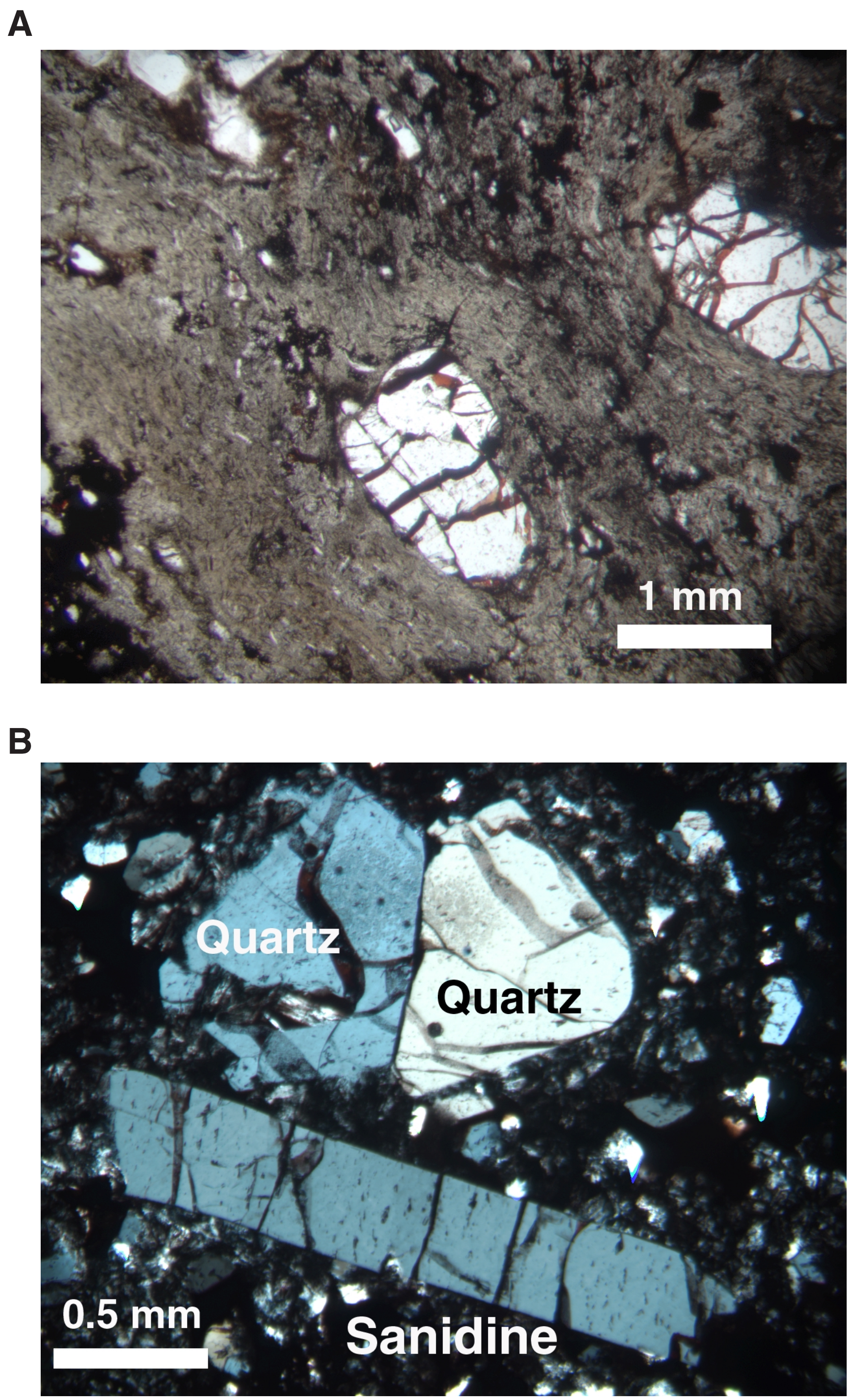

Figure F46. Photomicrograph of sanidine phenocrysts in a perlitic glassy groundmass (Unit 3) in Sample 183-1139A-56R-3, 93–97 cm (in cross-polarized light).

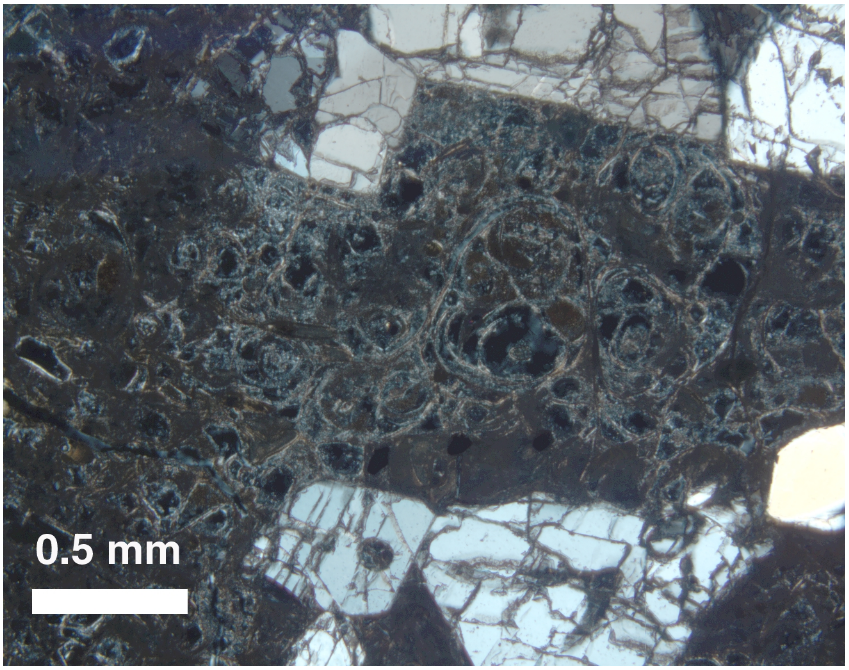

Figure F47. Photomicrographs (both in plane-polarized light) of sanidine and altered mafic (probably clinopyroxene) phenocrysts, the latter now replaced by siderite, (**A**) from the top of Unit 5 in Sample 183-1139A-60R-2, 100–104 cm, and (**B**) from the middle of Unit 5 in Sample 183-1139A-61R-1, 74–76 cm.

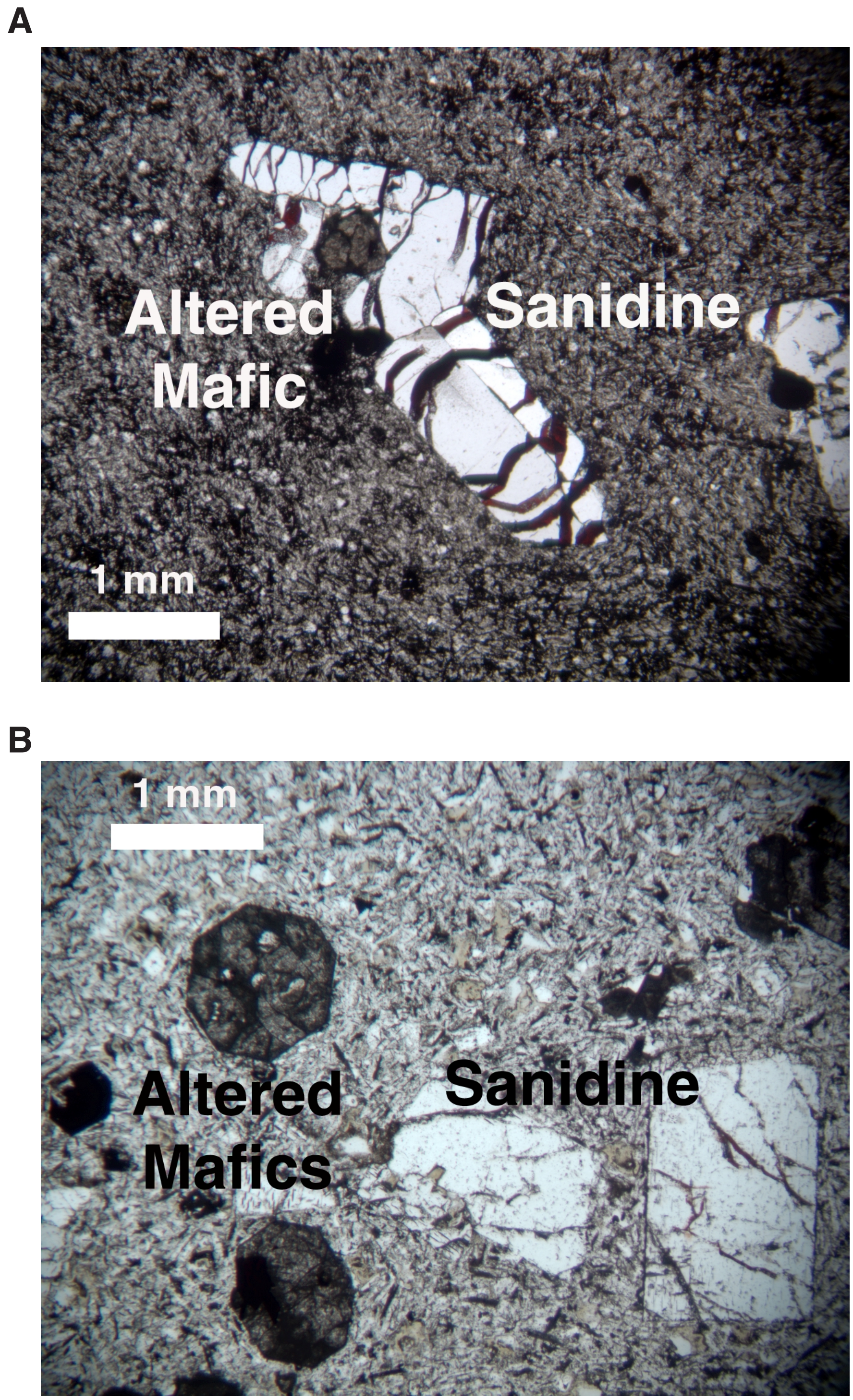

Figure F48. Photomicrographs (both in cross-polarized light) representing two different views of a sanidine-rich sandy layer at the top of Unit 7 in Sample 183-1139A-64R-1, 38–43 cm. **A.** Relatively matrix-rich area. **B.** Illustration of the clast-rich nature of the sandy layer.

A

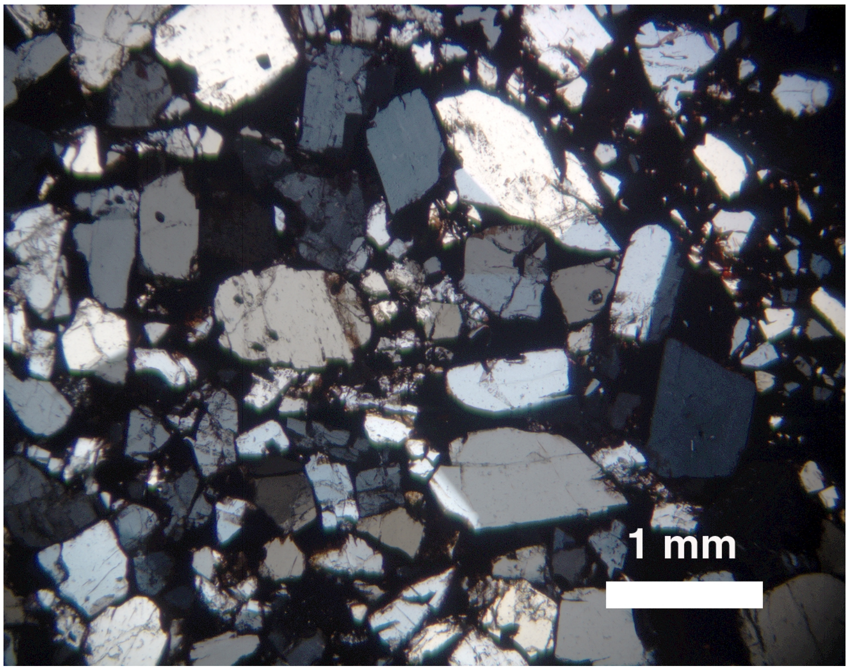

B

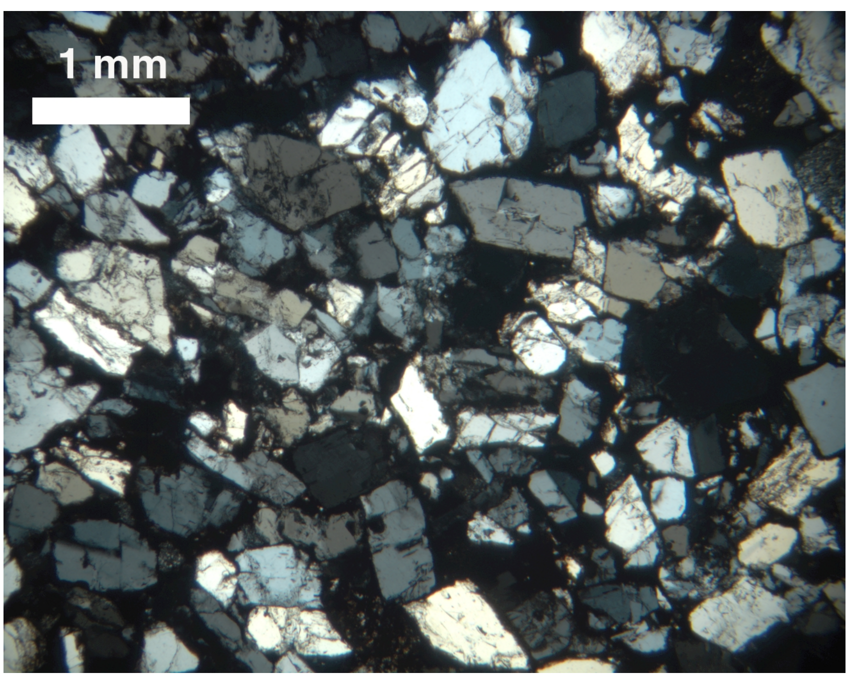

Figure F49. Photomicrograph (in cross-polarized light) of a plagioclase microphenocryst in Unit 14 slightly affected by the pervasive secondary alteration of the groundmass (Sample 183-1139A-67R-5, 100–103 cm).

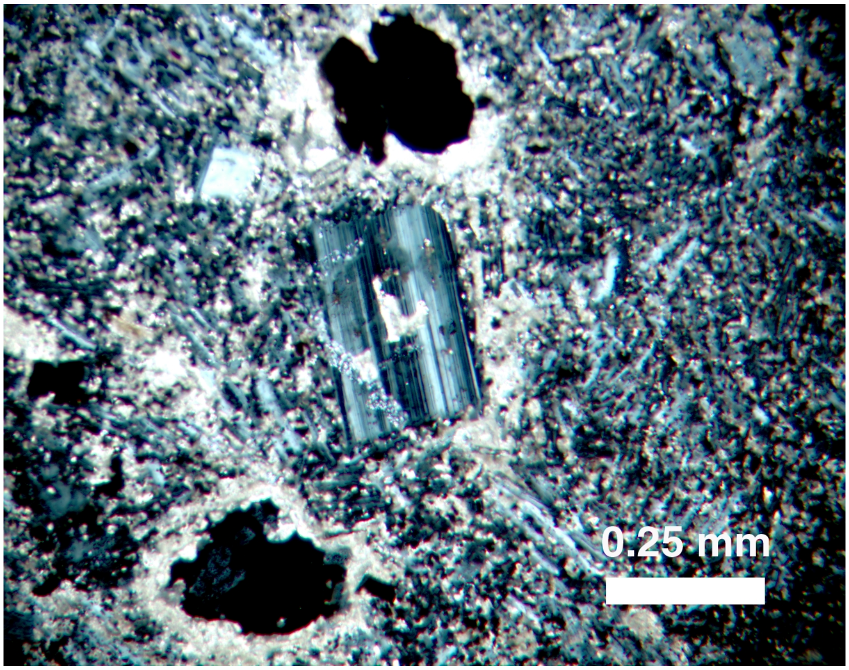

Figure F50. Photomicrographs (both in cross-polarized light) showing sanidine xenocrysts (in various degrees of preservation), which are characteristic of basaltic Units 6–17. **A.** A sanidine xenocryst with a developing sieve texture around the rim (Sample 183-1139A-64R-1, 81–84 cm; Unit 7); a plagioclase phenocryst (fractured by later secondary alteration) is also shown. **B.** A highly resorbed sanidine xenocryst from Unit 13 (Sample 183-1139A-66R-7, 5–8 cm).

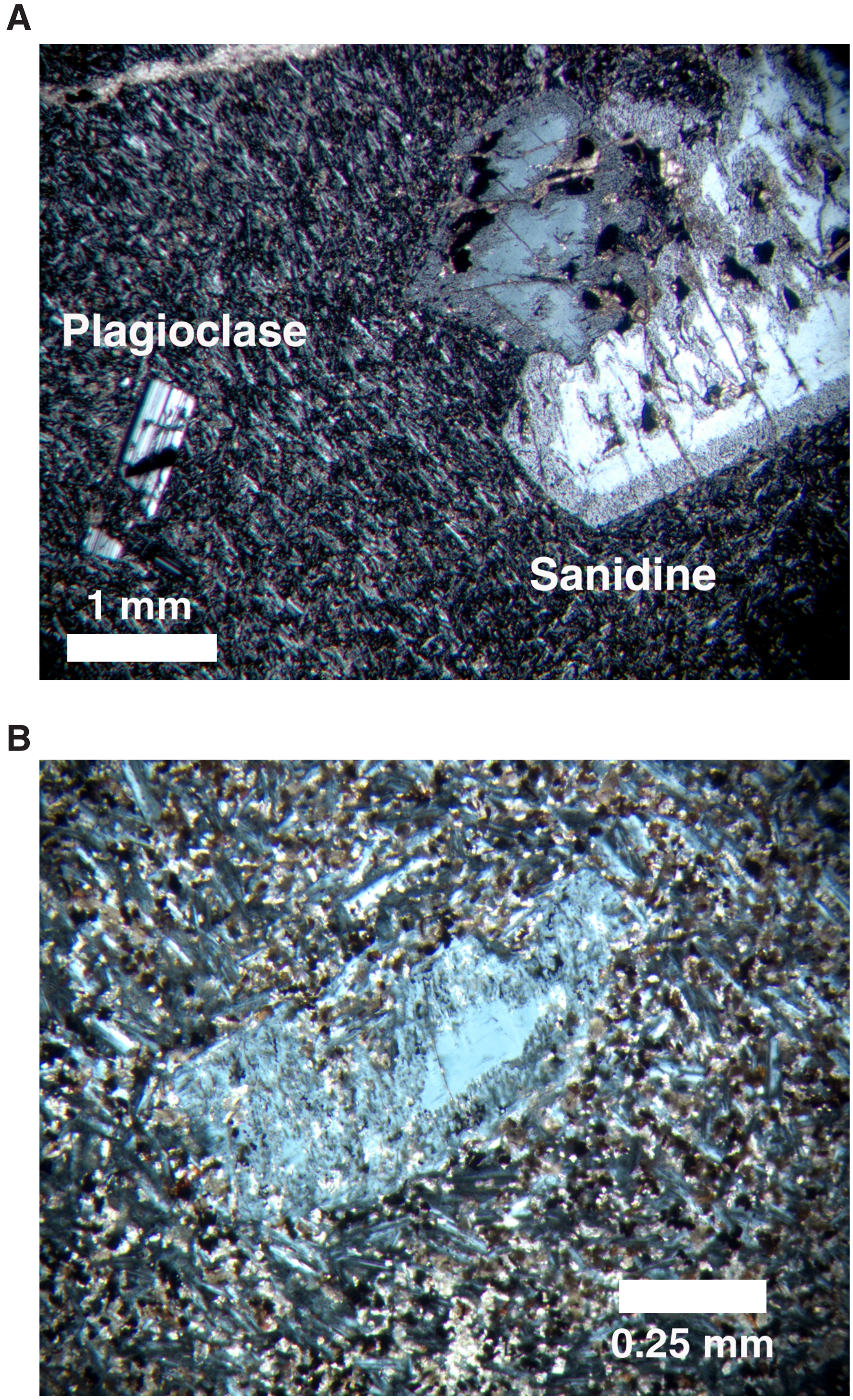

Figure F51. Photomicrograph (in reflected light) of a partially altered titanomagnetite from Unit 16 in Sample 183-1139A-68R-6, 54–57 cm.

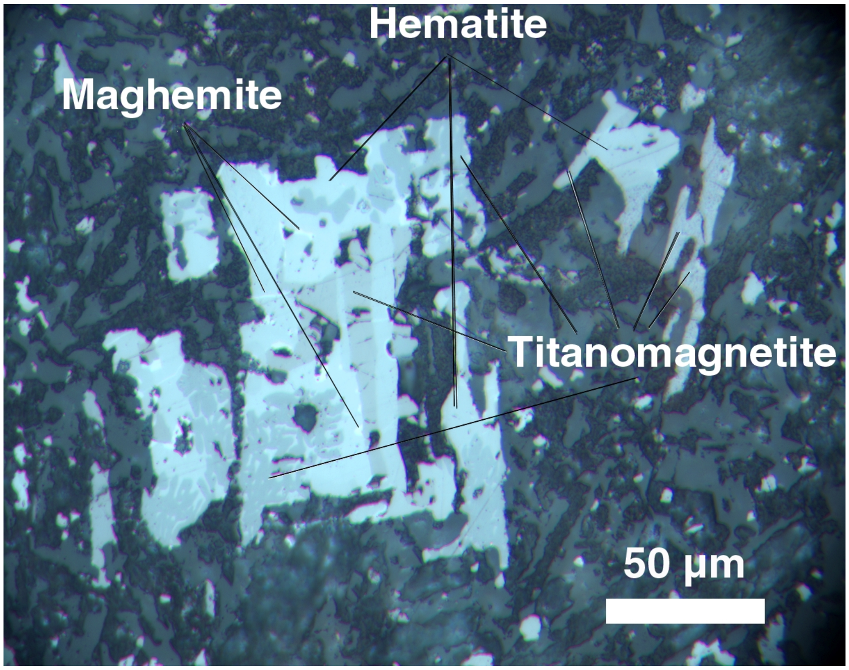

Figure F52. Photomicrographs (both in cross-polarized light) depicting an apparent alkali feldspar phenocryst from Unit 10 in Sample 183-1139A-65R-3, 16–18 cm. **A.** A large feldspar phenocryst, displaying only Carlsbad twinning, that is altered along fractures. Box A is the area shown in part B of this figure. Box B highlights another feldspar crystal in the groundmass that also only displays Carlsbad twinning, but the twin plane is more diffuse. This is interpreted to represent secondary alteration of plagioclase to alkali feldspar. **B.** A close-up of the base of the phenocryst in (A) showing zonation that has inhibited the development of characteristic albite twinning.

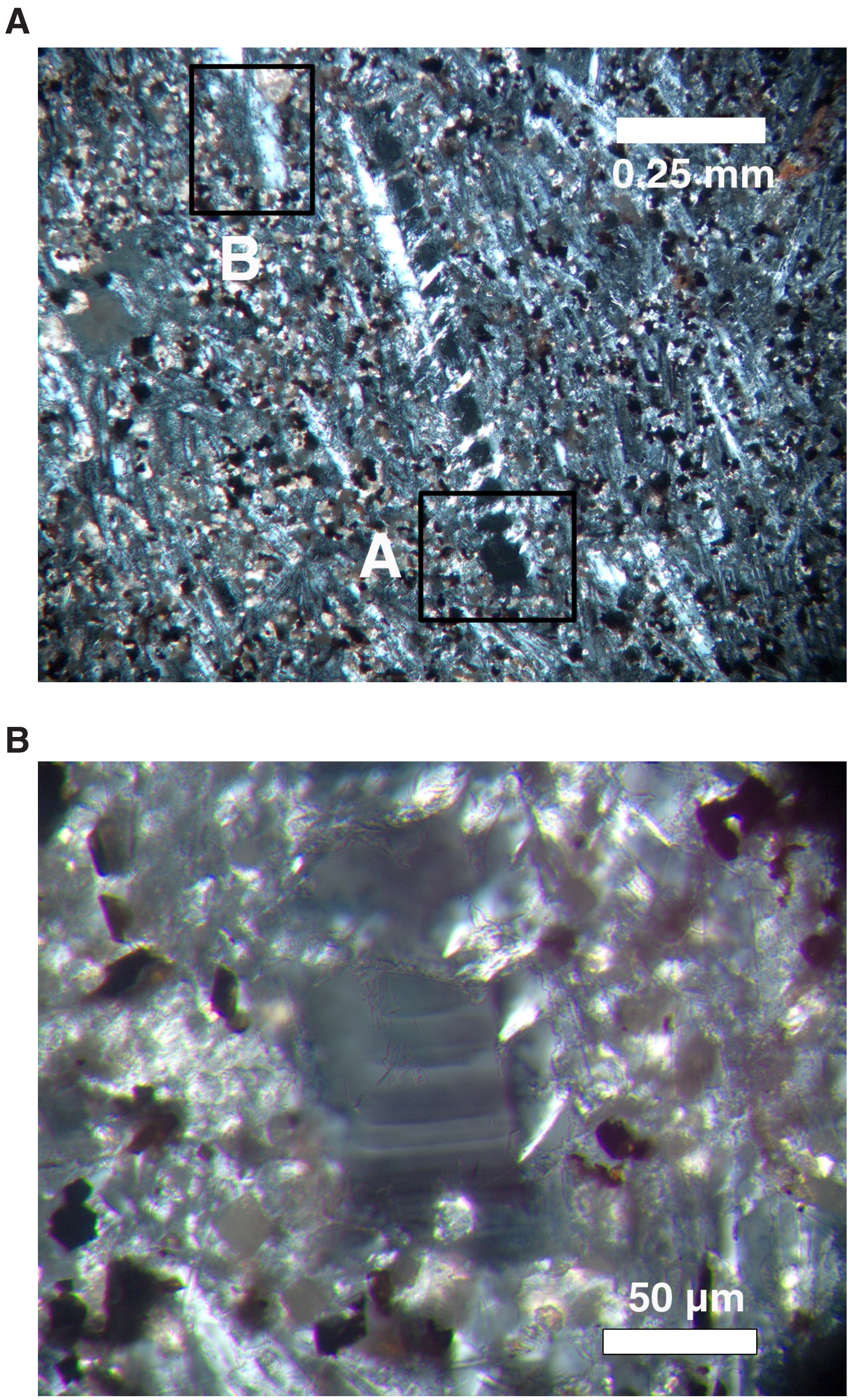

Figure F53. Photomicrograph (in cross-polarized light) of a sanidine phenocryst from the Unit 18 trachyte in Sample 183-1139A-71R-1, 0–6 cm. Note that this phenocryst is more euhedral and lacks the reaction textures displayed by sanidine xenocrysts in the trachybasalts.

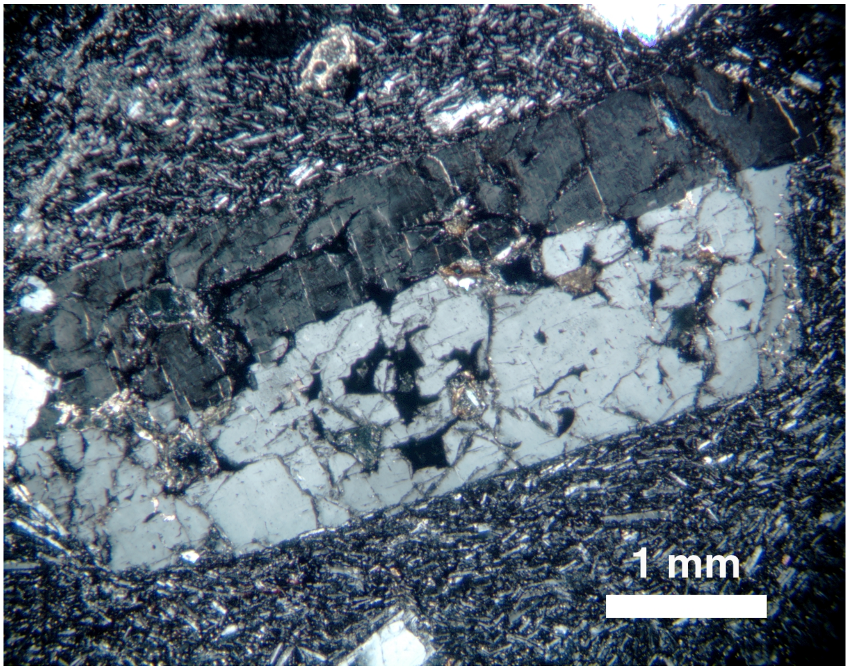

Figure F54. A. Color close-up of interval 183-1139A-71R-3, 56–69 cm (where the surface has been wetted to accentuate the primary igneous and secondary alteration features). Sanidine phenocrysts in Unit 18 have survived the intense alteration that has affected this flow. (Continued on next page.)

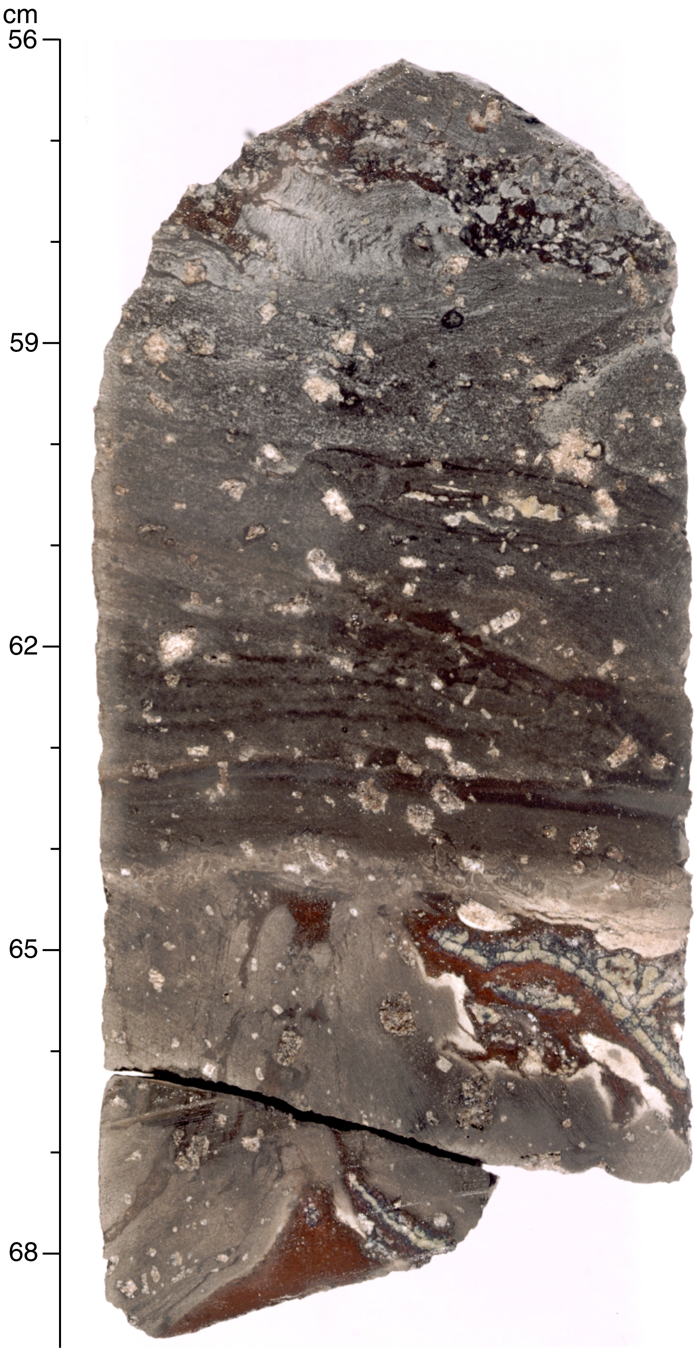

Figure F54 (continued). B. Color close-up of interval 183-1139A-72R-1, 15–25 cm. Sanidine phenocrysts of Unit 19 have also survived intense alteration. Note the change in phenocryst size from Unit 18 to 19.

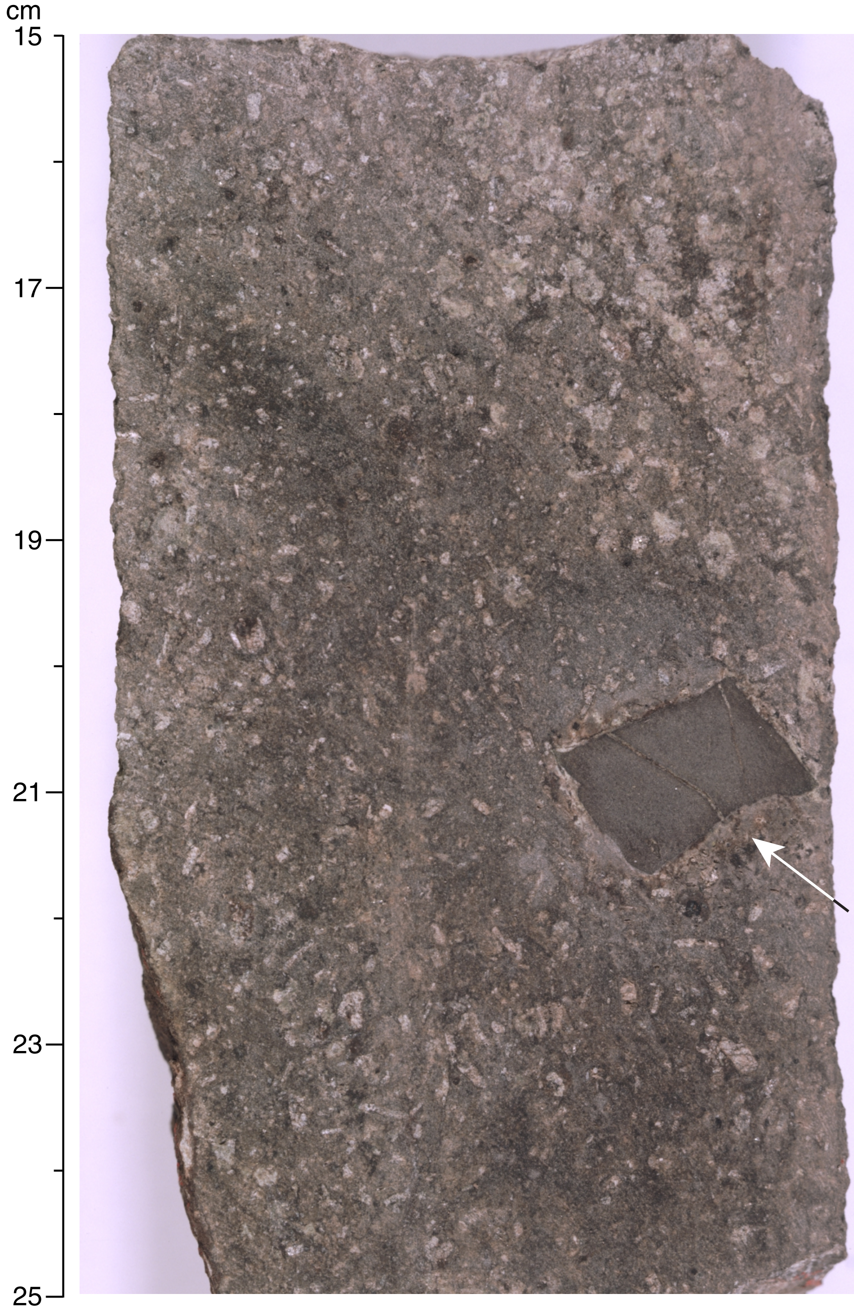

Figure F55. Photomicrographs (both in plane-polarized light) of altered mafic phenocrysts (probably clinopyroxene). **A.** Trachyandesite of Unit 18 (Sample 183-1139A-71R-1, 0–6 cm). **B.** Trachyte of Unit 19 (Sample 183-1139A-73R-3, 37–39 cm).

A

B

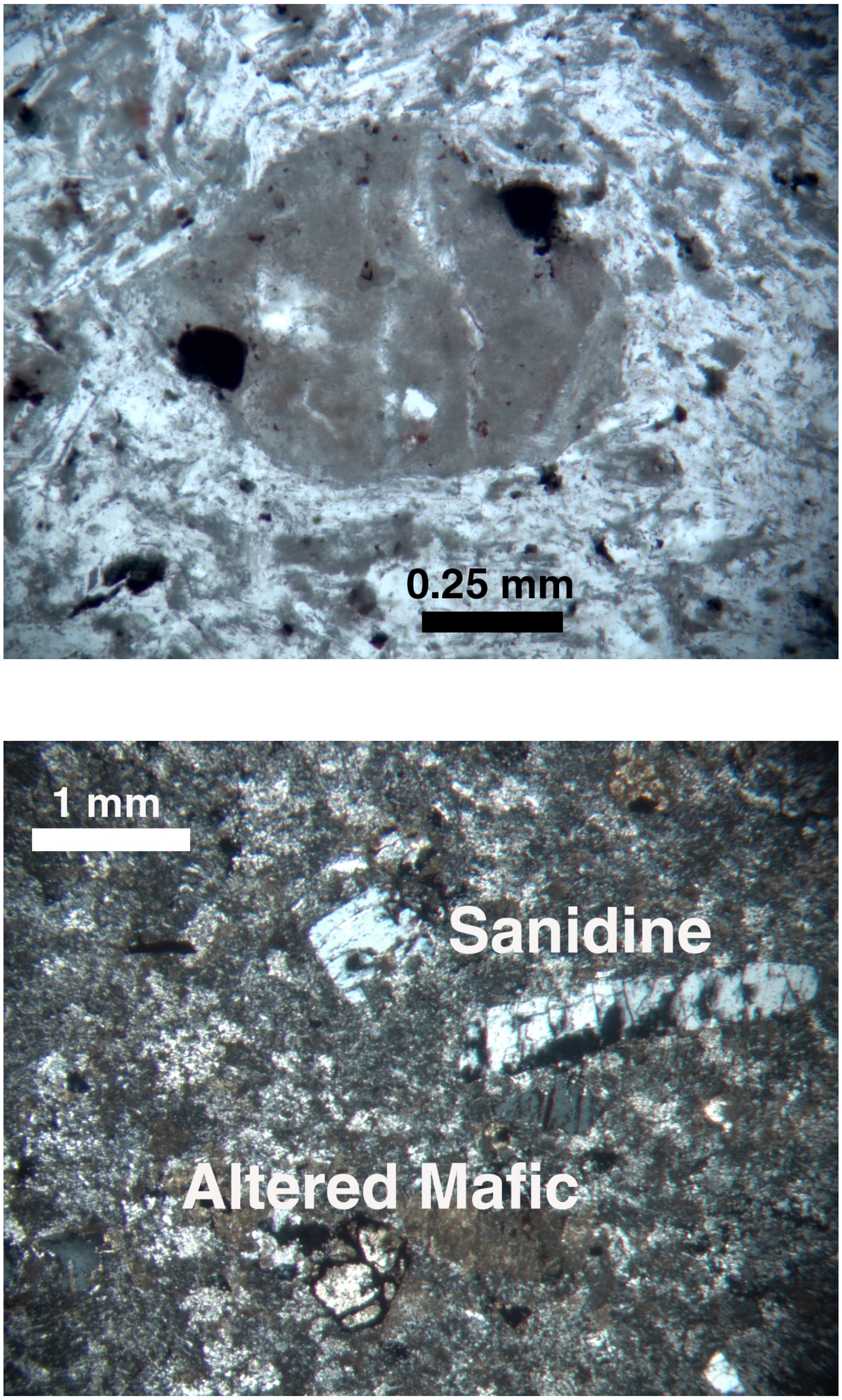

Figure F56. Photomicrograph (in cross-polarized light) highlighting the extreme veining evident in Unit 19 in Sample 183-1139A-71R-4, 134–135 cm. Veining is so intense that the rock has a brecciated appearance (Core 183-1139A-8R).

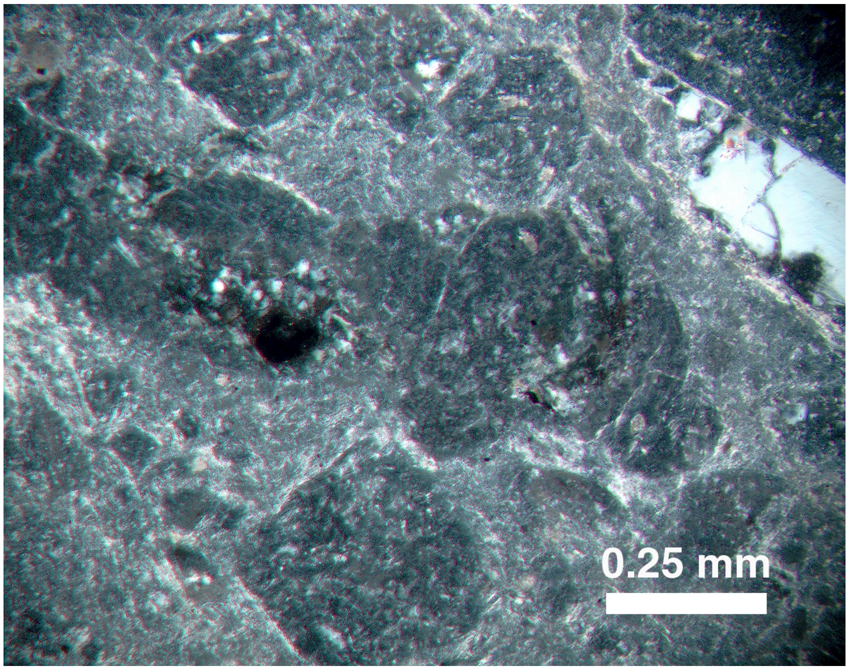

Figure F57. Photomicrographs demonstrating the trachytic texture still evident from Unit 18 in Sample 183-1139A-71R-1, 0–6 cm. Both views are of the same area with (**A**) in plane-polarized light and (**B**) in cross-polarized light.

A

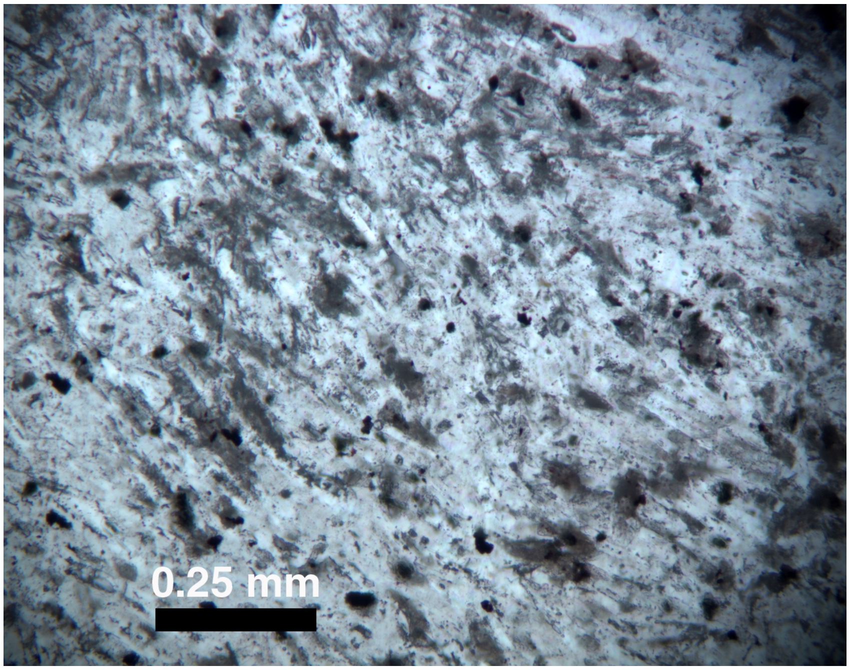

B

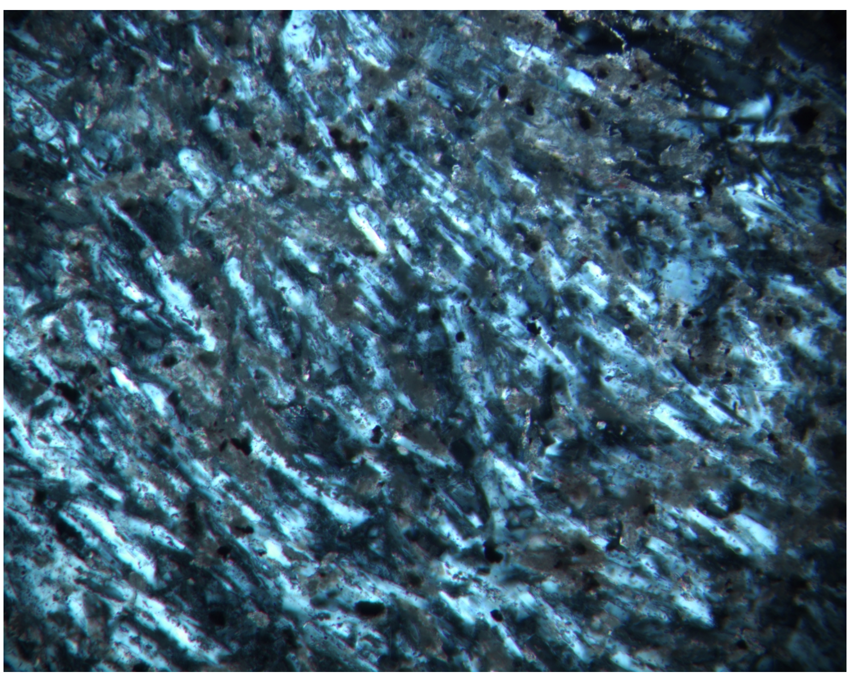

Figure F58. Photomicrographs (both in plane-polarized light) of the recrystallized mesostasis from Unit 18 in Sample 183-1139A-70R-1, 17–20 cm. (**A**) and (**B**) are different areas within the thin section.

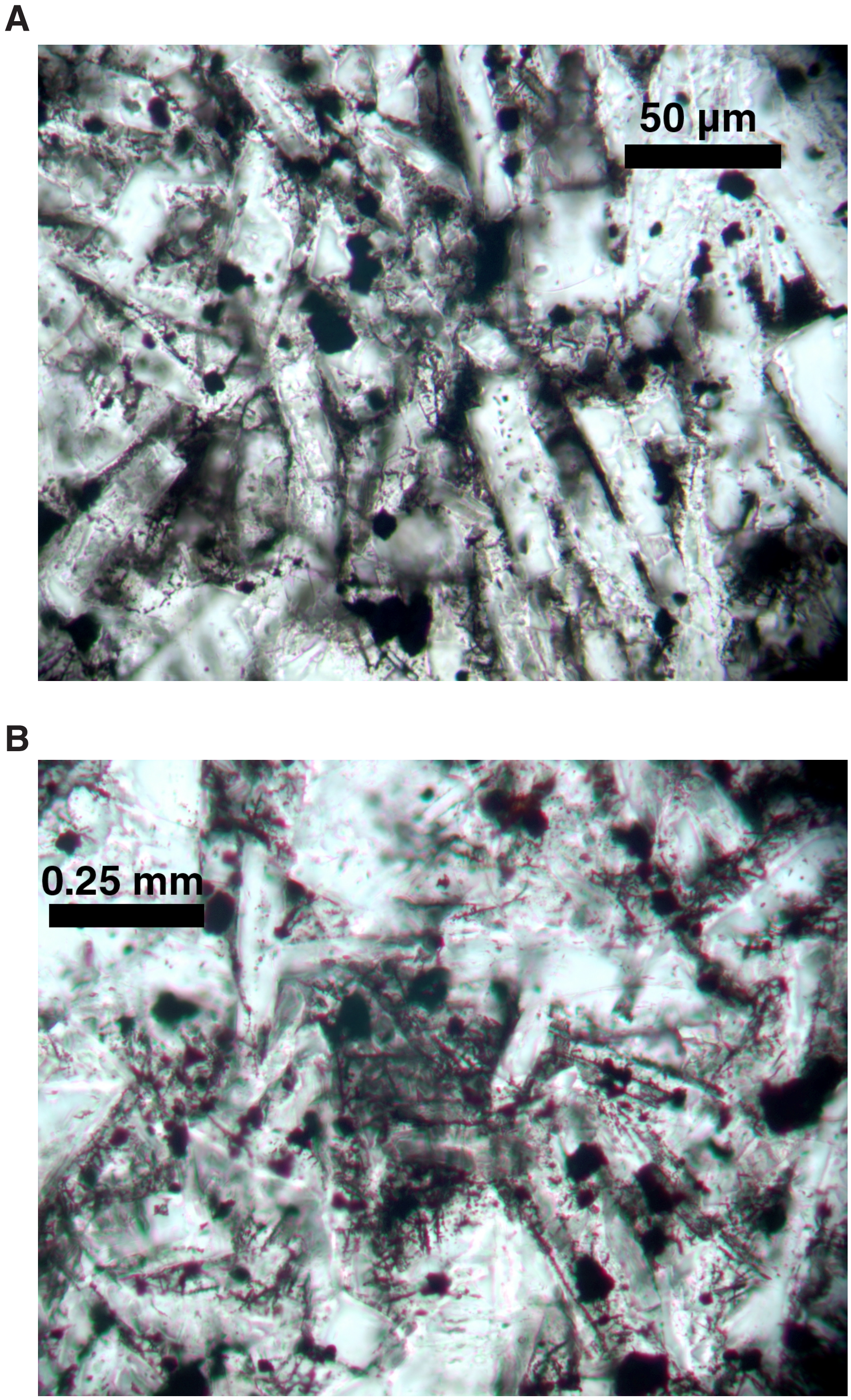

Figure F59. Photomicrograph (in cross-polarized light) of the recrystallized groundmass from Unit 19 in Sample 183-1139A-3R-3, 37–39 cm. The rock has a mottled appearance. See **"Alteration and Weathering," p. 42**. A relatively fresh sanidine phenocryst is present.

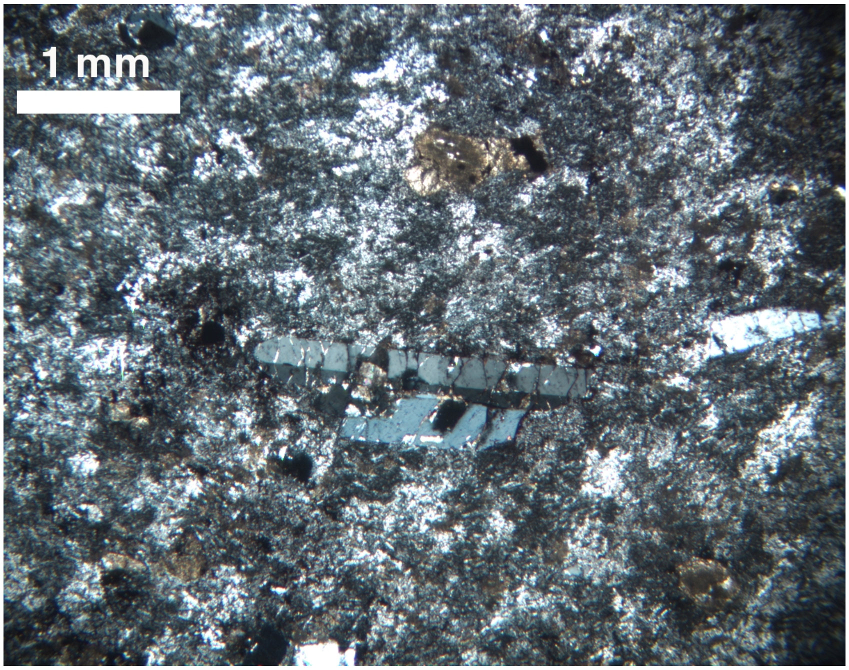

Figure F60. A. Site 1139 igneous rock compositions on the $Na_2O + K_2O$ vs. SiO_2 classification diagram (Le Bas et al., 1986); alkalic and tholeiitic basalt fields are distinguished by the Macdonald-Katsura (1964) line. Note that there is one chemical analysis per igneous unit except for Units 5, 18, and 19 from which two, two, and four samples, respectively, were analyzed. The least-altered Unit 18 and 19 samples are marked in bold, and other samples from these units show considerable spread caused by alteration. **B.** Site 1139 mafic compositions compared to samples from Kerguelen Plateau Sites 1136, 1137, and 1138. The fields represent data from previous dredging and drilling on the southern and central Kerguelen Plateau (Sites 738, 747, 749, 750, and dredge locations reported by Weis et al., 1989). Data sources are Davies et al. (1989), Alibert (1991), Mehl et al. (1991), Salters et al. (1992), Storey et al. (1992), Mahoney et al. (1995), and this study.

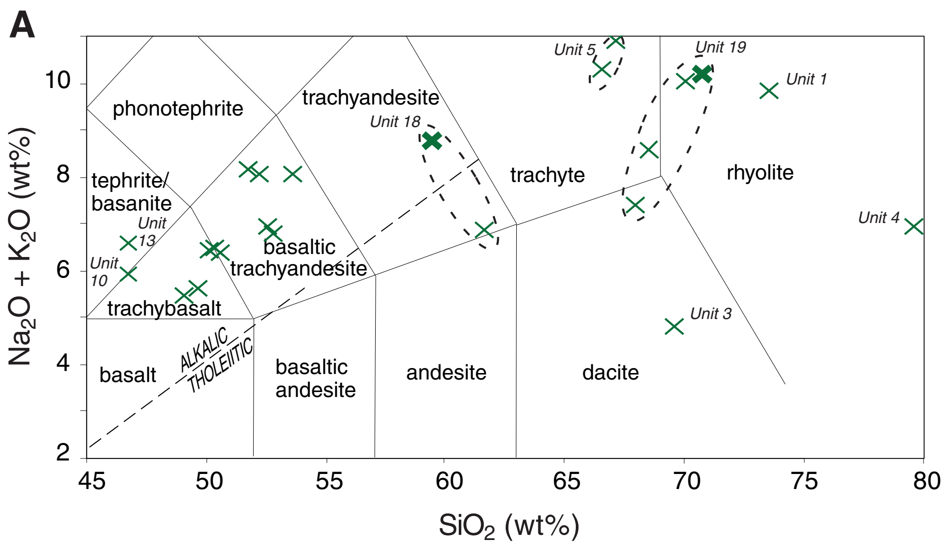

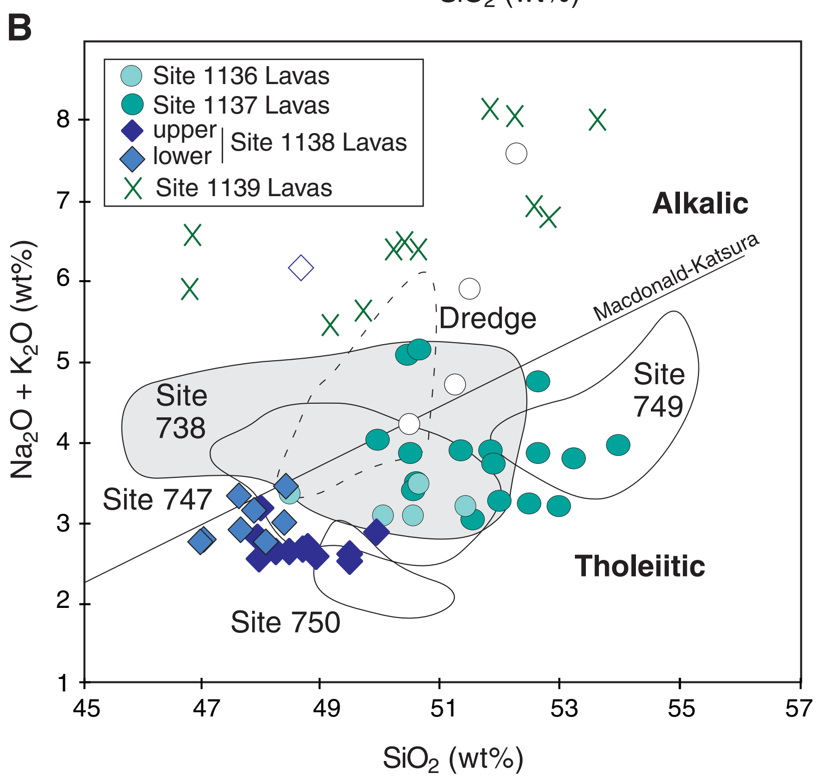

Figure F61. Downhole variations in CO_2 and H_2O for Site 1139 igneous rock compositions.

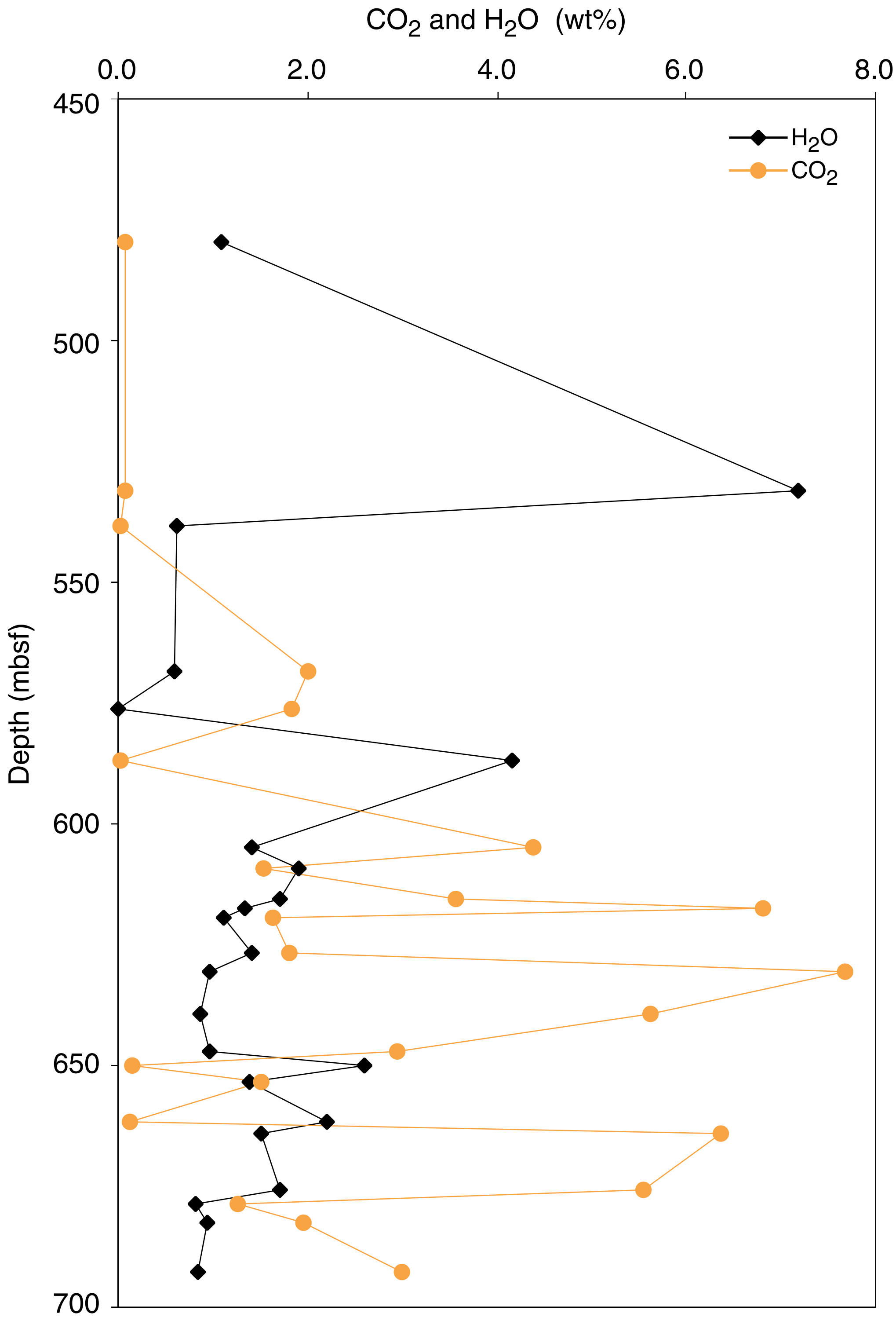

Figure F62. Compositions of four samples from Unit 19 arranged in order (left to right) of increasing alteration as observed petrographically. Loss on ignition data were incorporated into the sample analyses by renormalizing to 100 wt% totals.

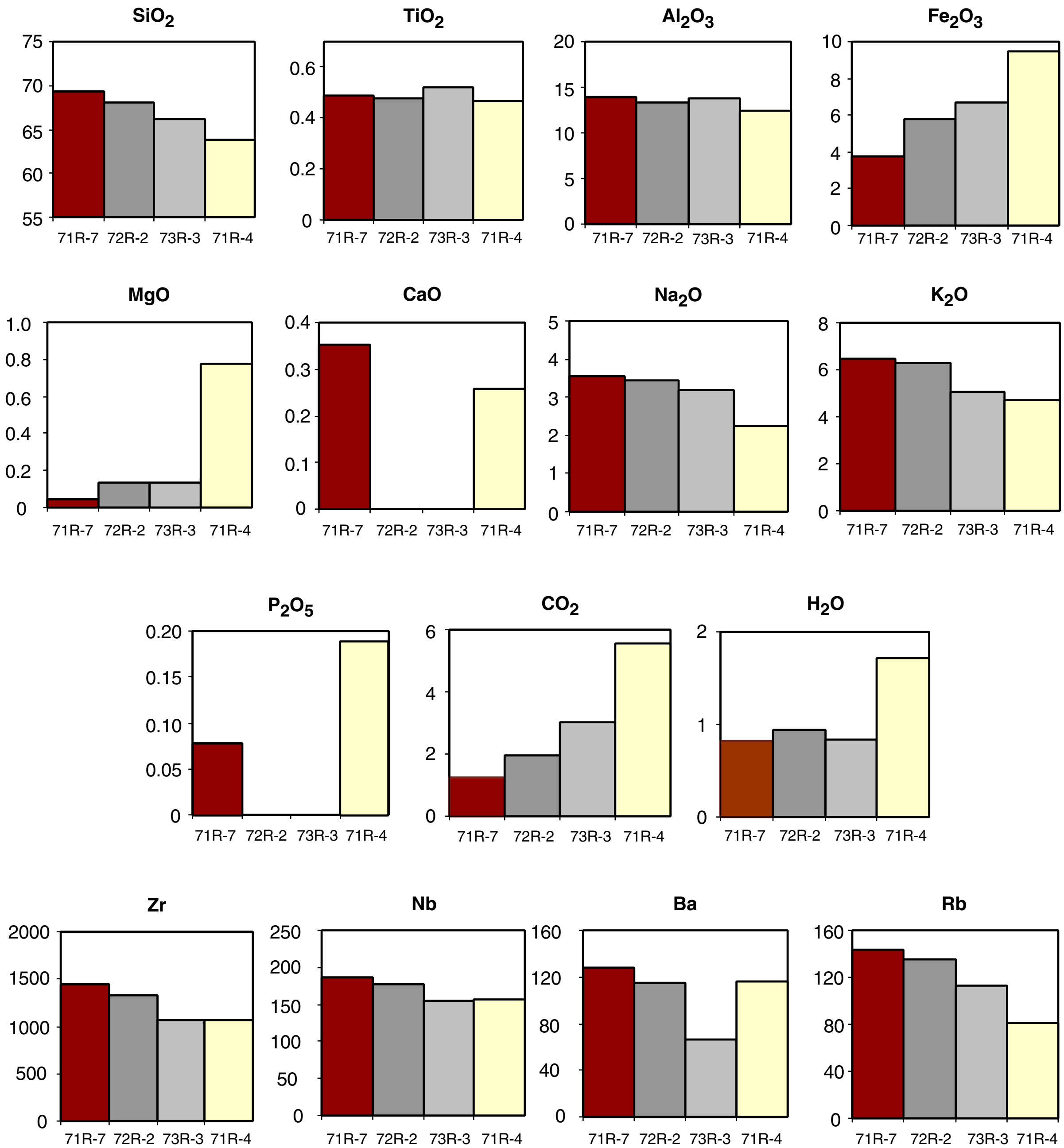

Figure F63. Site 1139 lavas and all other samples drilled from Kerguelen Plateau basement. Site 1139 lavas generally have lower MgO and the trachybasalts have higher TiO_2, Nb, and Zr than previously observed in plateau lavas. Large X symbol = trachybasalt and trachyandesite. Small x symbol = rhystite, trachyte, and trachyandesite. For data sources see Figure F60, p. 130.

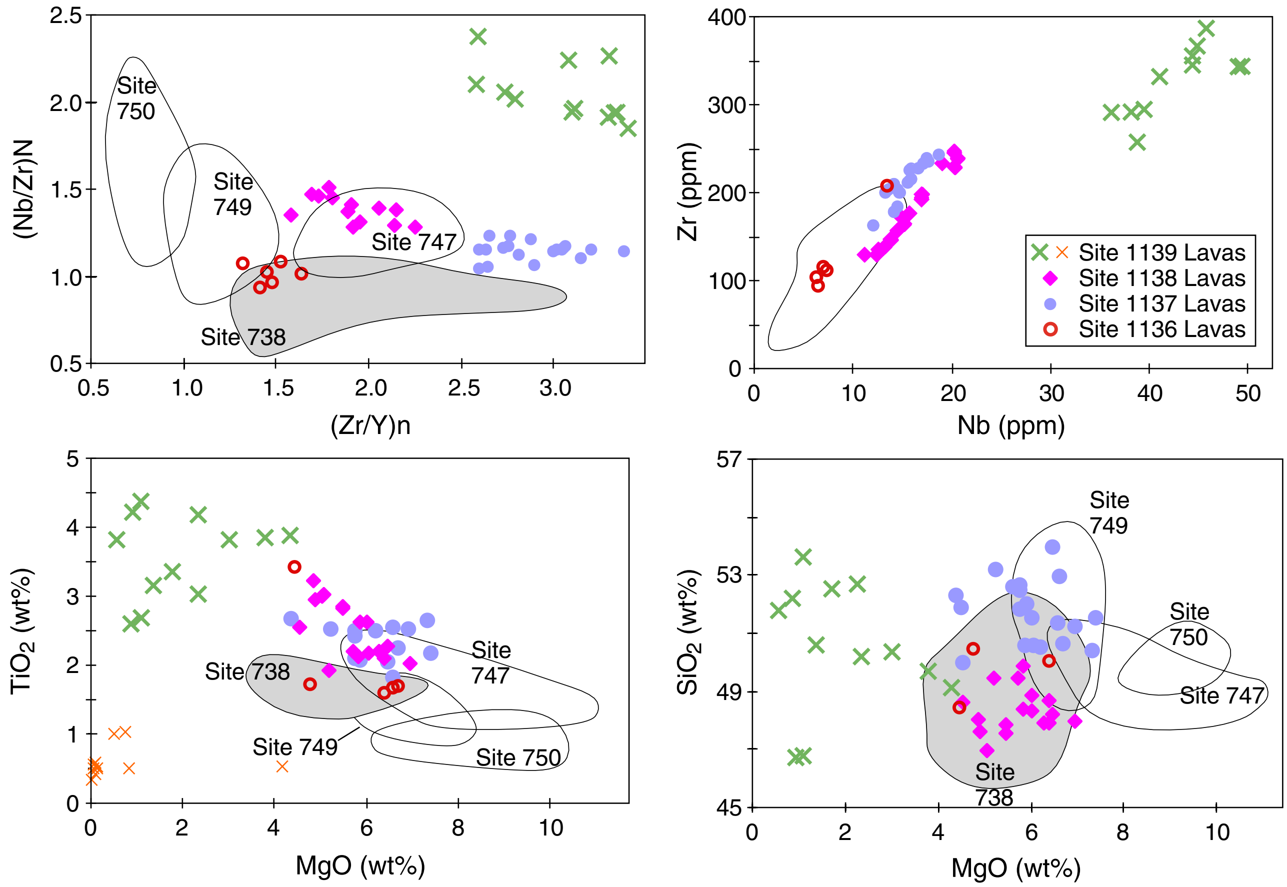

Figure F64. Downhole variations in selected major and trace elements (MgO, SiO_2, TiO_2, Nb, and Al_2O_3) and LOI for Site 1139 igneous rocks. Units 1–5 are rhyolite and trachyte, Units 6–17 are trachybasalt to basaltic trachyandesite, Unit 18 is a trachyandesite, and Unit 19 is a trachyte.

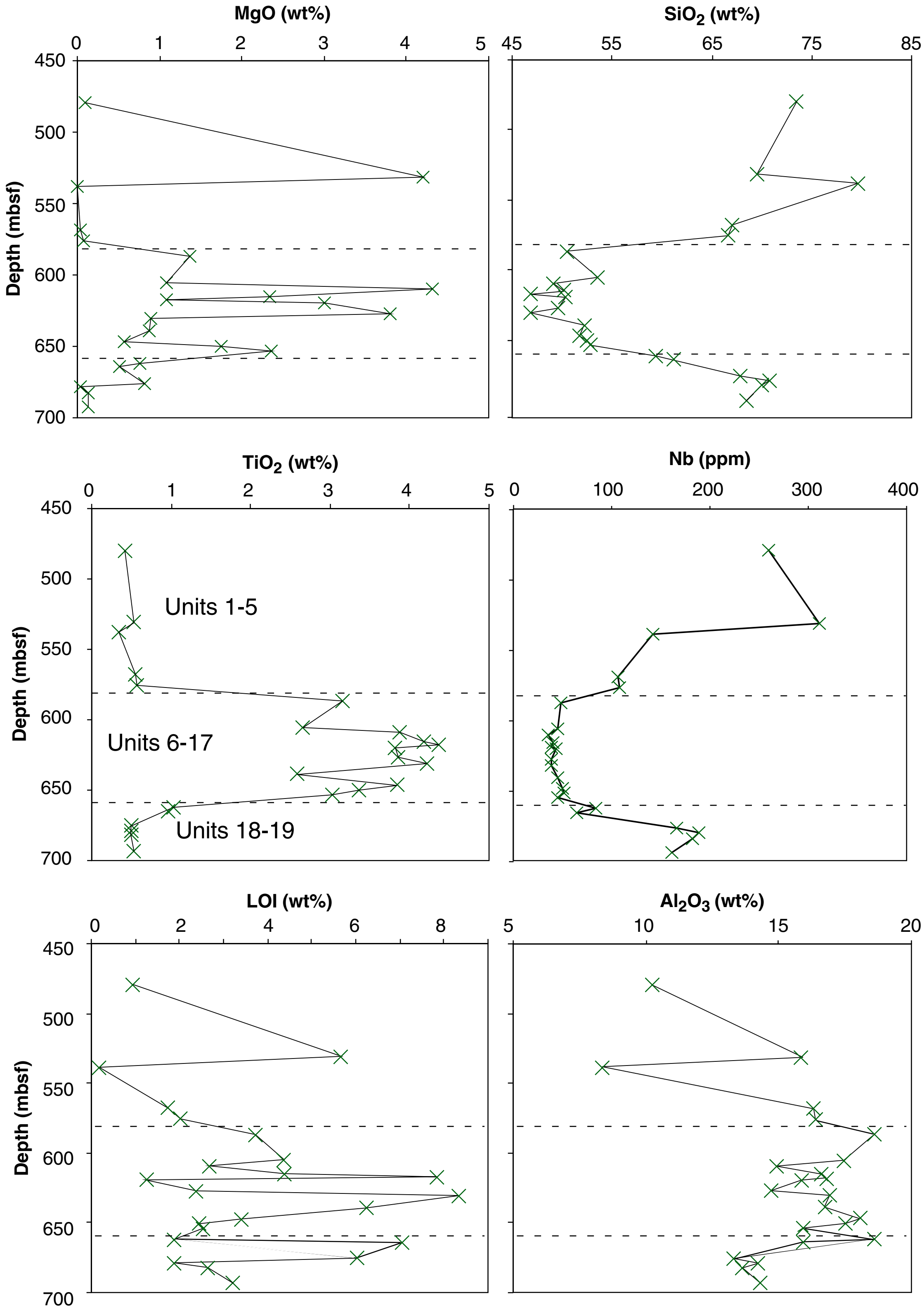

Figure F65. Primitive mantle–normalized (Sun and McDonough, 1989) incompatible trace element diagrams for Site 1139 igneous rocks. **A.** Mafic series. (Continued on next page.)

A

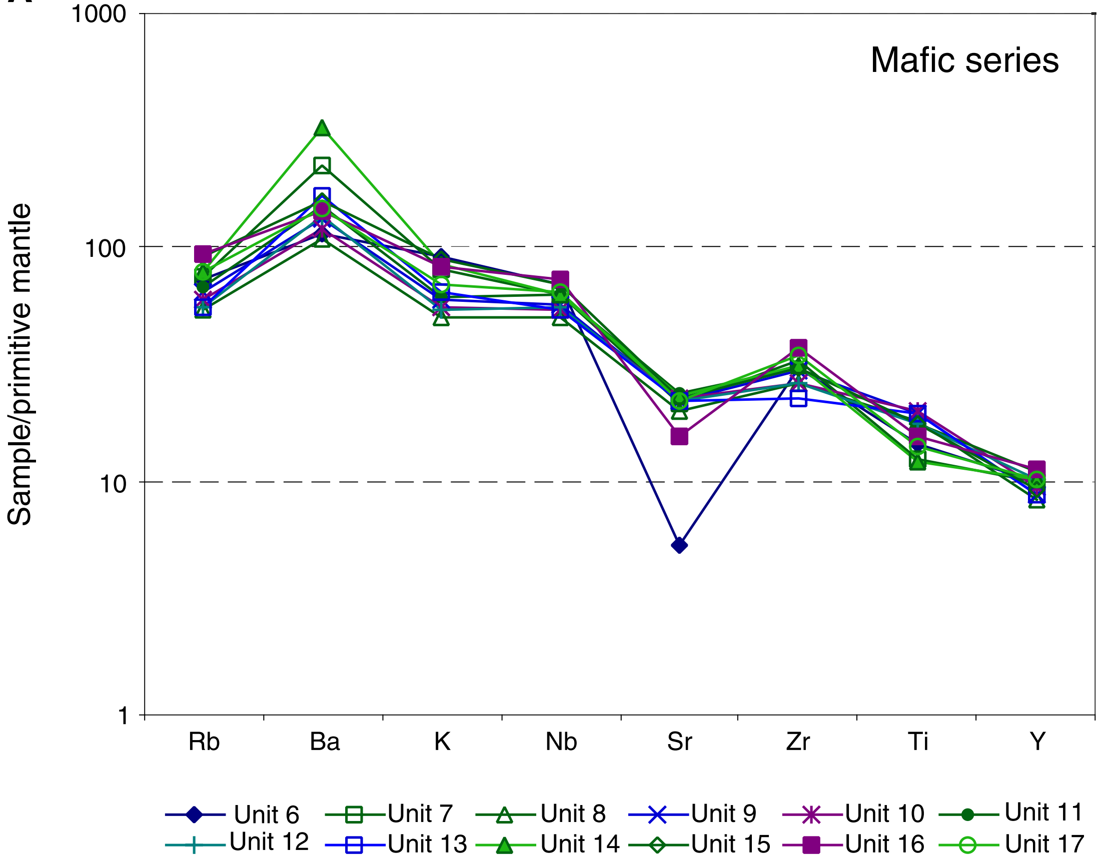

Figure F65 (continued). B. Felsic series.

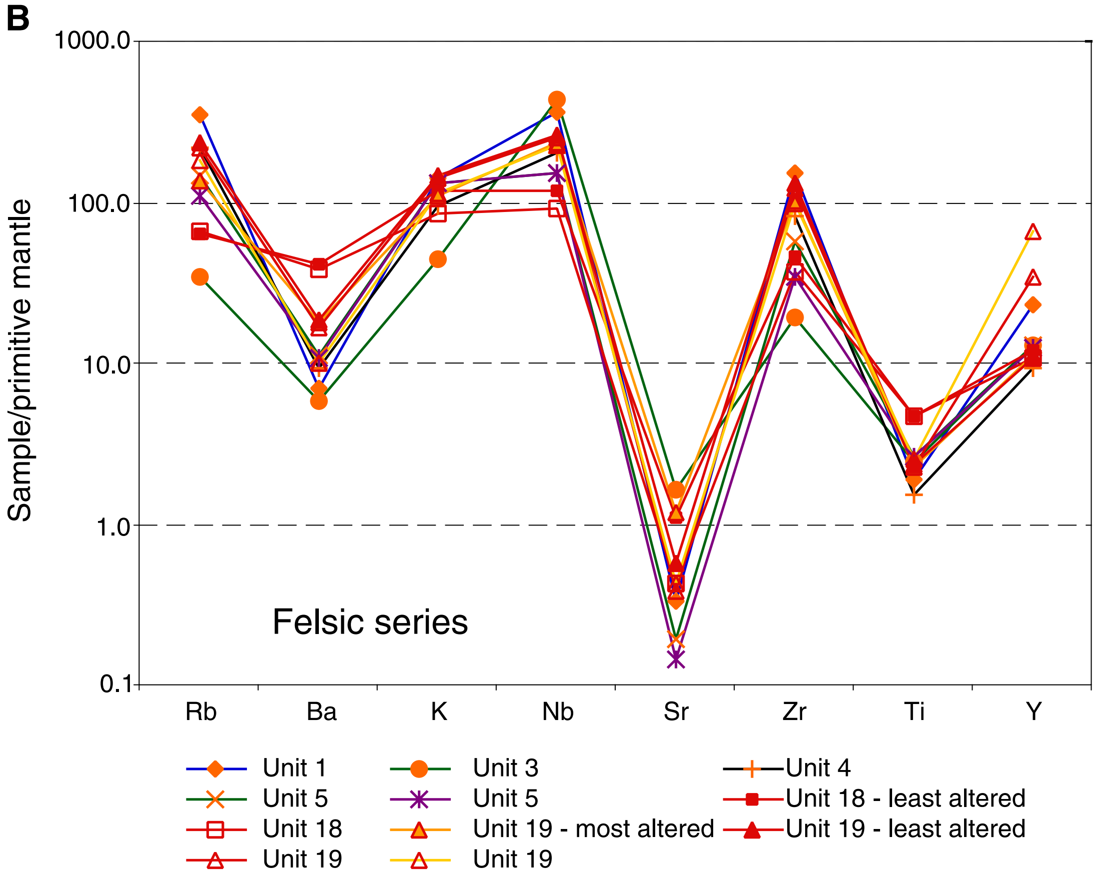

Figure F66. Major element compositional variations for Site 1139 compared with Kerguelen Archipelago alkalic volcanic series. The archipelago rocks are divided into three groups based on K-Ar ages: a lower Miocene alkalic basalt to trachyte series (~22 Ma), an upper Miocene basanite to tephrite series (6–10 Ma), and the Mount Ross stratovolcano (<1 Ma), which is the youngest edifice on the archipelago (Weis et al., 1993; Weis et al., 1998). The least-altered Unit 18 and 19 samples are indicated in bold.

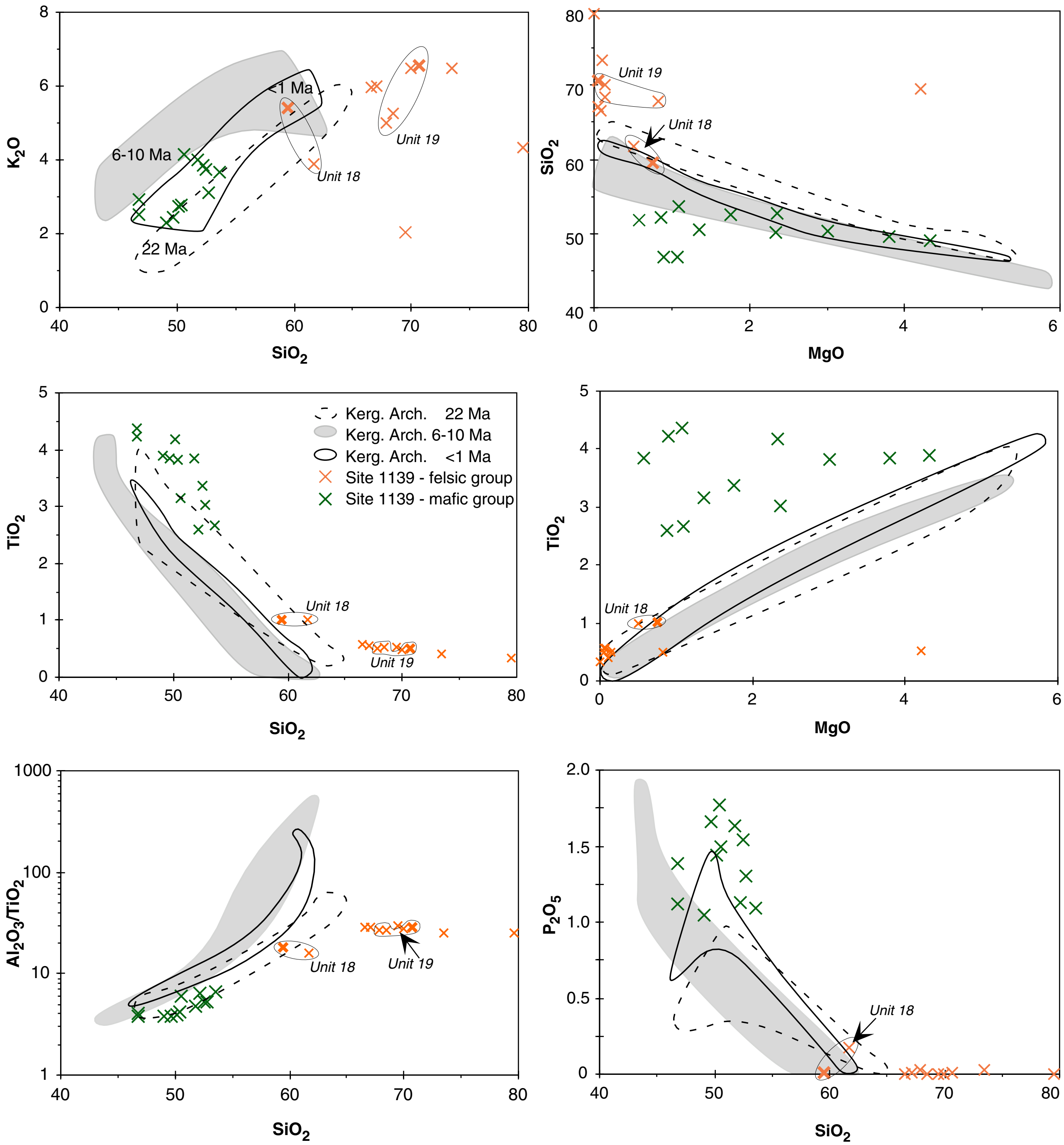

Figure F67. Trace element compositional variations for Site 1139 compared with Kerguelen Archipelago alkalic volcanic series which are divided as in Figure F66, p. 137. The Unit 3 highly altered crystal-vitric tuff has $(Nb/Zr)_N$ of 23.0 and $(Zr/Y)_N$ of 1.5, but the data point does not show at the scale in the figure. Data from Weis et al. (1993) and Weis et al. (1998).

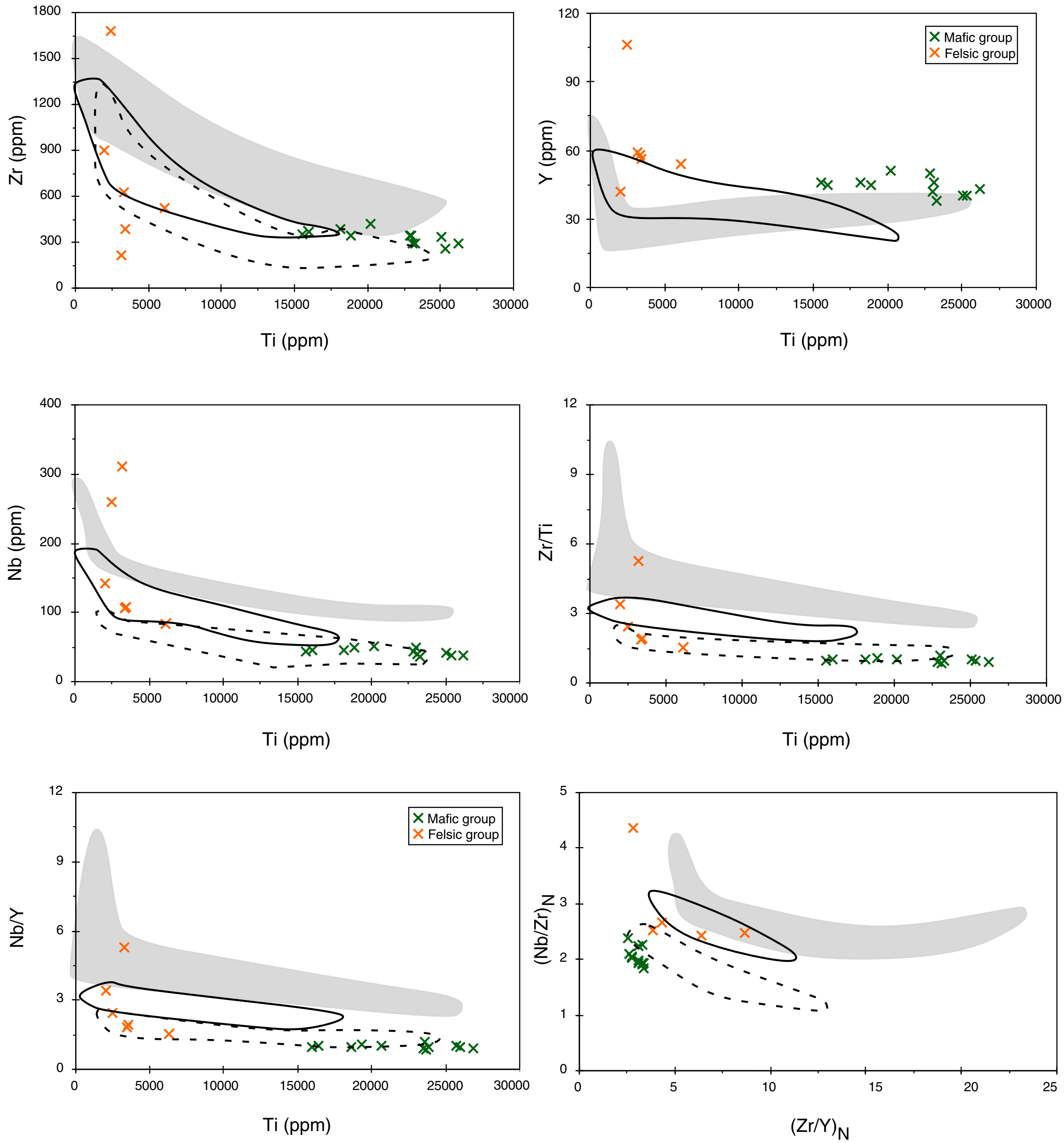

Figure F68. Alteration and distribution of secondary minerals in Hole 1139A vs. depth (mbsf), based upon macroscopic features and mineral occurrences observed in the core. Alteration: sl = slight, m = moderate, h = high, c = complete. SiO_2 = quartz and amorphous silica.

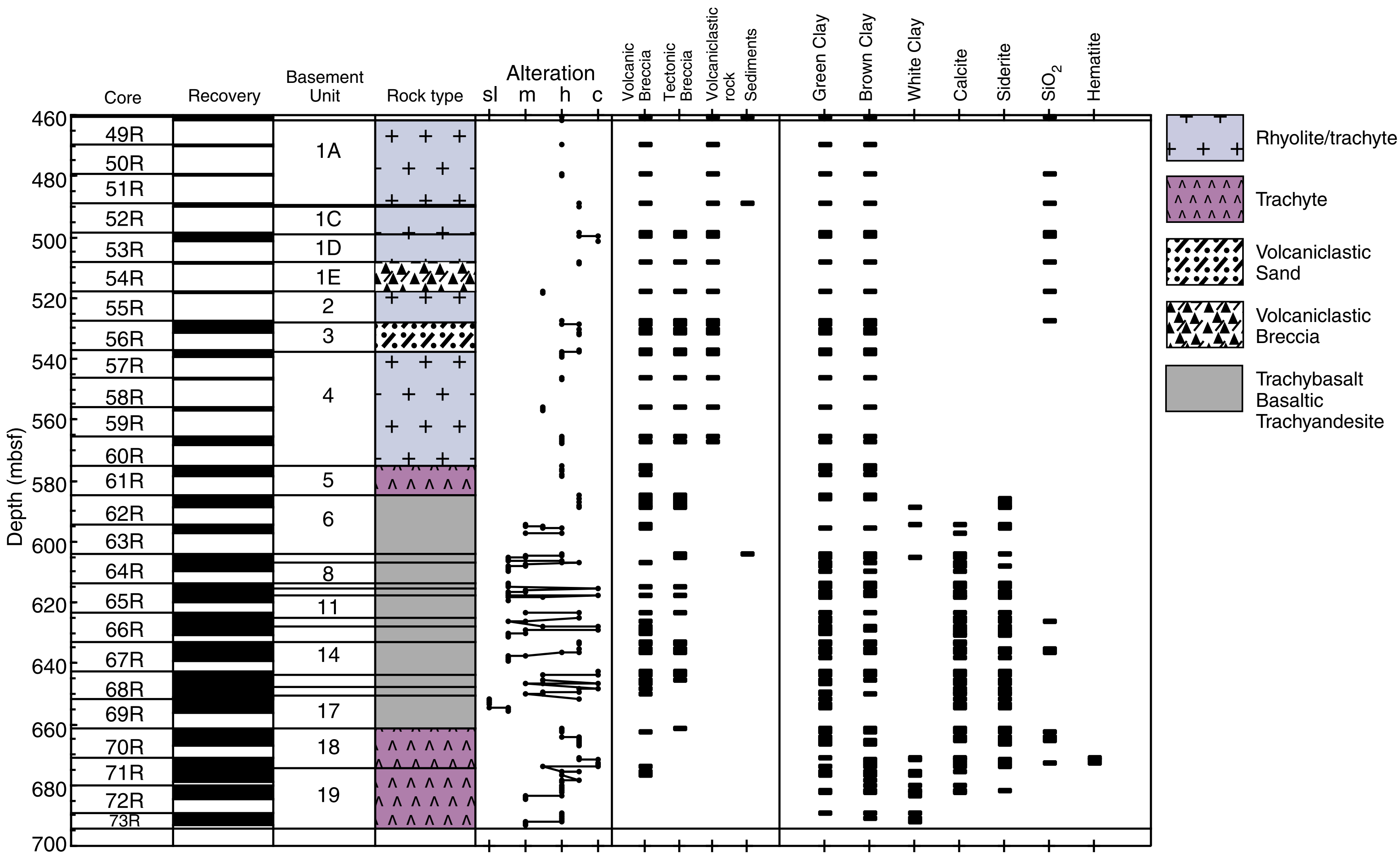

Figure F69. Color close-up photograph of Sample 183-1139A-64R-4 (Piece 3, 35–43 cm, dry surface). Slightly to moderately altered vesicular trachybasalt (Unit 8) with abundant veins and vesicles filled with calcite, siderite, and clay. Vesicles have colloform textures with light brown siderite linings and white calcite interiors. Subvertical and subhorizontal calcite veins form an orthogonal network and locally offset vesicles (e.g., 41 cm). Thin (<0.5 mm wide) calcite veins locally offset wider vertical calcite vein.

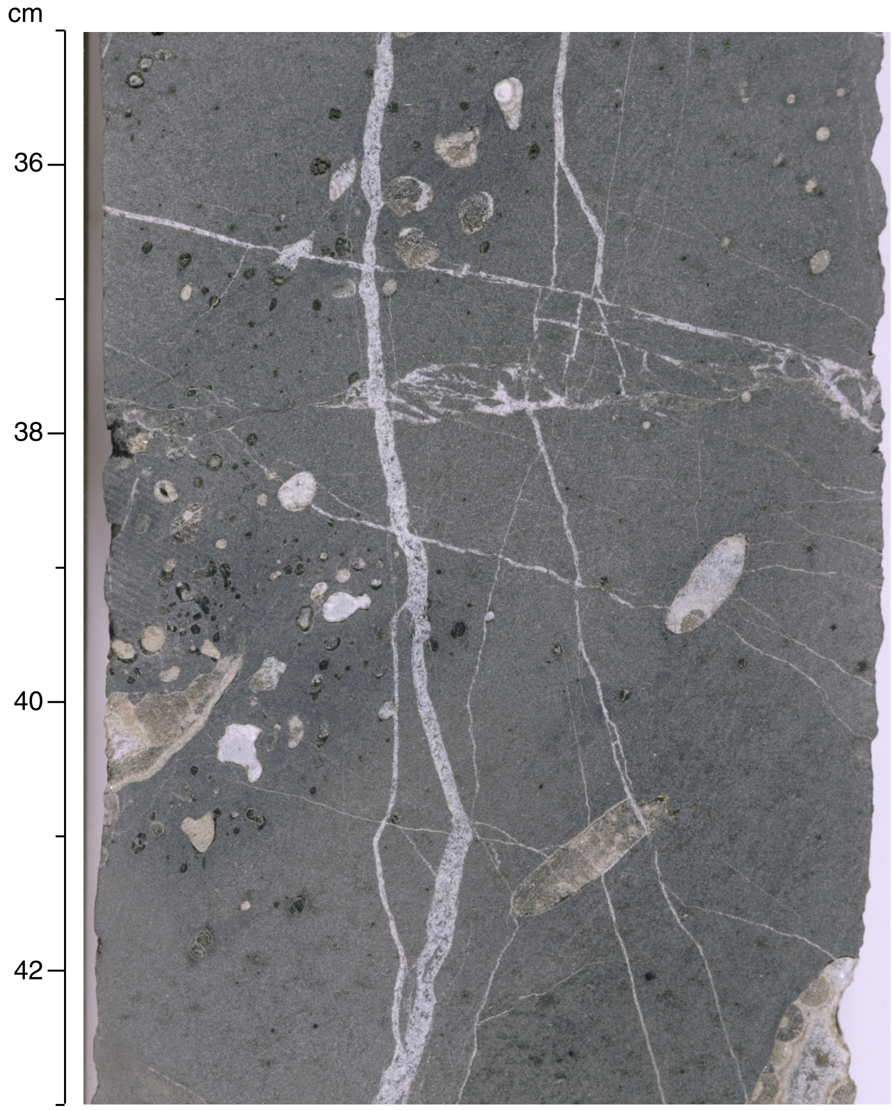

Figure F70. Color close-up photograph of Sample 183-1139A-70R-1 (Piece 3, 45–55 cm). Moderately altered red-gray sanidine-phyric trachyandesite with brecciated and possibly welded textures (Unit 18). This sample is variably oxidized and may be the less-altered "protolith" of the completely altered ("bleached") rocks deeper in the core.

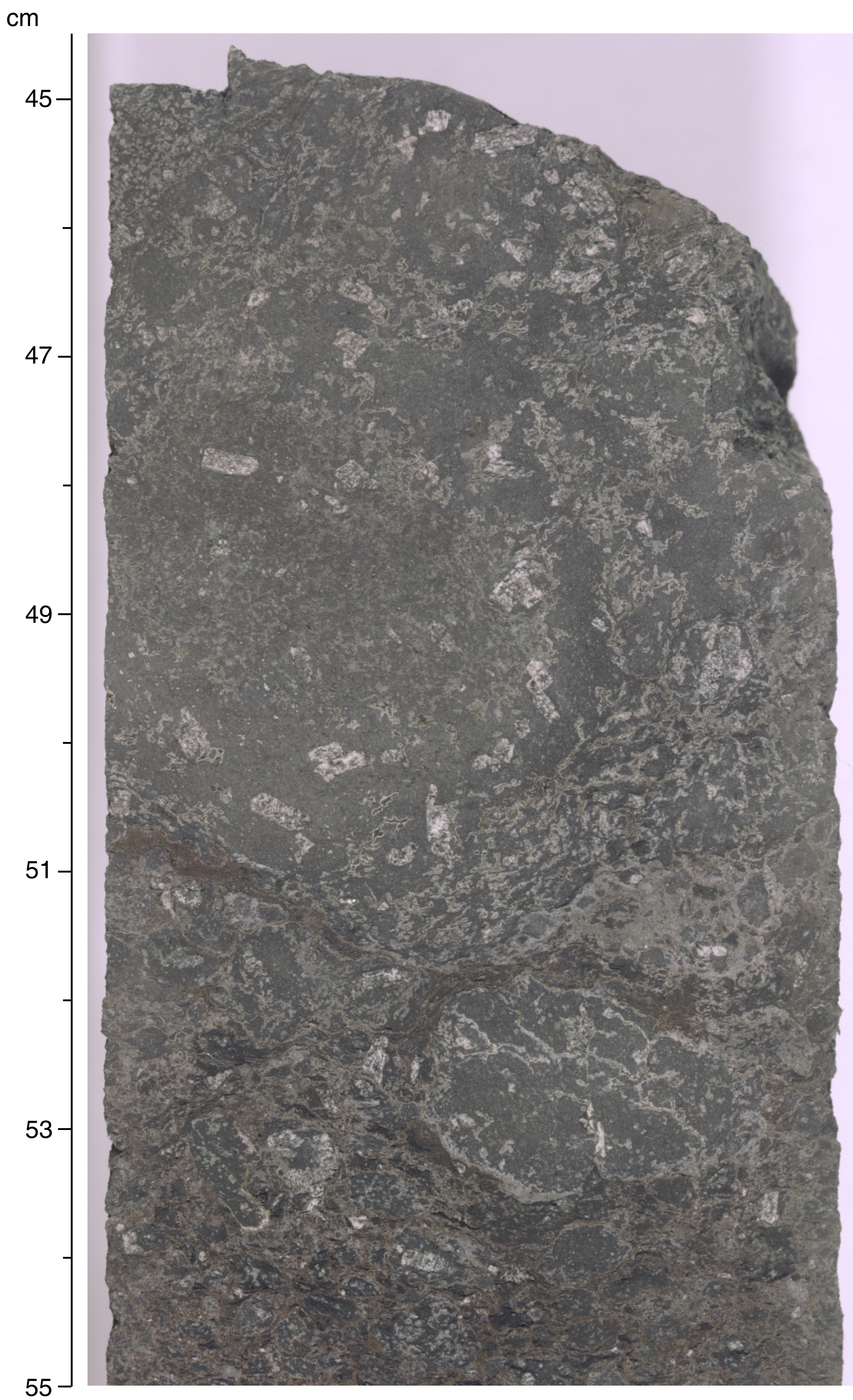

Figure F71. Color close-up photograph of Sample 183-1139A-70R-2 (Piece 1, 122–135 cm). Completely altered white to very pale green to light pink sanidine-phyric trachyandesite. Most intense alteration (white and pink) occurs as halos along veins filled with quartz, siderite, and calcite. Sanidine, siderite, and quartz were the only phases identified by XRD analysis of the white wall rock. Rock is locally brecciated between veins.

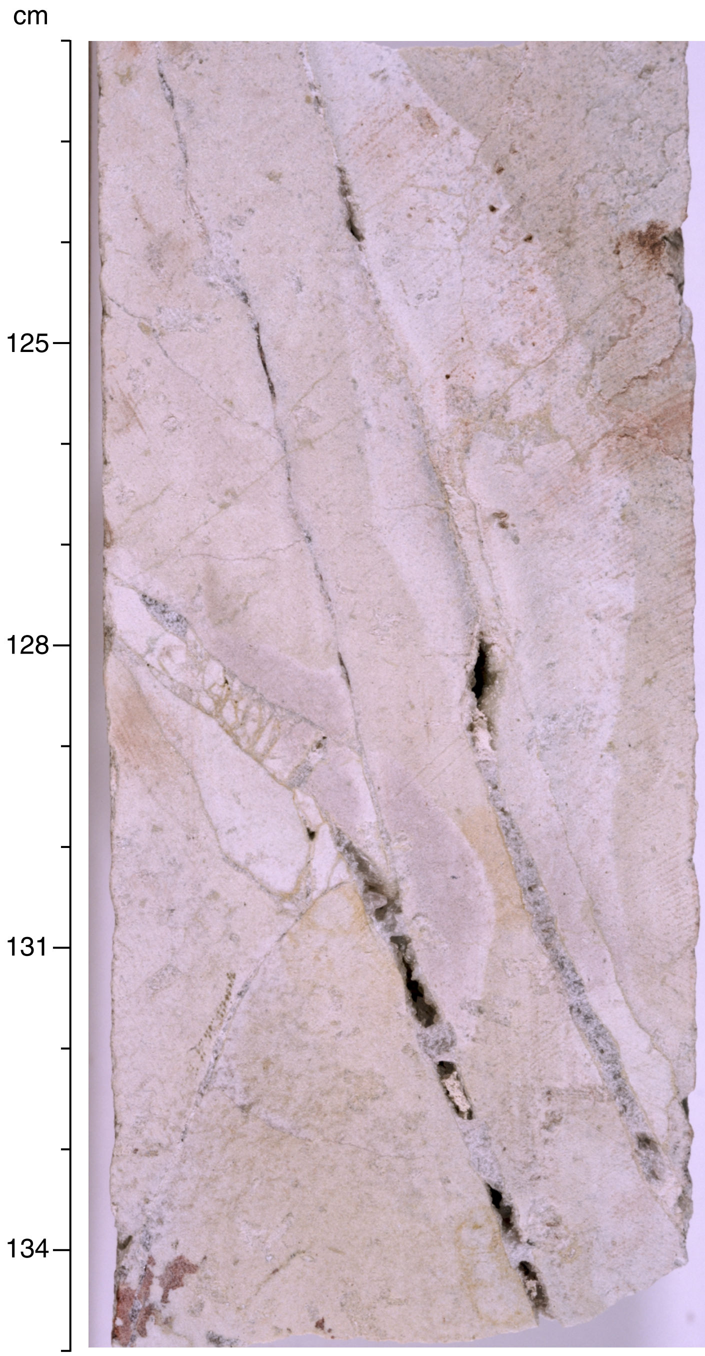

Figure F72. Color close-up photograph of Sample 183-1139A-70R-4 (Piece 4, 56–66 cm). Completely altered white to light pink moderately vesicular sanidine-phyric trachyandesite. Vesicles are filled with quartz and siderite. Surrounding whole rock contains sanidine, siderite, and quartz.

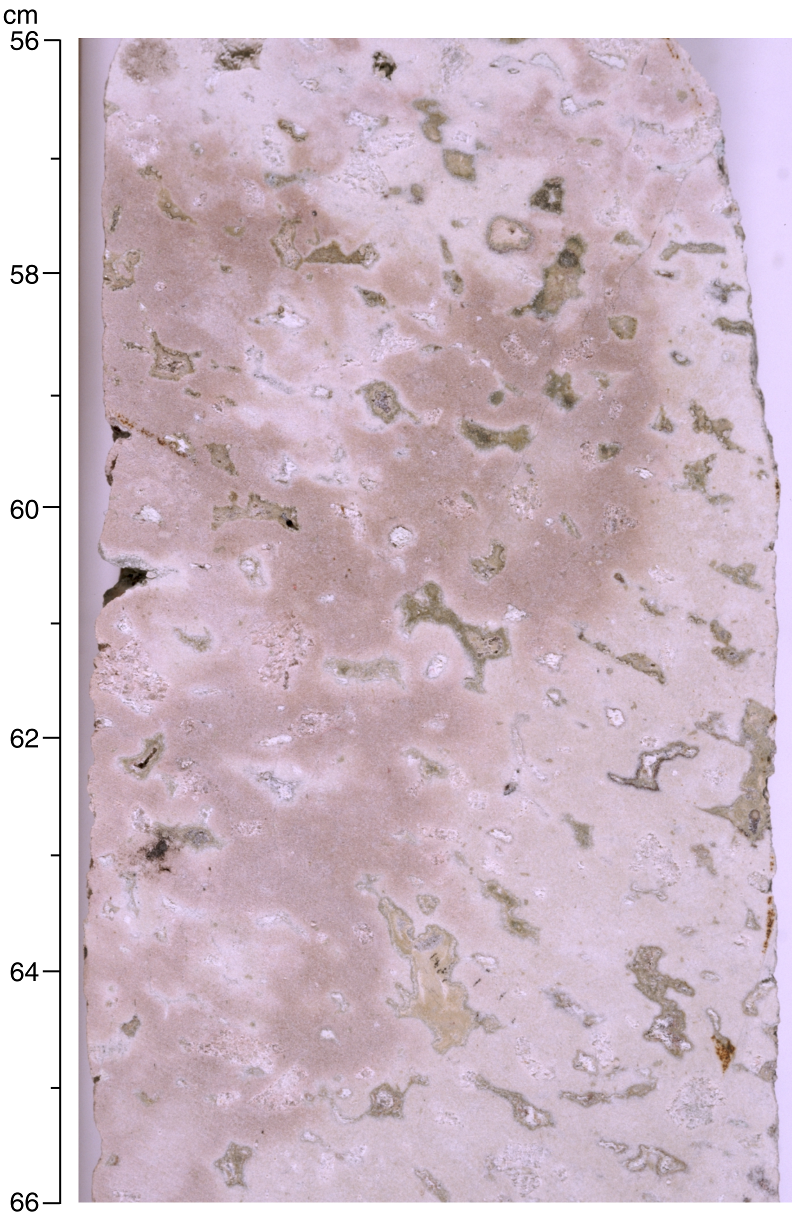

Figure F73. Color close-up photograph of Sample 183-1139A-70R-4 (Piece 5A, 94–104 cm). Highly to completely altered sanidine-phyric trachyandesite. Light gray rock with siderite-filled vesicles is overprinted by white (siderite and quartz) alteration. Quartz, siderite, and hematite(?) vein has prominent oxidation halo that cuts across the white alteration zone.

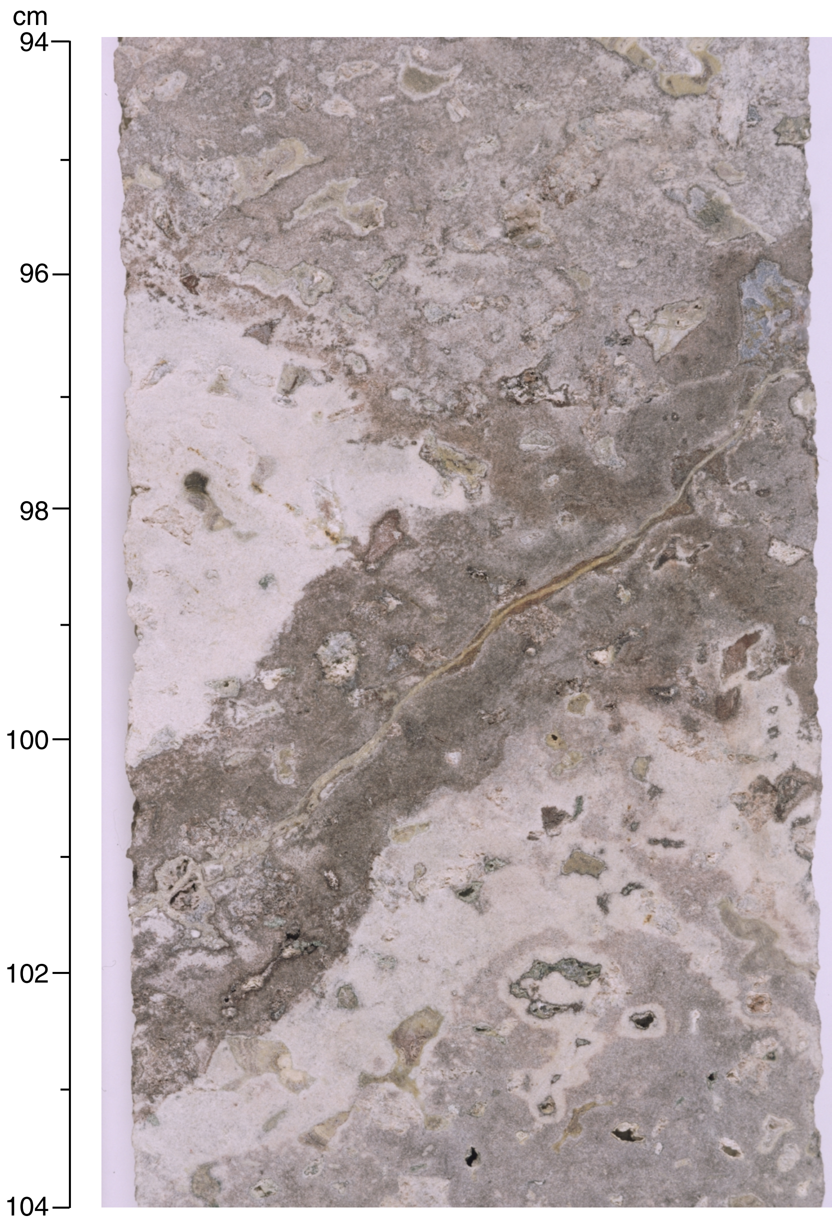

Figure F74. Color close-up photograph of Sample 183-1139A-71R-1 (Piece 2, 27–42 cm). Deep red vein with prominent alteration halo crosscutting highly altered gray sanidine-phyric trachyandesite. Vein minerals include hematite, quartz, calcite, and siderite.

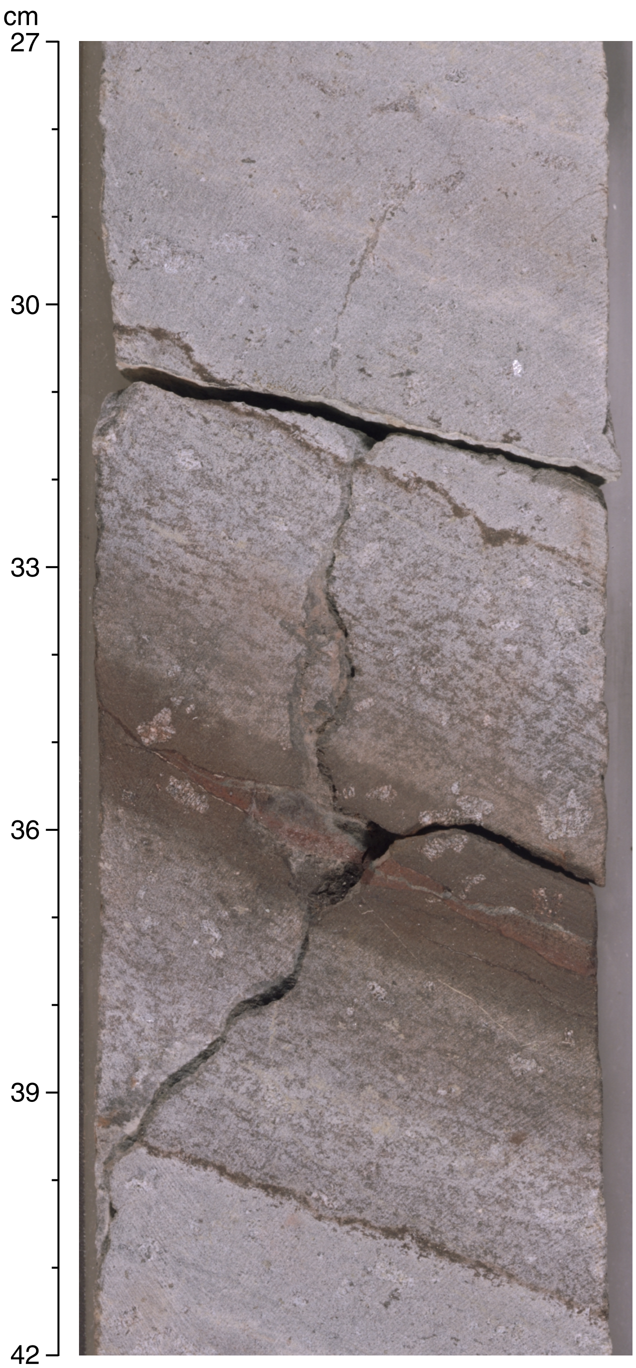

Figure F75. Color close-up photograph of Sample 183-1139A-71R-1 (Piece 2, 44–64 cm). Highly altered yellow-gray sanidine-phyric trachyandesite showing multiple alteration events. A moderately dipping transition into less-altered gray rock is visible at the top of the photo. The early yellow-gray alteration zone is overprinted by an oxidation halo near the bottom of the photo that is proximal to a deep red vein in Sample 183-1139A-71R-1 (Piece 3, 80 cm).

Figure F76. Color close-up photograph of Sample 183-1139A-71R-3 (Piece 2A, 62–67 cm). Irregular cavity filled with hematite, quartz, siderite, and calcite in red-stained sanidine-phyric trachyandesite. Oxidation accentuates primary igneous textures that suggest magmatic deformation.

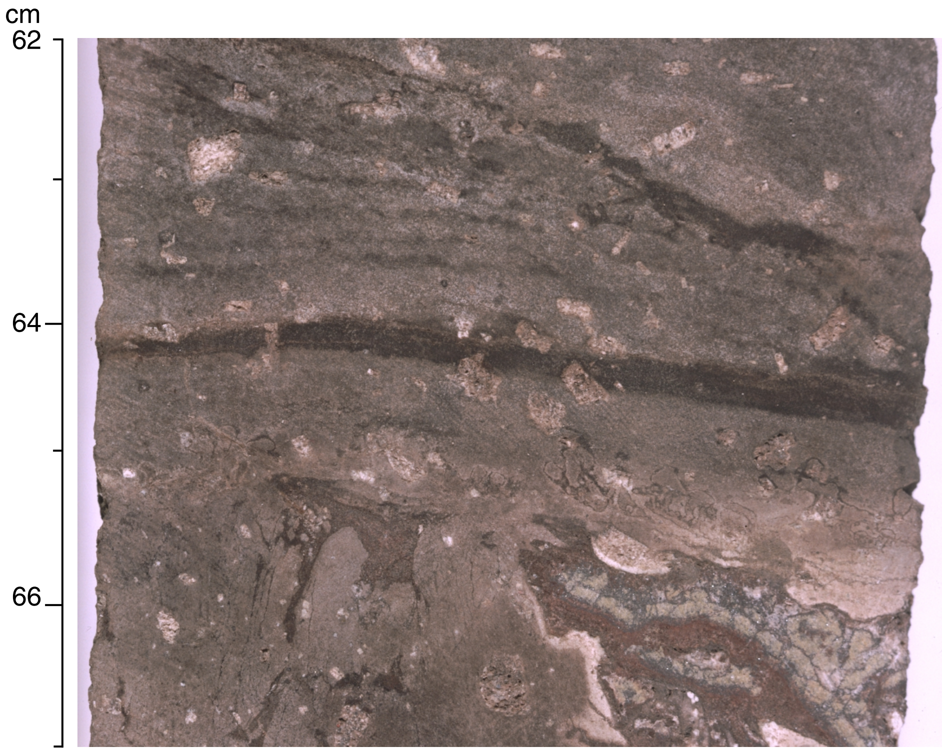

Figure F77. Color close-up photograph of Sample 183-1139A-71R-2 (Piece 1, 48–60 cm). White to pink alteration halo around vein filled with quartz, siderite, and calcite. The vein and halo cut across and locally offset dark red oxidation bands within variably oxidized sanidine-phyric trachyandesite that has been locally brecciated. An abrupt transition is visible from 56 to 57 cm between red-gray and light gray trachyte. The latter possibly represents an earlier alteration event.

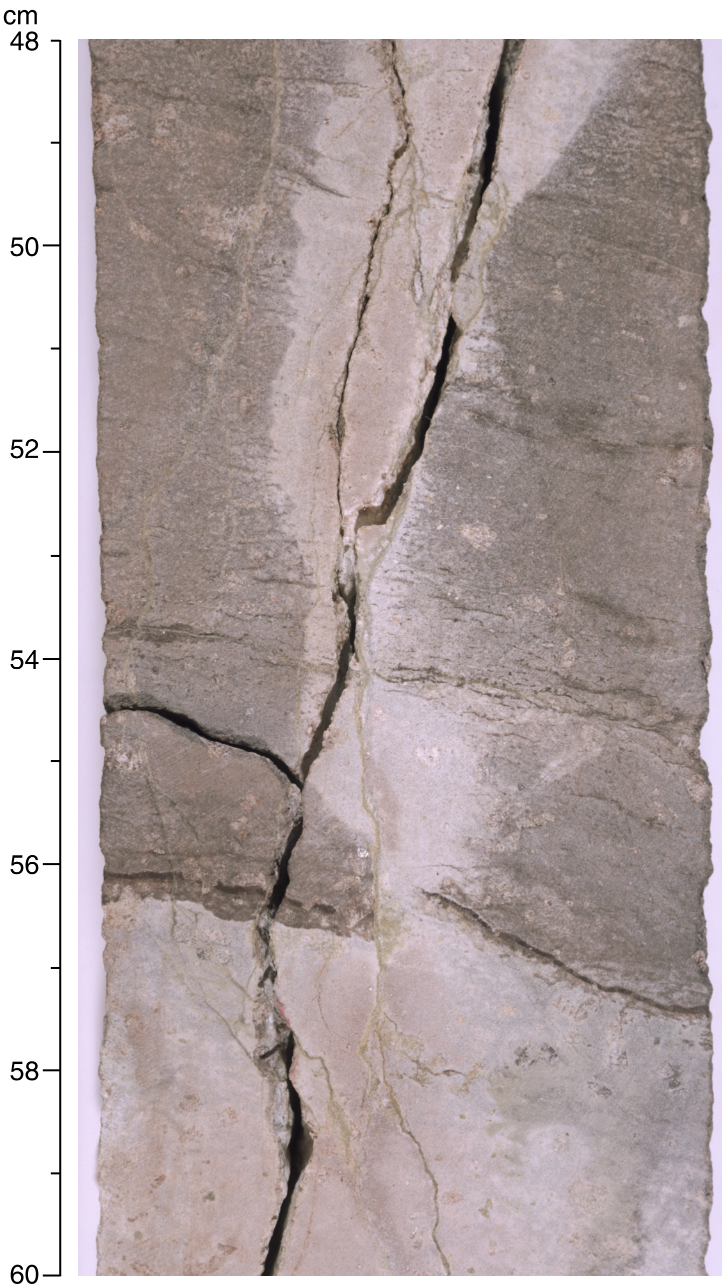

Figure F78. Color close-up photograph of Sample 183-1139A-71R-4 (Piece 1, 105–120 cm). Highly altered greenish gray sanidine-phyric trachyte breccia (Unit 18).

Figure F79. Color close-up photograph of Sample 183-1139A-71R-5 (Piece 1, 40–55 cm). Highly altered sanidine-phyric trachyte breccia. Pale brownish white clasts are set in a red oxidized matrix.

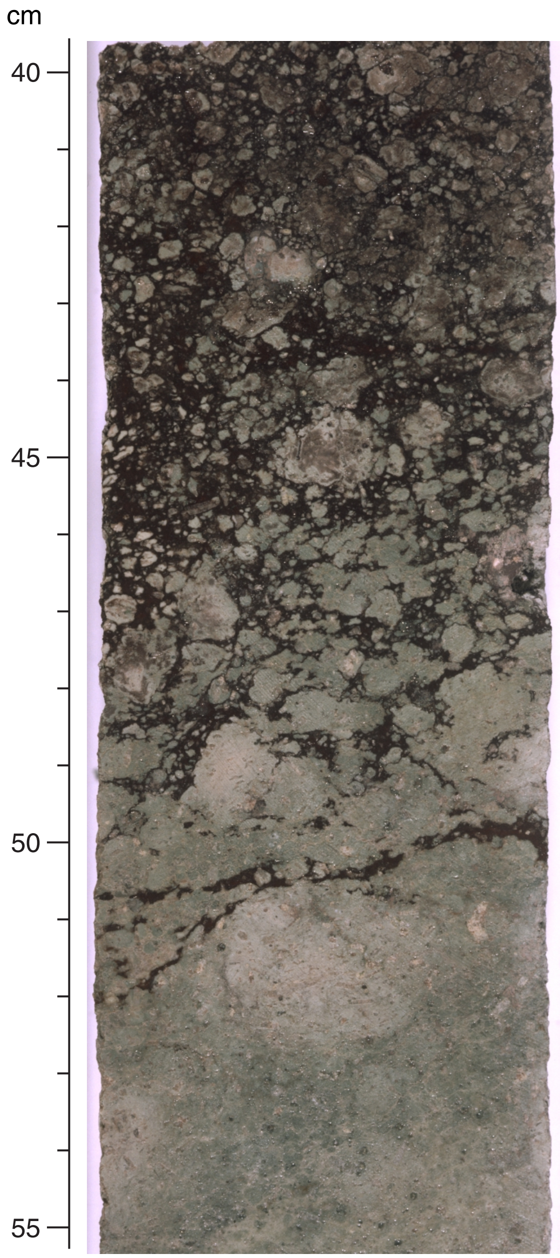

Figure F80. Color close-up photograph of Sample 183-1139A-71R-6 (Piece 1, 45–55 cm). Highly altered sanidine-phyric trachyte breccia. Clasts vary from pale green to light red, whereas matrix is red.

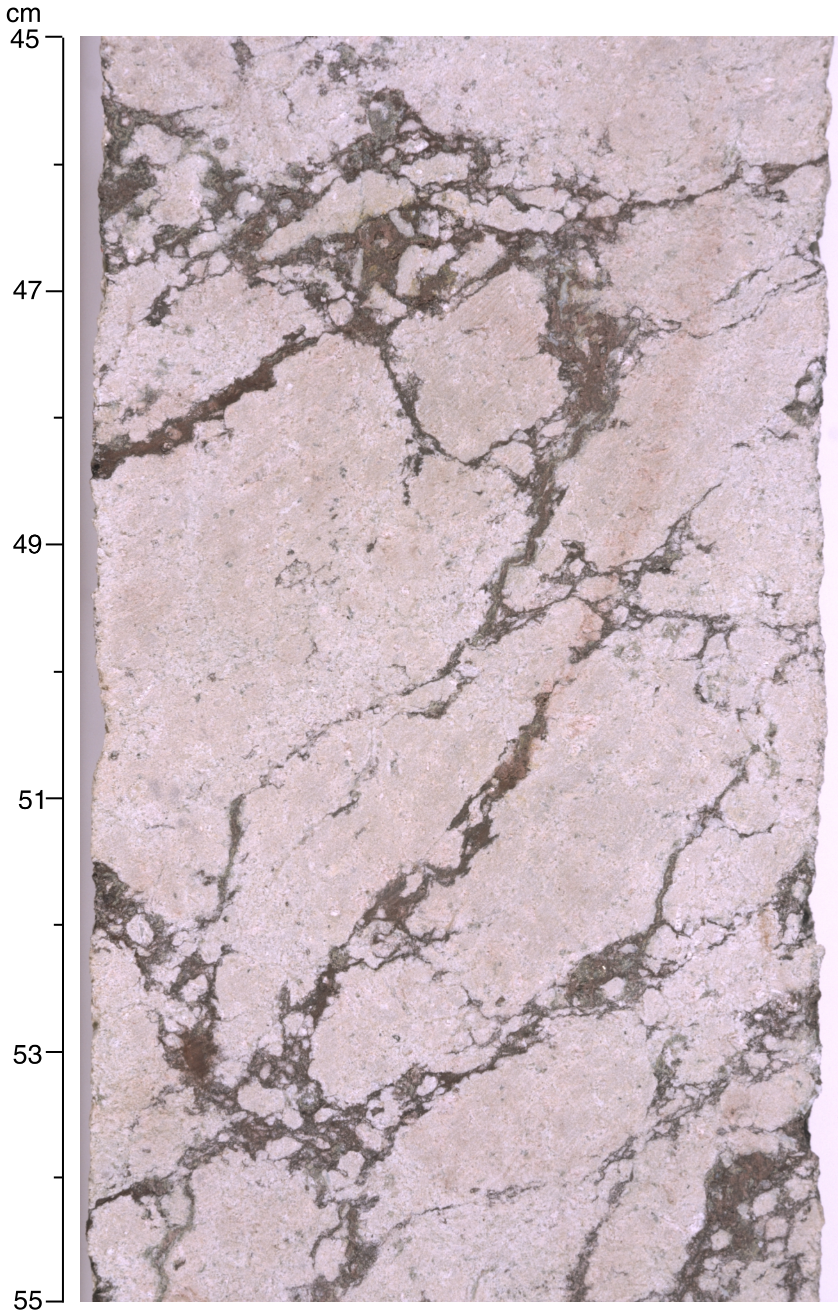

Figure F81. Color close-up photograph of Sample 183-1139A-73R-2 (Piece 12, 112–134 cm). Light gray variably oxidized sanidine-phyric trachyte. Red-oxidized halos around thin (<1 mm wide) hematite veins give the rock a banded appearance.

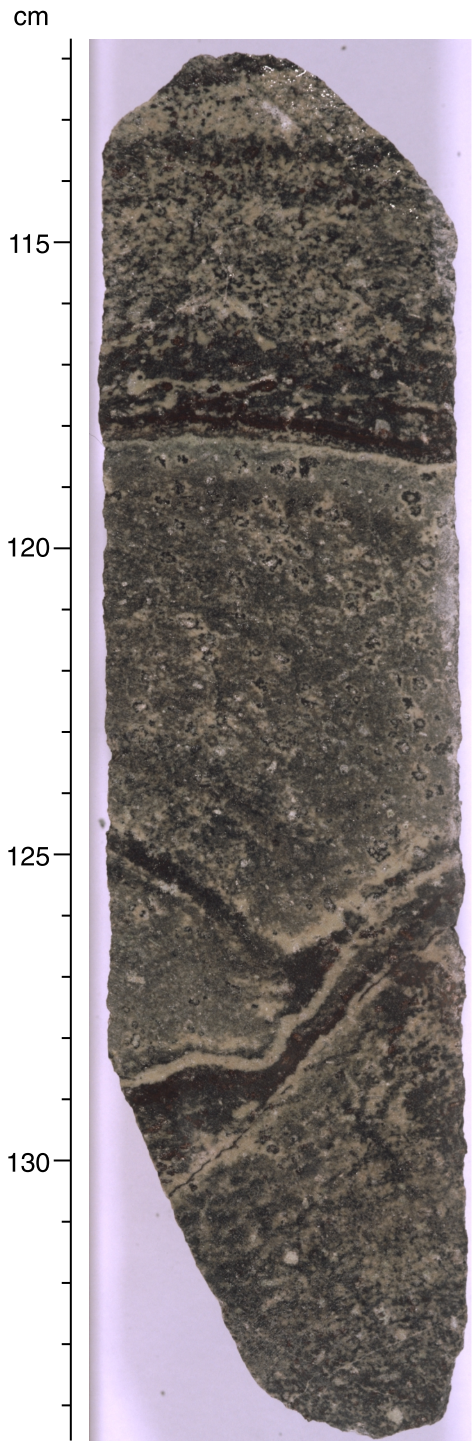

Figure F82. Net mass gain ("enrichment") or loss ("depletion") of rock components from the most highly altered ("bleached") intervals in Units 18 and 19. The composition of the altered rock was divided by the composition of the least-altered sample (assumed protolith) from that unit. Thus, values greater than unity represent mass gains during alteration, whereas values less than unity represent mass loss. Samples 183-1139A-70R-1 (Piece 2A, 17–20 cm) and 70R-2 (Piece 1F, 141–145 cm) were selected as highly altered and relatively unaltered pairs, respectively, in Unit 18. Corresponding samples from Unit 19 were Samples 183-1139A-71R-7 (Piece 1B, 25–27 cm) and 71R-4 (Piece 11, 135–138 cm). The assumed protoliths have H_2O and CO_2 concentrations of 0.8 to 2.3 wt% and, as a consequence, are only slightly altered. Missing histograms for CaO and MgO reflect cases where concentrations were below detection. For complete chemical analyses for Hole 1139A basement units, see "Igneous Petrology," p. 36, and Table T11, p. 198.

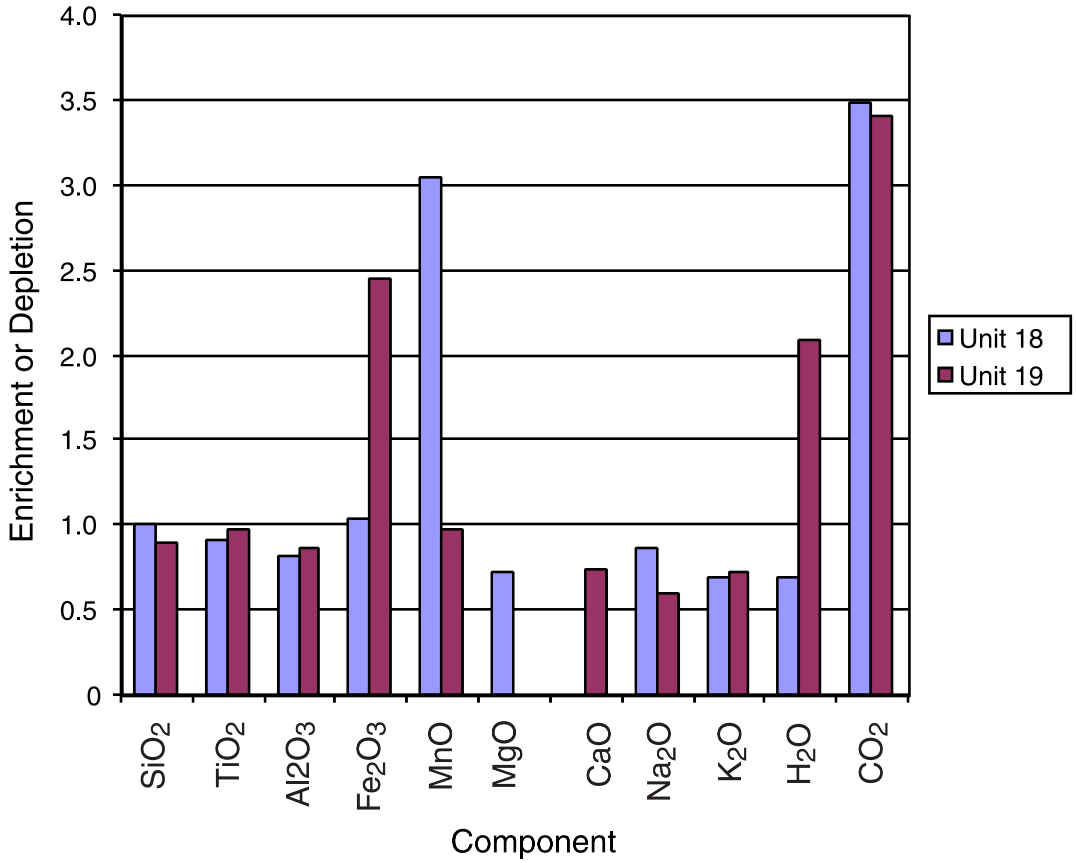

Figure F83. Example of progressive AF demagnetization of a discrete sediment sample (Sample 183-1139A-29R-5, 111–113 cm). The intensity decay curve is plotted on the left and the directional change is plotted on an orthogonal vector projection on the right. Magnetic directions that tend toward the origin with high median destructive fields are considered reliable. J_0 is the magnetization intensity before AF treatment.

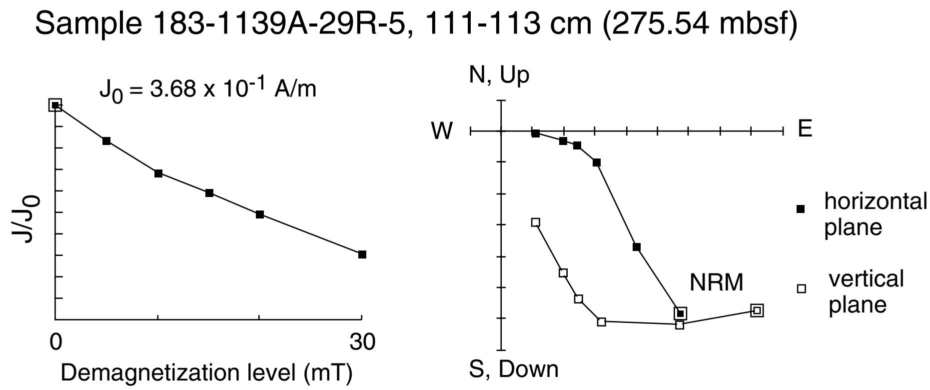

Figure F84. Hole 1139A inclination, intensity of remanent magnetization, and MST susceptibility of sediments from (**A**) 0–100 mbsf, (**B**) 100–200 mbsf, (**C**) 200–300 mbsf, and (**D**) 300–400 mbsf. Crosses and lines represent remanent magnetization before and after AF demagnetization at 20 mT, respectively. Inclination data used for polarity interpretations are shown by open circles. Interpreted normal and reversed geomagnetic chrons are shown by black and white rectangles, respectively. Inclinations from discrete samples are shown by solid circles. Lithologic units are shown on the right. (Continued on next three pages.)

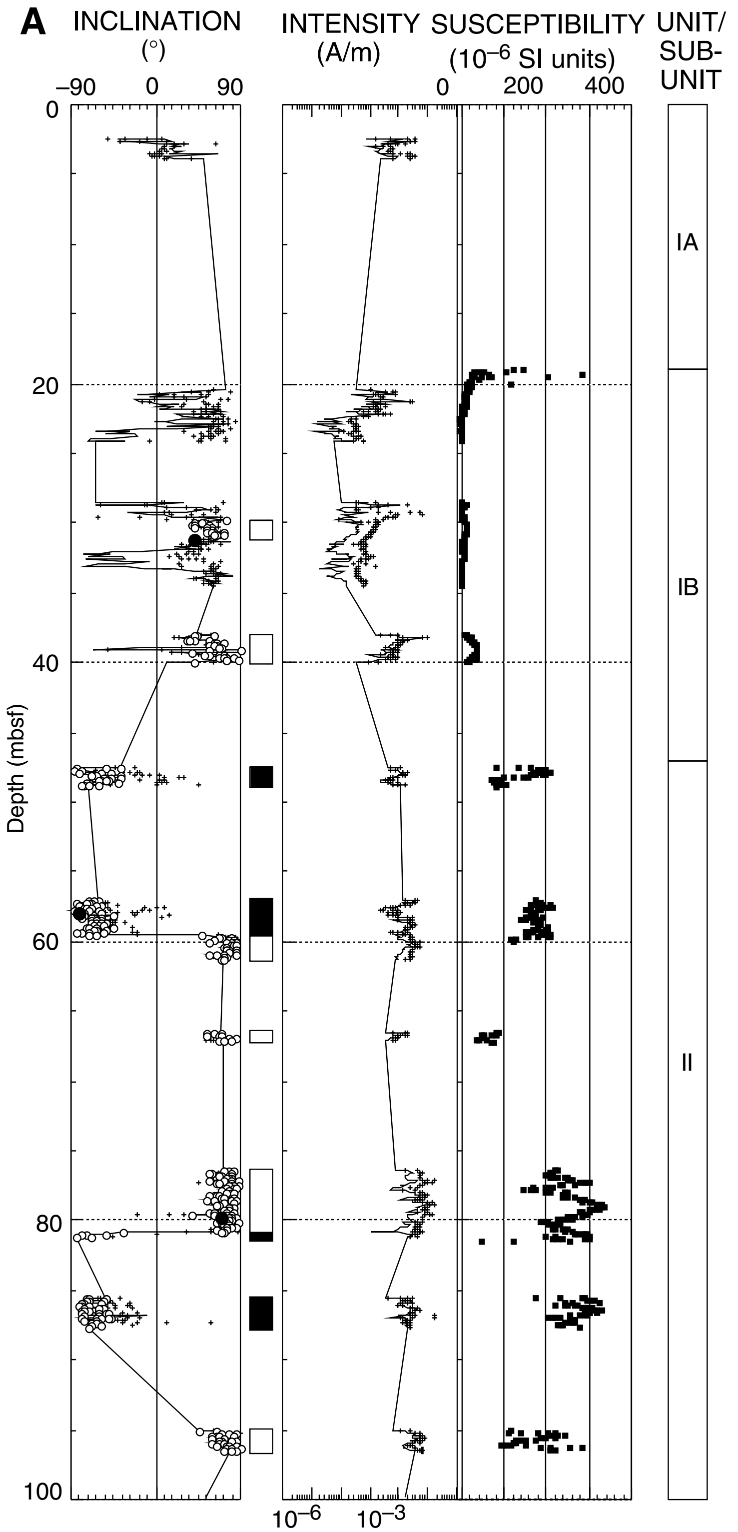

Figure F84 (continued).

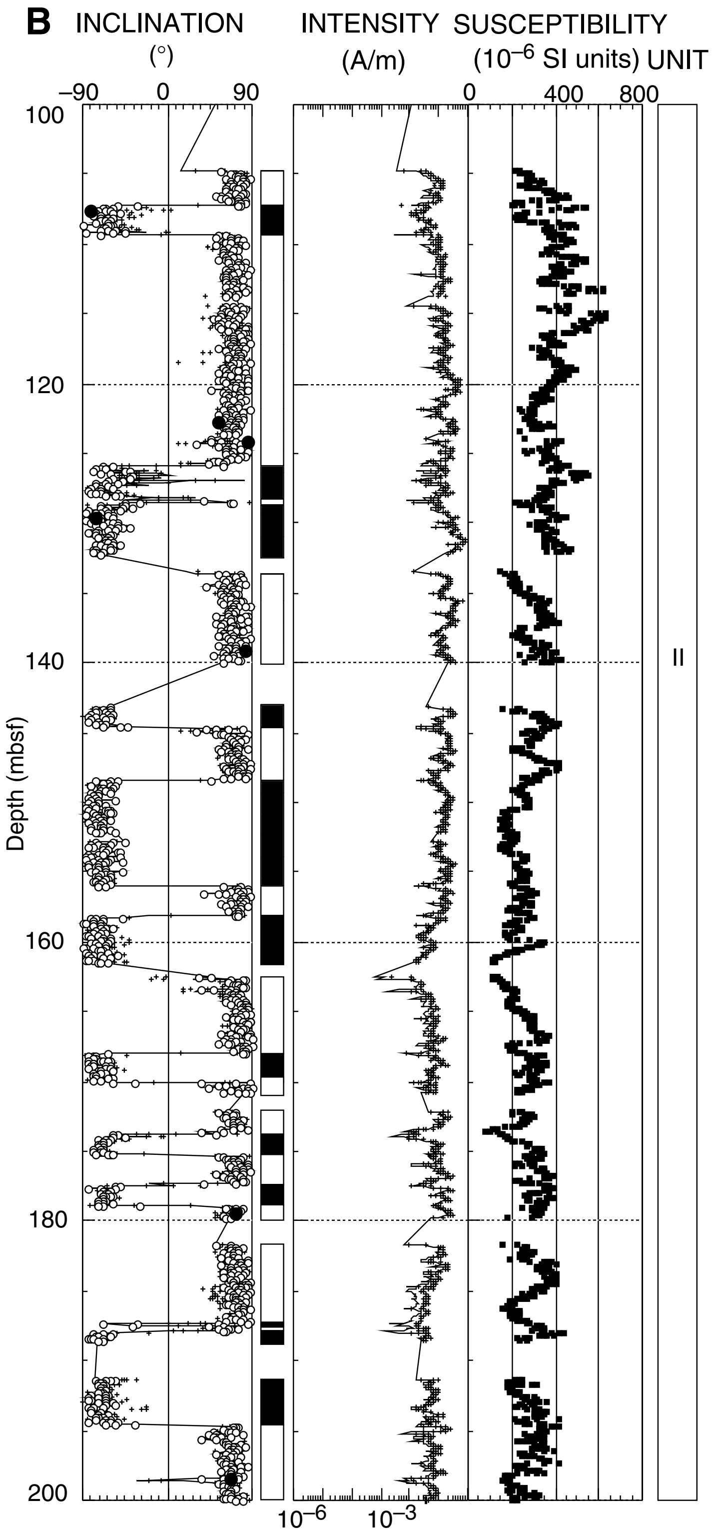

Figure F84 (continued).

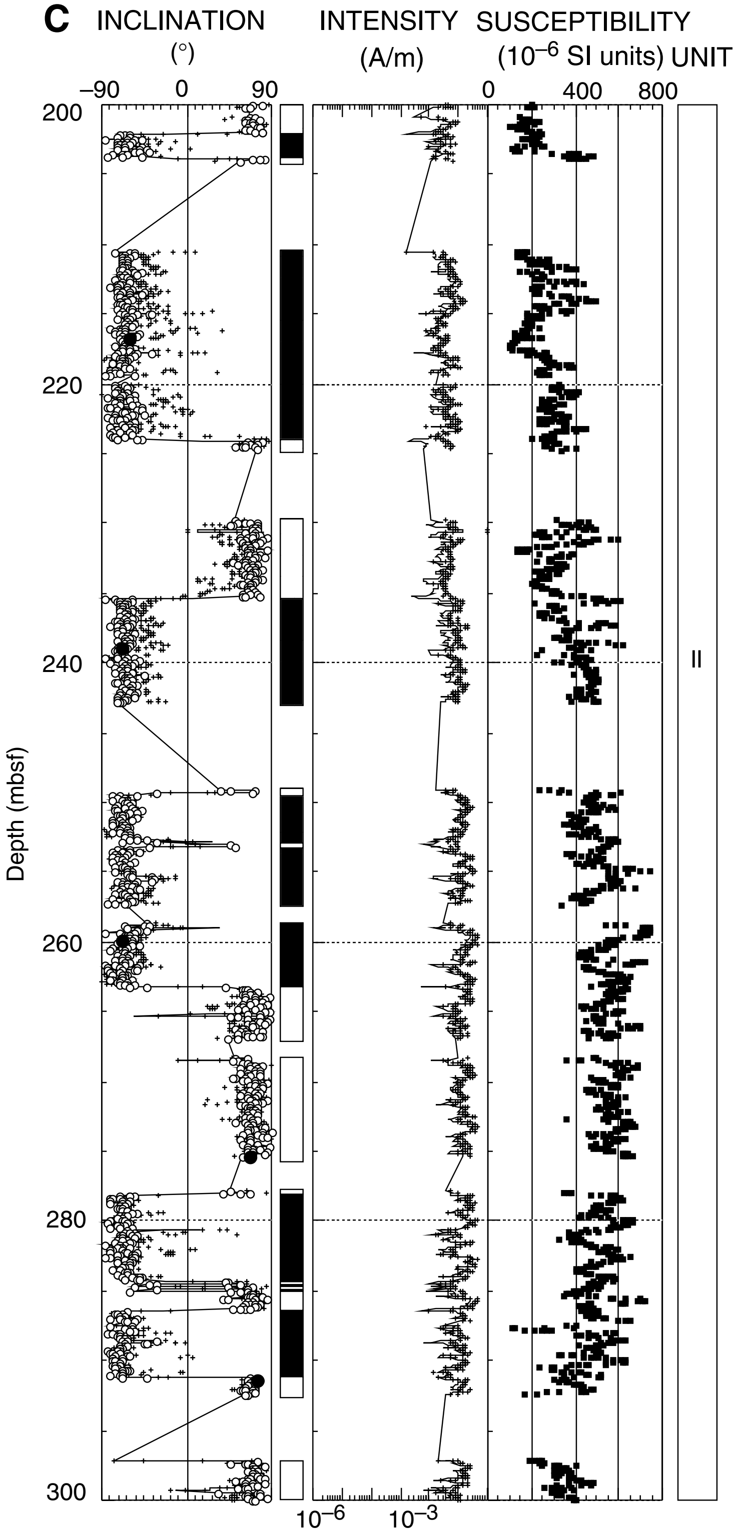

Figure F84 (continued).

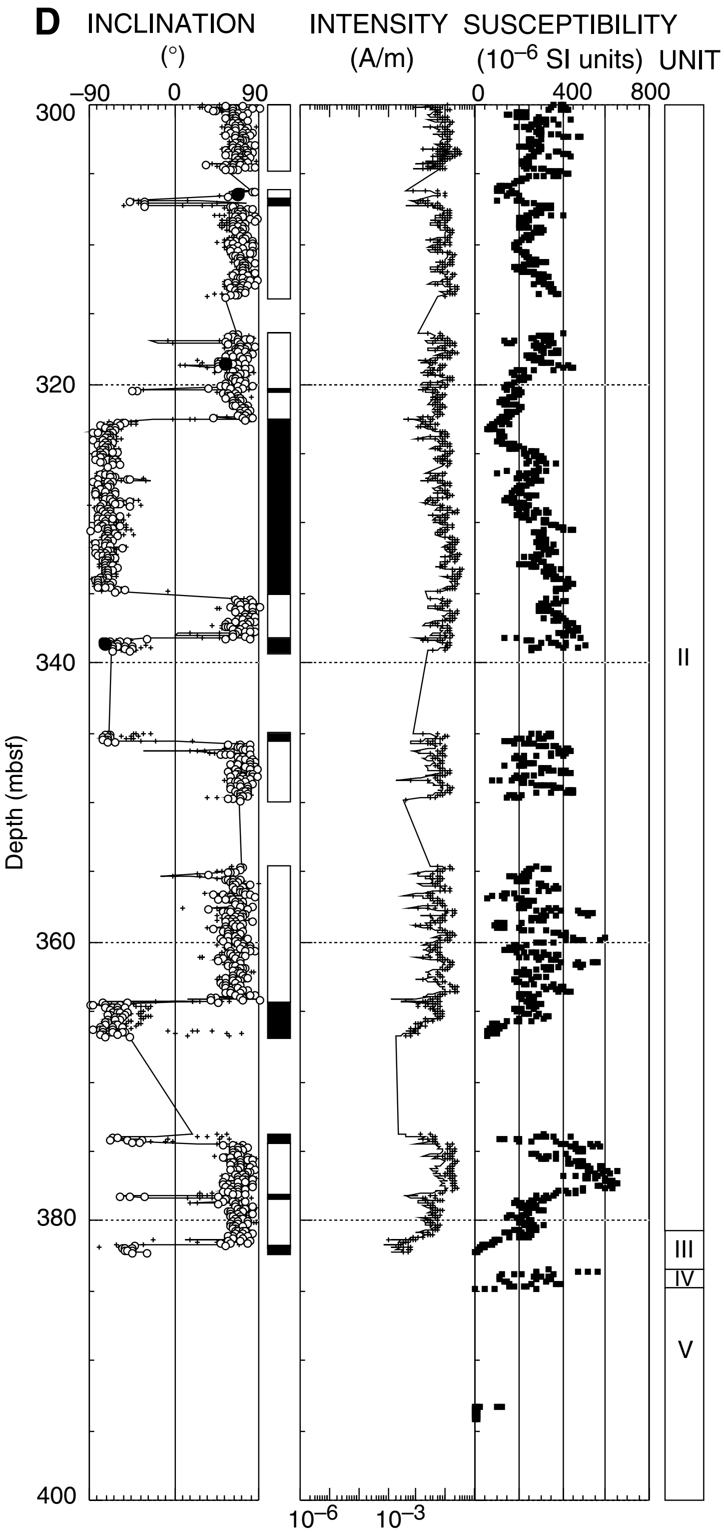

Figure F85. Average natural remanent magnetization intensity and MST susceptibility of each lithologic and basement unit. Open circles represent the average values of subunits. Large solid circles give the average values for all sediments and lava units. The horizontal bars show the range between maximum and minimum values in the respective units.

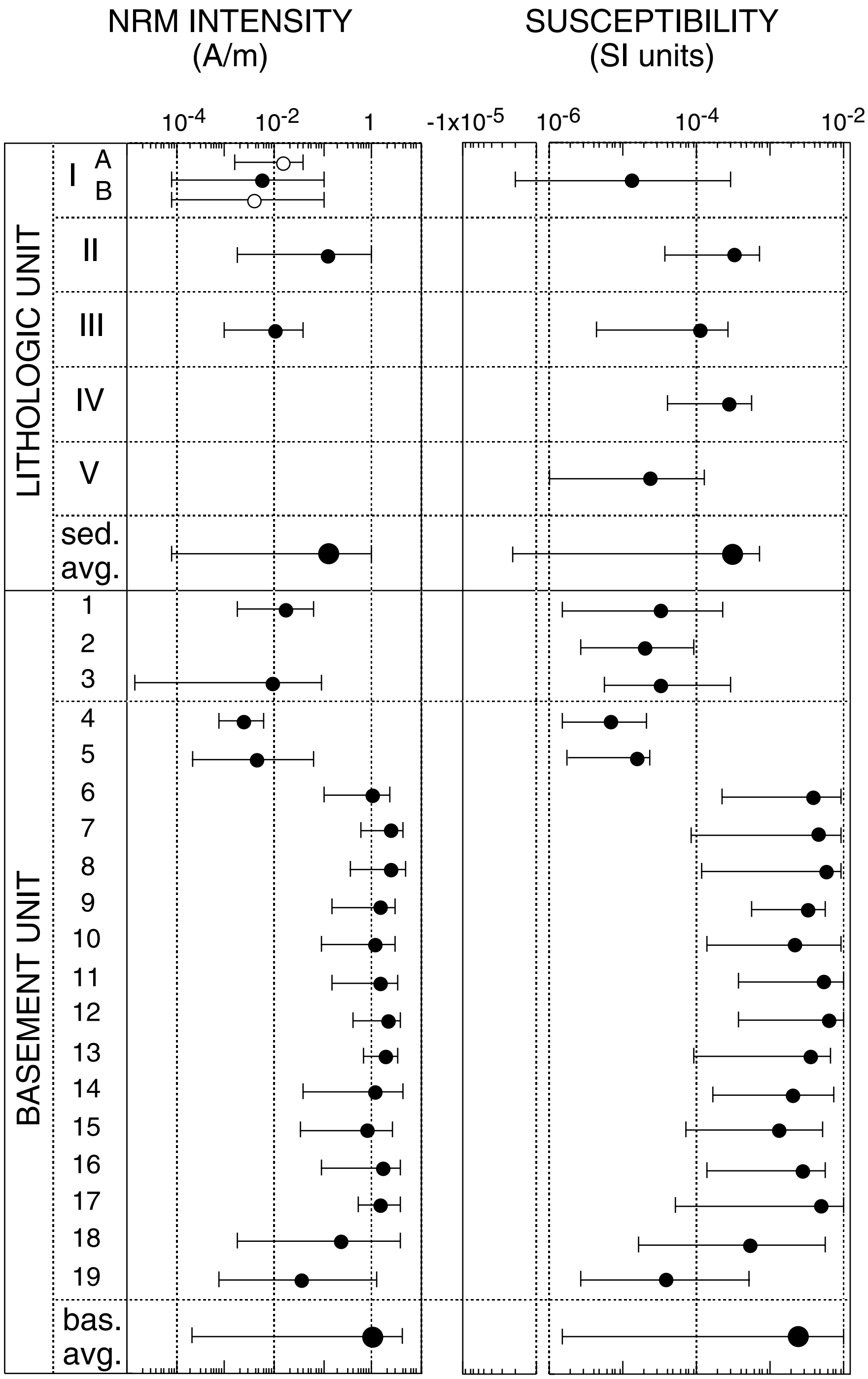

Figure F86. Hole 1139A inclination, intensity of remanent magnetization, and susceptibility of basement rocks from (**A**) 460–580 mbsf and (**B**) 580–700 mbsf. Crosses and lines represent remanent magnetization before and after AF demagnetization at 40 mT, respectively. Inclinations of NRM and characteristic inclinations of discrete samples are represented by solid and open circles, respectively. MST, AMST, and discrete-sample susceptibilities are represented by lines, crosses and open circles, respectively. Basement units are shown on the right. (Continued on next page.)

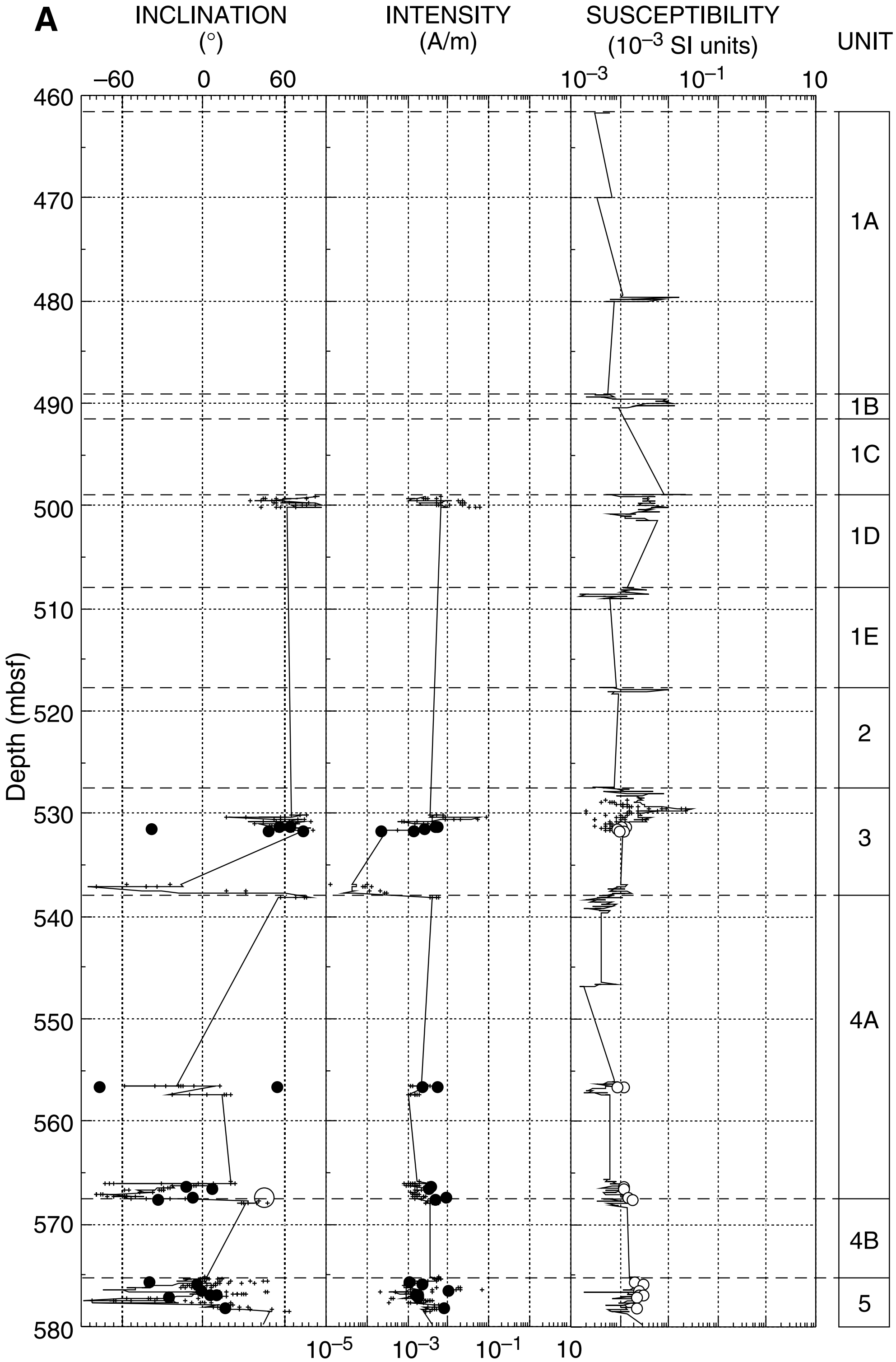

Figure F86 (continued).

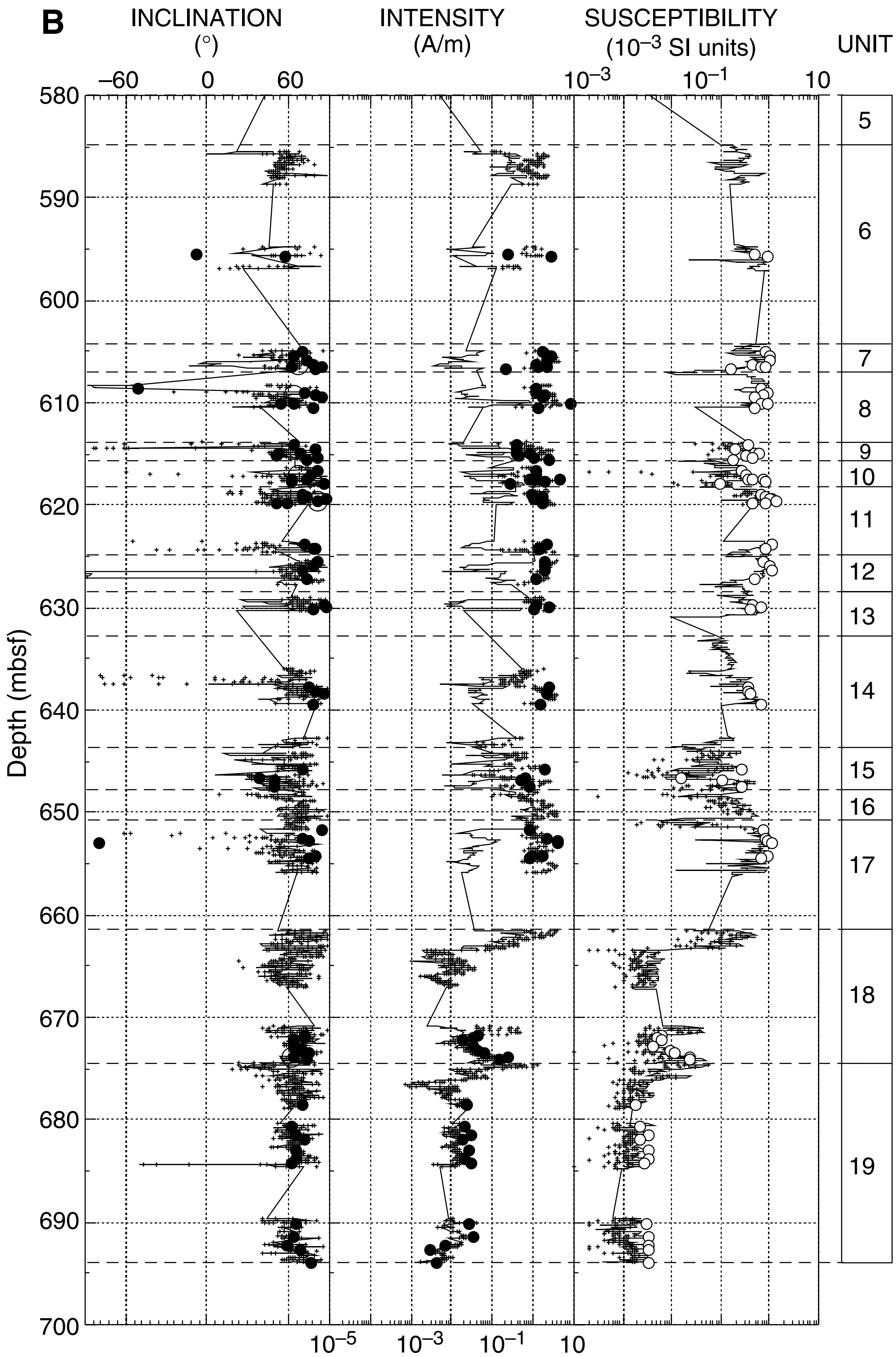

Figure F87. Directional anisotropy data from samples of basement Unit 7 plotted on an equal-area stereographic projection. The directions of maximum principal axes are plotted as open squares, of intermediate principal axes as shaded squares, and of minimum principal axes as solid squares.

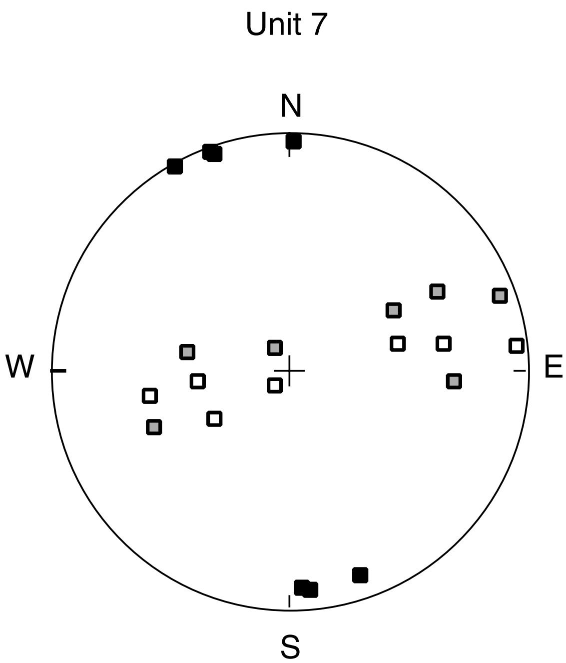

Figure F88. Stepwise AF demagnetization up to 60 mT at 72.5 cm of the archive half of Section 183-1139A-69R-2 from basement Unit 17. The magnetization has a MDF of 10 mT and a single-component magnetization as is evident by the straight lines in the orthogonal vector projections. J_0 is the magnetization intensity before AF treatment.

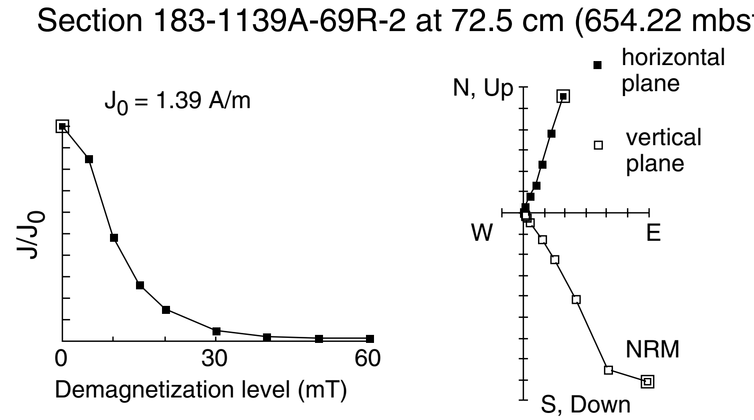

Figure F89. **A.** Thermal demagnetization of Sample 183-1139A-64R-2, 41–43 cm, from basement Unit 7. The NRM is a two-component magnetization. The low-temperature component is strongly scattered, and the high-temperature component has a stable direction toward the origin. **B.** Thermal demagnetization of Sample 183-1139A-65R-3, 22–24 cm, from Unit 10. The NRM is a two-component magnetization with only small scattering in both component directions. **C.** Thermal demagnetization of Sample 183-1139A-71R-3, 98–100 cm, from Unit 18. The NRM has only a high-temperature single component. J_0 is the magnetization intensity before thermal treatment.

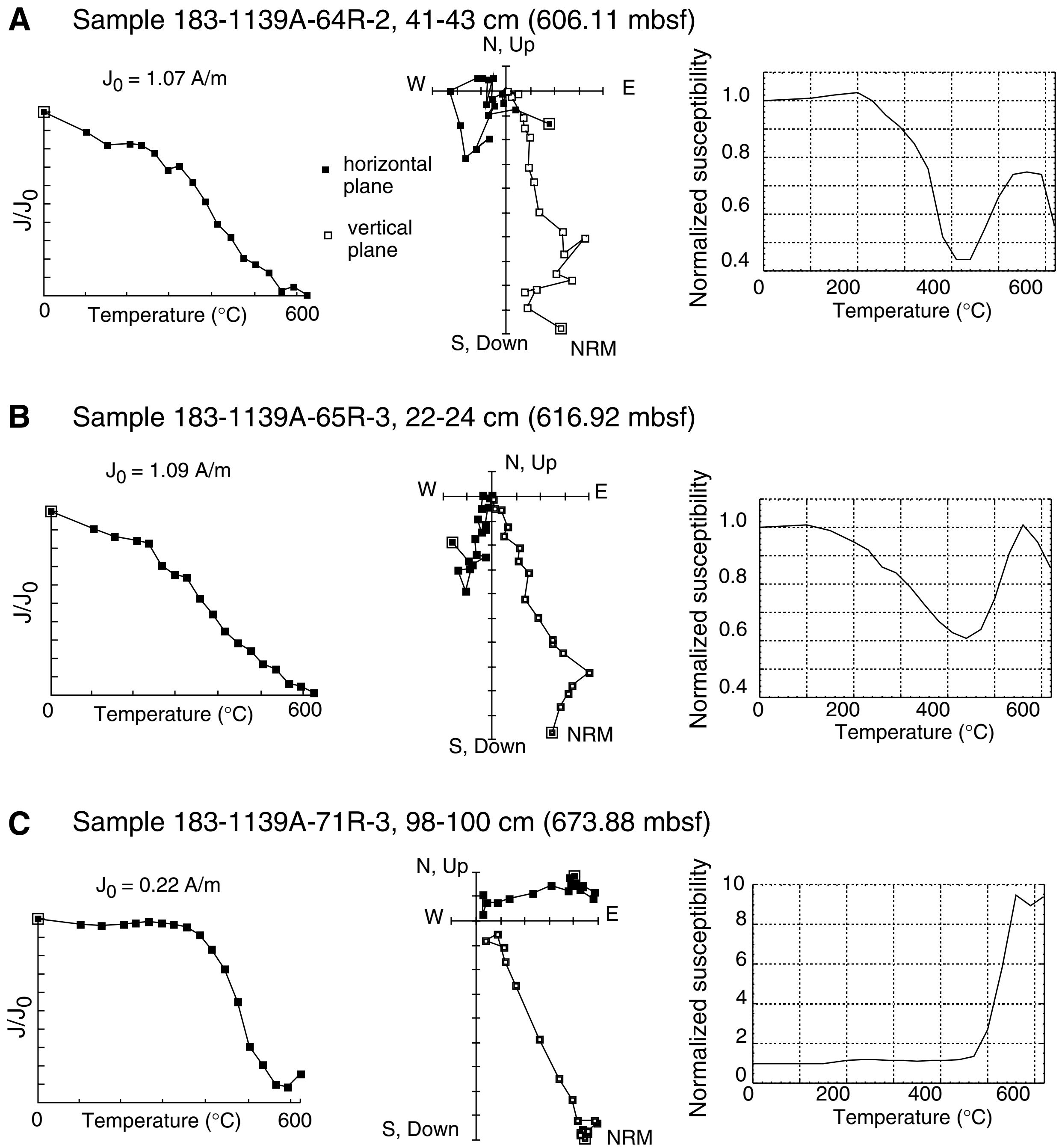

Figure F90. Downhole physical properties and compressional wave velocities at Site 1139. Horizontal solid lines separate the lithologic units and the dashed line shows the boundary between Subunits IA and IB. Lithologic units are shown on the right. Discrete measurements are of (**A**) bulk density, (**B**) grain density, (**C**) porosity, and (**D**) velocity. Arrows mark observed trends in the porosity data.

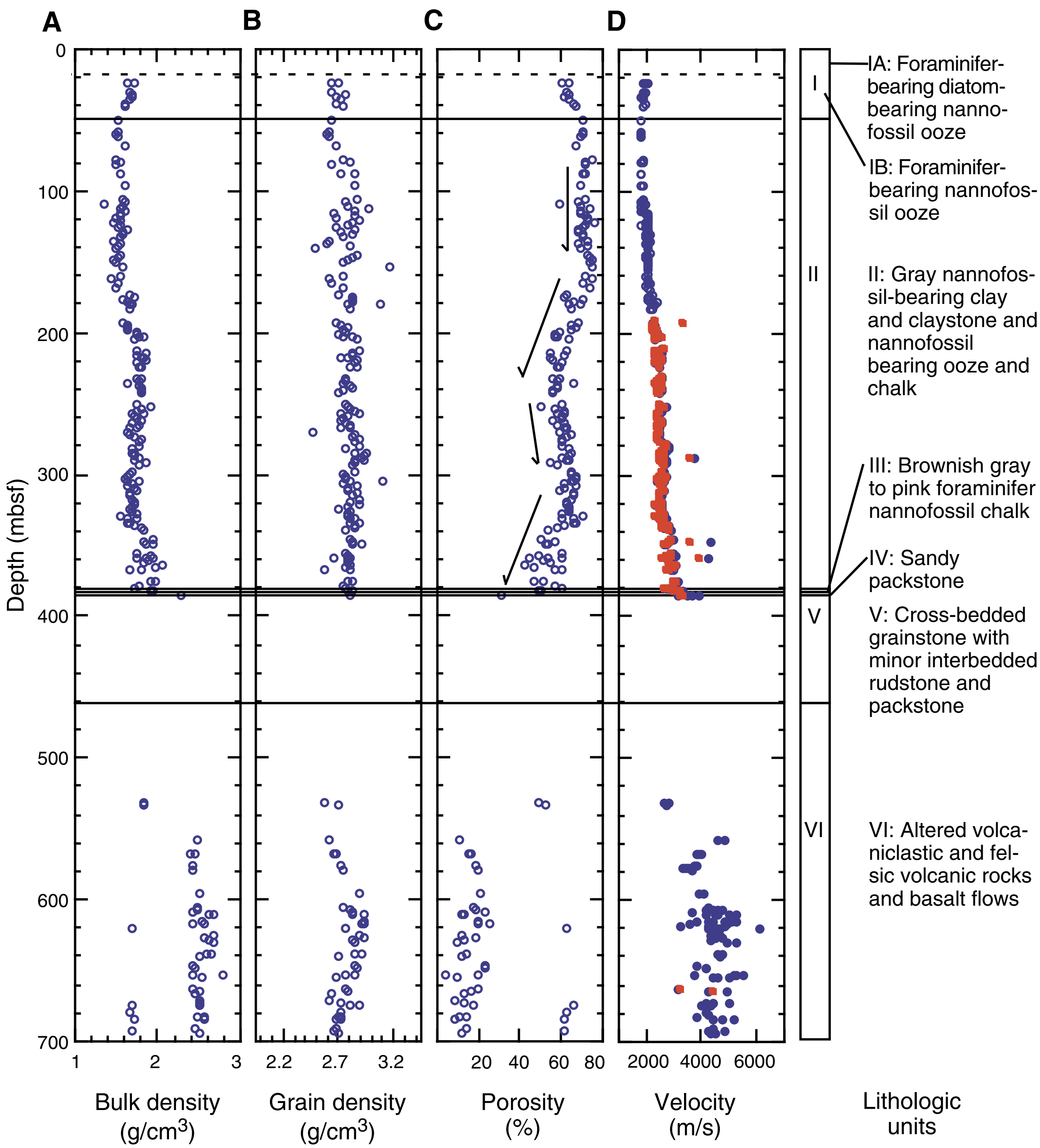

Figure F91. Downhole physical properties profiles of basement Units 2–19 in Hole 1139A. Discrete measurements are of (**A**) bulk density, (**B**) grain density, (**C**) porosity, and (**D**) discrete velocity. This figure is an subset of results shown in Figure F90, p. 165.

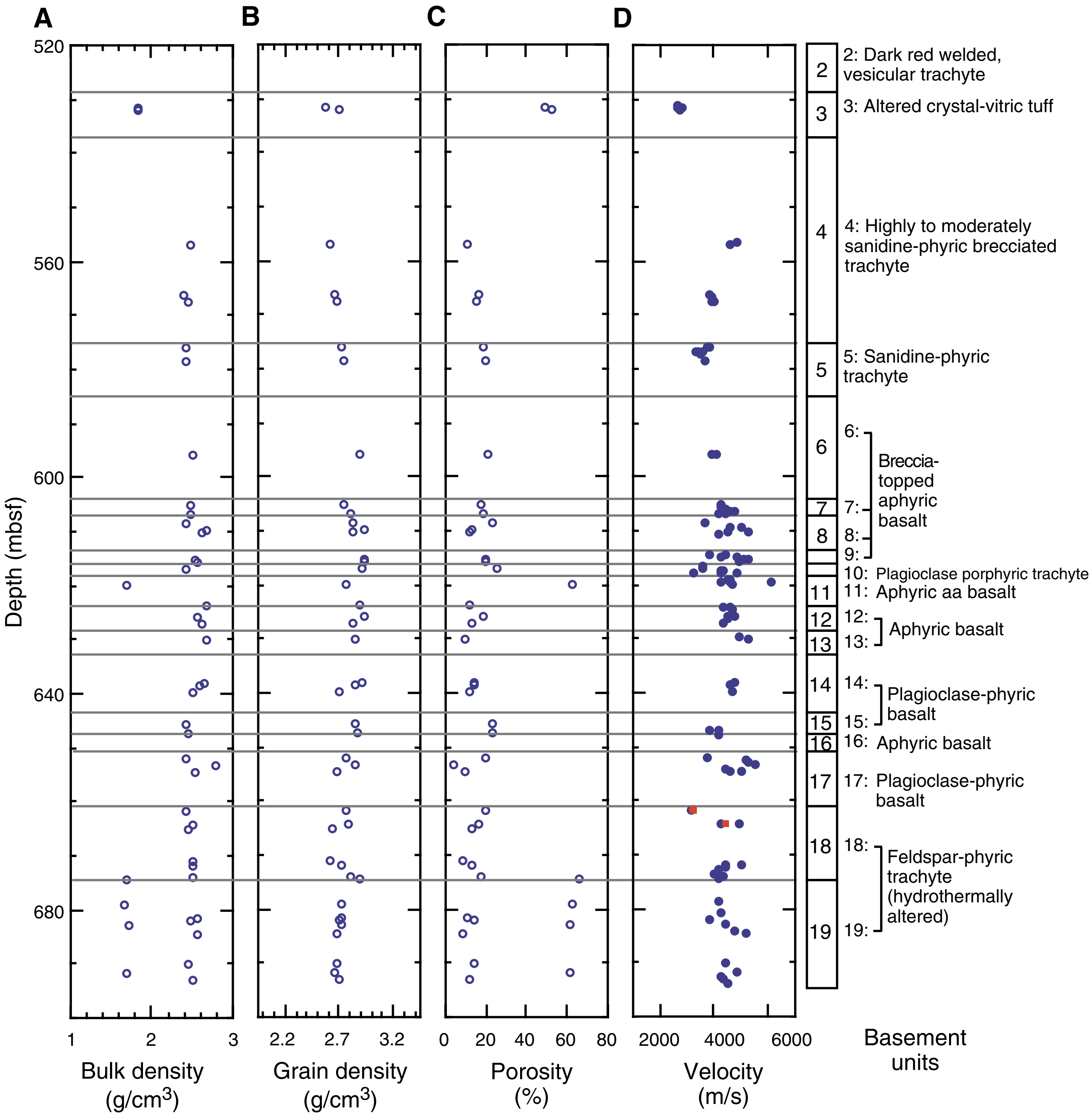

Figure F92. Downhole profiles of MST measurements along with discrete measurements. **A.** GRAPE bulk density (red) and bulk density derived from discrete samples at Site 1139 (dots associated with solid line). **B.** Whole-core measurements of magnetic susceptibility. **C.** Natural gamma ray. Horizontal solid lines separates the lithologic units, and the dashed line shows the boundary between Subunits IA and IB. Lithologic units are shown to the right.

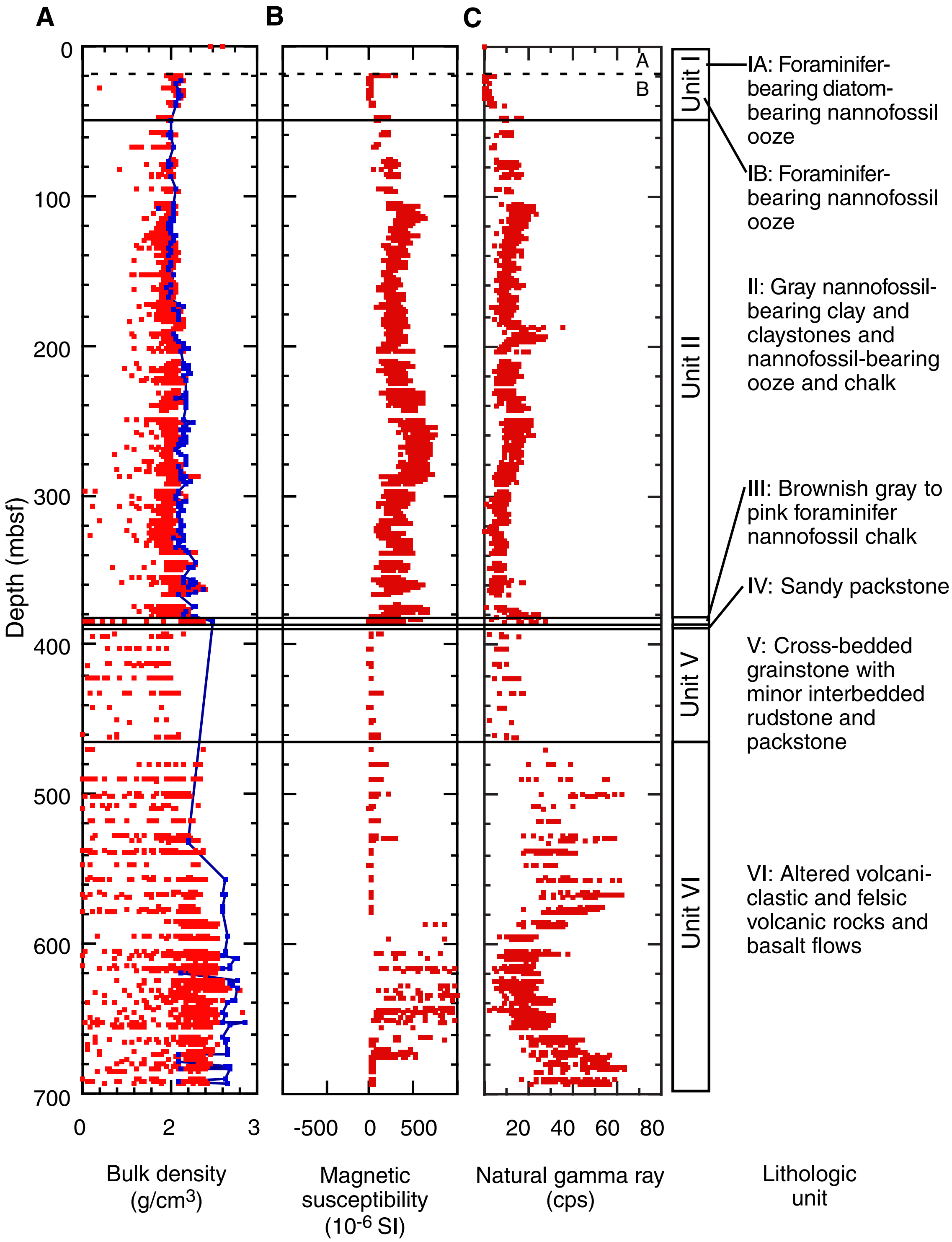

Figure F93. Downhole profile of whole-core measurements of thermal conductivity on whole-core soft sediments and on split-core pieces of hard rocks from Hole 1139A.

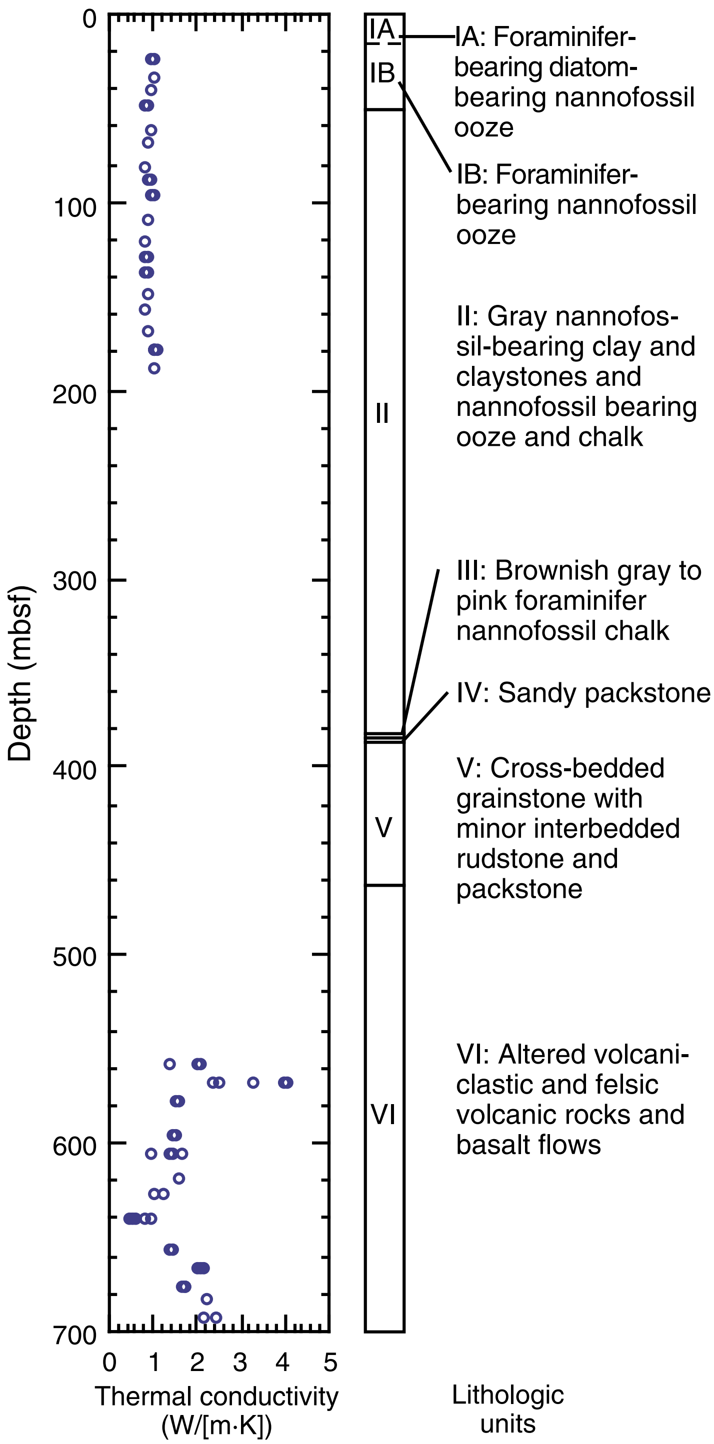

Figure F94. Comparison of densities determined from core samples and gamma-ray attenuation porosity evaluator and compressional wave velocities from downhole logs and core samples. Raw and robust mode filtered data are shown. Note the unexplained offset between log and sample velocities. **A.** 10–240 mbsf. (Continued on next two pages.)

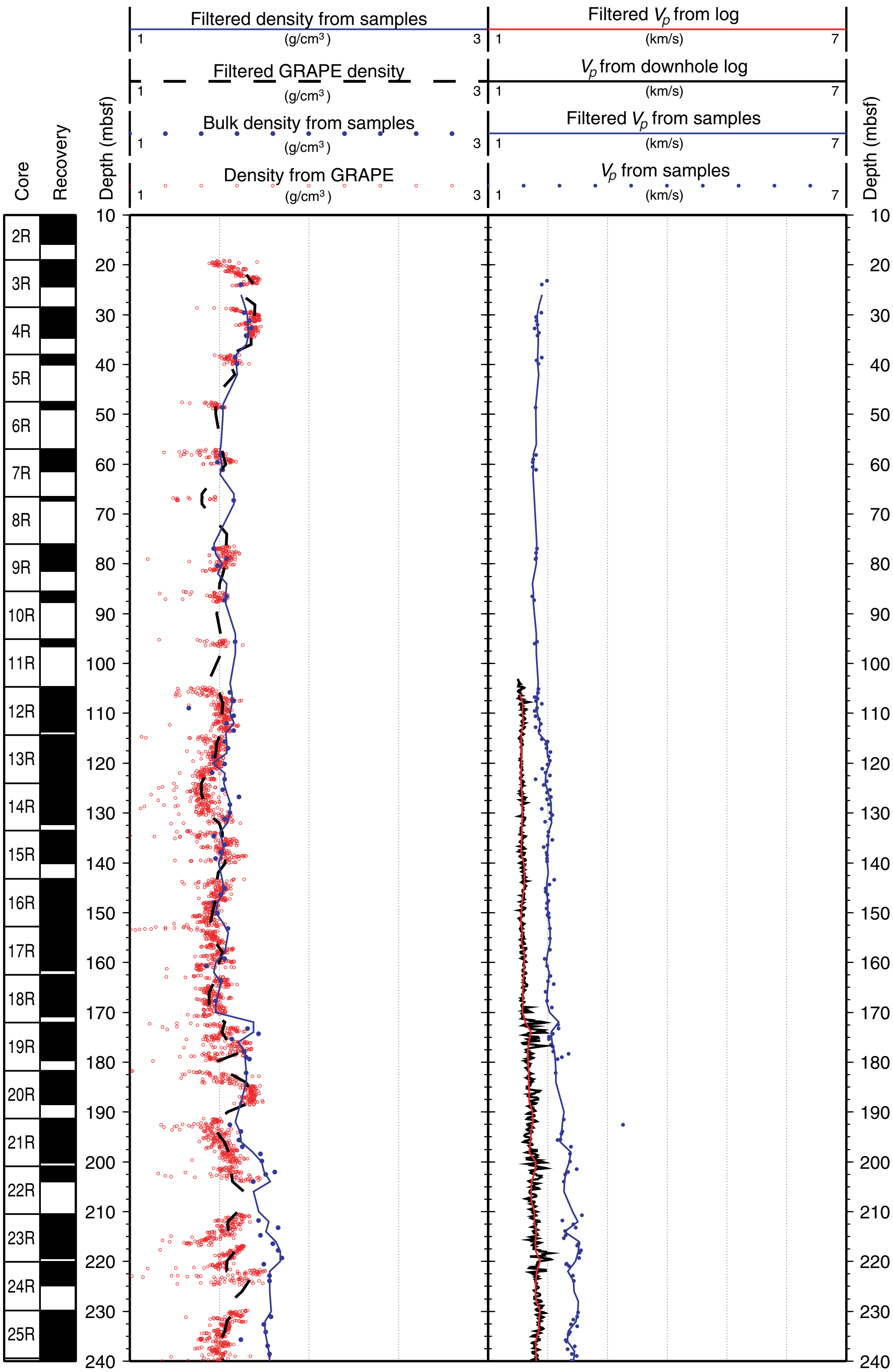

Figure F94 (continued). B. 240–470 mbsf.

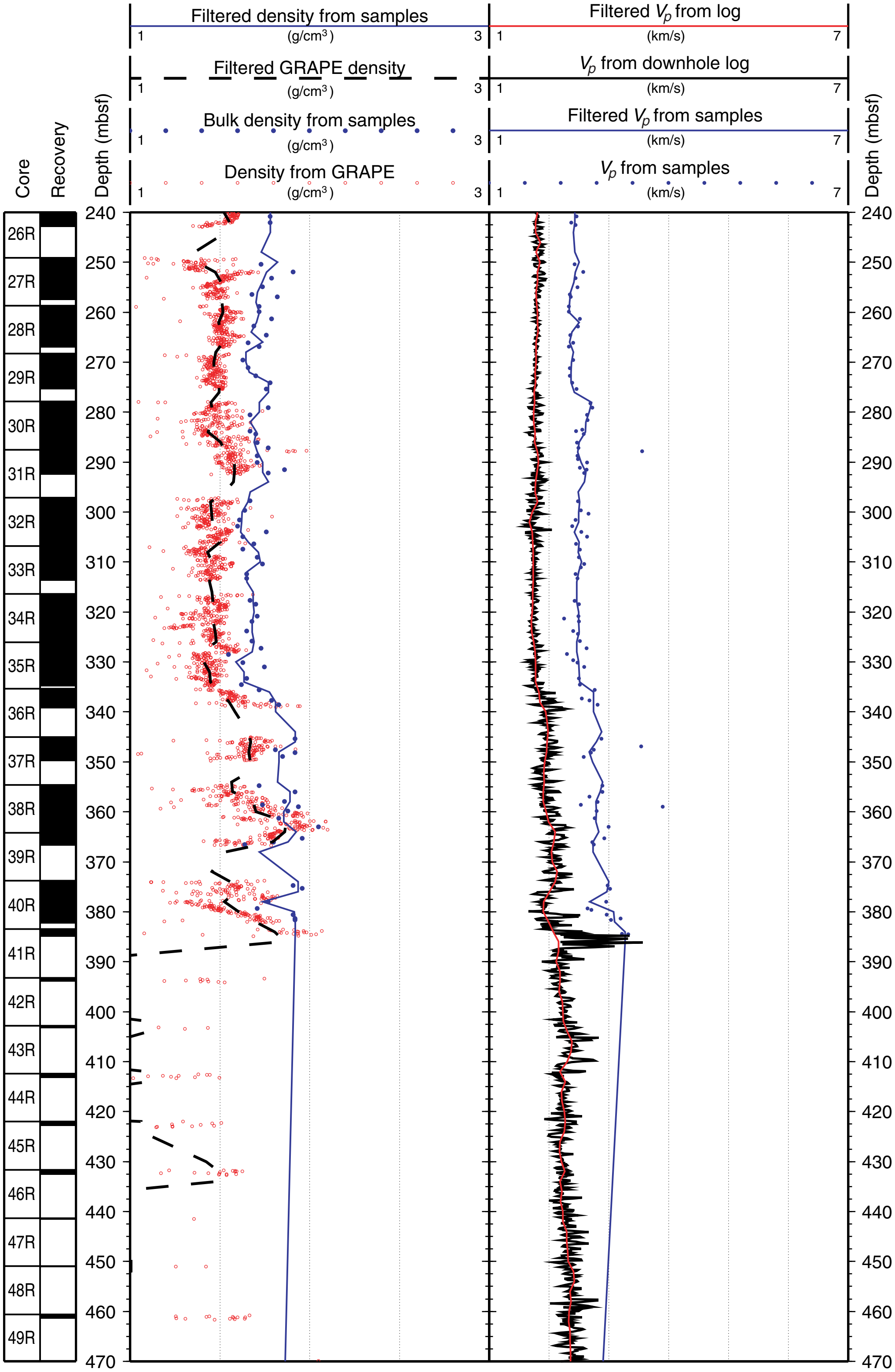

Figure F94 (continued). C. 470–700 mbsf.

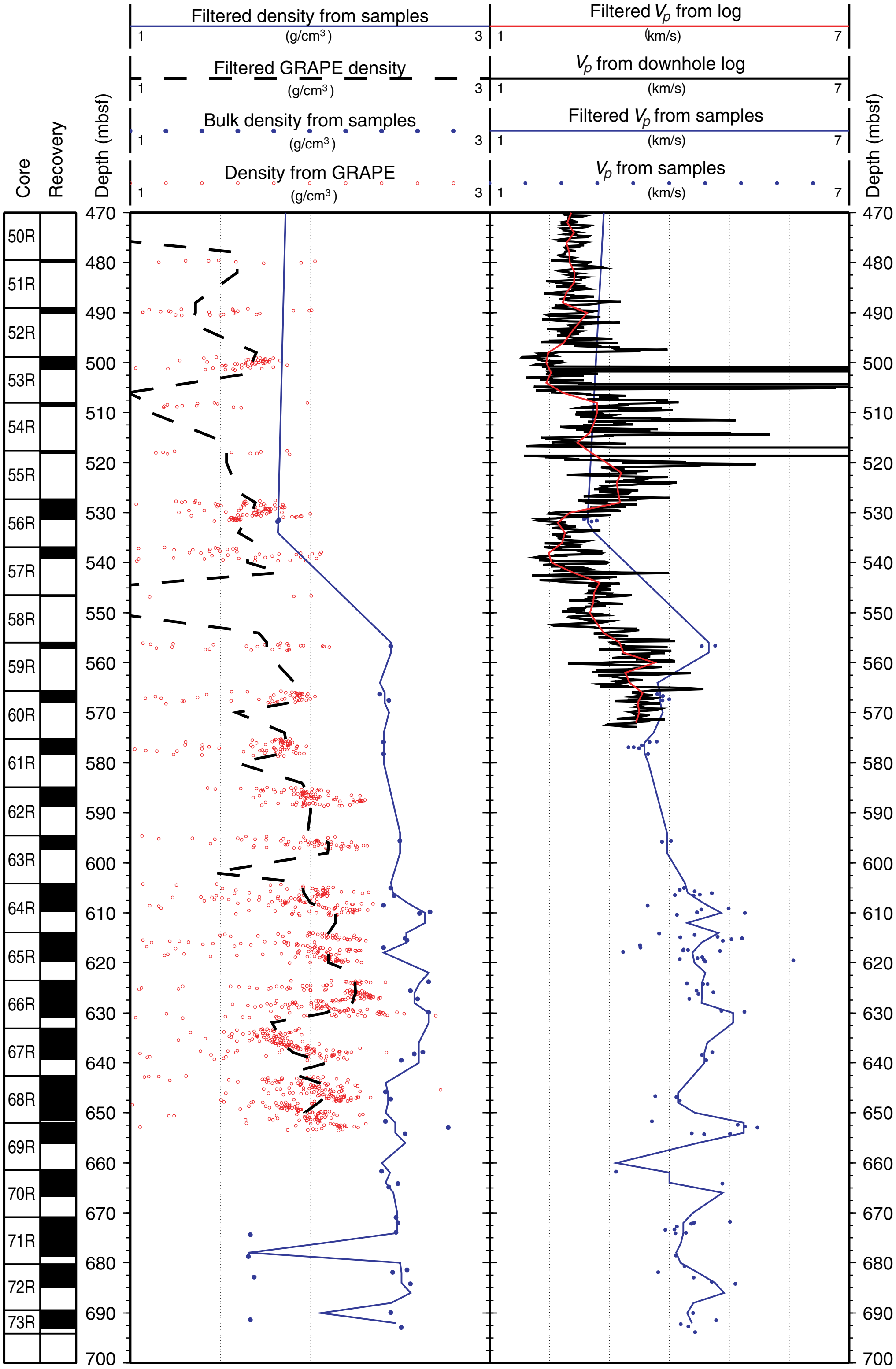

Figure F95. Composite of core recovery, curated stratigraphy, age, lithology, (**A**) density and velocity as a function of depth, (**B**) density and velocity as a function of two-way traveltime (TWT), (**C**) impedance, (**D**) reflection coefficients without interbed multiples and transmission losses, (**E**) reflection coefficients with interbed multiples and transmission losses, and (**F**) synthetic seismograms based on (D) (black) and (E) (red or gray) as a function of TWT. sbsf = seconds below seafloor. **(Figure shown on next page.)**

Figure F95 (Caption on previous page).

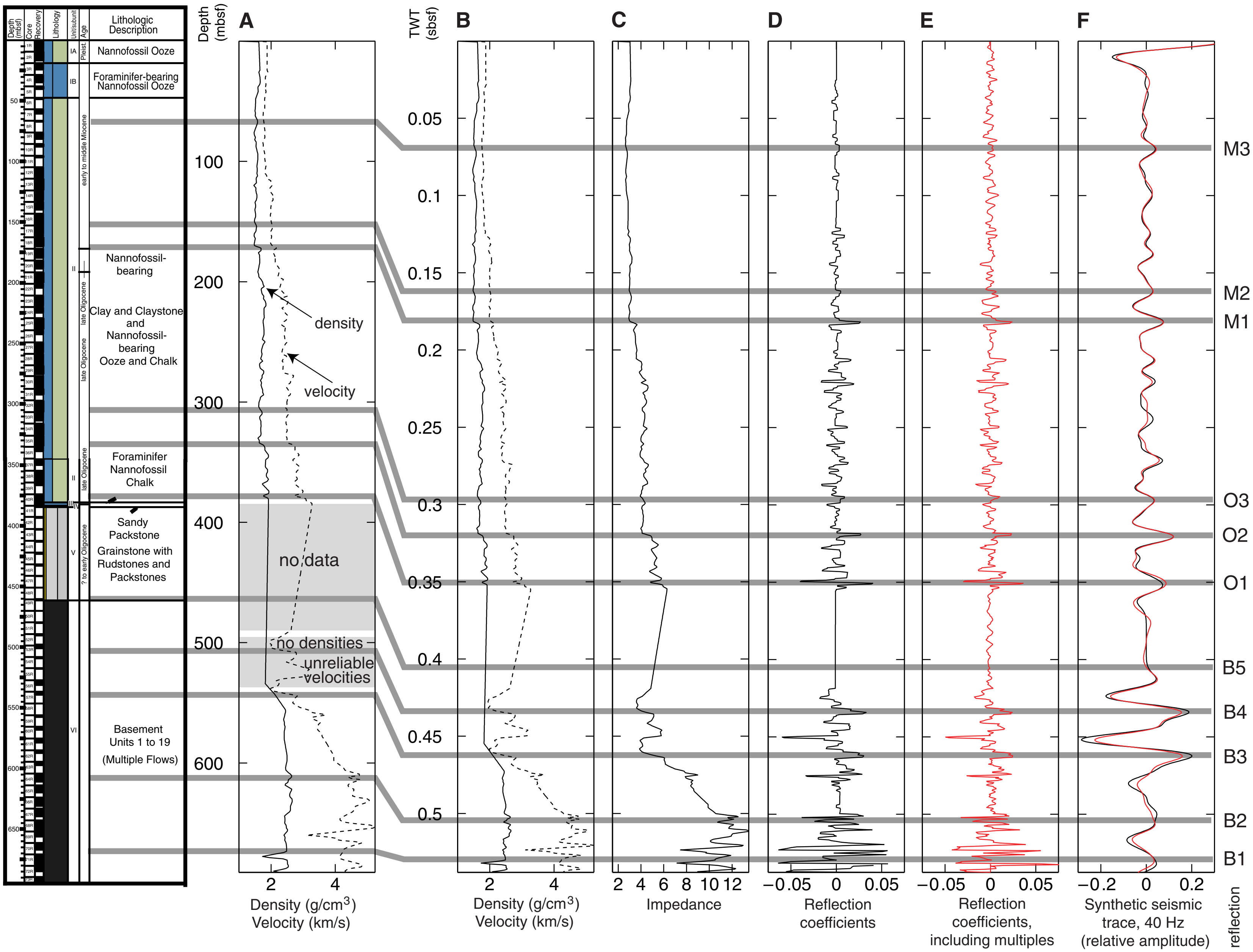

Figure F96. Portion of seismic reflection line 05 from *Marion Dufresne* cruise 109 across Site 1139 and a synthetic seismic trace from Figure F95, p. 172, including multiples and transmission losses. Reflections tied to the synthetic seismogram are labeled as follows: M = early to middle Miocene, O = Oligocene, B = basement. The vertical exaggeration is ~16:1 at the seafloor.

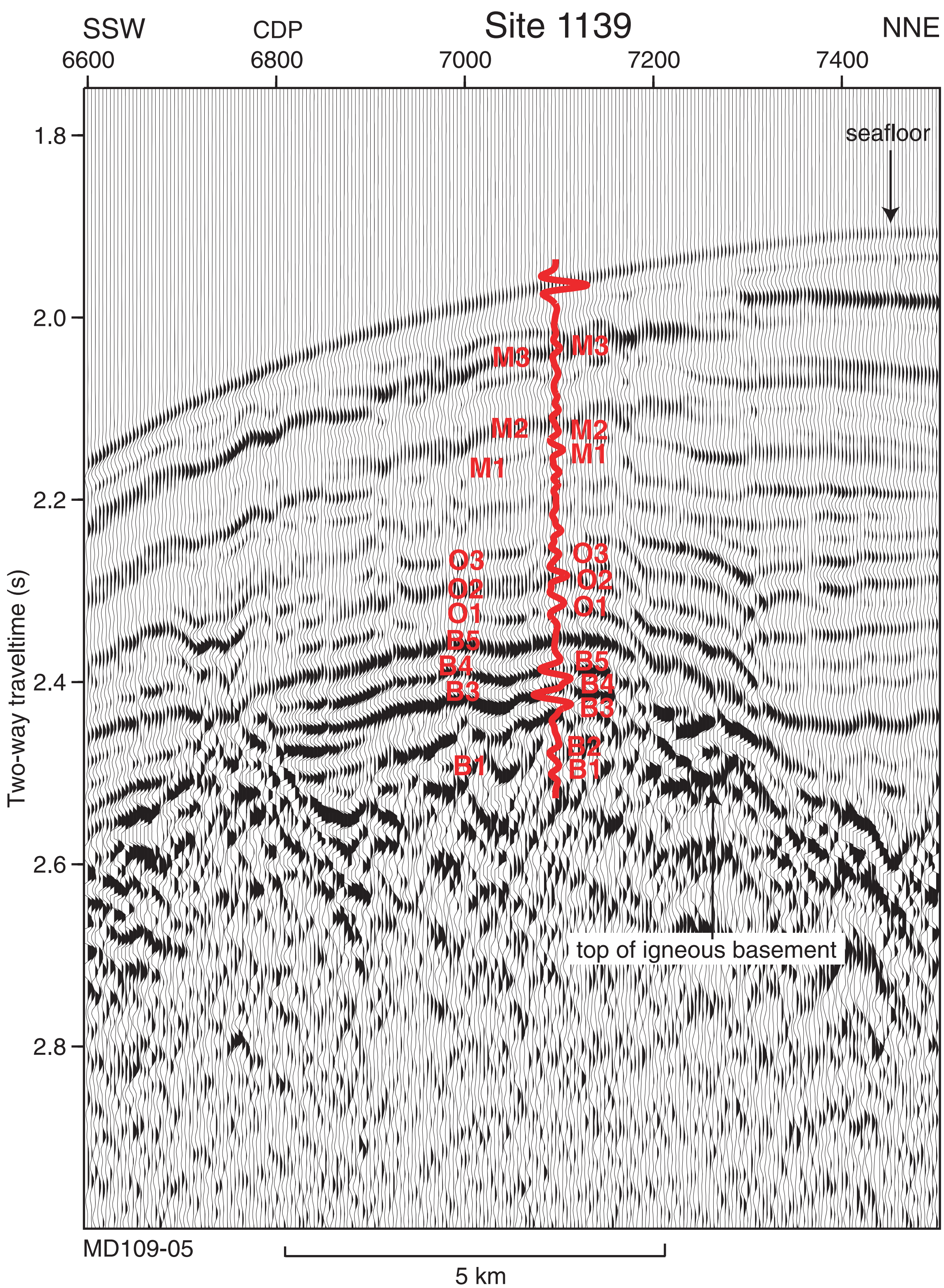

Figure F97. Overview of the logging data of Hole 1139A. (Continued on next page.)

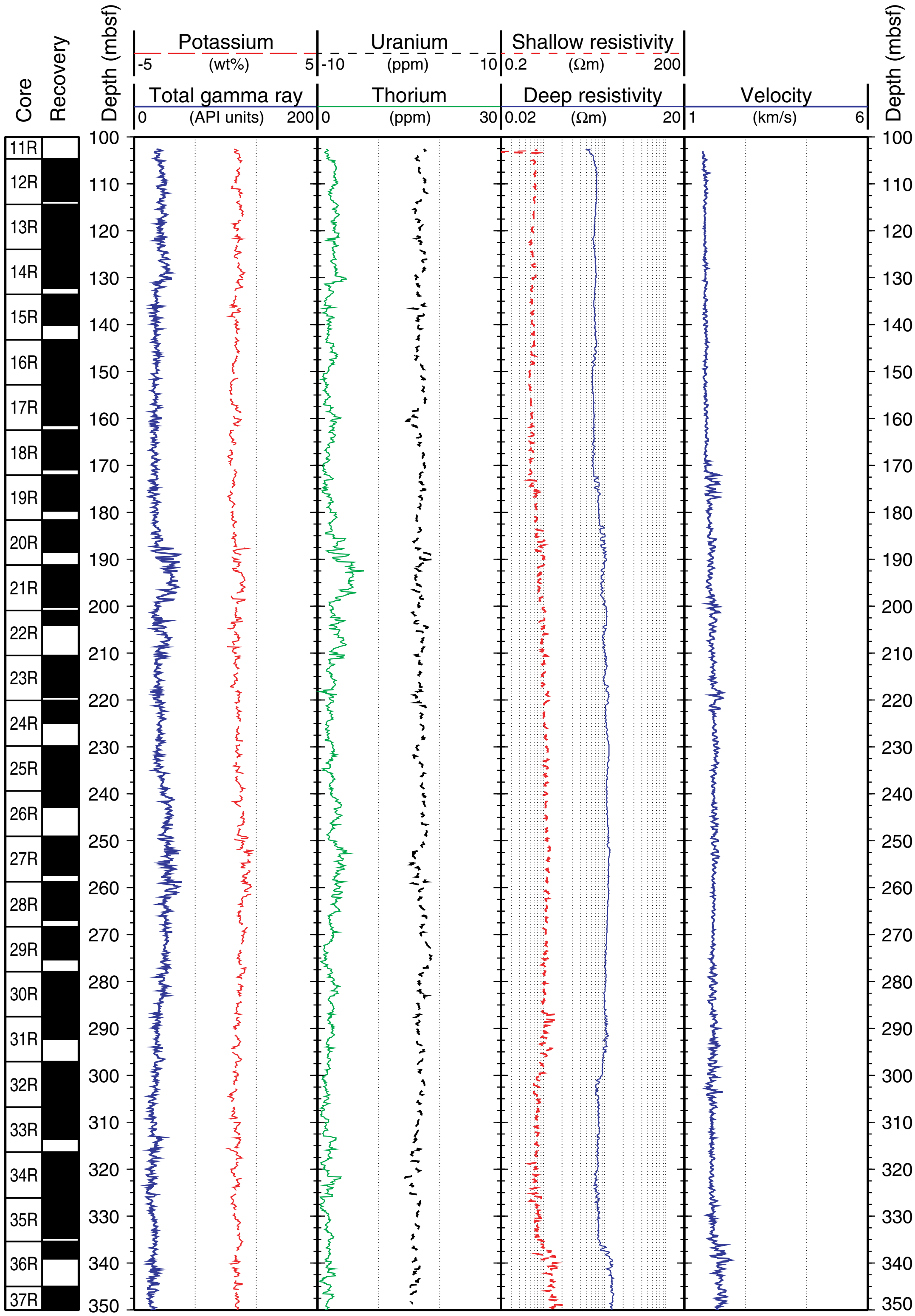

Figure F97 (continued).

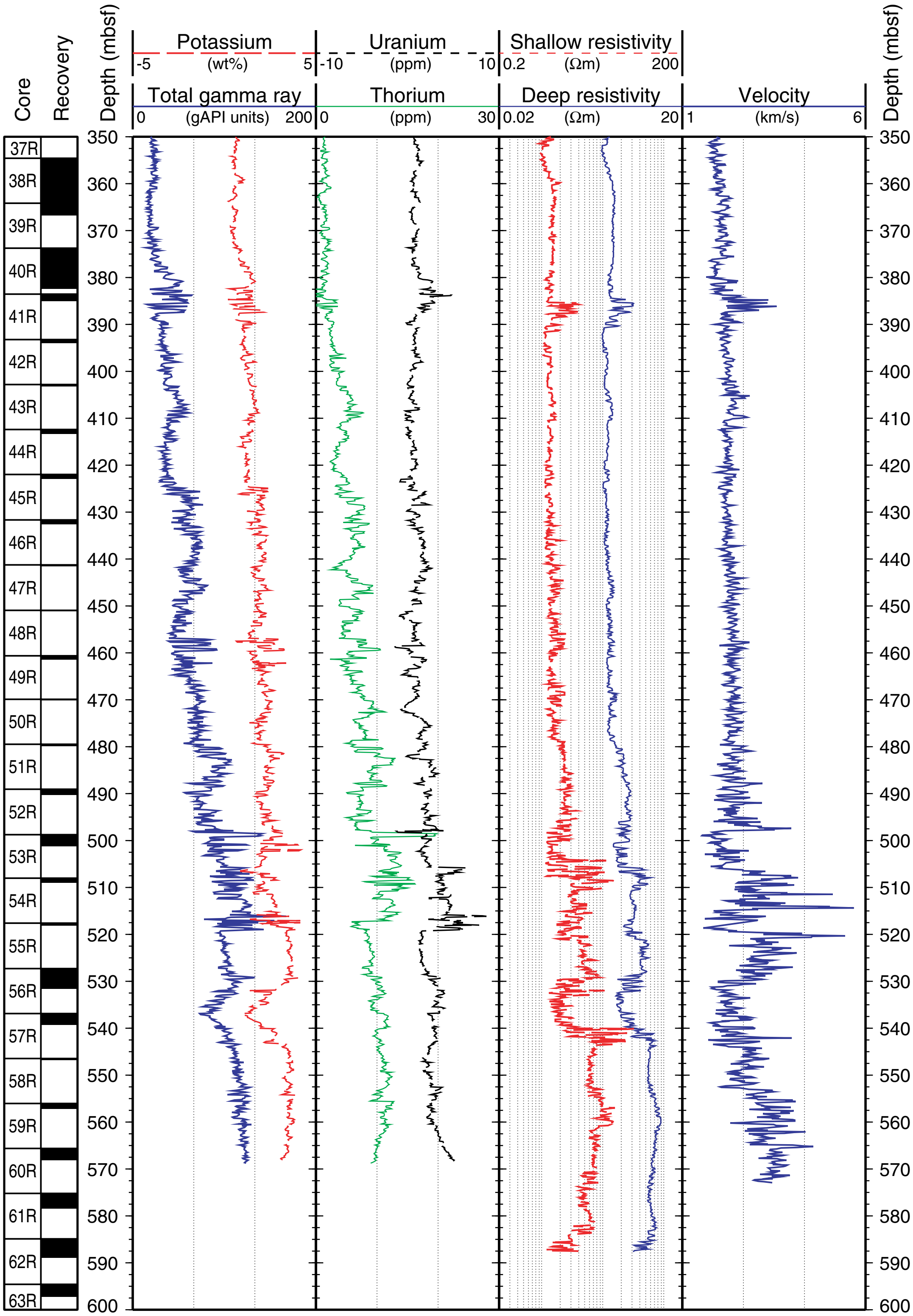

Figure F98. Comparison of core and log measurements to assess log quality from Hole 1139A. Thick lines may be correlated with unit boundaries; thin lines indicate variations within basement units. Total natural gamma radiation of the formation determined from downhole logs and multisensor track (MST) continuous measurements agree well. Velocity logging data and discrete core measurements are offset in the sediments (see **"Seismic Stratigraphy,"** p. 54). We compare shallow resistivity log data to MST density measurements to correlate general trends. In the sedimentary section, the shallow resistivity positively correlates with the density data.

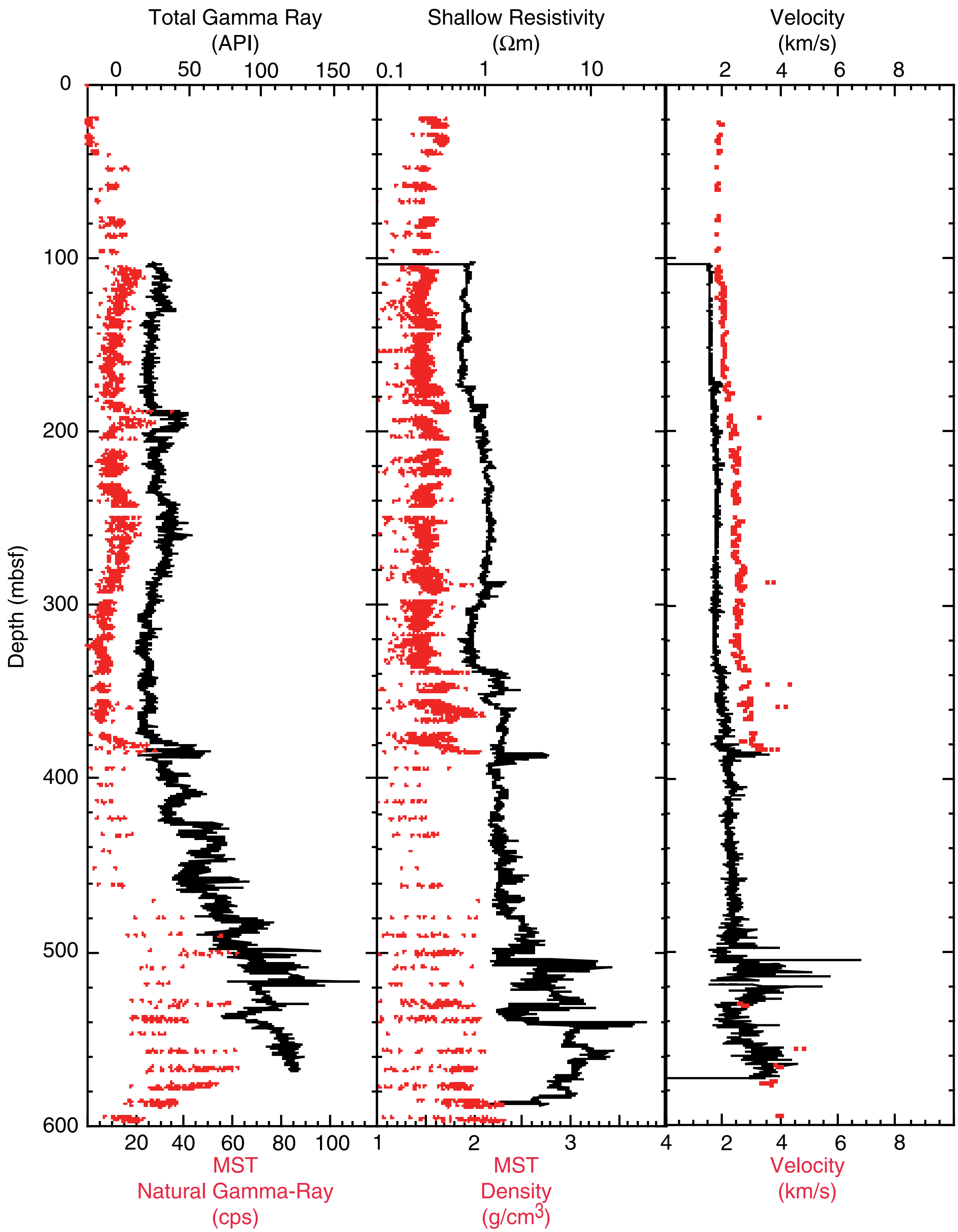

Figure F99. Correlation of core lithology and logging results from Hole 1139A.

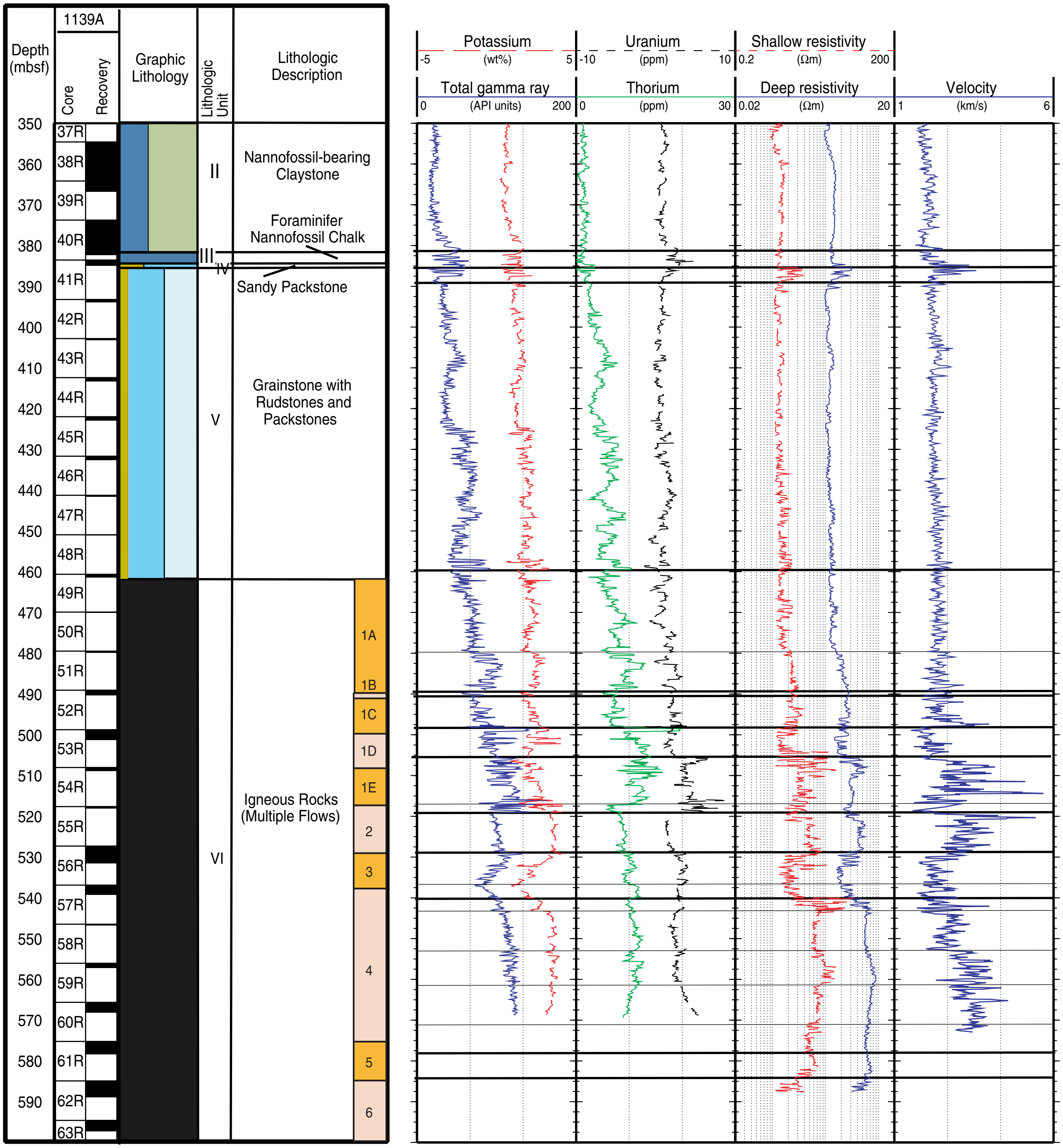

Figure F100. Temperatures measured in Hole 1139A by the Lamont-Doherty Earth Observatory (LDEO) temperature and pressure tool (TAP) show a different temperature gradient in the basement than in the overlying sediments.

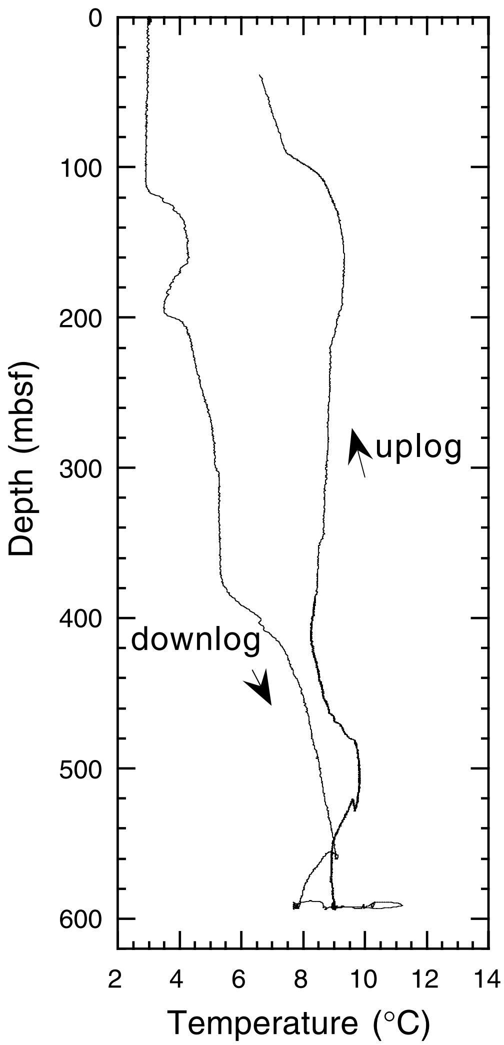

Table T1. Coring summary for Site 1139. (See table note. Continued on next page.)

Core	Date (Jan 1999)	Time (UTC)	Depth (mbsf)	Length (m) Cored	Length (m) Recovered	Recovery (%)
183-1139A-						
1R	15	0740	0.0-9.5	9.5	7.87	82.8
2R	15	0820	9.5-19.0	9.5	6.43	67.7
3R	15	0905	19.0-28.5	9.5	5.43	57.2
4R	15	0950	28.5-38.0	9.5	6.32	66.5
5R	15	1040	38.0-47.5	9.5	2.21	23.3
6R	15	1125	47.5-57.0	9.5	1.69	17.8
7R	15	1210	57.0-66.5	9.5	4.60	48.4
8R	15	1250	66.5-76.0	9.5	1.02	10.7
9R	15	1335	76.0-85.5	9.5	5.58	58.7
10R	15	1420	85.5-95.1	9.6	2.33	24.3
11R	15	1500	95.1-104.7	9.6	1.66	17.3
12R	15	1540	104.7-114.4	9.7	9.13	94.1
13R	15	1610	114.4-124.0	9.6	9.47	98.6
14R	15	1645	124.0-133.5	9.5	8.39	88.3
15R	15	1715	133.5-143.2	9.7	6.74	69.5
16R	15	1740	143.2-152.8	9.6	9.81	102.2
17R	15	1810	152.8-162.5	9.7	8.90	91.8
18R	15	1840	162.5-172.1	9.6	8.52	88.8
19R	15	1915	172.1-181.7	9.6	7.70	80.2
20R	15	1945	181.7-191.3	9.6	6.93	72.2
21R	15	2020	191.3-200.9	9.6	9.00	93.8
22R	15	2115	200.9-210.5	9.6	3.24	33.8
23R	15	2200	210.5-220.1	9.6	8.98	93.5
24R	15	2250	220.1-229.8	9.7	4.87	50.2
25R	15	2330	229.8-239.4	9.6	9.42	98.1
26R	16	0015	239.4-249.1	9.7	3.55	36.6
27R	16	0115	249.1-258.7	9.6	8.44	87.9
28R	16	0155	258.7-268.3	9.6	8.35	87.0
29R	16	0230	268.3-277.9	9.6	7.20	75.0
30R	16	0310	277.9-287.5	9.6	10.02	104.4
31R	16	0345	287.5-297.1	9.6	4.97	51.8
32R	16	0445	297.1-306.8	9.7	9.69	99.9
33R	16	0520	306.8-316.4	9.6	6.93	72.2
34R	16	0555	316.4-326.1	9.7	9.49	97.8
35R	16	0635	326.1-335.4	9.3	8.82	94.8
36R	16	0720	335.4-345.0	9.6	3.92	40.8
37R	16	0815	345.0-354.6	9.6	4.81	50.1
38R	16	0920	354.6-364.2	9.6	10.01	104.3
39R	16	1000	364.2-373.8	9.6	2.55	26.6
40R	16	1045	373.8-383.5	9.7	8.62	88.9
41R	16	1130	383.5-393.2	9.7	1.45	14.9
42R	16	1225	393.2-402.8	9.6	0.77	8.0
43R	16	1305	402.8-412.4	9.6	0.47	4.9
44R	16	1355	412.4-422.0	9.6	0.90	9.4
45R	16	1440	422.0-431.7	9.7	0.87	9.0
46R	16	1530	431.7-441.3	9.6	0.95	9.9
47R	16	1615	441.3-450.9	9.6	0.31	3.2
48R	16	1725	450.9-460.6	9.7	0.22	2.3
49R	16	1845	460.6-469.9	9.3	0.90	9.7
50R	16	1945	469.9-479.5	9.6	0.24	2.5
51R	16	2055	479.5-489.1	9.6	0.44	4.6
52R	16	2255	489.1-498.8	9.7	1.21	12.5
53R	17	0040	498.8-508.0	9.2	2.50	27.2
54R	17	0225	508.0-517.6	9.6	0.92	9.6
55R	17	0405	517.6-527.3	9.7	0.57	5.9
56R	17	0535	527.3-536.9	9.6	4.27	44.5
57R	17	0725	536.9-546.5	9.6	2.34	24.4
58R	17	0905	546.5-556.0	9.5	0.30	3.2
59R	17	1100	556.0-565.6	9.6	1.20	12.5
60R	17	1245	565.6-575.2	9.6	2.54	26.5
61R	17	1435	575.2-584.9	9.7	3.22	33.2
62R	17	1650	584.9-594.6	9.7	4.01	41.3
63R	17	2015	594.6-604.2	9.6	2.73	28.4
64R	17	2345	604.2-613.9	9.7	5.65	58.2

Table T1 (continued).

Core	Date (Jan 1999)	Time (UTC)	Depth (mbsf)	Length (m) Cored	Length (m) Recovered	Recovery (%)
65R	18	0315	613.9-623.5	9.6	5.90	61.5
66R	18	0720	623.5-633.1	9.6	7.54	78.5
67R	18	1035	633.1-642.6	9.5	6.19	65.2
68R	18	1345	642.6-652.0	9.4	8.88	94.5
69R	18	1725	652.0-661.5	9.5	4.17	43.9
70R	18	2050	661.5-670.9	9.4	5.36	57.0
71R	19	0045	670.9-680.3	9.4	7.89	83.9
72R	19	0455	680.3-689.5	9.2	4.57	49.7
73R	19	0715	689.5-694.2	4.7	3.79	80.6
			Totals:	694.2	356.88	51.4

Note: UTC = Universal Time Coordinated. This table is also available in **ASCII format.**

Table T2. Expanded coring summary for Hole 1139A. (See table note. Continued on next six pages.)

Core	Date (Jan 1999)	Time (UTC)	Depth (mbsf)	Length (m)		Recovery (%)	Section	Length (m)		Section depth (mbsf)	Catwalk samples	Comment
				Cored	Recovered			Liner	Curated			
183-1139A-												
1R	15	0740	0.0-9.5	9.5	7.87	82.8						
							1	0.90	0.90	0.0-0.9		
							2	1.50	1.50	0.9-2.4		
							3	1.50	1.50	2.4-3.9		
							4	0.26	0.26	3.9-4.16		
							5	1.50	1.50	4.16-5.66		
							6	1.50	1.50	5.66-7.16	HS	
							7	0.44	0.44	7.16-7.6		
							CC(w/7)	0.27	0.27	7.6-7.87	PAL	
								7.87	7.87			
2R	15	0820	9.5-19.0	9.5	6.43	67.7						
							1	1.50	1.50	9.5-11.0		
							2	1.50	1.50	11.0-12.5		
							3	1.50	1.50	12.5-14.0		
							4	1.50	1.50	14.0-15.5	HS	
							5	0.24	0.24	15.5-15.74		
							CC(w/5)	0.19	0.19	15.74-15.93	PAL	
								6.43	6.43			
3R	15	0905	19.0-28.5	9.5	5.43	57.2						
							1	1.50	1.50	19.0-20.5		
							2	1.50	1.50	20.5-22.0		
							3	1.50	1.50	22.0-23.5	HS	
							4	0.74	0.74	23.5-24.24		
							CC(w/4)	0.19	0.19	24.24-24.43	PAL	
								5.43	5.43			
4R	15	0950	28.5-38.0	9.5	6.32	66.5						
							1	1.50	1.50	28.5-30.0		
							2	1.50	1.50	30.0-31.5		
							3	1.50	1.50	31.5-33.0	MAI	
							4	1.50	1.50	33.0-34.5	HS	
							CC(w/CC)	0.32	0.32	34.5-34.82	PAL	
								6.32	6.32			
5R	15	1040	38.0-47.5	9.5	2.21	23.3						
							1	1.50	1.50	38.0-39.5		
							2	0.46	0.46	39.5-39.96	HS	
							CC(w/2)	0.25	0.25	39.96-40.21	PAL	
								2.21	2.21			
6R	15	1125	47.5-57.0	9.5	1.69	17.8						
							1	1.43	1.43	47.5-48.93	HS	
							CC(w/CC)	0.26	0.26	48.93-49.19	PAL	
								1.69	1.69			
7R	15	1210	57.0-66.5	9.5	4.6	48.4						
							1	1.50	1.50	57.0-58.5		
							2	1.50	1.50	58.5-60.0		
							3	1.33	1.33	60.0-61.33	HS	
							CC(w/CC)	0.27	0.27	61.33-61.6	PAL	
								4.60	4.60			
8R	15	1250	66.5-76.0	9.5	1.02	10.7						
							1	0.82	0.82	66.5-67.32	HS	
							CC(w/1)	0.20	0.20	67.32-67.52	PAL	
								1.02	1.02			
9R	15	1335	76.0-85.5	9.5	5.58	58.7						
							1	0.34	0.34	76.0-76.34		Disturbed
							2	1.50	1.50	76.34-77.84		Replaced liner
							3	1.50	1.50	77.84-79.34		Replaced liner
							4	1.50	1.50	79.34-80.84	HS	Liner patch
							5	0.31	0.31	80.84-81.15		
							CC(w/5)	0.43	0.43	81.15-81.58	PAL	
								5.58	5.58			
10R	15	1420	85.5-95.1	9.6	2.33	24.3						
							1	1.50	1.50	85.5-87.0		
							2	0.64	0.64	87.0-87.64	HS	
							CC(w/2)	0.19	0.19	87.64-87.83	PAL	
								2.33	2.33			
11R	15	1500	95.1-104.7	9.6	1.66	17.3						
							1	1.50	1.50	95.1-96.6	HS	
							CC(w/CC)	0.16	0.16	96.6-96.76	PAL	

Table T2 (continued).

Core	Date (Jan 1999)	Time (UTC)	Depth (mbsf)	Length (m) Cored	Length (m) Recovered	Recovery (%)	Section	Length (m) Liner	Length (m) Curated	Section depth (mbsf)	Catwalk samples	Comment
								1.66	1.66			
12R	15	1540	104.7-114.4	9.7	9.13	94.1						
							1	1.50	1.50	104.7-106.2		
							2	1.50	1.50	106.2-107.7		
							3	1.50	1.50	107.7-109.2		
							4	1.50	1.50	109.2-110.7	MAI	
							5	1.50	1.50	110.7-112.2		
							6	1.50	1.50	112.2-113.7	HS	
							CC(w/CC)	0.13	0.13	113.7-113.83	PAL	
								9.13	9.13			
13R	15	1610	114.4-124.0	9.6	9.47	98.6						
							1	1.50	1.50	114.4-115.9		
							2	1.50	1.50	115.9-117.4		
							3	1.50	1.50	117.4-118.9		
							4	1.50	1.50	118.9-120.4		
							5	1.50	1.50	120.4-121.9	HS	
							6	1.50	1.50	121.9-123.4		
							7	0.27	0.27	123.4-123.67		
							CC(w/7)	0.20	0.20	123.67-123.87	PAL	
								9.47	9.47			
14R	15	1645	124.0-133.5	9.5	8.39	88.3						
							1	1.50	1.50	124.0-125.5		
							2	1.50	1.50	125.5-127.0		
							3	1.50	1.50	127.0-128.5		
							4	1.50	1.50	128.5-130.0		
							5	1.50	1.50	130.0-131.5	HS	
							6	0.69	0.69	131.5-132.19		
							CC(w/6)	0.20	0.20	132.19-132.39	PAL	
								8.39	8.39			
15R	15	1715	133.5-143.2	9.7	6.74	69.5						
							1	1.50	1.50	133.5-135.0		
							2	1.50	1.50	135.0-136.5		
							3	1.50	1.50	136.5-138.0	HS	
							4	1.50	1.50	138.0-139.5		
							5	0.53	0.53	139.5-140.03		
							CC(w/5)	0.21	0.21	140.03-140.24		
								6.74	6.74			
16R	15	1740	143.2-152.8	9.6	9.81	102.2						
							1	1.50	1.50	143.2-144.7		
							2	1.50	1.50	144.7-146.2		
							3	1.50	1.50	146.2-147.7		
							4	1.50	1.50	147.7-149.2		
							5	1.50	1.50	149.2-150.7		
							6	1.50	1.50	150.7-152.2	HS	
							7	0.59	0.59	152.2-152.79		
							CC(w/7)	0.22	0.22	152.79-153.01		
								9.81	9.81			
17R	15	1810	152.8-162.5	9.7	8.9	91.8						
							1	1.50	1.50	152.8-154.3		
							2	1.50	1.50	154.3-155.8		
							3	1.50	1.50	155.8-157.3		
							4	1.50	1.50	157.3-158.8	HS	
							5	1.50	1.50	158.8-160.3		
							6	1.24	1.24	160.3-161.54		
							CC(w/6)	0.16	0.16	161.54-161.7		
								8.9	8.9			
18R	15	1840	162.5-172.1	9.6	8.52	88.8						
							1	1.50	1.50	162.5-164.0		
							2	1.50	1.50	164.0-165.5		
							3	1.50	1.50	165.5-167.0		
							4	1.50	1.50	167.0-168.5	HS	
							5	1.50	1.50	168.5-170.0		
							6	0.85	0.85	170.0-170.85		
							CC(w/6)	0.17	0.17	170.85-171.02		
								8.52	8.52			
19R	15	1915	172.1-181.7	9.6	7.7	80.2						
							1	1.50	1.50	172.1-173.6		Other
							2	1.50	1.50	173.6-175.1	HS	

Table T2 (continued).

Core	Date (Jan 1999)	Time (UTC)	Depth (mbsf)	Length (m) Cored	Length (m) Recovered	Recovery (%)	Section	Length (m) Liner	Length (m) Curated	Section depth (mbsf)	Catwalk samples	Comment
							3	1.50	1.50	175.1-176.6		
							4	1.50	1.50	176.6-178.1		
							5	1.00	1.00	178.1-179.1		
							6	0.65	0.65	179.1-179.75		
							CC(NS)	0.05	0.05	179.75-179.8	PAL	All to PAL
								7.70	7.70			
20R	15	1945	181.7-191.3	9.6	6.93	72.2						
							1	1.50	1.50	181.7-183.2		
							2	1.50	1.50	183.2-184.7		
							3	1.50	1.50	184.7-186.2	HS	
							4	1.50	1.50	186.2-187.7		
							5	0.88	0.88	187.7-188.58		
							CC(NS)	0.05	0.05	188.58-188.63	PAL	All to PAL
								6.93	6.93			
21R	15	2020	191.3-200.9	9.6	9.0	93.8						
							1	1.50	1.50	191.3-192.8		
							2	1.50	1.50	192.8-194.3		
							3	1.50	1.50	194.3-195.8	MAI	
							4	1.50	1.50	195.8-197.3	HS	
							5	1.50	1.50	197.3-198.8		
							6	1.45	1.45	198.8-200.25		
							CC(NS)	0.05	0.05	200.25-200.3	PAL	All to PAL
								9.00	9.00			
22R	15	2115	200.9-210.5	9.6	3.24	33.8						
							1	1.50	1.50	200.9-202.4		
							2	1.00	1.00	202.4-203.4		
							3	0.61	0.61	203.4-204.01	HS	
							CC(w/3)	0.13	0.13	204.01-204.14		
								3.24	3.24			
23R	15	2200	210.5-220.1	9.6	8.98	93.5						
							1	1.50	1.50	210.5-212.0		
							2	1.50	1.50	212.0-213.5		
							3	1.50	1.50	213.5-215.0		
							4	1.50	1.50	215.0-216.5		
							5	1.50	1.50	216.5-218.0	HS	
							6	1.43	1.43	218.0-219.43		
							CC(NS)	0.05	0.05	219.43-219.48	PAL	All to PAL
								8.98	8.98			
24R	15	2250	220.1-229.8	9.7	4.87	50.2						
							1	1.50	1.50	220.1-221.6		
							2	1.50	1.50	221.6-223.1	HS	
							3	1.50	1.50	223.1-224.6		
							4	0.19	0.19	224.6-224.79		
							CC(w/4)	0.18	0.18	224.79-224.97	PAL	
								4.87	4.87			
25R	15	2330	229.8-239.4	9.6	9.42	98.1						
							1	1.50	1.50	229.8-231.3		
							2	1.50	1.50	231.3-232.8		
							3	1.50	1.50	232.8-234.3		
							4	1.50	1.50	234.3-235.8		
							5	1.50	1.50	235.8-237.3	HS	
							6	1.50	1.50	237.3-238.8		
							7	0.37	0.37	238.8-239.17		
							CC(NS)	0.05	0.05	239.17-239.22	PAL	All to PAL
								9.42	9.42			
26R	16	0015	239.4-249.1	9.7	3.55	36.6						
							1	1.50	1.50	239.4-240.9		
							2	1.50	1.50	240.9-242.4	HS	
							3	0.50	0.50	242.4-242.9		
							CC(NS)	0.05	0.05	242.9-242.95	PAL	All to PAL
								3.55	3.55			
27R	16	0115	249.1-258.7	9.6	8.44	87.9						
							1	1.50	1.50	249.1-250.6		
							2	1.50	1.50	250.6-252.1		
							3	1.50	1.50	252.1-253.6		
							4	1.50	1.50	253.6-255.1		
							5	1.50	1.50	255.1-256.6	HS	
							6	0.75	0.75	256.6-257.35		
							CC(w/6)	0.19	0.19	257.35-257.54	PAL	
								8.44	8.44			

Table T2 (continued).

Core	Date (Jan 1999)	Time (UTC)	Depth (mbsf)	Length (m) Cored	Length (m) Recovered	Recovery (%)	Section	Length (m) Liner	Length (m) Curated	Section depth (mbsf)	Catwalk samples	Comment
28R	16	0155	258.7-268.3	9.6	8.35	87.0						
							1	1.50	1.50	258.7-260.2		
							2	1.50	1.50	260.2-261.7		
							3	1.50	1.50	261.7-263.2		
							4	1.50	1.50	263.2-264.7	HS	
							5	1.50	1.50	264.7-266.2		
							6	0.75	0.75	266.2-266.95		
							CC(NS)	0.10	0.10	266.95-267.05	PAL	All to PAL
								8.35	8.35			
29R	16	0230	268.3-277.9	9.6	7.2	75.0						
							1	1.50	1.50	268.3-269.8		
							2	1.50	1.50	269.8-271.3		
							3	1.50	1.50	271.3-272.8		
							4	1.50	1.50	272.8-274.3	HS, MAI	
							5	1.15	1.15	274.3-275.45		
							CC(NS)	0.05	0.05	275.45-275.5	PAL	All to PAL
								7.20	7.20			
30R	16	0310	277.9-287.5	9.6	10.02	104.4						
							1	1.50	1.50	277.9-279.4		
							2	1.50	1.50	279.4-280.9		
							3	1.50	1.50	280.9-282.4		
							4	1.50	1.50	282.4-283.9		
							5	1.50	1.50	283.9-285.4	HS	
							6	1.50	1.50	285.4-286.9		
							7	0.84	0.84	286.9-287.74		
							CC(w/7)	0.18	0.18	287.74-287.92	PAL	
								10.02	10.02			
31R	16	0345	287.5-297.1	9.6	4.97	51.8						
							1	1.50	1.50	287.5-289.0		
							2	1.50	1.50	289.0-290.5	HS	
							3	1.50	1.50	290.5-292.0		
							4	0.42	0.42	292.0-292.42		
							CC(NS)	0.05	0.05	292.42-292.47	PAL	All to PAL
								4.97	4.97			
32R	16	0445	297.1-306.8	9.7	9.69	99.9						
							1	1.50	1.50	297.1-298.6		
							2	1.50	1.50	298.6-300.1		
							3	1.50	1.50	300.1-301.6		
							4	1.50	1.50	301.6-303.1		
							5	1.50	1.50	303.1-304.6		
							6	1.50	1.50	304.6-306.1	HS	
							7	0.44	0.44	306.1-306.54		
							CC(w/7)	0.25	0.25	306.54-306.79	PAL	
								9.69	9.69			
33R	16	0520	306.8-316.4	9.6	6.93	72.2						
							1	1.50	1.50	306.8-308.3		
							2	1.50	1.50	308.3-309.8		
							3	1.50	1.50	309.8-311.3	HS	
							4	1.50	1.50	311.3-312.8		
							5	0.88	0.88	312.8-313.68		
							CC(NS)	0.05	0.05	313.68-313.73	PAL	All to PAL
								6.93	6.93			
34R	16	0555	316.4-326.1	9.7	9.49	97.8						
							1	1.50	1.50	316.4-317.9		
							2	1.50	1.50	317.9-319.4		
							3	1.50	1.50	319.4-320.9		
							4	1.50	1.50	320.9-322.4	HS	
							5	1.50	1.50	322.4-323.9		
							6	1.50	1.50	323.9-325.4		
							7	0.44	0.44	325.4-325.84		
							CC(NS)	0.05	0.05	325.84-325.89	PAL	All to PAL
								9.49	9.49			
35R	16	0635	326.1-335.4	9.3	8.82	94.8						
							1	0.25	0.25	326.1-326.35		
							2	1.50	1.50	326.35-327.85		
							3	1.50	1.50	327.85-329.35		
							4	1.50	1.50	329.35-330.85		
							5	1.50	1.50	330.85-332.35	HS	

Table T2 (continued).

Core	Date (Jan 1999)	Time (UTC)	Depth (mbsf)	Length (m) Cored	Length (m) Recovered	Recovery (%)	Section	Length (m) Liner	Length (m) Curated	Section depth (mbsf)	Catwalk samples	Comment
							6	1.50	1.50	332.35-333.85		
							7	1.02	1.02	333.85-334.87		
							CC(NS)	0.05	0.05	334.87-334.92	PAL	All to PAL
								8.82	8.82			
36R	16	0720	335.4-345.0	9.6	3.92	40.8						
							1	1.50	1.50	335.4-336.9		
							2	1.50	1.50	336.9-338.4	HS, HS	
							3	0.66	0.66	338.4-339.06		
							CC(w/3)	0.26	0.26	339.06-339.32	PAL	
								3.92	3.92			
37R	16	0815	345.0-354.6	9.6	4.81	50.1						
							1	1.50	1.50	345.0-346.5		
							2	1.50	1.50	346.5-348.0		
							3	0.34	0.34	348.0-348.34		
							4	1.42	1.42	348.34-349.76	HS	
							CC(NS)	0.05	0.05	349.76-349.81	PAL	All to PAL
								4.81	4.81			
38R	16	0920	354.6-364.2	9.6	10.01	104.3						
							1	0.53	0.53	354.6-355.13	MAI	
							2	1.50	1.50	355.13-356.63		
							3	1.50	1.50	356.63-358.13		
							4	1.50	1.50	358.13-359.63		
							5	1.50	1.50	359.63-361.13		
							6	1.50	1.50	361.13-362.63		
							7	1.50	1.50	362.63-364.13	HS	
							8	0.23	0.23	364.13-364.36		
							CC(w/8)	0.25	0.25	364.36-364.61	PAL	
								10.01	10.01			
39R	16	1000	364.2-373.8	9.6	2.55	26.6						
							1	1.26	1.26	364.2-365.46		
							2	1.29	1.29	365.46-366.75	PAL, HS	
								2.55	2.55			
40R	16	1045	373.8-383.5	9.7	8.62	88.9						
							1	1.50	1.50	373.8-375.3		
							2	1.50	1.50	375.3-376.8		
							3	1.50	1.50	376.8-378.3		
							4	1.50	1.50	378.3-379.8		
							5	1.50	1.50	379.8-381.3	HS	
							6	0.92	0.92	381.3-382.22		
							CC(w/6)	0.20	0.20	382.22-382.42	PAL	
								8.62	8.62			
41R	16	1130	383.5-393.2	9.7	1.45	14.9						
							1	0.95	0.89	383.5-384.39		
							2	0.25	0.59	384.39-384.98	PAL	
							CC(w/2)	0.25	0.00			
								1.45	1.48			
42R	16	1225	393.2-402.8	9.6	0.77	8.0						
							1	0.77	1.01	393.2-394.21	PAL	
								0.77	1.01			
43R	16	1305	402.8-412.4	9.6	0.47	4.9						
							1	0.47	0.66	402.8-403.46	PAL	
								0.47	0.66			
44R	16	1355	412.4-422	9.6	0.9	9.4						
							1	0.90	1.13	412.4-413.53	PAL	
								0.90	1.13			
45R	16	1440	422.0-431.7	9.7	0.87	9.0						
							1	0.87	1.24	422-423.24	PAL	
								0.87	1.24			
46R	16	1530	431.7-441.3	9.6	0.95	9.9						
							1	0.95	1.13	431.7-432.83	PAL	
								0.95	1.13			
47R	16	1615	441.3-450.9	9.6	0.31	3.2						
							1	0.31	0.37	441.3-441.67	PAL	
								0.31	0.37			
48R	16	1725	450.9-460.6	9.7	0.22	2.3						
							1	0.22	0.29	450.9-451.19	PAL	
								0.22	0.29			
49R	16	1845	460.6-469.9	9.3	0.9	9.7						
							1	0.90	1.21	460.6-461.81		
								0.90	1.21			

Table T2 (continued).

Core	Date (Jan 1999)	Time (UTC)	Depth (mbsf)	Length (m) Cored	Length (m) Recovered	Recovery (%)	Section	Length (m) Liner	Length (m) Curated	Section depth (mbsf)	Catwalk samples	Comment
50R	16	1945	469.9-479.5	9.6	0.24	2.5						
							1	0.24	0.25	469.9-470.15	PAL	
								0.24	0.25			
51R	16	2055	479.5-489.1	9.6	0.44	4.6						
							1	0.44	0.66	479.5-480.16		
								0.44	0.66			
52R	16	2255	489.1-498.8	9.7	1.21	12.5						
							1	1.21	1.50	489.1-490.6		
								1.21	1.50			
53R	17	0040	498.8-508	9.2	2.5	27.2						
							1	1.00	1.47	498.8-500.27		
							2	1.50	1.27	500.27-501.54		
								2.50	2.74			
54R	17	0225	508.0-517.6	9.6	0.92	9.6						
							1	0.92	1.08	508.0-509.08		
								0.92	1.08			
55R	17	0405	517.6-527.3	9.7	0.57	5.9						
							1	0.57	0.73	517.6-518.33		
								0.57	0.73			
56R	17	0535	527.3-536.9	9.6	4.27	44.5						
							1	1.12	1.34	527.3-528.64		
							2	1.50	1.50	528.64-530.14		
							3	1.50	1.50	530.14-531.64		
							4	0.15	0.15	531.64-531.79		
								4.27	4.49			
57R	17	0725	536.9-546.5	9.6	2.34	24.4						
							1	0.89	1.50	536.9-538.4		
							2	1.45	1.31	538.4-539.71		
								2.34	2.81			
58R	17	0905	546.5-556	9.5	0.3	3.2						
							1	0.30	0.39	546.5-546.89		
								0.30	0.39			
59R	17	1100	556.0-565.6	9.6	1.2	12.5						
							1	1.20	1.50	556.0-557.5		
								1.20	1.50			
60R	17	1245	565.6-575.2	9.6	2.54	26.5						
							1	1.39	1.48	565.6-567.08		
							2	1.15	1.28	567.08-568.36		
								2.54	2.76			
61R	17	1435	575.2-584.9	9.7	3.22	33.2						
							1	1.50	1.42	575.2-576.62		
							2	1.47	1.45	576.62-578.07		
							3	0.25	0.65	578.07-578.72		
								3.22	3.52			
62R	17	1650	584.9-594.6	9.7	4.01	41.3						
							1	0.83	0.83	584.9-585.73		
							2	1.20	1.20	585.73-586.93		
							3	1.20	1.20	586.93-588.13		
							4	0.56	0.56	588.13-588.69		
							5	0.22	0.22	588.69-588.91		
								4.01	4.01			
63R	17	2015	594.6-604.2	9.6	2.73	28.4						
							1	0.95	1.17	594.6-595.77		
							2	1.51	1.51	595.77-597.28		
							3	0.27	0.24	597.28-597.52		
								2.73	2.92			
64R	17	2345	604.2-613.9	9.7	5.65	58.2						
							1	1.09	1.50	604.2-605.7		
							2	1.49	1.44	605.7-607.14		
							3	1.45	1.50	607.14-608.64		
							4	1.38	1.50	608.64-610.14		
							5	0.24	0.46	610.14-610.6		
								5.65	6.4			
65R	18	0315	613.9-623.5	9.6	5.9	61.5						
							1	1.23	1.30	613.9-615.2		
							2	1.38	1.50	615.2-616.7		
							3	1.50	1.50	616.7-618.2		

Table T2 (continued).

Core	Date (Jan 1999)	Time (UTC)	Depth (mbsf)	Length (m) Cored	Length (m) Recovered	Recovery (%)	Section	Length (m) Liner	Length (m) Curated	Section depth (mbsf)	Catwalk samples	Comment
							4	1.37	0.44	618.2-618.64		
							5	0.42	1.34	618.64-619.98		
								5.90	6.08			
66R	18	0720	623.5-633.1	9.6	7.54	78.5						
							1	1.48	1.48	623.5-624.98		
							2	1.50	1.50	624.98-626.48		
							3	1.44	1.44	626.48-627.92		
							4	1.00	1.00	627.92-628.92		
							5	1.40	1.40	628.92-630.32		
							6	0.37	0.37	630.32-630.69		
							7	0.35	0.35	630.69-631.04		
								7.54	7.54			
67R	18	1035	633.1-642.6	9.5	6.19	65.2						
							1	0.57	0.68	633.1-633.78		
							2	1.40	1.40	633.78-635.18		
							3	1.50	1.50	635.18-636.68		
							4	1.42	1.42	636.68-638.1		
							5	1.30	1.43	638.1-639.53		
								6.19	6.43			
68R	18	1345	642.6-652	9.4	8.88	94.5						
							1	1.27	1.4	642.6-644.0		
							2	1.51	1.51	644.0-645.51		
							3	1.25	1.25	645.51-646.76		
							4	1.45	1.45	646.76-648.21		
							5	0.41	1.44	648.21-649.65		
							6	1.54	0.58	649.65-650.23		
							7	1.45	1.48	650.23-651.71		
								8.88	9.11			
69R	18	1725	652.0-661.5	9.5	4.17	43.9						
							1	1.60	1.50	652.0-653.5		
							2	1.12	1.40	653.5-654.9		
							3	1.45	1.36	654.9-656.26		
								4.17	4.26			
70R	18	2050	661.5-670.9	9.4	5.36	57.0						
							1	1.54	1.22	661.5-662.72		
							2	1.07	1.50	662.72-664.22		
							3	1.10	1.29	664.22-665.51		
							4	1.48	1.28	665.51-666.79		
							5	0.17	0.49	666.79-667.28		
								5.36	5.78			
71R	19	0045	670.9-680.3	9.4	7.89	83.9						
							1	0.99	0.95	670.9-671.85		
							2	1.50	1.05	671.85-672.9		
							3	1.50	1.30	672.9-674.2		
							4	1.24	1.46	674.2-675.66		
							5	1.44	1.41	675.66-677.07		
							6	1.22	1.38	677.07-678.45		
							7	0.00	0.57	678.45-679.02		
								7.89	8.12			
72R	19	0455	680.3-689.5	9.2	4.57	49.7						
							1	1.20	1.43	680.3-681.73		
							2	1.31	0.89	681.73-682.62		
							3	1.50	1.38	682.62-684.0		
							4	0.56	0.87	684.0-684.87		
								4.57	4.57			
73R	19	0715	689.5-694.2	4.7	3.79	80.6						
							1	0.81	1.50	689.5-691.0		
							2	1.50	1.50	691.0-692.5		
							3	1.48	1.48	692.5-693.98		
								3.79	4.48			
			Totals:	694.2	356.88	51.4						

Notes: UTC = Universal Time Coordinated. CC = core catcher (number in parenthesis indicates which section the core catcher is stored with). NS = all of the core catcher was used for paleontology sample. HS = headspace gas sample. PAL = paleontology sample. MAI = whole-round sample for shore-tossed physical properties study. This table is also available in **ASCII format.**

Table T3. Summary of lithologic and basement units at Hole 1139A.

Lithologic unit/subunit	Basement units	Core interval	Depth (mbsf)	Thickness (m)	Age	Lithology	Interpretation
IA		1R-1, 0 cm, to 2R-CC, 19 cm	0.00–19.00	19.00	middle to early Pleistocene	Foraminifer-bearing diatom-bearing nannofossil ooze	Pelagically deposited sediment; bathyal environment (cold water)
IB		3R-1, 0 cm, to 5R-CC, 25 cm	19.00–47.50	28.50	middle Miocene	Foraminifer-bearing nannofossil ooze	Pelagically deposited sediment; bathyal environment
II		6R-1, 0 cm, to 40R-5, 92 cm	47.50–380.72	333.22	middle Miocene to late Oligocene	Gray nannofossil-bearing clay and claystone and nannofossil-bearing ooze and chalk	Continuous pelagic with influx of terrigenous sediment-bathyal environment
III		40R-5, 92 cm, to 40R-CC, 20 cm	380.72–383.50	2.78	late Oligocene to late Eocene	Brownish gray to pink foraminifer nannofossil chalk	Pelagically deposited sediment; bathyal environment
IV		41R-1, 0 cm, to 41R-2, 40 cm	383.50–384.87	1.37	late Eocene or older	Sandy packstone	Low energy neritic environment
V		41R-2, 40 cm, to 49R-1, 110 cm	384.87–461.70	76.83	late Eocene or older	Cross-bedded grainstone with minor interbedded rudstone and packstone	High energy neritic carbonate shoal
VI	1-19	49R-1, 110 cm, to 73R-3, 148 cm	461.7–694.2	232.5	late Eocene or older	Altered volcaniclastic and felsic volcanic rocks and basalt flows	Evolving subaerial volcanism followed by hydrothermal alteration

Table T4. X-ray diffraction results, carbonate contents ($CaCO_3$), and total and organic carbon contents for Hole 1139A.

Core, section, interval (cm)	Depth (mbsf)	Minerals	$CaCO_3$ (wt%)	Total carbon (wt%)	Organic Carbon (wt%)
Unit IA					
183-1139A-					
1R-5, 68	4.83	Calcite, opal-A	64	7.93	0.24
2R-3, 93	13.43	Calcite, opal-A	75		
Unit IB					
183-1139A-					
3R-1, 92	19.91	Calcite, alkali-feldspar, (opal-A)	74		
4R-1, 92	29.41	Calcite	83	10.31	0.30
5R-1, 90	38.90	Calcite, alkali-feldspar, clay, (glauconite)	76		
Unit II					
183-1139A-					
6R-1, 90	48.40	Calcite, sanidine, clay, (glauconite)	61		
7R-1, 91	57.91	Calcite, sanidine, clay, (glauconite)	51	6.31	0.15
8R-1, 61	67.11	Calcite, clay, (sanidine)	73		
9R-2, 90	77.24	Calcite, clay, sanidine, maghemite, pyrite, (glauconite)	33		
10-1, 91	86.41	Calcite, clay, sanidine, maghemite, pyrite, (glauconite)	25	3.35	0.36
11R-1, 91	96.01	Calcite, clay, (sanidine)	62		
12R-1, 92	105.61	Calcite, clay, sanidine, maghemite, pyrite, (glauconite)	28		
13R-1, 92	115.31	Clay, sanidine, calcite, maghemite, pyrite, plagioclase?, quartz, (glauconite)	7	1.15	0.25
14R-1, 92	124.91	Calcite, clay, sanidine, maghemite, plagioclase?, (glauconite, pyrite, quartz)	21		
15R-1, 92	134.41	Calcite, sanidine, clay, maghemite, plagioclase?,	20		
16R-1, 92	144.11	Calcite, clay, sanidine, maghemite, plagioclase?, (glauconite, pyrite, quartz)	32	4.02	0.18
17R-1, 92	153.71	Calcite, sanidine, clay, maghemite, plagioclase?, (pyrite, glauconite)	33		
18R-1, 92	163.41	Calcite, clay, sanidine	59		
19R-1, 92	173.01	Calcite, clay, sanidine, feldspar?, (maghemite, pyrite)	58	7.1	0.11
20R-1, 92	182.61	Calcite, clay, sanidine, maghemite, (plagioclase?)	53		
21R-1, 92	192.21	Calcite, clay, sanidine, (glauconite)	49		
22R-1, 92	201.81	Calcite, clay, (sanidine)	71	8.54	0.03
23R-1, 92	211.41	Calcite, clay, (sanidine)	71		
24R-1, 92	221.01	Calcite, clay, sanidine, maghemite, (glauconite, pyrite)	44		
25R-1, 92	230.71	Calcite, clay, (sanidine, glauconite)	64	7.86	0.17
26R-1, 92	240.31	Calcite, clay, sanidine, glauconite, (maghemite, pyrite)	40		
27R-1, 92	250.01	Calcite, clay, sanidine, glauconite, maghemite, plagioclase?, (clinoptilolite, pyrite)	32		
28R-1, 92	259.61	Calcite, clay, sanidine, maghemite, glauconite, (pyrite, plagioclase?, quartz)	15	1.89	0.11
29R-1, 92	269.21	Calcite, clay, sanidine, maghemite, (pyrite, plagioclase?)	20		
30R-1, 92	278.81	Calcite, clay, sanidine, maghemite, glauconite, (pyrite, plagioclase?)	32		
31R-1, 92	288.41	Calcite, clay, sanidine, glauconite, (maghemite, clinoptilolite)	41	5.08	0.13
32R-1, 92	298.01	Calcite, clay, sanidine, maghemite, glauconite, (clinoptilolite, pyrite, plagioclase?)	45		
33R-1, 92	307.71	Calcite, clay, sanidine, glauconite, (maghemite)	42		
34R-1, 92	317.31	Calcite, sanidine, clay, glauconite, (maghemite plagioclase?)	39	4.83	0.2
36R-1, 92	336.31	Calcite, clay, sanidine, maghemite, (quartz, plagioclase?)	47		
37R-1, 92	345.91	Calcite, clay, (sanidine, clinoptilolite)	67		
38R-3, 31	356.93	Calcite, clay, sanidine, (pyrite, glauconite)	55	6.85	0.19
39R-1, 92	365.11	Calcite, pyrite, (clay, sanidine, clinoptilolite)	72		
40R-1, 120	375.00	----	48		
Unit III					
138-1139A-					
40R-CC, 12	382.33	Calcite	94	11.27	0.04

Notes: Minerals listed in parentheses are present only in trace amounts. Carbonate and carbon data are from **"Organic and Inorganic Geochemistry,"** p. 54.

Table T5. Summary of thin sections at Site 1139.

Core, section, interval (cm)	Lithologic unit	Lithology	Mineral components	Lithic components	Bioclastic components	Matrix and cement	Texture
183-1139A-							
41R-1, 40-43 cm	IV	Sandy packstone	Altered basaltic glass, vesicular glass	Altered volcanic rocks, unidentified brown grains, polycrystalline quartz	Benthic foraminifers, planktonic foraminifers, echinoderms, shell fragments, ostracodes	Microsparite, drusy calcite, fibrous calcite (rare), silicification	Poorly sorted packstone
41R-2, 50-54 cm	V	Sandy grainstone	Alkali feldspar	Basalt(?), opaque grains	Bryozoans, bivalves, echinoderms, benthic foraminifers	Dog-tooth calcite, cement, blocky calcite, syntaxial overgrowth on echinoderms	Well sorted, no matrix
42R-1, 67-70 cm	V	Sandy grainstone	Feldspar	None	Bryozoans, shell fragments, serpulids, echinoderms, benthic foraminifers	Syntaxial overgrowth on echinoderms, dog-tooth calcite, cement	Well sorted, no matrix

Table T6. Site 1139 basement unit contacts.

Unit/ Subunit	Description	Unit top (core, section, interval [cm])	Curated depth (mbsf)	Unit thickness* (m)	Recovery** (m)
		183-1139A-			
1A	Massive and flow-banded felsic volcanic cobbles	49R-1, 109	461.69	29.06	1.59
1B	Bioclastic sandstone	52R-1, 56	489.66	0.47	0.47
1C	Pumice/flow-banded felsic breccia	52R-1, 103	490.13	8.36	0.43
1D	Altered, perlitic felsic glass	53R-1, 25	499.05	8.95	2.25
1E	Sheared and altered volcaniclastic sediments (fault zone)	54R-1, 0	508.00	9.60	0.92
2	Dark red welded vesicular rhyolite	55R-1, 0	517.60	10.48	1.35
3	Altered crystal vitric tuff-breccia	56R-1, 78	528.08	9.74	4.63
4	Dark red welded vesicular rhyolite	57R-1, 92	537.82	38.69	6.54
5	Lava flow?	61R-1, 0	575.20	9.70	3.52
6	Lava flow(s?), type unknown	62R-1, 0	584.90	19.30	6.93
7	Breccia-topped lava flow	64R-1, 0	604.20	2.94	2.94
8	Spatter-topped? lava flow	64R-3, 0	607.14	6.76	3.46
9	Lava flow, type unknown	65R-1, 0	613.90	1.76	1.76
10	Compound pahoehoe and unknown lava flows	65R-2, 46	615.66	2.54	2.54
11	Aa lava flow	65R-4, 0	618.20	6.78	3.27
12	Transitional lava flow, type unknown	66R-2, 0	624.98	3.03	4.03
13	Breccia-topped lava flow	66R -4, 9	628.01	5.09	2.03
14	Breccia-topped transitional lava flow	67R-1, 0	633.10	9.50	7.44
15	Breccia-topped? lava flow	68R-1, 101	643.61	5.16	4.15
16	Breccia-topped transitional lava flow	68R-4, 100	647.76	2.85	2.85
17	Breccia-topped? lava flow	68R-7, 38	650.61	10.89	5.36
18	Breccia-topped lava flow	70R-1, 0	661.50	12.90	9.28
19	Breccia-topped lava flow	71R-4, 20	674.40	19.80	13.67

Note: * = unit thicknesses are based on curated depths of contacts, ** = recovery is based on curated lengths of recovered core from each unit.

Table T7. Summary of Site 1139 volcaniclastic components.

Unit/ Subunit	Core interval	Depth (mbsf)	Thickness (m)	Age	Lithologies with volcanic components	Volcanic components	Authigenic and secondary minerals
Lithologic							
I–V	1R-1, 0 cm, to 49R-1, 109 cm	0	272.01	early Pleistocene to late Eocene	Bathyal to neritic and shallow marine fossiliferous sediments	Disseminated and discrete tephra horizons, accumulations of terrigenous detritus, may be biologically disturbed (e.g., by burrowing)	Clay minerals after volcanic glass, zeolites (clinoptilolite), and glauconite
Basement							
1A	49R-1, 109 cm, to 52R-1, 56 cm	461.69	1.59	>late Eocene	Massive and flow-banded felsic volcanic cobbles	Massive, flow-banded, altered and silicified, abraded, loose rhyolite lava cobbles and pebbles	Clay minerals after volcanic glass, followed by silicification
1B	52R-1, 56 cm, to 52R-1, 103 cm	489.66	0.47	>late Eocene	Bioclastic sandstone	Intercalated nonvolcanic lens with angular bioclasts (e.g., bryozoan, bivalve, echinoderm, benthic foraminifer),	
						<1% volcanic lithic fragments	Clay minerals, hematitic staining
1C	52R-1, 103 cm, to 53R-1, 25 cm	490.13	0.72	>late Eocene	Pumice/flow-banded felsic breccia	Altered breccia, pale green, flow-banded clasts with banded perlite formation, in siliceous matrix	Pale green clay minerals (nontronite, kaolinite?), followed by silicification
1D	53R-1, 25 cm, to 54R-1, 0 cm	499.05	2.49	>late Eocene	Altered, perlitic felsic glass	Reddish orange, massive, felsic volcanic glass, well-developed spheroidal perlitic fractures, minor lithic volcanic fragments	White and pale green clay minerals (nontronite?), and silicification
1E	54R-1, 0 cm, to 55R-1-0 cm	508.00	1.08	>late Eocene	Sheared and altered volcaniclastic sediments (fault zone)	Green, resinous to powdery, highly altered sheared rock (Fault Zone), and less altered, sheared rock with clastic texture	Pale to dark green, resinous to powdery clay minerals
2	55R-1, 0 cm, to 56R-1, 78cm	517.60	1.51	>late Eocene	Dark red welded vesicular rhyolite	Welded, dark red, vesicular, sandine?-rich rhyolite agglutinate	Hematite staining of clay minerals (smectite?), and silicification
3	56R-1, 78 cm, to 57R-1, 92 cm	528.08	4.63	>late Eocene	Green, altered, crystal vitric tuff-breccia	Green, highly altered, sanidine-rich vitric rhyolite tuff breccia, incorporated flow-banded clasts and lithic fragments	Pale green clay minerals
4	57R-1, 92 cm, to 60R-2, 54 cm	537.82	6.54	>late Eocene	Dark red welded vesicular rhyolite	Welded, dark red, vesicular, sandine?-rich rhyolite agglutinate, to open-framework rhyolite breccia	Hematite staining of clay minerals (smectite?), and silicification

Table T8. Distribution of volcanic components in core catcher samples from lithologic Units I–V at Site 1139.

Unit/ Subunit	Lithologies with volcanic components	Section	Feldspar	Glass (brown)	Pumice	Lithics	Volcanic clay	Tephra layer	Age (Ma)
IA	Foraminifer/diatom-bearing nannofossil ooze	1R-CC							1.9-0.6
		2R-CC							1.9-0.6
IB	Foraminifer-bearing nannofossil ooze	3R-CC							18.0-11.5
		4R-CC		R					18.0-11.5
		5R-CC		R			P		18.0-11.5
		6R-CC		R					18.0-11.5
		7R-CC		P			P		18.0-11.5
		8R-CC		A					18.0-11.5
		9R-CC		R			R		24.0-18.0
		10R-CC	P	R			P		24.0-18.0
		11R-CC		P				T	24.0-18.0
		12R-CC	P						24.0-18.0
		13R-CC							24.0-18.0
		14R-CC	P	C					24.0-18.0
II	Nannofossil-bearing clay and claystone, and nannofossil-bearing ooze and chalk	15R-CC		C			P		24.0-18.0
		16R-CC		A					24.0-18.0
		17R-CC		R					24.0-18.0
		18R-CC							24.0-18.0
		19R-CC							26.5-23.8
		20R-CC	P			R			26.5-23.8
		21R-CC	C			C			26.5-23.8
		22R-CC							31.0-26.5
		23R-CC							31.0-26.5
		24R-CC				P	P		31.0-26.5
		25R-CC							31.0-26.5
		26R-CC	C	R		P			31.0-26.5
		34R-CC					C		31.0-26.5
		35R-CC					C		31.0-26.5
		36R-CC							31.0-26.5
		37R-CC							31.0-26.5
		38R-CC						TT	31.0-26.5
		39R-CC	P				P		31.0-26.5

Notes: Age from biostratigraphy. Volcanic components in >63-µm fraction of core catcher sample are represented by A = abundant, C = common, P = present, and R = rare. Volcanic components not abundant in Sections 183-1139A-27R-CC through 33R-CC and beyond 39R-CC in Unit II. T = discrete tephra are present in the core from which the core catcher was examined, TT = two tephra layers. Blanks = volcanic component not detected. Solid line = Sections 183-1139A-27R-CC through 33R-CC contain no data.

Table T9. Pyroclastic ash-fall deposits identified at Site 1139.

Lithologic unit	Core	Interval (cm)	Depth (mbsf)	Age (Ma)	Age type	Color	Volcanic components	Suggested composition
II	11R-1	107-109	96.17	24.0-18.0	D+F+N	Dark and light gray	Brown platy and vesicular glass shards	Basalt
	38R-3	17-19	356.80	31.0-26.5	F+N	Dark gray	Translucent glass shards and tube pumice	Trachyte
	38R-4	80-82	358.93	31.0-26.5	F+N	Dark brown	Brown, curviplanar-platy glass shards	Basalt

Note: D = diatoms, F = foraminifers, N = nannofossils.

Table T10. Petrographic summary of Site 1139 igneous units with mineralogies. (Continued on next page.)

Unit/ Subunit	Rock type	Drilled thickness (m)	Characteristics	Major phases	Minor phases	Core, section, interval (cm)	Figure number*
1A	Rhyolite cobbles	29.06	Massive and flow-banded	Sanidine (2%), lithic clasts (20%)	Quartz, biotite titanomagnetite altered amphibole	51R-1, 3-5 51R-1, 23-25	
1B	Bioclastic sandstone	0.47					
1C	Felsic pumice breccia	8.36	Pumiceous and flow banded	Glass (100%)		52R-1, 120-123	
1D	Perlitic felsic glass with lithics	8.95	Perlitic texture	Glass (98%), alkali feldspar (2%)		53R-1, 127-130	F45
1E	Volcaniclastic rocks	9.60	Sheared and altered (fault zone)				
2	Moderately sanidine-quartz-phyric rhyolite	10.48	Vesicular, welded	Sanidine (8%), quartz (1%)		56R-1, 37-40	F46A
3	Highly altered crystal vitric tuff-breccia	9.74	Highly altered	Perlitic glass (76%), alkali feldspar (15%), quartz (4%)	Altered mafic mineral	56R-3, 93-97	F47
4	Moderately to highly sanidine-quartz-phyric rhyolite	30.99	Vesicular, welded, spherulitic	Sanidine (10%-15%), quartz (5%-10%)	Quartz, titanomagnetite	57R-1, 120-123	F46B
5	Moderately sanidine-phyric trachyte	17.40	Altered; brecciated and massive	Sanidine (5%)	Clinopyroxene, titanomagnetite, quartz, plagioclase	60R-2, 100-104 61R-1, 74-76	F48A, F48B
6	Aphyric trachybasalt	19.30	Altered; brecciated and massive	Sanidine xenocrysts (<1%)	Plagioclase, sanidine, titanomagnetite	62R-2, 117-119	
7	Aphyric basaltic trachyandesite	2.94	Crystal-rich sand at top contact	Sanidine xenocrysts (<1%)	Plagioclase, clinopyroxene, titanomagnetite	64R-1, 38-43, 64R-1, 81-84	F49A, F49B F51A
8	Aphyric trachybasalt	6.76	Altered; brecciated and massive	Sanidine xenocrysts (<1%)	Plagioclase, clinopyroxene, titanomagnetite	64R-4, 77-78	
9	Aphyric trachybasalt	1.76	Altered; brecciated and massive	Sanidine xenocrysts (<1%)	Plagioclase, clinopyroxene, titanomagnetite	65R-2, 15-19 65R-2, 29-30 (basalt + xenolith)	
10	Sparsely plagioclase-phyric trachybasalt	2.54	Altered; trachytic groundmass texture: Carlsbad twinned feldspar	Plagioclase (1%), sanidine xenocrysts (<1%)	Clinopyroxene, titanomagnetite	65R-3, 16-18 65R-3, 90-93	F53A, F53B
11	Aphyric trachybasalt	6.78	Trachytic groundmass texture	Sanidine xenocrysts (<1%)	Plagioclase, clinopyroxene, titanomagnetite	65R-5, 49-53 65R-5, 81-85	
12	Aphyric trachybasalt	3.03	Brecciated and massive; trachytic groundmass texture	Sanidine xenocrysts (<1%)	Plagioclase, clinopyroxene, titanomagnetite	66R-3, 44-47	
13	Aphyric trachybasalt	5.09	Altered; brecciated and massive	Sanidine xenocrysts (<1%)	Plagioclase, clinopyroxene, titanomagnetite	66R-7, 5-8	F51B
14	Basaltic Trachyandesite	9.50	Brecciated and massive; trachytic groundmass texture	Plagioclase (2%), sanidine xenocrysts (<1%)	Olivine, clinopyroxene, titanomagnetite	67R-5, 100-103 67R-3, 109-111	F50
15	Sparsely plagioclase-phyric basaltic trachyandesite	5.16	Trachytic groundmass texture	Plagioclase (1%); sanidine xenocrysts (<1%)	Clinopyroxene, titanomagnetite	68R-4, 42-45	
16	Aphyric basaltic trachyandesite	2.85	Altered; brecciated and massive	Alkali feldspar xenocrysts (<1%)	Plagioclase, altered mafic mineral, magnetite	68R-6, 54-57	F52
17	Sparsely plagioclase-phyric basaltic trachyandesite	10.89	Altered; brecciated and massive	Plagioclase (1%); sanidine xenocrysts (<1%)	Clinopyroxene titanomagnetite sulfide	69R-2, 1-4	

Table T10 (continued).

Unit/ Subunit	Rock type	Drilled thickness (m)	Characteristics	Major phases	Minor phases	Core, section, interval (cm)	Figure number*
18	Moderately sanidine-phyric trachyandesite	12.90	Altered	Sanidine (5%-10%)	Titanomagnetite, altered mafic mineral, plagioclase, sulfide, secondary siderite	70R-1, 17-20	F54
						70R-2, 141-145	F55A
						70R-3, 64-68	F56A, F58
						71R-1, 0-6	F59A, F59B
						71R-3, 63-66	
						71R-4, 7-10	
19	Moderately sanidine-phyric trachyte	19.80	Altered	Sanidine (8%-15%)	Altered mafic mineral, titanomagnetite, plagioclase, secondary siderite	71R-4, 134-135	F55B
						71R7, 24-25	F56A, F57B
						72R2, 57-60	F60
						73R-3, 37-39	

Note: * = Correlating figures in the “Site 1139” chapter.

Table T11. X-ray fluorescence analyses of major and trace elements for Site 1139 igneous units. (Continued on next two pages.)

Hole:	1139A	1139A	1139A	1139A	1139A	1139A	1139A	1139A	1139A
Core, section:	51R-1	56R-3	57R-1	60R-2	61R-1	62R-2	64R-1	64R-4	65R-2
Interval (cm):	0-3	92-95	124-127	114-119	78-81	110-112	81-84	78-82	15-19
Piece:			21	15	1F	1	13B	3F	1A
Unit:	1	3	4	5	5	6	7	8	9
Rock type:	Rhyolite	Highly altered, crystal vitric tuff-breccia	Sanidine-quartz phyric rhyolite	Feldspar-phyric trachyte	Feldspar-phyric trachyte	Aphyric trachybasalt	Aphyric basaltic trachyandesite	Aphyric trachybasalt	Aphyric trachybasalt
Depth (mbsf):	479.5	531.06	538.14	568.22	575.98	586.83	605.01	609.42	615.35
Major element oxides (wt%):									
SiO_2	73.45	69.51	79.58	67.10	66.56	50.57	53.59	49.09	50.17
TiO_2	0.41	0.53	0.34	0.56	0.57	3.15	2.67	3.89	4.18
$Al2O_3$	10.24	15.92	8.36	16.30	16.38	18.62	17.45	14.89	16.64
Fe_2O_3	6.03	5.24	3.67	5.36	4.37	16.99	10.60	14.14	13.43
MnO	0.07	0.06	0.06	0.22	0.27	0.16	0.30	0.26	0.28
MgO	0.10	4.21	0	0.05	0.08	1.36	1.09	4.33	2.34
CaO	0	0	0	0	0	2.55	5.85	7.67	6.41
Na_2O	3.32	2.75	2.58	4.91	4.31	2.27	4.36	3.17	3.67
K_2O	6.50	2.04	4.34	6.02	5.98	4.13	3.68	2.31	2.75
P_2O_5	0.03	0.00	0.00	0.01	0.00	1.50	1.09	1.05	1.44
Total	100.14	100.24	98.91	100.50	98.50	101.29	100.66	100.77	101.28
Mg#*	0.02	0.53	0	0.01	0.02	0.10	0.12	0.30	0.19
LOI**	0.93	5.66	0.17	1.73	2.04	3.73	4.38	2.69	4.38
CO_2	1.2	7.3	0.7	2.6	1.8	4.2	5.8	3.5	5.3
H_2O	1.1	7.2	0.6	0.6	0.0	4.2	1.4	1.9	1.7
Trace elements (ppm):									
Rb	221	22	139	93	70	47	47	34	41
Ba	49	40	66	79	75	791	1570	757	923
Sr	7	34	0	4	3	113	451	421	466
Nb	259	311	142	107	108	49	45	36	41
Zr	1678	213	903	629	388	343	367	292	332
Y	106	59	42	58	56	45	45	38	40
V	98	14	19	19	19	99	138	350	338
Cr	23	18	25	24	26	13	24	21	9
Ni	11	2	1	3	3	3	4	12	7
Cu									
Zn	252	555	105	146	366	212	125	119	127
Normative mineralogy:									
Q	31.0	36.7	47.4	12.9	16.7	11.6	0.3		1.3
Or	38.5	12.0	26.0	35.5	35.9	24.4	21.7	13.7	16.2
Ab	16.6	23.7	19.1	41.3	37.1	19.2	36.9	26.9	31.1
An						2.8	17.2	19.7	20.7
Corundum		9.1		1.7	2.9	9.4			
Nepheline									
Leucite									
Acmite	3.5		2.2						
Na Metasilicate	1.8		0.2						
Wo (Di)							1.9	4.8	0.7
En (Di)							0.5	2.4	0.3
Fs (Di)							1.6	2.3	0.4
En (Hy)	0.2	10.6		0.2	0.2	3.4	2.2	7.8	5.5
Fs (Hy)	7.4	5.3	4.5	5.7	4.7	14.8	6.9	7.5	8.7
Ol (Fo)								0.4	
Ol (Fa)								0.5	
Ilmenite	0.8	1.0	0.6	1.1	1.1	6.0	5.1	7.4	7.9
Magnetite		1.5		1.6	1.3	4.9	3.1	4.1	3.9
Apatite						3.3	2.4	2.3	3.1
Total:	99.9	99.9	99.9	99.9	99.9	99.8	99.8	99.8	99.8

Table T11 (continued).

Hole:	1139A	1139A	1139A	1139A	1139A	1139A	1139A	1139A
Core, section:	65R-3	65R-5	66R-3	66R-7	67R-5	68R-4	68R-6	69R-2
Interval (cm):	90-93	81-85	44-47	8-12	105-108	42-45	54-57	1-4
Piece:	5C	1D	1B	3	9	1	1	1
Unit:	10	11	12	13	14	15	16	17
Rock type:	Sparsely plagioclase-phyric trachybasalt	Aphyric trachybasalt	Aphyric trachybasalt	Aphyric trachybasalt	Basaltic trachyandesite	Plagioclase-phyric basaltic trachyandesite	Aphyric basaltic trachyandesite	Plagioclase-phyric basaltic trachyandesite
Depth (mbsf):	617.6	619.45	626.92	630.77	639.15	647.18	650.19	653.51
Major element oxides (wt%):								
SiO_2	46.78	50.37	49.67	46.78	52.22	51.77	52.51	52.76
TiO_2	4.37	3.82	3.86	4.23	2.60	3.84	3.37	3.03
Al2O_3	16.81	15.87	14.72	16.93	16.73	18.03	17.50	15.89
Fe_2O_3	12.53	12.97	12.76	13.13	12.36	11.29	13.81	11.79
MnO	0.51	0.21	0.20	0.28	0.25	0.18	0.13	0.20
MgO	1.08	3.00	3.81	0.89	0.87	0.58	1.76	2.37
CaO	10.70	6.79	8.47	9.84	6.37	5.28	3.57	6.69
Na_2O	3.41	3.72	3.20	3.65	4.20	4.14	3.19	3.69
K_2O	2.51	2.77	2.44	2.94	3.85	4.01	3.75	3.12
P_2O_5	1.12	1.77	1.67	1.39	1.13	1.64	1.55	1.30
Total	99.80	101.27	100.77	100.05	100.56	100.74	101.11	100.82
Mg#*	0.11	0.24	0.29	0.08	0.09	0.07	0.15	0.22
LOI**	7.86	1.25	2.40	8.36	6.22	3.41	2.44	2.53
CO_2	8.2	2.8	3.2	8.7	6.5	3.9	2.7	2.9
H_2O	1.3	1.1	1.4	1.0	0.9	1.0	2.6	1.4
Trace elements (ppm):								
Rb	38	43	35	35	50	57	59	50
Ba	846	1061	939	1150	2286	1092	997	1015
Sr	474	499	467	461	488	481	326	460
Nb	38	44	39	39	44	49	52	46
Zr	292	345	295	256	354	343	420	387
Y	43	50	46	40	46	42	51	46
V	424	254	274	326	95	275	175	175
Cr	28	10	7	13	6	25	18	23
Ni	13	7	4	7	3	2	3	3
Cu								
Zn	148	140	137	319	131	149	142	133
Normative mineralogy:								
Q		1.0	1.4			1.5	8.5	2.6
Or	15.0	16.3	14.4	17.5	22.8	23.7	22.1	18.4
Ab	23.3	31.2	27.1	23.3	35.4	35.1	27.4	31.2
An	23.4	18.5	18.7	21.5	15.7	15.6	7.6	17.6
Corundum						1.2	5.3	
Nepheline	3.2			4.2				
Leucite								
Acmite								
Na Metasilicate								
Wo (Di)	9.6	1.5	5.2	7.8	3.6			3.0
En (Di)	2.5	0.7	2.7	1.6	0.7			1.2
Fs (Di	7.6	0.8	2.5	6.7	3.2			1.8
En (Hy)		6.8	6.8		0.5	1.4	4.4	4.7
Fs (Hy)		8.2	6.3		2.2	7.1	10.7	7.2
Ol (Fo)	0.2			0.4	0.7			
Ol (Fa)	0.5			1.6	3.9			
Ilmenite	8.4	7.2	7.4	8.1	5.0	7.3	6.4	5.8
Magnetite	3.7	3.7	3.7	3.9	3.6	3.3	4.0	3.4
Apatite	2.5	3.9	3.6	3.1	2.5	3.6	3.4	2.8
Total:	99.8	99.7	99.7	99.8	99.8	99.7	99.7	99.8

Table T11. (continued).

Hole:	1139A	1139A	1139A	1139A	1139A	1139A
Core, section:	70R-1	70R-2	71R-4	71R-7	72R-2	73R-3
Interval (cm):	17-20	141-145	135-138	25-27	57-60	39-42
Piece:	2A	1F	1I	1B	2B	2B
Unit:	18	18	19	19	19	19
Rock type:	Sanidine-phyric trachyandesite	Sanidine-phyric trachyandesite (altered)	Sanidine-phyric trachyte	Sanidine-phyric trachyte	Sanidine-phyric trachyte	Sanidine-phyric trachyte
Depth (mbsf):	661.67	664.13	675.55	678.7	682.3	692.89
Major element oxides (wt%)						
SiO_2	59.46	61.68	67.86	70.68	70.00	68.44
TiO_2	1.02	1.00	0.50	0.50	0.49	0.54
$Al2O_3$	18.59	15.95	13.30	14.24	13.67	14.29
Fe_2O_3	10.57	11.36	10.10	3.84	5.94	6.88
MnO	0.11	0.29	0.15	0.11	0.16	0.23
MgO	0.76	0.51	0.83	0.09	0.14	0.14
CaO	0.02	0	0.28	0.36	0	0
Na_2O	3.36	2.96	2.39	3.64	3.55	3.29
K_2O	5.41	3.90	5.01	6.57	6.48	5.25
P_2O_5	0.01	0.17	0.03	0.01	0	0
Total	99.30	97.81	100.42	100.04	100.42	99.05
Mg#*	0.09	0.06	0.10	0.03	0.03	0.03
LOI**	1.89	7.02	6.02	1.87	2.65	3.21
CO_2	2.3	7.9	7.3	2.1	2.9	3.8
H_2O	2.2	1.5	1.7	0.8	0.9	0.8
Trace elements (ppm)						
Rb	41	42	87	146	139	116
Ba	290	268	123	130	118	69
Sr	23	9	25	12	8	9
Nb	84	65	166	189	182	161
Zr	521	420	1131	1467	1372	1104
Y	54	49	50	49	156	296
V	13	13	15	20	19	17
Cr	17	13	12	20	18	13
Ni	2	1	1	2	3	3
Cu				5	6	6
Zn	209	207	212	76	164	221
Normative mineralogy			28.0	21.9	21.4	26.0
Q	13.4	23.9	29.7	38.9	38.3	31.5
Or	32.4	23.7	20.3	30.8	30.0	28.2
Ab	28.9	25.8	1.2	1.7		
An			3.5	0.5	0.8	3.3
Corundum	7.3	7.1				
Nepheline						
Leucite						
Acmite						
Na Metasilicate						
Wo (Di)						
En (Di)						
Fs (Di			2.1	0.1	0.3	0.4
En (Hy)	1.9	1.3	11.2	3.8	6.4	7.6
Fs (Hy)	10.9	12.4				
Ol (Fo)						
Ol (Fa)			0.9	1.0	0.9	1.0
Ilmenite	2.0	2.0	2.9	1.1	1.7	2.0
Magnetite	3.1	3.4	0.1			
Apatite		0.4	99.9	99.9	99.9	99.9
Total:	99.9	99.9	28.0			

Notes: * = determined using Mg# = MgO/(MgO + Fe), mol%, with FeO calculated (as 80% of total Fe). ** = loss on ignition at 1025°C for 4 hr.

Table T12. Alteration minerals within basement units in Hole 1139A identified by X-ray diffraction.

Core, section, interval (cm)	Depth (mbsf)	Description	XRD identification
183-1139A-			
63R-1 (Piece 10, 49-50)	595.09	Vein and vesicle filling	Siderite
64R-5 (Piece 1, 1-5)	610.15	Green carbonate in vein	Calcite
65R-5 (Piece 1, 47-48)	619.11	Vesicle filling	Calcite, siderite
66R-2 (Piece 1, 127-128)	626.25	Vesicle filling with concentric bands	Calcite, siderite
67R-3 (Piece 1, 18)	635.36	Blue clay in breccia matrix	Saponite, quartz
67R-4 (Piece 2, 100-101)	637.68	Vesicle filling	Siderite, calcite, quartz
70R-3 (Piece 4, 66-67)	664.88	Vein cutting white alteration zone	Quartz, siderite, calcite
70R-4 (Piece 2, 110-116)	666.61	White alteration zone (whole rock)	Quartz, sanidine, siderite
70R-4 (Piece 2, 110-112)	666.61	Pink alteration zone (whole rock)	Quartz, sanidine, siderite
70R-4 (Piece 4A, 60-68)	666.11	Vesicle fill in white alteration zone	Quartz, siderite
71R-3 (Piece 2, 67-68)	673.57	Vein filling	Hematite, quartz, siderite, calcite
71R-3 (Piece 2, 67)	673.57	Vein filling	Hematite, quartz, siderite
71R-4 (Piece 1, 85-86)	675.05	Clast within light green breccia	Quartz, illite
71R-4 (Piece 1, 134-135)	675.54	Clast within white/gray breccia	Sanidine, quartz
71R-5 (Piece 1, 49-50)	676.15	White clast in breccia with red matrix	Quartz, sanidine
71R-6 (Piece 1, 55-57)	677.62	Clast and matrix in light green breccia	Quartz, sanidine

Note: XRD = X-ray diffraction.

Table T13. Characteristic inclinations and natural remanent magnetization intensities of discrete basalt samples from Hole 1139A.

Core, section, interval (cm)	Basement unit	Inclination (°)	NRM intensity (A/m)	Depth (mbsf)	Demagnetization range (°)
183-1139A-					
60R-2, 18-20	4	44	0.009	567.26	TH 260-620
64R-2, 41-43	7	66	1.07	606.11	TH 470-560
64R-4, 54-56	8	64	1.73	609.18	TH 530-620
65R-3, 22-24	10	66	1.09	616.92	TH 470-620
65R-5, 87-89	11	80	1.64	619.51	TH 470-620
71R-3, 98-100	18	62	0.22	673.88	TH 380-560

Notes: Inclination = characteristic inclination determined from progressive demagnetization. NRM = natural remanent magnetization. Demagnetization range = demagnetization method and characteristic inclination is determined from the component in this range. TH = thermal demagnetization.

Table T14. Index properties data from Site 1139. (**See table note.** Continued on next two pages.)

Core, section, interval (cm)	Depth (mbsf)	Water content (%)		Density (g/cm³)			Porosity (%)	Void ratio
		Bulk	Dry	Bulk	Dry	Grain		
183-1139A-								
3R-3, 111-113	23.11	36.1	56.6	1.69	1.08	2.69	59.8	1.49
3R-4, 39-41	23.89	39.9	66.5	1.62	0.97	2.64	63.2	1.72
4R-1, 102-104	29.52	38.4	62.3	1.64	1.01	2.63	61.5	1.60
4R-2, 114-116	31.14	38.5	62.6	1.67	1.03	2.75	62.7	1.68
4R-3, 115-117	32.65	37.0	58.7	1.68	1.06	2.68	60.5	1.53
4R-4, 114-116	34.14	38.8	63.3	1.65	1.01	2.71	62.6	1.67
5R-1, 51-53	38.51	42.3	73.4	1.59	0.92	2.68	65.7	1.92
5R-2, 31-33	39.81	42.5	74.1	1.60	0.92	2.73	66.4	1.97
6R-1, 111-113	48.61	47.1	88.9	1.52	0.80	2.64	69.6	2.29
7R-1, 107-109	58.07	47.5	90.4	1.51	0.79	2.62	69.8	2.31
7R-2, 107-109	59.57	48.5	94.0	1.49	0.77	2.59	70.4	2.38
7R-3, 106-108	61.06	46.4	86.5	1.52	0.82	2.62	68.9	2.21
8R-1, 67-69	67.17	42.9	75.0	1.58	0.91	2.68	66.3	1.96
9R-2, 53-55	76.87	51.7	107.2	1.47	0.71	2.74	74.1	2.87
9R-3, 111-113	78.95	47.2	89.3	1.54	0.81	2.78	70.8	2.42
9R-4, 96-98	80.30	48.8	95.2	1.49	0.76	2.64	71.0	2.45
10R-1, 99-101	86.49	47.7	91.3	1.54	0.80	2.82	71.5	2.51
10R-2, 25-27	87.25	46.7	87.5	1.53	0.82	2.71	69.9	2.32
11R-1, 47-49	95.57	44.5	80.2	1.59	0.88	2.84	69.0	2.22
12R-1, 108-110	105.78	46.3	86.1	1.56	0.84	2.84	70.5	2.39
12R-2, 126-128	107.46	43.7	77.8	1.58	0.89	2.76	67.7	2.09
12R-3, 120-122	108.90	45.6	83.7	1.33	0.72	1.76	59.1	1.44
12R-4, 128-130	110.48	44.4	79.8	1.58	0.88	2.78	68.4	2.17
12R-5, 130-132	112.00	48.5	94.3	1.54	0.79	2.95	73.1	2.72
12R-6, 116-118	113.36	44.7	80.8	1.58	0.88	2.83	69.1	2.23
13R-1, 117-119	115.57	46.1	85.7	1.53	0.82	2.65	68.9	2.22
13R-2, 108-110	116.98	47.0	88.8	1.55	0.82	2.82	71.0	2.45
13R-3, 115-117	118.55	50.5	101.8	1.47	0.73	2.67	72.6	2.65
13R-4, 125-127	120.15	48.3	93.6	1.53	0.79	2.87	72.4	2.62
13R-5, 141-143	121.81	52.8	111.8	1.46	0.69	2.81	75.4	3.07
13R-6, 130-132	123.20	47.7	91.2	1.53	0.80	2.78	71.2	2.47
14R-1, 126-128	125.26	46.8	88.1	1.52	0.81	2.66	69.6	2.29
14R-2, 119-121	126.69	43.0	75.4	1.61	0.92	2.83	67.6	2.08
14R-3, 123-125	128.23	44.7	80.7	1.56	0.86	2.71	68.1	2.13
14R-4, 136-138	129.86	46.0	85.2	1.56	0.84	2.80	70.0	2.33
14R-5, 110-112	131.10	47.0	88.8	1.53	0.81	2.72	70.2	2.36
15R-1, 106-108	134.56	50.5	101.9	1.47	0.73	2.61	72.2	2.59
15R-2, 134-136	136.34	45.4	83.0	1.53	0.84	2.59	67.8	2.10
15R-3, 138-140	137.88	49.5	98.0	1.51	0.76	2.79	72.7	2.67
15R-4, 106-108	139.06	47.3	89.9	1.48	0.78	2.49	68.6	2.19
16R-2, 38-40	145.08	48.5	94.0	1.53	0.79	2.86	72.4	2.62
16R-3, 16-18	146.36	49.7	98.8	1.51	0.76	2.81	73.1	2.72
16R-4, 33-37	148.03	52.2	109.2	1.47	0.70	2.77	74.7	2.96
16R-5, 88-90	150.08	50.4	101.4	1.49	0.74	2.73	73.0	2.70
17R-1, 38-40	153.18	49.2	96.9	1.55	0.79	3.12	74.7	2.95
17R-5, 37-39	159.17	47.4	90.0	1.53	0.80	2.74	70.6	2.41
17R-6, 34-36	160.64	53.0	112.7	1.43	0.67	2.62	74.2	2.88
18R-1, 115-117	163.65	47.4	90.3	1.51	0.79	2.63	69.9	2.32
18R-4, 65-67	167.65	50.7	102.9	1.48	0.73	2.72	73.2	2.74
19R-1, 110-111	173.20	38.2	61.8	1.66	1.02	2.68	61.8	1.62
19R-2, 63-64	174.23	36.4	57.3	1.72	1.09	2.80	61.1	1.57
19R-3, 20-21	175.30	45.5	83.5	1.57	0.86	2.82	69.7	2.30
19R-4, 121-122	177.81	41.2	70.0	1.64	0.96	2.81	65.8	1.92
19R-5, 87-88	178.97	42.8	74.8	1.65	0.95	3.05	69.0	2.22
19R-6, 22-23	179.32	38.8	63.5	1.67	1.02	2.77	63.2	1.72
20R-1, 44-46	182.14	40.2	67.2	1.65	0.99	2.78	64.6	1.83
21R-1, 130-132	192.60	44.6	80.6	1.56	0.86	2.67	67.8	2.11
21R-2, 113-115	193.93	40.9	69.1	1.62	0.96	2.71	64.6	1.83
21R-3, 130-132	195.60	42.4	73.5	1.61	0.93	2.78	66.6	1.99
21R-4, 118-120	196.98	40.7	68.8	1.63	0.96	2.74	64.8	1.84
21R-5, 108-110	198.38	34.9	53.6	1.73	1.13	2.75	59.0	1.44
21R-6, 109-111	199.89	33.5	50.4	1.74	1.16	2.69	56.9	1.32
22R-1, 117-119	202.07	31.7	46.5	1.81	1.23	2.81	56.0	1.27
22R-2, 14-16	202.54	33.1	49.5	1.76	1.18	2.74	57.0	1.32
22R-3, 55-57	203.95	38.3	62.0	1.69	1.05	2.85	63.3	1.72
23R-1, 120-122	211.70	37.0	58.7	1.72	1.08	2.86	62.1	1.64

Table T14 (continued).

Core, section, interval (cm)	Depth (mbsf)	Water content (%)		Density (g/cm³)			Porosity (%)	Void ratio
		Bulk	Dry	Bulk	Dry	Grain		
23R-2, 117-119	213.17	30.4	43.7	1.83	1.28	2.80	54.4	1.20
23R-3, 123-125	214.73	35.9	55.9	1.73	1.11	2.82	60.6	1.54
23R-4, 138-140	216.38	30.8	44.6	1.80	1.24	2.71	54.1	1.18
23R-5, 129-131	217.79	30.3	43.4	1.83	1.28	2.78	54.1	1.18
23R-6, 129-131	219.29	30.4	43.6	1.85	1.29	2.84	54.8	1.21
24R-1, 44-46	220.54	35.2	54.4	1.75	1.13	2.83	60.1	1.51
24R-2, 124-126	222.84	33.1	49.5	1.78	1.19	2.80	57.5	1.35
24R-3, 79-81	223.89	33.9	51.2	1.78	1.17	2.84	58.7	1.42
25R-1, 126-128	231.06	32.0	47.0	1.79	1.22	2.76	55.8	1.26
25R-2, 130-132	232.60	34.1	51.7	1.75	1.15	2.75	58.1	1.39
25R-3, 131-133	234.11	33.3	49.8	1.76	1.18	2.74	57.2	1.34
25R-4, 142-144	235.72	41.2	70.0	1.62	0.95	2.73	65.1	1.87
25R-5, 118-120	236.98	33.5	50.3	1.77	1.18	2.78	57.7	1.37
25R-6, 124-126	238.54	33.1	49.5	1.78	1.19	2.81	57.6	1.36
26R-1, 138-140	240.78	32.0	47.2	1.78	1.21	2.74	55.7	1.26
26R-2, 111-113	242.01	31.6	46.1	1.78	1.22	2.70	54.8	1.21
27R-1, 124-126	250.34	35.3	54.6	1.73	1.12	2.76	59.5	1.47
27R-2, 131-133	251.91	26.3	35.7	1.91	1.41	2.77	49.1	0.96
27R-3, 99-101	253.09	32.2	47.5	1.79	1.21	2.78	56.3	1.29
27R-4, 130-132	254.90	35.6	55.3	1.74	1.12	2.83	60.4	1.53
27R-5, 132-134	256.42	37.5	59.9	1.68	1.05	2.71	61.3	1.59
27R-6, 30-32	256.90	32.1	47.3	1.82	1.24	2.88	57.1	1.33
28R-1, 10-12	258.80	35.8	55.8	1.72	1.10	2.77	60.1	1.51
28R-1, 109-111	259.79	35.4	54.7	1.72	1.11	2.74	59.4	1.46
28R-2, 104-106	261.24	31.5	45.9	1.79	1.23	2.72	54.9	1.22
28R-3, 105-107	262.75	37.3	59.4	1.69	1.06	2.75	61.4	1.59
28R-4, 133-135	264.53	33.7	50.8	1.76	1.17	2.78	58.0	1.38
28R-5, 133-135	266.03	38.5	62.7	1.66	1.02	2.72	62.4	1.66
28R-6, 60-62	266.80	35.9	55.9	1.72	1.11	2.79	60.4	1.52
29R-1, 125-127	269.55	37.0	58.8	1.63	1.02	2.48	58.8	1.43
29R-2, 129-131	271.09	39.9	66.5	1.66	1.00	2.82	64.7	1.83
29R-3, 137-139	272.67	37.4	59.8	1.70	1.06	2.80	62.1	1.64
29R-4, 129-131	274.09	34.2	51.9	1.78	1.17	2.88	59.3	1.46
29R-5, 109-111	275.39	34.7	53.1	1.76	1.15	2.83	59.5	1.47
30R-1, 116-118	279.06	34.7	53.2	1.77	1.15	2.88	59.9	1.49
30R-2, 109-111	280.49	38.7	63.0	1.67	1.02	2.76	62.9	1.70
30R-4, 140-142	283.80	39.4	65.1	1.67	1.01	2.83	64.3	1.80
30R-5, 49-51	284.39	39.1	64.1	1.70	1.03	2.93	64.7	1.83
30R-6, 68-70	286.08	38.1	61.7	1.71	1.06	2.90	63.6	1.75
30R-7, 23-25	287.13	34.9	53.6	1.77	1.15	2.89	60.1	1.51
31R-1, 122-124	288.72	37.3	59.5	1.71	1.07	2.84	62.2	1.65
31R-2, 106-108	290.06	37.8	60.9	1.71	1.07	2.90	63.3	1.73
31R-3, 96-98	291.46	29.6	42.1	1.86	1.31	2.84	53.8	1.17
31R-4, 17-19	292.17	33.5	50.4	1.77	1.18	2.80	58.0	1.38
32R-1, 62-64	297.72	39.5	65.3	1.67	1.01	2.83	64.4	1.81
32R-2, 101-103	299.61	39.9	66.5	1.64	0.98	2.72	63.9	1.77
32R-3, 140-142	301.50	42.0	72.5	1.61	0.93	2.76	66.1	1.95
32R-4, 114-116	302.74	43.0	75.3	1.60	0.91	2.75	66.9	2.02
32R-5, 79-81	303.89	37.3	59.6	1.76	1.10	3.06	64.1	1.78
32R-6, 26-28	304.86	41.2	70.2	1.63	0.96	2.78	65.6	1.91
32R-7, 25-27	306.35	37.0	58.8	1.69	1.06	2.74	61.1	1.57
33R-1, 61-63	307.41	41.9	72.0	1.63	0.95	2.85	66.7	2.01
33R-2, 70-72	309.00	36.5	57.6	1.71	1.08	2.77	60.9	1.56
33R-3, 50-52	310.30	34.6	52.8	1.74	1.14	2.78	58.9	1.43
33R-4, 106-108	312.36	41.0	69.4	1.65	0.97	2.85	65.9	1.93
33R-5, 44-46	313.24	40.3	67.5	1.65	0.99	2.80	64.9	1.85
34R-1, 126-128	317.66	39.7	65.7	1.67	1.01	2.87	64.8	1.84
34R-2, 51-53	318.41	37.1	58.9	1.70	1.07	2.78	61.6	1.60
34R-3, 141-143	320.81	37.3	59.6	1.71	1.07	2.86	62.5	1.66
34R-4, 96-98	321.86	38.3	62.1	1.68	1.03	2.77	62.6	1.68
34R-5, 132-134	323.72	38.9	63.6	1.65	1.01	2.70	62.6	1.68
34R-7, 33-35	325.73	38.2	61.9	1.68	1.04	2.78	62.7	1.68
35R-2, 83-85	327.18	35.1	54.0	1.73	1.13	2.76	59.3	1.46
35R-3, 57-59	328.42	46.2	85.8	1.55	0.83	2.76	69.8	2.31
35R-4, 70-72	330.05	41.2	70.2	1.63	0.96	2.78	65.6	1.91
35R-5, 11-13	330.96	35.4	54.7	1.75	1.13	2.84	60.3	1.52
35R-6, 87-89	333.22	40.8	69.0	1.65	0.98	2.87	65.9	1.93
35R-7, 62-64	334.47	41.7	71.6	1.62	0.95	2.80	66.1	1.95
36R-1, 13-15	335.53	36.6	57.7	1.72	1.09	2.82	61.4	1.59

Table T14 (continued).

Core, section, interval (cm)	Depth (mbsf)	Water content (%)		Density (g/cm^3)			Porosity (%)	Void ratio
		Bulk	Dry	Bulk	Dry	Grain		
36R-2, 77-79	337.67	32.8	48.8	1.79	1.20	2.83	57.4	1.35
36R-3, 8-10	338.48	29.8	42.5	1.83	1.28	2.75	53.3	1.14
37R-1, 35-37	345.35	26.1	35.4	1.92	1.42	2.79	49.1	0.96
37R-2, 105-107	347.55	31.9	46.8	1.81	1.23	2.82	56.3	1.29
37R-3, 7-9	348.07	27.8	38.4	1.92	1.39	2.89	52.1	1.09
37R-4, 56-58	348.90	29.6	42.0	1.85	1.31	2.81	53.5	1.15
38R-1, 13-15	354.73	35.4	54.8	1.72	1.11	2.75	59.5	1.47
38R-2, 83-85	355.96	26.1	35.3	1.92	1.42	2.76	48.7	0.95
38R-3, 128-130	357.91	29.0	40.9	1.86	1.32	2.79	52.6	1.11
38R-4, 39-41	358.52	35.0	53.8	1.74	1.13	2.78	59.4	1.46
38R-4, 80-82	358.93	23.0	29.8	1.94	1.50	2.65	43.6	0.77
38R-5, 14-16	359.77	27.8	38.5	1.88	1.36	2.78	51.1	1.04
38R-6, 13-15	361.26	30.1	43.1	1.83	1.28	2.77	53.8	1.16
38R-7, 32-34	362.95	20.9	26.4	2.05	1.62	2.80	41.9	0.72
39R-1, 102-104	365.22	23.9	31.4	1.96	1.49	2.75	45.8	0.84
39R-2, 58-60	366.04	31.9	46.8	1.80	1.23	2.79	56.1	1.28
39R-2, 101-103	366.47	37.5	60.0	1.64	1.03	2.57	60.1	1.51
40R-1, 96-98	374.76	27.2	37.3	1.91	1.39	2.81	50.6	1.02
40R-2, 6-8	375.36	24.5	32.4	1.96	1.48	2.78	46.8	0.88
40R-3, 119-121	377.99	32.9	49.0	1.77	1.19	2.74	56.7	1.31
40R-4, 100-102	379.30	35.7	55.6	1.71	1.10	2.74	59.8	1.49
40R-5, 77-79	380.57	26.7	36.4	1.91	1.40	2.78	49.7	0.99
40R-6, 6-8	381.36	26.0	35.2	1.92	1.42	2.76	48.7	0.95
40R-6, 32-34	381.62	26.5	36.0	1.92	1.42	2.81	49.7	0.99
41R-2, 5-7	384.44	13.8	16.0	2.26	1.95	2.80	30.5	0.44
56R-3, 124-126	531.38	27.2	37.3	1.83	1.33	2.58	48.4	0.94
56R-4, 4-6	531.68	29.4	41.6	1.82	1.29	2.70	52.4	1.10
59R-1, 62-64	556.62	4.1	4.2	2.45	2.35	2.61	9.7	0.11
60R-1, 65-67	566.25	6.8	7.3	2.39	2.23	2.65	15.8	0.19
60R-2, 42-44	567.50	6.2	6.6	2.44	2.29	2.68	14.6	0.17
61R-1, 63-65	575.83	7.7	8.4	2.41	2.22	2.72	18.1	0.22
61R-3, 8-10	578.15	8.0	8.6	2.41	2.21	2.72	18.7	0.23
63R-1, 92-94	595.52	8.2	9.0	2.50	2.30	2.87	20.1	0.25
64R-1, 85-87	605.05	6.9	7.5	2.45	2.28	2.74	16.6	0.20
64R-2, 86-88	606.56	7.7	8.3	2.47	2.28	2.80	18.5	0.23
64R-3, 138-140	608.52	9.6	10.6	2.41	2.18	2.81	22.6	0.29
64R-4, 116-118	609.80	4.8	5.0	2.67	2.54	2.90	12.4	0.14
64R-5, 0-2	610.14	4.5	4.7	2.61	2.49	2.81	11.4	0.13
65R-1, 115-117	615.05	7.9	8.5	2.53	2.33	2.90	19.5	0.24
65R-2, 29-31	615.49	7.7	8.4	2.54	2.34	2.90	19.2	0.24
65R-3, 22-24	616.92	10.7	12.0	2.41	2.16	2.88	25.2	0.34
65R-5, 116-118	619.80	38.0	61.3	1.68	1.04	2.76	62.3	1.65
66R-1, 20-22	623.70	4.2	4.4	2.66	2.55	2.86	11.0	0.12
66R-2, 57-59	625.55	7.4	8.0	2.56	2.37	2.90	18.4	0.23
66R-3, 64-66	627.12	4.8	5.1	2.60	2.47	2.82	12.3	0.14
66R-5, 89-90	629.81	3.7	3.8	2.66	2.56	2.83	9.6	0.11
67R-4, 109-111	637.77	5.4	5.7	2.63	2.49	2.89	13.8	0.16
67R-5, 8-10	638.18	5.6	5.9	2.58	2.43	2.83	14.0	0.16
67R-5, 130-132	639.40	4.7	4.9	2.51	2.39	2.70	11.5	0.13
68R-3, 21-23	645.72	9.6	10.6	2.42	2.19	2.83	22.6	0.29
68R-4, 42-44	647.18	9.2	10.2	2.45	2.22	2.85	22.1	0.28
68R-7, 146-148	651.69	7.9	8.6	2.42	2.23	2.74	18.7	0.23
69R-1, 98-100	652.98	1.2	1.2	2.77	2.74	2.83	3.3	0.03
69R-2, 70-72	654.20	3.5	3.6	2.53	2.45	2.68	8.6	0.09
70R-1, 17-20	661.67	8.4	9.2	2.40	2.20	2.74	19.7	0.25
70R-2, 141-145	664.13	6.7	7.2	2.49	2.32	2.78	16.4	0.20
70R-3, 64-68	664.86	5.1	5.4	2.44	2.31	2.63	12.2	0.14
71R-1, 4-6	670.90	3.4	3.5	2.48	2.40	2.61	8.2	0.09
71R-2, 3-5	671.88	5.3	5.6	2.49	2.36	2.70	12.8	0.15
71R-3, 98-100	673.88	7.1	7.7	2.48	2.31	2.79	17.3	0.21
71R-4, 8-10	674.28	39.9	66.3	1.67	1.00	2.86	65.0	1.86
71R-7, 29-31	678.74	38.4	62.3	1.66	1.02	2.71	62.2	1.65
72R-1, 111-113	681.41	4.1	4.3	2.54	2.44	2.71	10.1	0.11
72R-2, 11-13	681.84	5.5	5.9	2.46	2.33	2.68	13.3	0.15
72R-3, 27-29	682.89	36.5	57.6	1.69	1.07	2.71	60.4	1.53
72R-4, 22-24	684.22	3.0	3.1	2.56	2.48	2.68	7.4	0.08
73R-1, 48-50	689.98	5.6	5.9	2.45	2.31	2.67	13.4	0.15
73R-2, 42-44	691.42	37.1	59.1	1.67	1.05	2.65	60.4	1.53
73R-3, 37-39	692.87	4.7	4.9	2.51	2.39	2.70	11.4	0.13

Note: This table is also available in **ASCII format.**

Table T15. Compressional wave velocity, Site 1139. (See table note. Continued on next three pages.)

Core, section, interval (cm)	Depth (mbsf)	Direction	Velocity (m/s)
183-1139A-			
3R-3, 39	22.39	LX	1850
3R-3, 112	23.12	LX	1989
3R-4, 37	23.87	LX	1903
4R-1, 103	29.53	LX	1898
4R-2, 37	30.37	LX	1810
4R-2, 114	31.14	LX	1819
4R-3, 49	31.99	LX	1835
4R-3, 117	32.67	LX	1787
4R-4, 59	33.59	LX	1852
4R-4, 113	34.13	LX	1834
5R-1, 52	38.52	LX	1906
5R-1, 116	39.16	LX	1814
5R-2, 31	39.81	LX	1844
6R-1, 112	48.62	LX	1801
7R-1, 109	58.09	LX	1805
7R-2, 49	58.99	LX	1763
7R-2, 108	59.58	LX	1753
7R-3, 48	60.48	LX	1752
7R-3, 108	61.08	LX	1806
9R-2, 54	76.88	LX	1823
9R-2, 137	77.71	LX	1808
9R-3, 95	78.79	LX	1810
9R-3, 113	78.97	LX	1800
10R-1, 98	86.48	LX	1744
10R-2, 27	87.27	LX	1775
11R-1, 48	95.58	LX	1827
11R-1, 91	96.01	LX	1785
12R-1, 40	105.10	LX	1845
12R-1, 110	105.80	LX	1841
12R-2, 47	106.67	LX	1781
12R-2, 75	106.95	LX	1835
12R-2, 127	107.47	LX	1804
12R-3, 34	108.04	LX	1904
12R-3, 121	108.91	LX	1824
12R-4, 26	109.46	LX	1785
12R-4, 129	110.49	LX	1798
12R-5, 40	111.10	LX	1855
12R-5, 133	112.03	LX	1885
12R-6, 52	112.72	LX	1799
12R-6, 117	113.37	LX	1863
13R-1, 76	115.16	LX	1902
13R-1, 118	115.58	LX	2003
13R-2, 17	116.07	LX	1978
13R-2, 109	116.99	LX	1983
13R-3, 32	117.72	LX	2049
13R-3, 116	118.56	LX	2014
13R-4, 50	119.40	LX	2040
13R-4, 127	120.17	LX	2001
13R-5, 64	121.04	LX	1910
13R-5, 141	121.81	LX	1972
13R-6, 53	122.43	LX	2039
13R-6, 131	123.21	LX	1802
13R-7, 13	123.53	LX	1983
14R-1, 31	124.31	LX	1936
14R-1, 124	125.24	LX	2042
14R-2, 41	125.91	LX	1988
14R-2, 120	126.70	LX	2052
14R-3, 20	127.20	LX	1995
14R-3, 125	128.25	LX	2027
14R-4, 62	129.12	LX	1904
14R-4, 138	129.88	LX	2051
14R-5, 39	130.39	LX	2082
14R-5, 111	131.11	LX	2050
14R-6, 19	131.69	LX	1958
15R-1, 21	133.71	LX	2016
15R-1, 106	134.56	LX	2010
15R-2, 33	135.33	LX	2080
15R-2, 136	136.36	LX	2002
15R-3, 31	136.81	LX	1938
15R-3, 139	137.89	LX	1980
15R-4, 43	138.43	LX	1995
15R-4, 108	139.08	LX	1988
15R-5, 14	139.64	LX	1989
16R-1, 18	143.38	LX	2110
16R-1, 115	144.35	LX	2030
16R-2, 40	145.10	LX	1965
16R-2, 109	145.79	LX	1970
16R-3, 17	146.37	LX	1997
16R-3, 137	147.57	LX	2013
16R-4, 35	148.05	LX	1990
16R-4, 141	149.11	LX	1980
16R-5, 89	150.09	LX	2016
16R-5, 132	150.52	LX	1997
16R-6, 25	150.95	LX	2027
17R-1, 40	153.20	LX	2037
17R-2, 86	155.16	LX	2037
17R-4, 13	157.43	LX	2039
17R-5, 38	159.18	LX	1953
17R-6, 35	160.65	LX	1993
18R-1, 18	162.68	LX	2049
18R-1, 121	163.71	LX	2005
18R-2, 28	164.28	LX	2107
18R-3, 31	165.81	LX	1971
18R-4, 67	167.67	LX	1994
18R-5, 48	168.98	LX	2072
19R-1, 38	172.48	LX	2177
19R-1, 112	173.22	LX	2183
19R-2, 64	174.24	LX	2089
19R-2, 119	174.79	LX	2026
19R-3, 20	175.30	LX	2026
19R-3, 139	176.49	LX	2055
19R-4, 28	176.88	LX	2090
19R-4, 121	177.81	LX	2093
19R-5, 16	178.26	LX	2355
19R-5, 89	178.99	LX	2238
19R-6, 19	179.29	LX	2164
20R-1, 46	182.16	LX	2132
20R-1, 46	182.16	LX	2216
21R-1, 17	191.47	CZ	2276
21R-1, 131	192.61	CZ	3263
21R-1, 131	192.61	CY	2173
21R-2, 113	193.93	CZ	2251
21R-2, 114	193.94	CY	2270
21R-3, 10	194.40	CZ	2228
21R-3, 121	195.51	CZ	2216
21R-3, 121	195.51	CY	2200
21R-3, 131	195.61	CZ	2168
21R-4, 119	196.99	CZ	2393
21R-4, 119	196.99	CZ	2174
21R-4, 119	196.99	CY	2166
21R-5, 109	198.39	CZ	2377
21R-5, 109	198.39	CY	2376
21R-6, 110	199.90	CZ	2378
21R-6, 110	199.90	CY	2330
22R-1, 56	201.46	CZ	2491
22R-1, 56	201.46	CY	2473
22R-1, 118	202.08	CZ	2340
22R-1, 118	202.08	CY	2245
22R-2, 15	202.55	CZ	2294
22R-2, 15	202.55	CY	2253
22R-3, 56	203.96	CZ	2270
22R-3, 56	203.96	CY	2293
23R-1, 22	210.72	CZ	2577
23R-1, 22	210.72	CY	2548
23R-1, 121	211.71	CZ	2251

Table T15 (continued).

Core, section, interval (cm)	Depth (mbsf)	Direction	Velocity (m/s)
23R-1, 121	211.71	CY	2309
23R-2, 51	212.51	CZ	2435
23R-2, 51	212.51	CY	2457
23R-2, 118	213.18	CZ	2470
23R-2, 118	213.18	CY	2487
23R-3, 29	213.79	CZ	2300
23R-3, 29	213.79	CY	2311
23R-3, 124	214.74	CZ	2306
23R-3, 124	214.74	CY	2299
23R-4, 28	215.28	CZ	2273
23R-4, 28	215.28	CY	2276
23R-4, 139	216.39	CZ	2519
23R-4, 139	216.39	CY	2492
23R-5, 27	216.77	CZ	2495
23R-5, 27	216.77	CY	2401
23R-5, 130	217.80	CZ	2560
23R-5, 130	217.80	CY	2458
23R-6, 25	218.25	CZ	2532
23R-6, 25	218.25	CY	2454
23R-6, 25	218.25	CY	2498
23R-6, 130	219.30	CZ	2529
23R-6, 130	219.30	CY	2495
24R-1, 38	220.48	CZ	2317
24R-1, 38	220.48	CY	2301
24R-1, 45	220.55	CZ	2309
24R-1, 45	220.55	CY	2327
24R-1, 87	220.97	CZ	2361
24R-1, 87	220.97	CY	2326
24R-2, 125	222.85	CZ	2425
24R-2, 125	222.85	CY	2458
24R-3, 80	223.90	CZ	2440
25R-1, 40	230.20	CZ	2515
25R-1, 40	230.20	CY	2501
25R-1, 127	231.07	CZ	2493
25R-1, 127	231.07	CY	2532
25R-2, 33	231.63	CZ	2435
25R-2, 33	231.63	CY	2454
25R-2, 131	232.61	CZ	2396
25R-2, 131	232.61	CY	2425
25R-3, 24	233.04	CZ	2493
25R-3, 133	234.13	CZ	2376
25R-3, 133	234.13	CY	2424
25R-4, 31	234.61	CZ	2352
25R-4, 144	235.74	CZ	2308
25R-4, 144	235.74	CY	2398
25R-4, 144	235.74	CY	2378
25R-5, 26	236.06	CZ	2317
25R-5, 119	236.99	CZ	2458
25R-5, 119	236.99	CY	2460
25R-6, 27	237.57	CZ	2338
25R-6, 27	237.57	CY	2350
25R-6, 125	238.55	CZ	2407
25R-6, 125	238.55	CY	2436
25R-7, 18	238.98	CZ	2488
25R-7, 18	238.98	CY	2530
26R-1, 51	239.91	CZ	2403
26R-1, 51	239.91	CY	2439
26R-1, 139	240.79	CZ	2465
26R-1, 139	240.79	CY	2528
26R-2, 112	242.02	CZ	2374
26R-2, 112	242.02	CY	2418
26R-3, 6	242.46	CZ	2448
26R-3, 6	242.46	CY	2449
27R-1, 125	250.35	CZ	2434
27R-1, 125	250.35	CY	2418
27R-2, 132	251.92	CZ	2578
27R-2, 132	251.92	CY	2691
27R-3, 100	253.10	CZ	2446
27R-3, 100	253.10	CY	2517
27R-4, 131	254.91	CZ	2480
27R-4, 131	254.91	CY	2524
27R-5, 133	256.43	CZ	2354
27R-5, 133	256.43	CY	2423
27R-6, 31	256.91	CZ	2366
27R-6, 31	256.91	CY	2426
28R-1, 10	258.80	CZ	2334
28R-1, 10	258.80	CY	2369
28R-1, 110	259.80	CZ	2334
28R-1, 110	259.80	CY	2415
28R-2, 105	261.25	CZ	2522
28R-2, 105	261.25	CY	2555
28R-3, 107	262.77	CZ	2485
28R-3, 107	262.77	CY	2555
28R-4, 134	264.54	CZ	2358
28R-4, 134	264.54	CY	2425
28R-5, 136	266.06	CZ	2404
28R-5, 136	266.06	CY	2467
28R-6, 60	266.80	CZ	2337
29R-1, 126	269.56	CZ	2405
29R-1, 126	269.56	CY	2458
29R-2, 130	271.10	CZ	2352
29R-2, 130	271.10	CY	2405
29R-3, 138	272.68	CZ	2349
29R-3, 138	272.68	CY	2360
29R-4, 129	274.09	CZ	2394
29R-4, 129	274.09	CY	2447
29R-5, 110	275.40	CZ	2461
29R-5, 110	275.40	CY	2528
30R-1, 30	278.20	CY	2679
30R-1, 30	278.20	CZ	2698
30R-1, 117	279.07	CZ	2729
30R-1, 117	279.07	CY	2757
30R-2, 110	280.50	CY	2732
30R-2, 110	280.50	CZ	2640
30R-3, 69	281.59	CY	2741
30R-3, 69	281.59	CZ	2649
30R-4, 110	283.50	CY	2682
30R-4, 110	283.50	CZ	2559
30R-4, 141	283.81	CY	2557
30R-4, 141	283.81	CZ	2452
30R-5, 50	284.40	CY	2629
30R-5, 50	284.40	CZ	2586
30R-6, 69	286.09	CY	2599
30R-6, 69	286.09	CZ	2469
30R-7, 21	287.11	CZ	2498
30R-7, 24	287.14	CY	2550
31R-1, 28	287.78	CY	3750
31R-1, 28	287.78	CZ	3557
31R-1, 123	288.73	CY	2545
31R-1, 123	288.73	CZ	2479
31R-2, 36	289.36	CY	2532
31R-2, 36	289.36	CZ	2487
31R-2, 107	290.07	CY	2726
31R-2, 107	290.07	CZ	2642
31R-3, 57	291.07	CY	2593
31R-3, 57	291.07	CZ	2518
31R-3, 97	291.47	CY	2669
31R-3, 97	291.47	CZ	2635
31R-4, 18	292.18	CY	2632
31R-4, 18	292.18	CZ	2595
32R-1, 64	297.74	CY	2613
32R-1, 64	297.74	CZ	2489
32R-2, 102	299.62	CY	2514
32R-2, 102	299.62	CZ	2534

Table T15 (continued).

Core, section, interval (cm)	Depth (mbsf)	Direction	Velocity (m/s)
32R-3, 20	300.30	CY	2665
32R-3, 20	300.30	CZ	2662
32R-3, 140	301.50	CY	2504
32R-3, 140	301.50	CZ	2451
32R-4, 115	302.75	CY	2412
32R-4, 115	302.75	CZ	2390
32R-5, 81	303.91	CY	2606
32R-5, 81	303.91	CZ	2543
32R-6, 27	304.87	CY	2397
32R-6, 27	304.87	CZ	2637
32R-7, 24	306.34	CZ	2459
32R-7, 27	306.37	CY	2541
33R-1, 63	307.43	CY	2560
33R-1, 63	307.43	CZ	2521
33R-2, 74	309.04	CY	2568
33R-2, 74	309.04	CZ	2500
33R-3, 52	310.32	CY	2589
33R-3, 52	310.32	CZ	2589
33R-3, 125	311.05	CY	2590
33R-3, 125	311.05	CZ	2540
33R-4, 108	312.38	CY	2487
33R-4, 108	312.38	CZ	2447
33R-5, 46	313.26	CY	2505
33R-5, 46	313.26	CZ	2478
34R-1, 128	317.68	CY	2476
34R-1, 128	317.68	CZ	2433
34R-2, 52	318.42	CY	2543
34R-2, 52	318.42	CZ	2500
34R-3, 143	320.83	CY	2558
34R-3, 143	320.83	CZ	2493
34R-4, 34	321.24	CY	2314
34R-4, 34	321.24	CZ	2260
34R-4, 98	321.88	CY	2544
34R-4, 98	321.88	CZ	2505
34R-5, 133	323.73	CY	2508
34R-5, 133	323.73	CZ	2406
34R-6, 42	324.32	CY	2512
34R-6, 42	324.32	CZ	2487
34R-7, 34	325.74	CY	2539
34R-7, 34	325.74	CZ	2520
35R-2, 83	327.18	CY	2632
35R-2, 83	327.18	CZ	2628
35R-3, 53	328.38	CY	2392
35R-3, 53	328.38	CZ	2301
35R-4, 22	329.57	CY	2477
35R-4, 22	329.57	CZ	2409
35R-4, 78	330.13	CY	2532
35R-4, 78	330.13	CZ	2481
35R-5, 12	330.97	CY	2657
35R-5, 12	330.97	CZ	2588
35R-6, 88	333.23	CY	2553
35R-6, 88	333.23	CZ	2503
35R-7, 62	334.47	CY	2557
35R-7, 62	334.47	CZ	2521
36R-1, 14	335.54	CY	2767
36R-1, 14	335.54	CZ	2771
36R-2, 37	337.27	CY	2578
36R-2, 37	337.27	CZ	2555
36R-2, 79	337.69	CY	2752
36R-2, 79	337.69	CZ	2679
36R-3, 10	338.50	CY	2880
36R-3, 10	338.50	CZ	2815
37R-1, 36	345.36	CY	2929
37R-1, 36	345.36	CZ	2881
37R-2, 37	346.87	CY	4331
37R-2, 37	346.87	CZ	3543
37R-2, 106	347.56	CY	2814
37R-2, 106	347.56	CZ	2751
37R-3, 9	348.09	CY	2681
37R-3, 9	348.09	CZ	2704
37R-4, 58	348.92	CY	2605
37R-4, 58	348.92	CZ	2586
38R-1, 14	354.74	CY	2979
38R-1, 14	354.74	CZ	2897
38R-2, 84	355.97	CY	2995
38R-2, 84	355.97	CZ	2896
38R-3, 28	356.91	CY	2844
38R-3, 28	356.91	CZ	2678
38R-3, 130	357.93	CZ	2818
38R-3, 130	357.93	CY	2932
38R-4, 39	358.52	CY	2662
38R-4, 39	358.52	CZ	2535
38R-4, 81	358.94	CY	4191
38R-4, 81	358.94	CZ	3907
38R-5, 15	359.78	CY	2791
38R-5, 15	359.78	CZ	2796
38R-6, 14	361.27	CY	2777
38R-6, 14	361.27	CZ	2770
38R-7, 34	362.97	CY	2993
38R-7, 34	362.97	CZ	2999
39R-1, 102	365.22	CY	2938
39R-1, 102	365.22	CZ	2931
39R-2, 60	366.06	CY	2880
39R-2, 60	366.06	CZ	2726
39R-2, 104	366.50	CY	2948
39R-2, 104	366.50	CZ	2748
40R-1, 97	374.77	CY	3101
40R-1, 97	374.77	CZ	2985
40R-2, 7	375.37	CY	3045
40R-2, 7	375.37	CZ	3021
40R-3, 120	378.00	CY	3022
40R-3, 120	378.00	CZ	2958
40R-4, 101	379.31	CY	2676
40R-4, 101	379.31	CZ	2644
40R-4, 130	379.60	CY	2775
40R-4, 130	379.60	CZ	2708
40R-5, 78	380.58	CY	2962
40R-5, 78	380.58	CZ	2966
40R-6, 7	381.37	CY	3301
40R-6, 7	381.37	CZ	3203
40R-6, 33	381.63	CY	3112
40R-6, 33	381.63	CZ	3036
41R-1, 6	384.44	CX	3663
41R-1, 6	384.44	CY	3153
41R-1, 6	384.44	CZ	3225
41R-1, 10	384.48	CX	3915
41R-1, 10	384.48	CY	3491
41R-1, 10	384.48	CZ	3324
56R-3, 98	531.12	MX	2590
56R-3, 110	531.24	MX	2577
56R-3, 140	531.54	MX	2792
56R-4, 5	531.68	MX	2705
59R-1, 52	556.52	MX	4770
59R-1, 63	556.63	MX	4547
60R-1, 66	566.26	MX	3802
60R-1, 99	566.59	MX	3898
60R-2, 19	567.27	MX	4001
60R-2, 43	567.51	MX	3889
61R-1, 49	575.69	MX	3791
61R-1, 64	575.84	MX	3675
61R-1, 131	576.51	MX	3540
61R-2, 19	576.81	MX	3405
61R-2, 23	576.85	MX	3322
61R-2, 47	577.09	MX	3496
61R-3, 9	578.16	MX	3649
63R-1, 95	595.55	MX	4031
63R-1, 110	595.70	MX	3883
64R-1, 79	604.99	MX	4245
64R-1, 120	605.40	MX	4179
64R-2, 4	605.74	MX	4424
64R-2, 42	606.12	MX	4710
64R-2, 68	606.38	MX	4513

Table T15 (continued).

Core, section, interval (cm)	Depth (mbsf)	Direction	Velocity (m/s)
64R-2, 79	606.49	MX	4094
64R-2, 85	606.55	MX	4409
64R-3, 139	608.53	MX	3641
64R-4, 53	609.17	MX	4989
64R-4, 67	609.31	MX	4535
64R-4, 129	609.93	MX	4465
64R-4, 141	610.05	MX	5268
64R-5, 26	610.40	MX	4131
65R-1, 22	614.12	MX	3833
65R-1, 54	614.44	MX	4420
65R-1, 90	614.80	MX	4810
65R-1, 96	614.86	MX	4183
65R-1, 120	615.10	MX	5218
65R-2, 6	615.26	MX	5039
65R-2, 35	615.55	MX	4896
65R-2, 128	616.48	MX	3512
65R-3, 23	616.93	MX	3519
65R-3, 62	617.32	MX	4242
65R-3, 71	617.41	MX	4313
65R-3, 80	617.50	MX	4231
65R-3, 86	617.56	MX	4844
65R-3, 104	617.74	MX	3234
65R-5, 20	618.84	MX	4555
65R-5, 42	619.06	MX	4475
65R-5, 58	619.22	MX	4175
65R-5, 65	619.29	MX	4574
65R-5, 87	619.51	MX	6068
65R-5, 109	619.73	MX	4600
66R-1, 60	624.10	MX	4299
66R-1, 65	624.15	MX	4570
66R-1, 71	624.21	MX	4636
66R-2, 57	625.55	MX	4459
66R-2, 88	625.86	MX	4735
66R-2, 126	626.24	MX	4488
66R-3, 65	627.13	MX	4336
66R-5, 69	629.61	MX	4868
66R-5, 88	629.80	MX	5257
67R-4, 110	637.78	MX	4716
67R-5, 32	638.42	MX	4545
67R-5, 131	639.41	MX	4619
68R-3, 107	646.58	MX	3765
68R-4, 8	646.84	MX	4121
68R-4, 68	647.44	MX	4173
68R-7, 147	651.70	MX	3713
69R-1, 39	652.39	MX	5140
69R-1, 71	652.71	MX	5265
69R-1, 99	652.99	MX	5469
69R-2, 60	654.10	MX	4372
69R-2, 71	654.21	MX	5014
69R-2, 79	654.29	MX	4582
70R-1, 22	661.72	MX	3109
70R-1, 22	661.72	CY	3132
70R-1, 22	661.72	CZ	3190
70R-2, 142	664.14	CX	4884
70R-2, 142	664.14	CY	4177
70R-2, 142	664.14	CZ	4420
71R-1, 87	671.77	MX	5017
71R-2, 5	671.90	MX	4417
71R-2, 24	672.09	MX	4371
71R-2, 83	672.68	MX	4131
71R-3, 33	673.23	MX	4090
71R-3, 43	673.33	MX	3935
71R-3, 99	673.89	MX	4276
71R-3, 116	674.06	MX	4103
71R-7, 12	678.57	MX	4111
72R-1, 35	680.65	MX	4252
72R-2, 12	681.85	MX	3818
72R-3, 28	682.90	MX	4407
72R-3, 114	683.76	MX	4709
72R-4, 23	684.23	MX	5107
73R-1, 49	689.99	MX	4396
73R-2, 43	691.43	MX	4784
73R-2, 123	692.23	MX	4194
73R-3, 23	692.73	MX	4321
73R-3, 135	693.85	MX	4434

Notes: Type of samples is denoted by prefix: L = split-core section with core liner, C = oriented cubes, M = oriented minicore, and no prefix = split core sections without core liner. The directions of the velocity measurements are represented by X (into the core), Z (along the core), and Y (across the core). This table is also available in **ASCII format**.

Table T16. Thermal conductivity values for Site 1139.

Core, section, interval (cm)	Depth (mbsf)	Thermal conductivity (W/[m·K])
183-1139A-		
3R-3, 75	22.75	0.94
4R-3, 75	32.25	1.10
5R-1, 75	38.75	0.95
6R-1, 75	48.25	0.81
7R-3, 75	60.75	0.91
8R-1, 41	66.91	0.84
9R-5, 16	81.00	0.80
10R-2, 32	87.32	0.88
11R-1, 75	95.85	0.95
12R-3, 75	108.45	0.87
13R-4, 54	119.44	0.77
14R-3, 75	127.75	0.80
15R-3, 75	137.25	0.81
16R-4, 80	148.50	0.84
17R-3, 75	156.55	0.80
18R-4, 75	167.75	0.85
19R-4, 75	177.35	1.02
20R-4, 75	186.95	0.99
59R-1, 55-68	556.62	1.78
60R-1, 90-108	566.59	2.36
60R-2, 14-26	567.28	3.74
61R-2, 45-60	577.15	1.52
63R-1, 33-39	594.96	1.50
64R-1, 99-104	604.56	1.23
65R-3, 44-49	617.17	1.54
66R-3, 1-10	626.54	1.07
67R-5, 45-55	638.60	0.66
69R-3, 1-13	654.97	1.40
70R-4, 43-53	665.99	2.06
71R-5, 1-13	675.73	1.68
72R-2, 1-13	681.80	2.20
73R-2, 21-35	691.28	2.18

Note: This table is also available in **ASCII format.**

Table T17. Carbon, nitrogen, sulfur, and hydrogen analyses of sediments from Site 1139.

Core, Section	Depth (mbsf)	$CaCO_3$ (wt%)	IC (wt%)	OC (wt%)	N (wt%)	S (wt%)	H (wt%)
183-1139A-							
1R-5	4.82–4.83	64.06	7.69	0.24	0.03	BD	0.42
2R-3	13.42–13.43	75.24	9.03				
3R-1	19.89–19.90	73.61	8.84				
4R-1	29.39–29.40	83.34	10.01	0.30	0.02	BD	0.17
5R-1	38.89–38.90	76.32	9.16				
6R-1	48.39–48.40	60.65	7.28				
7R-1	57.89–57.90	51.33	6.16	0.15	0.05	0.14	0.34
8R-1	67.09–67.10	72.89	8.75				
9R-2	77.23–77.24	32.78	3.94				
10R-1	86.39–86.40	24.94	2.99	0.36	0.06	0.38	0.42
11R-1	95.99–96.00	62.13	7.46				
12R-1	105.59–105.60	28.08	3.37				
13R-1	115.29–115.30	7.46	0.90	0.25	0.05	0.41	0.36
14R-1	124.89–124.90	21.19	2.54				
15R-1	134.39–134.40	19.92	2.39				
16R-1	144.09–144.10	31.99	3.84	0.18	0.03	BD	0.31
17R-1	153.69–153.70	32.61	3.92				
18R-1	163.39–163.40	58.51	7.03				
19R-1	172.99–173.00	58.22	6.99	0.11	BD	0.15	0.16
20R-1	182.59–182.60	52.78	6.34				
21R-1	192.19–192.20	49.30	5.92				
22R-1	201.79–201.80	70.91	8.51	0.03	BD	BD	0.20
23R-1	211.39–211.40	70.56	8.47				
24R-1	220.99–221.00	44.09	5.29				
25R-1	230.69–230.70	64.08	7.69	0.17	0.02	BD	0.24
26R-1	240.29–240.30	39.75	4.77				
27R-1	249.99–250.00	32.34	3.88				
28R-1	259.59–259.60	14.83	1.78	0.11	0.01	0.27	0.52
29R-1	269.19–269.20	20.41	2.45				
30R-1	278.79–278.80	32.04	3.85				
31R-1	288.39–288.40	41.23	4.95	0.13	0.02	BD	0.32
32R-1	297.99–298.00	45.25	5.43				
33R-1	307.69–307.70	41.77	5.02				
34R-1	317.29–317.30	38.54	4.63	0.20	0.02	BD	0.31
36R-1	336.29–336.30	47.33	5.68				
37R-1	345.89–345.90	66.70	8.01				
38R-3	356.92–356.94	55.46	6.66	0.19	0.03	BD	0.30
39R-1	365.09–365.10	71.62	8.60				
40R-1	374.99–375.00	47.54	5.71				
40R-CC	382.32–382.34	93.54	11.23	0.04	0.03	BD	0.03

Note: BD = below detection limit. This table is also available in **ASCII format.**

Table T18. Carbon, nitrogen, sulfur, and hydrogen analyses of volcanic and volcaniclastic rocks from Site 1139.

Core, section, piece	Depth (mbsf)	TC (wt%)	N (wt%)	S (wt%)	H (wt%)
183-1139A-					
51R-1	479.50-479.53	0.02	BD	BD	0.12
56R-3	531.06-531.09	0.02	BD	0.04	0.80
57R-1 (Piece 21)	538.14-538.17	0.01	BD	BD	0.07
60R-2 (Piece 15)	568.22-568.27	0.55	BD	BD	0.07
61R-1 (Piece 1F)	575.98-576.01	0.50	0.01	BD	BD
62R-2 (Piece 1)	586.83-586.85	0.01	BD	BD	0.46
64R-1 (Piece 13B)	605.05-605.07	1.20	0.01	BD	0.16
64R-4 (Piece 3F)	609.42-609.46	0.42	BD	BD	0.21
65R-2 (Piece 1A)	615.35-615.39	0.97	BD	BD	0.19
65R-3 (Piece 5C)	617.60-617.63	1.86	BD	BD	0.15
65R-5 (Piece 1D)	619.45-619.49	0.45	0.01	BD	0.12
66R-3 (Piece 1B)	626.92-626.95	0.49	BD	BD	0.16
66R-7 (Piece 3)	630.77-630.81	2.09	BD	BD	0.11
67R-5 (Piece 9)	639.15-639.18	1.53	BD	BD	0.10
68R-4 (Piece 1)	647.18-647.21	0.81	BD	BD	0.11
68R-6 (Piece 1)	650.19-650.22	0.04	BD	BD	0.29
69R-2 (Piece 1)	653.51-653.54	0.41	BD	BD	0.16
70R-1 (Piece 2A)	661.67-661.70	0.03	BD	BD	0.24
70R-2 (Piece 1F)	664.13-664.17	1.74	BD	BD	0.17
71R-4 (Piece 1I)	675.55-675.58	1.51	0.01	BD	0.19
71R-7 (Piece 1B)	678.70-678.72	0.34	BD	BD	0.09
72R-2 (Piece 2B)	682.30-682.33	0.53	BD	BD	0.10
73R-3 (Piece 2B)	692.89-692.92	0.82	BD	BD	0.09

Note: BD = below detection limit. This table is also available in **ASCII format.**

Table T19. Summary of logging operations.

Date (January 1999)	Time (UTC)	Logging operations
20	0200	Hole preparation complete. Rig up wireline.
	0355	Rig into hole with NGT-DSI-DITE(+TAP).
	0505	Bridge at 593 mbsf prevents going down to bottom of hole. Start logging upward at 900 ft/hr. No response from any of the tools. Pull out of hole.
	0640	Tool back on the rig floor. Check for tool failure.
	0815	DSI is replaced by LSS.
	0855	Rig into hole with NGT-LSS-DITE(+TAP).
	1000	Log upward at 900 ft/hr from 593 mbsf to the end of pipe.
	1155	Tool back on rig floor. End of logging operations. Pull out of hole.

Note: Drillers total depth = 2121 mbsf, water depth = 1427 mbrf, end of pipe = 101.7 mbsf. Tool acronyms are defined in **"Downhole Measurements,"** p. 39, in the "Explanatory Notes" chapter.